BUOYANCY-THERMOCAPILLARY CONVECTION OF VOLATILE FLUIDS IN CONFINED AND SEALED GEOMETRIES

A Dissertation
Presented to
The Academic Faculty

By

Tongran Qin

In Partial Fulfillment
of the Requirements for the Degree
Doctor of Philosophy
in

George W. Woodruff School of Mechanical Engineering
Georgia Institute of Technology
May 2016

BUOYANCY-THERMOCAPILLARY CONVECTION OF VOLATILE FLUIDS IN CONFINED AND SEALED GEOMETRIES

Approved by:

Dr. Roman O. Grigoriev, Co-chair
Associate Professor, School of Physics
Georgia Institute of Technology

Dr. Minami Yoda, Co-chair
Professor, George W. Woodruff School of Mechanical Engineering
Georgia Institute of Technology

Dr. G. Paul Neitzel
Professor, George W. Woodruff School of Mechanical Engineering
Georgia Institute of Technology

Dr. Marc K. Smith
Professor, George W. Woodruff School of Mechanical Engineering
Georgia Institute of Technology

Dr. Michael Schatz
Professor, School of Physics
Georgia Institute of Technology

Date Approved: January 6, 2016

ACKNOWLEDGMENTS

TABLE OF CONTENTS

LIST OF TABLES

LIST OF FIGURES

NOMENCLATURE

α	Thermal Diffusivity
β	Coefficient of Thermal Expansion
χ	Accommodation Coefficient
$\delta_{d,v}$	Standard Kronecker Delta
Γ	Aspect Ratio
γ	Temperature Coefficient of Surface Tension
μ	Dynamic Viscosity
μ_i	Reduced Mass
ν	Kinematic Viscosity
κ	Curvature of the Interface
κ_{av}	Collision Parameter
λ	Wavelength of the Convection Pattern
λ_c	Coefficient of Bulk Viscosity
Ω	Interfacial Resistance associated with Phase Change
ω	Cross-collision Frequency
Φ	Heat Generation Rate Due to Viscous Dissipation
ψ	Stream Function
ρ	Density
ϱ	Density Gradient
τ	Temperature Gradient
$\bar{\tau}$	Average Temperature Gradient
θ	Contact Angle
$\tilde{\theta}$	Dimensionless Temperature Variation about the Reference Value
Σ	Stress Tensor
Σ'	Deviatoric Part of Stress Tensor (Shear Stress)

σ	Surface Tension
σ_q	Growth Rate
ς	Air Concentration Gradient
A_v, B_v, C_v	Empirical Coefficients for the Antoine Equation
Bi	Biot Number
Bi_q	Biot Coefficient
Bo	Bond Number
Bo_D	Dynamic Bond Number
Ca	Capillary Number
Cr	Dimensionless Parameter that Characterizes Cross-collision
C_p	Heat Capacity
c	Mole Fraction
$\bar{c}$	Average Mole Fraction
D	Binary Mass Diffusion Coefficient
D_p	Diffusion Coefficient for Barodiffusion
D_T	Diffusion Coefficient for Thermodiffusion
d	Liquid/Gas Layer Thickness
d_c	Capillary Rise of the Liquid on the Wall
E	Evaporation Number
e	Internal Energy
$\mathbf{f}$	Body Force
Gr	Grashof Number
g	Gravitational Acceleration
h	Heat Transfer Coefficient
h_e	Enthalpy
h_w	Wall Thickness
$\mathbf{j}$	Diffusive Mass Flux

J	Mass Flux
k	Thermal Conductivity
k_B	Boltzmann's Constant
L, W, H	Test Cell Dimensions
l_c	Capillary Length
$\mathcal{L}$	Latent Heat of Vaporization
M	Molar Mass
m	Mass
$\dot{m}$	Mass Flow Rate
n	Number Density of Molecules
Ma	Marangoni Number
$\mathbf{n}$	Unit Normal Vector
Pe	Thermal Peclet Number
Pe_m	Mass Peclet Number
Pr	Prandtl Number
p	Pressure
p_c	Capillary Pressure
p_o	Pressure Offset
p_{cr}	Critical Pressure
Q^a	Heat Flow Rate due to Advection
Q^c	Heat Flow Rate due to Thermal Conduction
Q^p	Heat Flow Rate due to Phase Change
$\dot{Q}$	Volumetric Flow Rate
$\mathbf{q}$	Heat Flux
$\dot{q}$	Heat Source
q	(Complex) Wavenumber
R	Universal Gas Constant

$\bar{R}$	Specific Gas Constant
Ra	Rayleigh Number
Re	Reynolds Number
$r_{11}, r_{12}, r_{21}, r_{22}$	Dimensionless Resistivities used in the
	Non-Equilibrium Thermodynamics (NET) Model
t	Time
T	Temperature
T_0	Ambient Temperature
ΔT	Applied Temperature Difference
δT	Temperature Variation about the Average Value
$\mathcal{T}$	Time Period of the Periodic Flow
$\boldsymbol{\tau}$	Unit Tangent Vector
$\mathbf{u}$	Velocity
u_t	Thermal Velocity
V	Volume
We	Weber Number
x, y, z	Coordinate Axes

Superscript

0	Reference Value

Subscript

L	"Laboratory" Value
l	Liquid Phase
g	Gas Phase
d	Dominant Component
r	Dilute Component

v	Vapor Component
a	Air Component
i	Liquid-Gas Interface
s	Saturation
n	Normal Component
c	Cold End
h	Hot End
min	Minimum Value
max	Maximum Value

SUMMARY

Convection in a layer of fluid with a free surface due to a combination of thermocapillary stresses and buoyancy is a classic problem of fluid mechanics. It has attracted increasing attentions recently due to its relevance for two-phase cooling. Many of the modern thermal management technologies exploit the large latent heats associated with phase change at the interface of volatile liquids, allowing compact devices to handle very high heat fluxes. To enhance phase change, such cooling devices usually employ a sealed cavity from which almost all noncondensable gases, such as air, have been evacuated. Heating one end of the cavity, and cooling the other, establishes a horizontal temperature gradient that drives the flow of the coolant. Although such flows have been studied extensively at atmospheric conditions, our fundamental understanding of the heat and mass transport for volatile fluids at reduced pressures remains limited.

A comprehensive and quantitative numerical model of two-phase buoyancy-thermocapillary convection of confined volatile fluids subject to a horizontal temperature gradient has been developed, implemented, and validated against experiments as a part of this thesis research. Unlike previous simplified models used in the field, this new model incorporates a complete description of the momentum, mass, and heat transport in both the liquid and the gas phase, as well as phase change across the entire liquid-gas interface.

Numerical simulations were used to improve our fundamental understanding of the importance of various physical effects (buoyancy, thermocapillary stresses, wetting properties of the liquid, etc.) on confined two-phase flows. In particular, the effect of noncondensables (air) was investigated by varying their average concentration from that corresponding to ambient conditions to zero, in which case the gas phase becomes a pure vapor. It was found that the composition of the gas phase has a crucial impact on heat and mass transport as well as on the flow stability.

A simplified theoretical description of the flow and its stability was developed and used

to explain many features of the numerical solutions and experimental observations that were not well understood previously. In particular, an analytical solution for the base return flow in the liquid layer was extended to the gas phase, justifying the previous ad-hoc assumption of the linear interfacial temperature profile. Linear stability analysis of this two-layer solution was also performed. It was found that as the concentration of noncondensables decreases, the instability responsible for the emergence of a convective pattern is delayed, which is mainly due to the enhancement of phase change.

Finally, a simplified transport model was developed for heat pipes with wicks or microchannels that gives a closed-form analytical prediction for the heat transfer coefficient and the optimal size of the pores of the wick (or the width of the microchannels).

CHAPTER 1

INTRODUCTION

1.1   Motivation

Convection in a layer of fluid with a free surface due to an external horizontal tempera-
ture gradient is a classic problem of fluid mechanics. Much of the early interest in this
problem was driven by applications to crystal growth in microgravity environments, with
the focus on liquid metals (which have low Prandtl numbers, typically $Pr_l < 0.05$), where
evaporation is negligible, buoyancy plays no role, and the flow is driven primarily by ther-
mocapillarity.

   More recently the motivation for further studies of this problem has shifted due to the
increased demands on various cooling technologies. Thermal management is a major issue
for a wide range of applications. Many of the modern cooling technologies exploit the large
latent heats associated with phase change at the free surface of volatile liquids, allowing
compact devices to handle very high heat fluxes. Such cooling devices typically use a
sealed cavity with inner walls coated by a liquid film coexisting with a mixture of its own
vapor and noncondensable gases, such as air. When one end of the cavity is heated, and
the other end is cooled, phase change is expected to occur across the interface, absorbing
the heat at the hot end and releasing the heat at the cold end. Although capillarity and
thermocapillary stresses always play a role, under terrestrial conditions, buoyancy also
becomes an important driving force. Hence, the focus of the studies has shifted to flows
driven by a combined action of capillary pressure, thermocapillary stresses, and buoyancy
with phase change playing an increasingly important role.

   A fundamental understanding of heat and mass flow in confined two-phase buoyancy-
thermocapillary convection is therefore essential for improving two-phase cooling technol-
ogy. In general, a complete description of a two-phase cooling device involves four basic
components: (1) the fluid flow and the heat transport in the liquid phase, (2) the fluid flow

and the heat transport in the gas phase, (3) the dynamics at the interface between the two phases (*e.g.* the heat and mass transport across the interface), and (4) the heat conduction within the solid walls of the device. These four transport problems are coupled with each other and therefore should be solved simultaneously. For instance, the fluid flow and heat transport in the liquid and in the gas are coupled through the boundary conditions at the liquid-gas interface.

Noncondensable gases (such as air) are well known to degrade the thermal performance of two-phase cooling devices, which rely primarily on latent heat associated with phase change. This degradation is due to the noncondensable gases impeding phase change, and condensation especially, as the vapor has to diffuse through the noncondensable gases. In practice, completely removing the noncondensables from a sealed device is impractical, since air tends to dissolve in liquids and be adsorbed into solids, hence the liquid film almost always remains in contact with a mixture of its own vapor and some air.

However, the fundamental understanding of confined two-phase flows with varying levels for noncondensable gases is currently incomplete. The majority of experimental studies of buoyancy thermocapillary convection has been performed at ambient (atmospheric) pressure in which case the gas phase is mostly air with a small admixture of vapor. There are almost no experimental studies at reduced pressures when the vapor dominates. One exception is a recent experimental study by Li *et al.* [1] which showed that noncondensables can play an important and nontrivial role and that the results in one limit (e.g. when the gas phase is dominated by noncondensables) cannot be simply extrapolated to the opposite limit (e.g., when the vapor dominates).

Theoretical studies, on the other hand, tend to use a lot of assumptions, often with little justification, to simplify the problem. For example, most of them are based on one-sided models, where only the liquid phase is described in detail, while the gas phase is considered indirectly through the boundary conditions at the interface. Moreover, phase change is typically treated in a rather crude manner. The fundamental studies of convection

tend to ignore phase change entirely. The applied studies of two-phase cooling typically divide a device into three sections: "evaporator", "condenser," and "adiabatic region" in between [2, 3]. The evaporator and condenser are not modeled in detail; in the adiabatic region phase change is ignored, and the vapor flux is simply related to the applied heat flux. Although models based on such partitioning have been used extensively in the engineering literature, few if any studies have been carried out to check whether it is justified or attempt to correlate the transport processes in the three regions.

1.2 Previous Studies

In order to identify the key open questions and define the scope of the present thesis, below we provide a review of the present state of knowledge in the field.

1.2.1 Buoyancy-Thermocapillary Convection

The first systematic study of nonvolatile free surface fluid flows driven by a horizontal temperature gradient is likely due to Birikh [4] who derived an analytical solution for a planar return flow in a laterally unbounded layer due to both buoyancy and thermocapillary stresses. This solution also describes the flow away from the end walls in a laterally bounded geometry: the fluid flows from the hot end towards the cold end near the free surface and returns near the bottom. Kirdyashkin [5] repeated (not entirely correctly) Birikh's theoretical analysis and validated the analytical solutions experimentally.

Smith and Davis [6, 7] performed a linear stability analysis of such flows in the limit of zero dynamic Bond number, $Bo_D = 0$ (i.e., ignoring buoyancy effects). They predicted that, depending on the Prandtl number of the liquid, the base state characterized by a return flow would undergo an instability towards either surface waves (for $Pr_l < 0.15$, which corresponds to liquid metals) or hydrothermal waves (for $Pr_l > 0.15$, which corresponds to gases and nonconducting liquids) above a critical Marangoni number Ma, which characterizes the magnitude of thermocapillary stresses. In particular, hydrothermal waves were

3

predicted to form at an angle to the direction of the thermal gradient and travel in the direction of thermal gradient. As Pr_l increases, the angle changes smoothly from nearly transverse to nearly parallel to the thermal gradient. The predictions of Smith and Davis [6, 7] have since been thoroughly tested and verified both in microgravity and for thin films in terrestrial conditions. A thorough overview of these experiments is presented in a review paper by Schatz and Neitzel [8].

Various other instabilities have been observed at $Bo_D = O(1)$ (when buoyancy is non-negligible). Villers and Platten [9] studied buoyancy-thermocapillary convection in a rectangular cavity for acetone ($Pr_l = 4.24$) experimentally and numerically. Although acetone is volatile, good agreement was found between the experimental observations at atmospheric conditions and the predictions of a one-sided model that ignored heat and mass transfer in the gas phase. For low Ma a featureless planar return flow was found, which is well-described by Birikh's solution. However, as Ma was increased, instead of hydrothermal waves a steady cellular pattern featuring multiple convection rolls emerged. The convection rolls were found to rotate in the same direction, unlike the case of pure buoyancy (or Rayleigh-Bénard) convection. Moreover, unlike the hydrothermal waves which form at an angle to the direction of the thermal gradient, the convective pattern featured rolls aligned in the transverse direction. At even higher Ma the steady state was found to be replaced by an oscillatory pattern that was also unlike a hydrothermal wave: the convection rolls were observed to travel in the direction opposite the thermal gradient. Similar results were obtained later by De Saedeleer *et al.* [10] for decane ($Pr_l = 15$) and Garcimartin *et al.* [11] for decane ($Pr_l = 15$) and 0.65 cSt and 2.0 cSt silicone oil ($Pr_l = 10$ and 30, respectively) in rectangular cavities with strong confinement in the spanwise direction.

Riley and Neitzel [12] performed one of the most extensive and detailed experimental studies of convection in a 1 cSt silicone oil with $Pr_l = 13.9$ in a rectangular cavity with a spanwise dimension comparable to the streamwise dimension. They discovered that a direct transitions from steady, unicellular flow to hydrothermal waves takes place for small

values of the dynamic Bond number ($Bo_D \lesssim 0.2$), while for $Bo_D \gtrsim 0.2$ the results are similar to those of Refs. [9–11]: the featureless return flow first transitions to steady co-rotating multicells and, upon further increase in Ma, to an oscillatory multicellular pattern. Riley and Neitzel also determined the critical values of Ma and the wavelength λ of the convective pattern as a function of Bo_D. Burguete *et. al* [13] performed experiments on convection in a 0.65 cSt silicone oil with $Pr_l = 10.3$ in a rectangular cavity with different aspect ratios where spanwise dimensions were greater than streamwise dimensions. Similarly, they found that the base return flow destabilizes into either oblique traveling waves or longitudinal stationary rolls, respectively, for small and large thickness of the liquid layer (i.e., low and high Bo_D).

Since it does not account for buoyancy, the linear stability analysis of Smith and Davis [6, 7] fails to predict the stationary patterns that emerge for $Bo_D = O(1)$. However, most of the linear stability analyses accounting for buoyancy also failed to predict the correct pattern, i.e., stationary (transverse) multicells that were observed in the experiments [9–12]. Using adiabatic boundary conditions at the top and bottom of the liquid layer, Parmentier *et al.* [14] predicted transition to traveling waves rather than steady multicellular pattern for a range of Pr_l from 0.01 to 10, regardless of the value of Bo_D. Chan and Chen [15], who used similar assumptions, also predicted transition to traveling waves for a $Pr_l = 13.9$ fluid. Moreover, the predicted critical Ma and wavelength λ do not match the experiment [12]. In both cases the predicted traveling waves are oblique for smaller Bo_D and become transverse for Bo_D greater than some critical $O(1)$ value.

Mercier and Normand [16] showed that transition to a stationary convective pattern can take place if the adiabatic boundary conditions are replaced with Newton's cooling law, although that requires an unrealistically large surface Biot number ($Bi \gtrsim 185/Bo_D$). Moreover, the predicted pattern corresponds to longitudinal convection rolls, while in the experiments [9–12] transverse rolls were observed. In a subsequent paper Mercier and

Normand [17] considered the effects of the end walls, which they described as spatial disturbances superimposed on the uniform base flow. Their analysis predicted that, depending upon the Prandtl number, recirculation rolls would develop near the hot end (for $Pr_l > 4$), near the cold end (for $Pr_l < 0.01$) or at both end walls (for $0.01 < Pr_l < 4$).

The study by Priede and Gerbeth [18] is the only one to date which correctly predicts the formation of a stationary pattern at $Bo_D = O(1)$. They argued that traveling waves run into one of the lateral end walls and dissipate before they can be sufficiently amplified as a result of linear instability. At the same time the lateral walls induce stationary disturbances with relatively large amplitude, which will penetrate into the bulk of the liquid layer as the zero-frequency mode becomes unstable. The predicted critical values of Ma are also in reasonable agreement with the threshold values found by Riley and Neitzel [12].

Convective patterns above the threshold of the primary instability have also been studied using numerical simulations. To date the bulk of these studies [9, 19–22] used one-sided models which ignore the transport in the gas phase, assumed that the temperature gradient is generated by imposing different temperatures on the two end walls, the free surface is flat and non-deformable, the bottom wall and the interface are adiabatic, and phase change is negligible. These numerical simulations were able to reproduce some features of the experimental studies [9–12]. For example, Villers and Platten [9] found transitions from the base return flow to steady multicells and to oscillatory multicells as Ma increases for acetone ($Pr_l = 4.24$) when $Bo_D = O(1)$. Shevtsova *et al.* [22, 23] performed numerical simulations for decane ($Pr_l = 14.8$) in a rectangular layer at different Bo_D. They found that as Ma number increases, the primary instability leads to hydrothermal waves for $Bo_D \leq 0.25$, while for $Bo \geq 0.32$ the primary instability produces a steady multicellular flow, and the secondary instability produces an oscillatory multicellular flow.

Li *et al.* [24] investigated non-adiabatic effects by using Newton's cooling law with a small Biot number. Their numerical simulations ignored phase change but were able to reproduce many features of the experimental observations at atmospheric conditions. Ji *et*

al. [25] considered phase change, but ignored buoyancy, so their analysis is only applicable for thin films or under microgravity when $Bo_D \to 0$.

Although buoyancy-thermocapillary convection has been studied extensively, very few investigations considered the transport in the gas phase and the effect of noncondensables, both of which could significantly affect the flow and its stability at reduced pressures. Most of the experimental studies were performed at atmospheric conditions where air dominates. Similarly, the vast majority of the theoretical studies used one-sided models which completely ignore the gas phase, and the validity of the other assumptions made in these studies is questionable. As a result, they fail partially or completely in describing other features of convective flows, most notably the structure of the boundary layers near the end walls which defines both the temperature gradient in the bulk and controls the dynamics of oscillatory states at higher Ma. Description of these boundary layers requires a detailed model of transport of heat (and mass) in both the liquid and the gas layer, as well as a proper description of phase change at their interface.

1.2.2 Modeling of Two-Phase Cooling Devices

The main motivation for this work is provided by applications to thermal management. Hence, some more applied studies of two-phase flows where phase change plays an important role are also relevant, and are discussed below. We group different modeling approaches into two broad classes: One-sided models which do not explicitly treat the bulk transport of either heat, mass, or momentum in one of the two phases and instead incorporate (some or all of) the corresponding fluxes through effective boundary conditions. Two-sided models, on the other hand, include an explicit description of bulk transport (of at least one of the three quantities) in both phases.

1.2.2.1 One-Sided Transport Models

Nusselt [26] performed the first theoretical study of film condensation on a vertical plate. This study is a classical example of one-sided description of a two-phase system (vapor

and liquid condensate film), where transport in the gas phase is not modeled explicitly and is incorporated implicitly through the boundary conditions at the interface. Specifically, Nusselt described the phase change by incorporating the associated mass and heat flux at the interface into the respective conservation laws inside a control volume. The gas phase was assumed to be saturated and stagnant, which is not always a good approximation. Numerous approximations were also made in describing the liquid phase, e.g., the heat was assumed to be transported via conduction alone.

The Nusselt model was later modified to incorporate the effect of heat advection [27,28] in the condensate film by empirical modifications of the latent heat. It was also extended to incorporate the effect of the shear stress at the liquid-vapor interface [29], which could be important for film condensation under forced convection. Butterworth [30] studied film condensation in the limit when body forces are negligible compared with the interfacial shear stresses, and proposed a simple asymptotic expression for the heat transfer coefficient in the limits when either body forces of shear stresses dominate.

Using the boundary layer analysis, Sparrow and Gregg [31] derived similarity solutions for the velocity and temperature field of the condensate film on a vertical plate, where both the heat advection and the inertia were considered. However, the transport in the gas phase was ignored. In particular, shear stress at the liquid-vapor interface was not considered. The study was also extended to the film condensation subject to the forced convection [32], but, the interfacial temperature and the flow speed were simply set to the values in the bulk of the vapor flow. Koh *et al.* [33] studied the effect of the interfacial shear stress on laminar film condensation on a vertical plate by solving the viscous boundary layer equations in both the liquid and the gas phase. Again, heat and mass transport in the vapor phase were not considered and the vapor was assumed saturated.

A few recent studies have focused on evaporation, as opposed to condensation. For instance, Ranjan *et al.* [34] numerically investigated the evaporating liquid meniscus in the pores of wicks. At the interface, the shear stresses induced by the vapor flow were

neglected and phase change was described using Kinetic Theory of Gases. The vapor was assumed saturated, similar to the studies of condensation, i.e., the heat and mass transport in the gas phase where prescribed rather than computed.

Nusselt-like models were also applied to describe liquid films within various two-phase devices. One example is a thermosyphon, which is essentially a gravity-assisted wickless heat pipe where the flow of the condensate film back to the evaporator is driven primarily by gravity (cf. Fig. 1). In such a closed system, the vapor flows in the opposite direction to that of the liquid. Transport is almost universally described using a piecemeal approach, where the device is partitioned into the "evaporator", the "condenser" and the "adiabatic section". In the "adiabatic section" phase change is typically ignored, while the interfacial shear stress is described using the friction factor for counterflow of a layer of liquid and a layer of gas obtained from empirical correlations [36–39]. In the "evaporator" and the "condenser", phase change and the associated heat flux are incorporated the same way as in the Nusselt model [26], while various empirical approaches are used to describe the effect of phase change on the liquid film flow. Often the interfacial shear stress was computed by adding the so-called "dynamic shear stress" to the that found in the "adiabatic section"
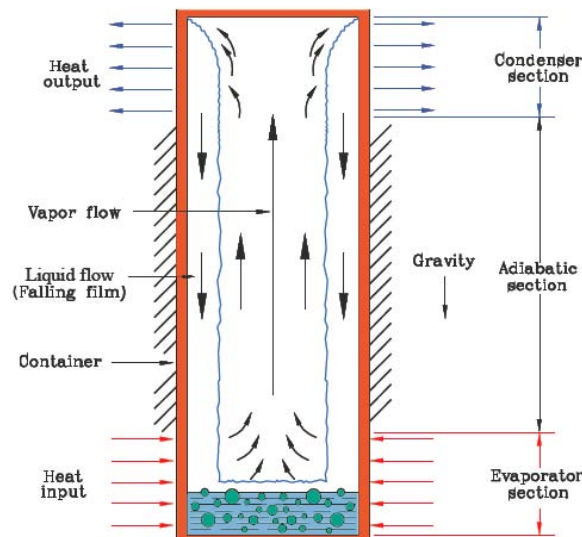
Figure 1: A schematic for a gravity-assisted wickless two-phase closed thermosyphon. [35]

9

[40–43]. Another approach was to multiply the interfacial shear stress in the "adiabatic section" by a modification factor [44–46]. None of these studies described heat and mass transport in the gas phase or calculated the shear stress, or the phase change at the liquid-vapor interface by a physically justified model (e.g., using vapor recoil [47]), which may explain why the entrainment limit predicted by different studies varies by as much as a factor of five [48]. Furthermore, even the validity of partitioning thermosyphons and heat pipes into the three sections is itself highly questionable.

Kafeel and Turan [49] and Fadhl *et al.* [50] proposed and investigated crude models of thermosyphons which treat the fluid as a mixture of the liquid and vapor phase, with phase change occurring in the bulk rather than at a (non-existing) interface.

One-sided models were also used extensively for the studies of micro heat pipes [52] (cf. Fig. 2), where the flow is driven primarily by the capillary force due to the interface curvature variation between the heated and the cooled end [53–59], vs. gravity. In order to predict the capillary limit, the critical heat input [60], or the dry-out length, theoretical studies typically relied on partitioning heat pipes into the same three regions as
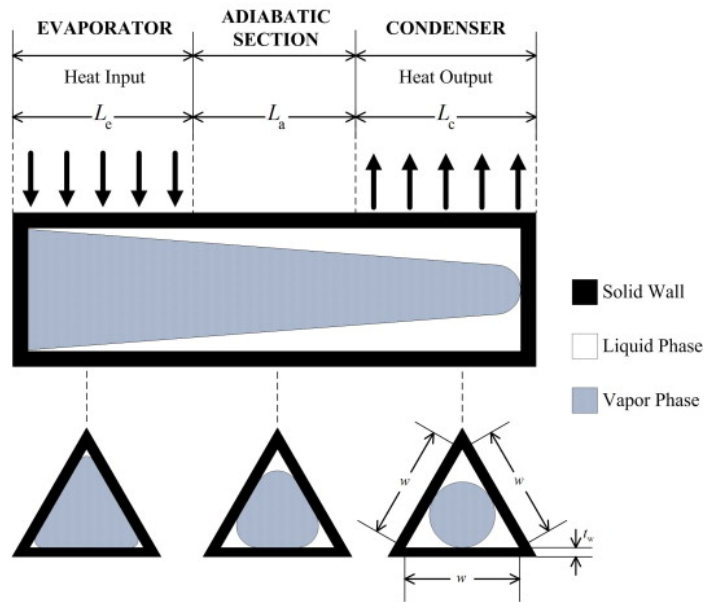
Figure 2: A schematic diagram of a micro heat pipe of triangular cross-section, showing three liquid saturation profiles at typical axial locations in the evaporator section, adiabatic section and condenser section, respectively. [51]

thermosyphons. The variation of the temperature in the direction normal to the interface was typically ignored (in both phases), and phase change was directly related to the pre-scribed heat flux through the substrate, typically assumed to be uniform in the "evaporator" and the "condenser" and to vanish in the "adiabatic section."

Suman and his colleagues conducted studies of micro heat pipes with various cross-sectional geometries using 1D transport model. Besides the capillary pressure and the wall shear stress [61], they have incorporated the effect of body force (gravity) [62–64], the iner-tia in the liquid [62, 63], heat conduction through the substrate [65], and the linear variation of the surface tension [63] (e.g., due to an interfacial temperature gradient). However, their treatment of transport in the gas phase was incomplete in all of these studies. In particular, the shear stress at the liquid-vapor interface was completely ignored, while the interfacial temperature was assumed (incorrectly, as shown below), rather than computed.

The effect of the gas phase was considered for the most part only in terms of the shear stress that it exerts on the liquid layer [66–74]. The latter was typically incorporated by modifying the friction factor or the Poiseuille number (the product of the friction factor and the Reynolds number for the liquid flow), which was typically obtained from the solu-tions of a fully developed duct flow of the vapor [75] or from relevant correlations [76, 77]. Various studies were conducted to predict the friction factor and the Poiseuille number in different geometries [60, 78–80]. Kim *et. al.* [81] developed an iterative method for cal-culating the ratio of the effective pressure gradient in the liquid in the presence of vapor counterflow to that in the absence of counterflow, for an open channel with an arbitrary cross-section. It should be noted that with few exceptions [60], most of the studies ne-glected the spatial variation of the interfacial shear stress.

Zhang *et al.* [82] performed an analytical investigation of a model of a sealed rect-angular heat-pipe with an essentially flat interface. The model neglected advective fluxes in the momentum and heat transport in the liquid and assumed a fully developed unidi-rectional flow in the vapor. At the interface, the heat balance considered the latent heat

and conduction through the liquid layer, but not the gas layer. The model considered the thermocapillary stresses but neglected shear stresses induced by the vapor flow.

One-sided models have also been used for modeling the vapor flow in a concentric annular heat pipe (cf. Fig. 3), which consists of two concentric pipes of different diameters that are attached and enclosed at the end, creating an annular vapor space between the two pipes. In such a geometry, sonic limit and entrainment limit are of increased importance, and one-sided models for the vapor phase were commonly used for predicting these operation limits [84–86]. The effect of phase change was incorporated into the boundary condition for the velocity field of vapor, where a uniform blowing or suction velocity at the inner and outer walls in the "evaporator" and "condenser" were calculated based on the prescribed heat flux. The temperature at the liquid-vapor interface was assumed equal to the saturation temperature based on the local vapor pressure. In the concentric annular heat pipe, vapor speed could be large (e.g. near the sonic limit), and the variation in the vapor pressure is not neglected in these studies. The pressure drop in the vapor could be comparable to that in the liquid.

While one-sided models are easier to construct and solve, they involve assumptions that are not always justified. For example, shear stress at the liquid vapor interface is often ignored or estimated based on correlations rather than computed using the actual flow fields. Most importantly, while various methods were developed to incorporate the effect of the momentum transport in the gas phase, the phase change and the associated heat and
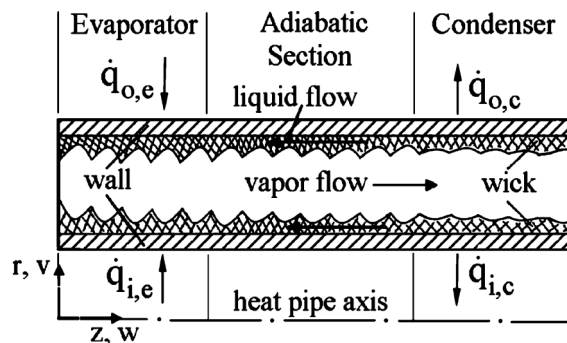
Figure 3: A schematic of a concentric annular heat pipe. [83]

momentum flux are computed in a rather crude way. For instance, the relation between the (externally imposed) heat flux and phase change used in the studies of condensation is only valid in extremely simplified geometries (e.g., thin liquid films on essentially flat solid surfaces) and cannot be applied to quantitative modeling of two-phase evaporative cooling devices which usually have a more complicated geometry. Furthermore, this relation cannot be used to model evaporation – an equally important process – since no liquid film forms on heated surfaces. Finally, the heat flux in general cannot be specified/prescribed, but must instead be computed based on the solutions to the transport equations.

1.2.2.2   *Two-Sided Transport Models*

In comparison with one-sided models, there have been relatively few studies that attempted to model transport phenomena in both phases. Numerical models which account for the momentum, heat, and mass transport in both phases were used to study the evaporation from a concave meniscus [87], a heated groove [88], and a convex meniscus [89]. In these models, mass transport of vapor through a vapor-air mixture was described using advection-diffusion equation for the vapor concentration. Phase change was modeled using Kinetic Theory of Gases, while latent heat and heat conduction in both phases were taken into account in the heat balance at the interface. It should be noted that these studies focused on evaporation under ambient conditions, vs. transport in a confined geometry which is more relevant to two-phase evaporative cooling devices.

Sobhan *et al.* [74] developed a two-sided model of a micro heat pipe which considered the 1D heat and mass transport in the vapor phase and solved for the vapor temperature. However, at the interface, only the latent heat was considered in the heat transport across the interface, even though the predicted temperatures were different between the two phases. Kuznetsov and Sitnikov [90] and Kaya and Goldak [91] proposed and numerically investigated models of wicked heat pipes. The mass, momentum and heat transport were considered in both the liquid and the vapor phase. The liquid phase was described using Darcy's law [90] or its modification which considered the viscous and inertial effects [91].

At the interface, the tangential velocity was assumed to be zero, the mass balance coupled phase change with the normal velocity in both phases, and the heat balance considered the latent heat and the heat conduction in both phases.

1.2.3 Effect of Noncondensable Gases

It should be noted that most of the studies discussed in Section 1.2.2 assumed the gas phase to be either pure vapor or a saturated air-vapor mixture at ambient pressure. Neither of these limits describes a typical two-phase evaporative cooling device, where the gas phase is a mixture of vapor and noncondensable gases dominated by the vapor. Furthermore, none of the studies discussed in this Section investigated the effect of the noncondensable gases on the fluid flow and heat or mass transport. In fact, it is well-known that noncondensable gases suppress phase change (especially condensation) and degrade the overall thermal performance. For instance, one of the earliest systematic experimental studies [92] on condensation of steam on a horizontal cylinder predicted that even very small amounts of noncondensables (air) – as small 0.5% (mass fraction) – could halve the condensation rate, and the corresponding heat transfer coefficient. This adverse effect of noncondensable gases was later verified experimentally for the condensation process in the presence of various kinds of noncondensable gases and different orientations of the condensing surfaces for both natural and forced convection [93–96].

The effect of noncondensable gases on condensation heat transfer is usually described using empirical correlations for the average heat transfer coefficient or the Nusselt number. One common metric is the "degradation factor" [97–99], which is defined as the ratio of the heat transfer coefficient in the presence of noncondensables to that in the absence of noncondensables predicted by the Nusselt model. The "degradation factor" is typically given as a function of the Reynolds number and the mass fraction of the noncondensable gas. The analogy between the heat and mass transfer has been used to predict the mass flux in the presence of noncondensables based on to heat flux [100–106]. Specifically, the relationship between the Sherwood number, the Reynolds (or Grashof) number, and the Schmidt

number is assumed to be the same as that between the Nusselt number, the Reynolds (or Grashof) number, and the Prandtl number, which are usually based on correlations.

Although the models based on empirical correlations are intuitive, they are typically restricted to certain ranges of parameters, geometries, orientation of the flow, etc. Sparrow and Eckert [107] performed one of the earliest theoretical studies of the effect of noncondensables on film condensation. They extended the two-sided boundary layer analysis for film condensation of pure vapor [33] and included the boundary layer equation for the conservation of species in the gas phase, in terms of mass fraction of the air. The model was further extended by considering the effect of buoyancy in the gas phase [108], and the interfacial resistance for phase change [109, 110] where the difference between the interfacial temperature and the saturation temperature is considered. It was found that the decrease of the heat transfer coefficient was mainly due to the diffusion of the vapor through a layer of noncondensables that accumulate next to the condensate film. Even the presence of a minute amount of noncondensable gases in the bulk could cause the buildup of a large concentration gradient at the interface, which reduces the partial pressure of the vapor, the saturation temperature at the interface, and therefore the temperature difference that drives the heat transfer [108, 109].

Mori and Hijikata [111] studied the effect of noncondensables on film condensation on a vertical plate subject to natural convection by performing boundary layer analysis for a saturated "two-phase boundary layer", which consists of small droplets generated by condensation, the vapor and noncondensables, between the liquid film, and the gas phase. The liquid film was described using the Nusselt model, while transport in the gas phase was neglected. The results showed that the heat transfer coefficient approached that for natural convection (without phase change) when noncondensables dominated, and approached the solution of the Nusselt model [26] when vapor dominated. The effect of noncondensables was found to be the most significant in the limiting cases (mass fraction of the vapor approaching zero or unity).

Denny *et al.* [112,113] performed numerical studies of laminar film condensation on a vertical plate in the presence of air and forced convection. The boundary layer equations were used to describe the transport of momentum, heat, and mass in the gas phase, and the Nusselt model was used for the liquid phase. Siow *et al.* studied laminar film condensation in the presence of noncondensables in different geometries [114–116] by numerically solving the boundary layer equations in both phases. By introducing different turbulence models [117, 118], Yuann *et al.* [119] and Groff *et al.* [120] studied turbulent film condensation in vertical tubes using numerical simulations. It was found that the presence of noncondensables decreased the condensation rate and the film thickness, as well as the heat transfer coefficient, especially near the inlet. It should be noted that numerical studies [112–116, 119, 120] used a forward marching technique in the numerical implementation and hence were limited to co-flow (of the liquid and gas) configurations.

The recent developments in computational fluid dynamics and increases in computing power enabled numerical simulations based on models incorporating the conservation equations for mass, momentum, energy, and species (vs. boundary layer equations) [121–124]. Typical numerical implementations [121, 123, 124] only model transport in the gas phase and incorporate phase change through boundary conditions. It should be noted that except for a few studies [109, 110] the interfacial resistance for phase change is usually neglected and the interfacial temperature is assumed to be equal to the (local) saturation temperature. This is a reasonable approximation for the studies of condensation where noncondensables accumulate near the interface. However, in confined geometries, noncondensables can become depleted in certain regions (e.g., as a result of significant evaporation), and the interfacial resistance can be important.

Most of the existing studies of the effects of noncondensables focus on simple geometries and simple processes, most typically condensation. However, in sealed two-phase cooling devices, noncondensable gases will have a significant effect not just on the condensation, but also on evaporation and phase equilibrium along the entire interface. Phase

equilibrium is a function of the local composition of the gas, which is influenced by (i) the diffusion of vapor through the gas phase and (ii) the flow in the gas phase. On the other hand, the fluid flow in both phases itself depends on the thermocapillary stresses (i.e., the interfacial temperature which is determined by the phase equilibrium). To better understand the interdependence of these effects, fundamental studies are required which fully describe the transport in both phases and phase change along the entire interface at varying levels of noncondensables. However, such fundamental studies are exceedingly rare. In fact, there is only one experimental study that considered the effect of noncondensables (air) on the convection problem discussed in Sect. 1.2.1. Li *et al.* [1] investigated buoyancy-thermocapillary convection in a layer of volatile silicone oil. A sealed cavity was used to achieve air concentrations varying from 14% (lowest pressure) to 96% (atmospheric pressure). It is found that as the noncondensable concentration decreases, the base flow speed remains almost unchanged, while transition thresholds between different flow patterns in the liquid layer are substantially delayed.

The effect of varying the amount of noncondensables was also investigated in the context of pool boiling. In particular, it was found that even small amounts of noncondensables could induce a temperature gradient along the bubble surface leading to thermocapillary convection around the bubble [125]. Barthes *et al.* [126, 127] performed experiments on the flow instability around a single bubble in the subcooled FC-72. For non-degassed liquid, thermocapillary convection was observed in the liquid next to the bubble, transitioning from steady vortex to oscillatory (time-periodic) motion; however, for degassed liquid, no convective flow patterns were observed.

Chauvet *et al.* [128] studied the evaporation-driven Bénard-Marangoni instability in films of volatile liquids experimentally and analytically. Their linear stability analysis showed that transport in the gas phase can be represented via a wavenumber-dependent generalization of the Biot coefficient which includes two terms, one of which describes the heat conduction and the other – the vapor (mass) diffusion through the gas phase. Both

terms depend on the gas phase composition, while the latter also depends on the volatility of the liquid; increasing the volatility has the same effect as decreasing the amount of non-condensables. Although the study did not investigate how the flow stability is affected by varying the amount of noncondensables, experiments confirmed the theoretical prediction that increasing the volatility of the liquid film increases the critical Marangoni number for the instability.

1.2.4 Direct Numerical Simulation of Two-Phase Flows

In order to study two-phase flows with two-sided models, appropriate boundary conditions are required across the liquid-gas interface. Moreover, in complex geometries or when strong lateral confinement (by the wick, the walls of the microchannels, grooves, etc.) is absent, the shape of the interface should be computed as part of the solution which takes into account not just the contact angle, but also the effect of fluid flow, phase change, the variation of surface tension along the interface. Analytical solutions are only available in special geometries and do not account for any of the above effects. Direct numerical simulations therefore become indispensable. The existing numerical methods for simulating free-surface flows can be classified into three broad categories: the surface capturing method, the surface tracking method, and the moving mesh method.

Surface capturing method solves the governing equations on a stationary grid, where an additional field, known as the indicator function, is introduced to define both the phase which occupies a particular computational cell and the position of the interface. Different techniques of capturing the interface include volume of fluid (VoF) [129–132], level set method (LSM) [133–136], constrained interpolation profile (CIP) method [137], phase field method [138], etc. The most commonly used method is VoF, where the volume fraction occupied by, say, the liquid phase serves as the indicator function and LSM, where the indicator function determines the (signed) distance to the interface. The major challenges of this approach include maintaining a sharp interface and applying boundary conditions such as calculating surface stresses and phase change. In particular, the velocity field is not

divergence free after phase change is incorporated, which requires compressible Navier-Stokes equations to be solved in both phases. The stiffness of the compressible equations associated with the large density ratio between the liquid and the vapor phase requires extremely small time step in the numerical simulations. Other drawbacks include spurious forces which emerge in the neighborhood of the interface [139–141] and the requirement of rather fine meshes.

The surface tracking method also uses a stationary grid to solve the governing equations, while the interface is tracked using a set of marker particles or a lower dimension grid [140, 142–146]. Surface tracking maintains a sharp interface, which allows more accurate evaluation of surface stresses without requiring very fine meshes, but has difficulties with volume conservation and handling topological changes. The approach also makes implementation of some types of boundary conditions nontrivial.

In the moving mesh method [147–155] separate computational meshes represent different phases, while the interface is represented by the mesh boundaries. As the interface moves with the flow, computational meshes on both sides of the interface are continuously distorted. This method therefore is not well-suited for complex geometries when interface experiences large deformation or changes in topology. However, it provides the most accurate description of the interface and makes the calculation of the surface stresses and implementation of the boundary conditions at the interface simpler and more straightforward than in the other two approaches.

The pioneering work in developing the moving mesh method was done by Ryskin and Leal [147] who used a structured orthogonal mesh to study the steady rise of an axisymmetric bubble driven by buoyancy. Indeed, most of the early numerical studies based on this method were limited to either the axisymmetric or 2D geometry [148–151]. Schmidt and his colleagues [152–154] implemented the moving mesh method for 3D simulation using finite volume method on a stagged tetrahedral mesh. Tukovic and Jasak [155] developed a second order accurate moving mesh finite volume method for the bulk equations combined

with finite area method on the mesh boundary representing the interface.

1.3   Objectives of This Work

The main motivation for this work is provided by applications to thermal management, specifically, evaporative two-phase cooling devices which involve confined two-phase flow of volatile fluids where both body forces and surface stresses could be important. As discussed previously, the existing models of evaporative two-phase cooling devices are mainly one-sided and use numerous assumptions, few of which are well justified. In order to verify these assumptions and quantify the accuracy of the existing approximate models, it is essential to understand the effect of the gas phase and its composition on the confined two-phase flow.

The main focus of this thesis is therefore on developing a comprehensive two-sided model of two-phase flow of volatile fluids, implementing it numerically, and using numerical simulations of buoyancy-thermocapillary convection to improve our fundamental understanding of transport in both phases. Since the convection problem has been investigated extensively, there is an abundance of results that can be used for validating the two-sided model, at least under atmospheric conditions. Once validated, the two-sided model can be used to investigate two-phase flow under reduced pressures, which are more relevant for the operating conditions of evaporative cooling devices. The two-sided model can help answer the following key open questions:

1. Can one-sided models provide an accurate descriptions of two-phase flow of volatile fluids and under what conditions?

2. How do the noncondensable gases affect various transport phenomena and phase change in confined geometries?

3. Under what conditions can the two-phase cooling devices be partitioned into the evaporator, condenser, and adiabatic sections?

4. Is it possible to construct a simple analytical model of transport in both phases based on the improved fundamental understandings of the problem?

In order to answer these questions, a theoretical study was conducted with the following specific objectives:

1. Formulate, implement numerically, and validate a comprehensive two-sided model of two-phase flows of confined volatile fluids, which properly describes momentum, mass, and heat transport in both the liquid and the gas phase, as opposed to the one-sided models that have been used in most of the previous studies.

2. Improve the fundamental understanding of the two-phase buoyancy-thermocapillary convection in confined and sealed geometries and quantify the importance of various physical effects (buoyancy, themocapillary stresses, phase change, etc) in this problem. In particular, investigate the effects of noncondensable gases on the convection patterns and heat transport.

3. Validate the various assumptions that have been used with minimal justification in previous studies, in particular, the assumptions that neglect transport in the gas phase and phase change in the "adiabatic section". Whenever possible, derive analytical estimates and/or formulate simpler, but still accurate, description of the problem valid in various limits.

4. Leverage the improved fundamental understanding of the transport problem to construct an analytical model of simple evaporative cooling devices, which can be used to provide guidance for the design and evaluation of the thermal performance of such devices. In particular, quantify the impact of noncondensables on the thermal performance.

In order to validate the two-sided model against the existing results, a canonical problem was chosen, where a layer of liquid is confined, below a layer of gas, in a sealed

rectangular cavity subject to a horizontal temperature gradient. The only (to the author's knowledge) systematic experimental study of two-phase buoyancy-thermocapillary convection of volatile fluid driven by a horizontal temperature gradient with varying levels of noncondensables is due to Li *et al.* [1]. Therefore the exact same working fluid and geometry will be used in this study in order to facilitate direct comparison.

The test cell used in the study of Li *et al.* [1] is shown in Fig. 4. The inner cavity had the following dimensions: length L = 48.5 mm, width W = 10 mm, and height H = 10 mm. The walls of the test cell were made of quartz (fused silica) with thermal conductivity k_w = 1.4 W/m-K and had a thickness h_w = 1.25 mm. Above the layer of liquid was a layer of gas – a mixture of vapor and air. The horizontal temperature gradient was generated by imposing constant temperatures T_c and $T_h > T_c$ on the outside of the left and right end wall, respectively, by using temperature controlled copper blocks. Although the liquid flow in this geometry is at best qualitatively similar to that in evaporative cooling devices, the transport in the gas phase as well as phase change at the liquid-vapor interface should be quite similar, and hence this study should help improve the fundamental understanding of two-phase transport also in the geometries relevant for thermal management devices.

The working fluid used in the study of Li *et al.* [1] was a volatile 0.65 cSt silicone oil,
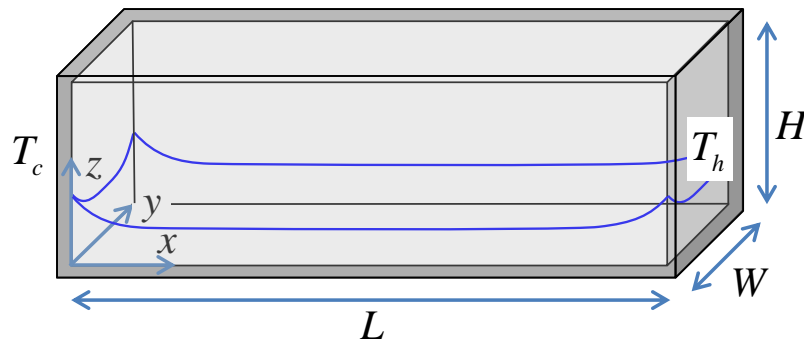
Figure 4: The test cell containing the liquid and air/vapor mixture. Gravity is pointing in the negative z direction. The shape of the contact line reflects the curvature of the free surface.

hexamethyldisloxane (HDMS, NMR grade with purity $\geq$ 99.5%, Sigma Aldrich 326739-100G). Although this working fluid is not a typical coolant for thermal management devices, it has relatively high volatility and latent heat, which are the key properties for the coolants. It should be mentioned that not all of the properties of the working fluid used in the study of Li *et al.* [1], especially for the vapor phase, have been reported. Moreover, different values for some material parameters have been reported in the literature. In this study, two sets of properties for the liquid and vapor of the silicone oil have been used, and will be specified clearly in the corresponding Chapters.

The thesis is organized as follows. Chapter 2 describes the mathematical model (governing equations and boundary conditions) of the two-phase confined buoyancy thermocapillary convection in the presence of noncondensable gases. Chapters 3, 4, and 5 present the results at atmospheric conditions, under pure vapor, and under vapor with a small amount of air, respectively. The linear stability analysis which describes the transition between different convective regimes is presented in Chapter 6. The main conclusions and contributions of this work are presented in Chapter 7. A summary of the dimensionless parameters and their values at atmospheric conditions and under pure vapor are presented in Appendix A. The numerical methods used for simulating the two-phase flow are described in Appendix B. Finally, the procedure for setting up the numerical simulations with OpenFOAM is described in Appendix C.

CHAPTER 2

MATHEMATICAL MODEL

2.1 Introduction

The vast majority of theoretical and numerical studies of buoyancy-thermocapillary convection use one-sided models [9, 19–22] that only consider the convection in the liquid phase, while ignoring transport through the gas phase and the phase change across the liquid-gas interface. The heat and mass transport in the gas phase are incorporated indirectly through boundary conditions at the liquid-gas interface, and the interface is assumed to be rigid (and, in most of the cases, flat). Such an approach might be justifiable for nonvolatile liquids, since air is a relatively poor conductor of heat, and for the volatile liquids at ambient (atmospheric) conditions when phase change is strongly suppressed. Indeed, the predictions of such models are for the most part consistent with experimental studies of volatile and nonvolatile fluids at ambient (atmospheric) conditions [1, 9–12]. However, for volatile liquids at reduced air pressure, phase change can lead to significant heat fluxes in the liquid layer due to the latent heat released or absorbed at the interface, and the interfacial mass flux (which defines the latent heat flux) cannot be computed reliably without a proper model of bulk mass transport in the gas phase. Therefore a two-sided model is required, where the heat and mass transport in both phases are modeled explicitly. Two-sided models have been formulated previously [49, 50, 82, 87–91]. These models, however, assume rather than compute the shape of the liquid-gas interface, employ extremely restrictive assumptions and/or use a very crude description of one of the two phases.

This Chapter describes a comprehensive two-sided model of buoyancy-thermocapillary convection in confined two-phase fluids with a sharp free interface. The model describes the momentum, heat, and mass transport in both the liquid and the gas phase, with the motion of the liquid-gas interface being calculated based on the flow conditions. Most importantly, phase change across the entire liquid-gas interface is considered, which provides a detailed

description of the momentum, heat, and mass transport between the two phases.

2.2 Fundamental Equations for Simple Fluid Flow

The characteristic length and time scales for this study are much larger than the mean free path, therefore the continuum hypothesis can be applied. The governing equations for single component fluid flow include the *conservation of mass* (continuity)

$$\partial_t \rho + \nabla \cdot (\rho \mathbf{u}) = 0, \tag{1}$$

the *conservation of momentum* (Newton's second law)

$$\rho \left(\partial_t \mathbf{u} + \mathbf{u} \cdot \nabla \mathbf{u} \right) = \nabla \cdot \mathbf{\Sigma} + \mathbf{f}, \tag{2}$$

and the *conservation of energy* (first law of thermodynamics)

$$\rho \left(\partial_t e + \mathbf{u} \cdot \nabla e \right) = \mathbf{\Sigma} : \nabla \mathbf{u} - \nabla \cdot \mathbf{q} + \dot{q}, \tag{3}$$

where:

ρ is the mass density,

k is the thermal conductivity,

$\mathbf{f}$ is the body force density,

$\mathbf{u}$ is the velocity field,

T is the temperature field,

e is the specific internal energy density,

$\mathbf{q}$ is the heat flux,

$\dot{q}$ is the heat source density, and

$\mathbf{\Sigma}$ is the stress tensor, which can be written as a sum of an isotropic part (normal stress) and a deviatoric part (shear stress)

$$\mathbf{\Sigma} = -p \mathbb{1} + \mathbf{\Sigma}' \tag{4}$$

and p is the pressure.

The model described here uses a more common form of the conservation of energy, based on the enthalpy $h_e = e + p/\rho$, which can be obtained from (3). Based on the conservation of mass (1),

$$p\nabla \cdot \mathbf{u} = -\frac{p}{\rho}D_t\rho = \rho D_t\left(\frac{p}{\rho}\right) - D_t p, \tag{5}$$

where $D_t = \partial_t + \nabla \cdot \mathbf{u}$ is the material derivative. Combing (4) and (5), the conservation of energy (3) can be rewritten as

$$\rho\left(\partial_t h + \mathbf{u} \cdot \nabla h\right) = \partial_t p + \mathbf{u} \cdot \nabla p - \nabla \cdot \mathbf{q} + \dot{q} + \Phi, \tag{6}$$

where $\Phi = \mathbf{\Sigma}' : \nabla\mathbf{u}$ is the rate at which heat is generated due to viscous dissipation.

The conservation laws (1), (2), and (6) are fairly general and apply to any simple (i.e., single-component) fluid.

2.3   Fundamental Equations for Binary Fluid Flow

In this work the liquid phase is a simple liquid, however, the gas phase is in general a binary mixture of vapor and air, where air is a noncondensable gas, which requires modifications to the transport equations in the gas phase. The generalization of the transport equations will be used for the mass, momentum, and energy of multi-component mixtures following Chapman and Enskog [156]. Using the classic kinetic Boltzmann equation, a range of transport equations could be obtained for various Knudsen numbers, including the Euler, Navier-Stokes, and Burnett equations [157]. In particular, the transport equations (1), (2), and (6) represent the first order of the Chapman-Enskog expansion for simple gases.

For the gas mixtures, the Chapman-Enskog expansion uses the locally Maxwellian distribution which corresponds to the average temperature of the mixture, and yields the transport equations for the mass, momentum, and energy of the mixture that have the same form as (1), (2) and (6). However, for the gas mixture, $\mathbf{u}$ and e correspond to the average values for all components, while ρ is the sum of the densities of all components, and the body force $\mathbf{f}$ and heat source term $\dot{q}$ include the contributions from all components.

The Chapman-Enskog expansion is valid when the differences between the temperatures and velocities of of different components are negligible (*e.g.* for strongly collisional gases). When there are large differences in the temperature and/or velocity, the Chapman-Enskog expansion does not converge, and alternative approaches have been developed to describe transport under such conditions. For example, Grad [158] applied an expansion about the Maxwellian distribution which converges more rapidly. Hamel [159] showed that when the molecular masses of components are substantially different, (for instance, for hexamethyldisiloxane (HMDS) $M_v \approx 162$ g/mol^{-1}, while for air $M_a \approx 29$ g/mol^{-1}), a more accurate description would require the introduction of different temperatures $T_v \neq T_a$ and separate momentum and energy transport equations for each of the components, coupled through cross-collision terms.

The effect of cross-collision is characterized by a dimensionless parameter

$$Cr = \frac{\ell \omega_{av}}{u},\tag{7}$$

where ℓ and u are the characteristic length and velocity scales of the flow,

$$\omega_{av} = n_a \kappa_{av} \mu_a \mu_v\tag{8}$$

is the dimensional cross-collision frequency, and $\mu_i = m_i/m_0 = m_i/(m_a + m_v)$ is the reduced mass of the molecules of component $i = (a, v)$, and n_i is the corresponding number density. The collision parameter κ_{av} can be estimated based on the mass diffusivity $D = k_B T_a/(\mu_a n_v \kappa_{av} m_0)$, where k_B is Boltzmann's constant, yielding

$$\omega_{av} = \frac{n_a}{n_v} \frac{k_B T_a}{D m_0} \mu_v.\tag{9}$$

Hence (7) can be rewritten as

$$Cr = \frac{\ell}{u} \frac{n_a}{n_v} \frac{k_B T_a \mu_v}{D m_0}.\tag{10}$$

The temperature of the two components equilibrates, and the Hamel's description reduces to the Chapman-Enskog description when $Cr \gg 1$, which indicates strong cross-collision momentum and heat transport. This condition is equivalent to $c_a \gg c_a^*$, where

$$c_a^* = \left(\frac{\ell}{u} \frac{k_B T_0 \mu_v}{D m_0} + 1 \right)^{-1}. \tag{11}$$

In this study the characteristic length, velocity, and temperature scales are $\ell = 10^{-2}$ m, $u = 10^{-2}$ m/s, and $T_0 = 293$ K. The binary mass diffusivity D reaches the maximum value at the total pressure equal to the saturation pressure of the vapor $p_v = 4.1 \times 10^3$ Pa, which yields $c_a^* \approx 1.4 \times 10^{-8}$. Such low concentrations cannot be reached in practice (and below this concentration the effect of air can be simply ignored, with gas treated as pure vapor). Hence the Champan-Enskog description is valid in the entire range of concentrations for which the model for the mixture has been used, and the transport equations (1), (2), and (6) can be used to describe the mixture of HMDS vapor and air.

An additional transport equation is needed to describe the composition of the binary mixture. The conservation of mass for the dilute component is used

$$\partial_t \rho_r + \nabla \cdot (\rho_r \mathbf{u}) = -\nabla \cdot \mathbf{j}_r, \tag{12}$$

where ρ_r is the mass density and $\mathbf{j}_r$ is the diffusive mass flux which arises when the composition varies spatially. Here and below the subscript denotes the components in the gas mixtures (a for air, v for vapor of HMDS, d for the dominant component, and r for the dilute component) or the phase (l for the liquid, g for the gas), and i denotes the liquid-gas interface. In particular, in (12) $r = a$ when the vapor is dominant and $r = v$ when the air is dominant.

2.4 Constitutive Relations

The transport equations determine the evolution of the velocity $\mathbf{u}$, pressure p, temperature T field, and the mass density ρ_r of the dilute component. However, they also involve a

number of other variables and parameters, which are determined using the constitutive relations introduced below.

2.4.1 Equations of State

For the temperature and pressure range of this study, the air can be assumed ideal [160]. The critical pressure of HMDS $p_{cr} = 1.9 \times 10^6$ Pa is much higher than its vapor pressure $p_v \approx 4.1 \times 10^3$ Pa [161, 162]. Hence, the vapor of HMDS can also be assumed ideal [160]. Therefore, in the gas phase,

$$\rho_g = \rho_a + \rho_v, \tag{13}$$

and the partial pressures of the two components, considered to be ideal gases, are

$$p_b = \rho_b \bar{R}_b T, \tag{14}$$

where $\bar{R}_b = R/M_b$, R is the universal gas constant, and M_b is the molar mass of component $b = a$ or v. The total gas pressure is the sum of partial pressures

$$p_g = p_a + p_v. \tag{15}$$

The partial pressures define the concentrations

$$c_b = p_b/p_g \tag{16}$$

of the individual components of the mixture. For the binary mixture $c_v = 1 - c_a$.

The Boussinesq approximation is used following standard practice, where the variation in the density ρ of the fluid (within a single phase) is ignored expect when it appears in the body force term $\mathbf{f} = \rho\mathbf{g}$, where $\mathbf{g}$ is the gravitational acceleration, which represents the effect of buoyancy. In the liquid phase a linear relation

$$\rho_l = \rho_l^0[1 - \beta_l(T - T_0)], \tag{17}$$

is assumed, where ρ_l^0 is the reference density at the reference temperature T_0 and $\beta_l = -\rho_l^{-1}\partial\rho_l/\partial T$ is the coefficient of thermal expansion. In the gas phase the temperature dependence of the density follows directly from the ideal gas law, $\beta_g = 1/T$, and the dependence

on the composition is also considered based on the ideal gas law (13). As found below, the relative change in the density due to the temperature variation is quite small (less than 10% for the gas and less than 4% for the liquid in the examples considered in this study). The relative change in the density due to the composition variation is also fairly small (less than 12% for the gas in the examples considered in this study), so ignoring it in the other terms has a minor effect on solutions. Both equations of state (17) and (14) can be easily generalized as needed.

Since the density variation about the average is relatively small, local variations in density are ignored on the right-hand-side of the momentum conservation equation (2), and the spatially averaged density is used instead for each phase. As a result, the mass conservation equation (1) reduces to the incompressibility constraint

$$\nabla \cdot \mathbf{u} = 0. \tag{18}$$

The equations of state also allows the enthalpy to be evaluated as a function of temperature and pressure. In general

$$dh_e = C_p dT + (1 - \beta T)\frac{dp}{\rho}, \tag{19}$$

where C_p is the heat capacity at constant pressure. For an ideal gas $1 - \beta T = 0$, so enthalpy is independent of pressure. In the liquid phase the pressure is essentially constant. Hence, in both phases

$$dh_e = C_p dT. \tag{20}$$

2.4.2 Molecular Diffusion

Molecular diffusion restores local thermodynamic equilibrium by generating a flux of various quantities in response to external gradients. In particular, a gradient in the temperature ∇T generates a heat flux $\mathbf{q}$, which leads to Fourier's law of heat conduction,

$$\mathbf{q} = -k\nabla T, \tag{21}$$

where k is the thermal conductivity of the fluid.

The mass flux $\mathbf{j}_b$ is caused by the gradients in the concentration, pressure, and temperature [156, 163],

$$\mathbf{j}_b = -\rho_g D\nabla(\rho_b/\rho_g) - (\rho_g/T)D_T\nabla T - (\rho_g/p_g)D_p\nabla p, \tag{22}$$

where D is the binary diffusion coefficient, D_T is the coefficient for "thermodiffusion" (or "Soret effect" in the liquid) [164], and D_p is the coefficient for "barodiffusion" [165]. In this problem, the diffusion due to pressure gradient, i.e., barodiffusion, is negligible since the gradient of the total pressure is much smaller than the gradient of the concentration. The diffusion due to temperature is also negligible since D_T is in general much smaller than D, moreover, with the Boussinesq approximation, ρ_g is assumed to be constant. So the diffusive mass flux simplifies to

$$\mathbf{j}_b = -D\nabla\rho_b. \tag{23}$$

Similarly, the gradient in the velocity causes the flux of momentum. The fluids considered in this study are Newtonian, with a linear relation between the stress and the strain rate. For Newtonian fluids the stress tensor can be written as

$$\mathbf{\Sigma} = \mu\left[\nabla\mathbf{u} + (\nabla\mathbf{u})^T\right] + \lambda_c\mathbb{1}\nabla\cdot\mathbf{u} - p\mathbb{1}, \tag{24}$$

where μ is the dynamic viscosity, and λ_c is the coefficient of bulk viscosity. When the flow is incompressible, the stress tensor simplifies to

$$\mathbf{\Sigma} = \mu\left[\nabla\mathbf{u} + (\nabla\mathbf{u})^T\right] - p\mathbb{1}, \tag{25}$$

2.4.3 Material Parameters

The material parameters representing various transport phenomena in simple and multi-component fluids can be calculated from the kinetic theory of gases [156, 163, 166, 167], and/or empirical formulas [160, 160, 168, 169]. Within the range of the pressure and temperature variation of the present work, the variation in the fluid properties is relatively small

[161, 162] and it is sufficient to consider only the dominant effect, i.e., the linear variation of various material parameters with temperature,

$$\zeta^m(T) = \zeta_0^m[1 - \beta^m (T - T_0)], \tag{26}$$

where ζ^m, for different m, represents the dynamic viscosity μ, thermal conductivity k, specific heat C_p for all components in both phases, the coefficient of thermal expansion for the liquid, the latent heat $\mathcal{L}$, the surface tension σ, and the temperature coefficient of the surface tension γ, ζ_0^m represents the reference values at the reference temperature T_0, and the coefficients $\beta^m = -(\partial\zeta^m/\partial T)/\zeta^m$ are obtained based on the linear fits of the tabulated values found in Refs. [161, 162], with the exceptions for the dynamic viscosity and thermal conductivity of the air, where the coefficients are computed using Sutherland's law [170, 171].

Most of the properties of the gas phase (when it is a binary mixture) can be determined from a weighted average of the properties of the two components

$$\zeta^m = c_a\zeta_a^m + (1 - c_a)\zeta_v^m. \tag{27}$$

Exceptions are the mass density which, according to (13) and (14), is

$$\rho_g = \left[\frac{c_a}{1 - c_a}\frac{\bar{R}_v}{\bar{R}_a} + 1\right]\rho_v. \tag{28}$$

where ρ_v is the saturated vapor density, and the transport coefficients which obey Wilke's rule [169]. For instance, the dynamic viscosity is

$$\mu_g = \sum_i \frac{c_i\mu_i}{\sum_j c_j\Phi_{ij}} \tag{29}$$

and thermal conductivity is

$$k_g = \sum_i \frac{c_i k_i}{\sum_j c_j\Phi_{ij}}, \tag{30}$$

where

$$\Phi_{ij} = \frac{\left[1 + \left(\frac{\mu_i}{\mu_j}\right)^{1/2}\left(\frac{M_j}{M_i}\right)^{1/4}\right]^2}{\sqrt{8}\left[1 + \frac{M_i}{M_j}\right]^{1/2}}. \tag{31}$$

Based on these values, the kinematic viscosity $\nu_g = \mu_g/\rho_g$ and the thermal diffusivity $\alpha_g = k_g/(\rho_g C_p)$ can be calculated. Finally, the binary mass diffusivity D is a function of both pressure and temperature

$$D = D_0 \frac{p_g^0}{p_g} \left(\frac{T}{T_0}\right)^{3/2}, \tag{32}$$

where D_0 is the diffusion coefficient at reference temperature T_0 and pressure p_g^0 (taken to be equal to the average temperature and atmospheric pressure below).

2.5 Simplified Form of the Governing Equations

Incorporating the constitutive relations into the transport equations (1), (2), (6) and (12) four evolution equations are obtained for the four unknown fields, $\mathbf{u}$, p, T, and ρ_r. In particular, the mass conservation equation (1) reduces to the divergence-free condition (18) for the velocity field.

With the help of (18), the constitutive relation for a Newtonian fluid (4), and the Boussinesq approximation, the momentum conservation is reduced to the Navier-Stokes equation

$$\rho \left(\partial_t \mathbf{u} + \mathbf{u} \cdot \nabla \mathbf{u}\right) = -\nabla p + \mu \nabla^2 \mathbf{u} + \rho(c, T)\mathbf{g}, \tag{33}$$

where the density dependence on the temperature and, for the gas phase, the composition, is explicitly included in the buoyancy force term to illustrate that it is not constant. In contrast, the density on the left-hand-side is considered constant for each phase (defined as the spatial average of ρ_l or ρ_g).

In the problem considered here there are no internal heat sources or sinks, i.e., $\dot{q} = 0$, so substituting the expressions for enthalpy (19) and heat flux (21), the energy conservation (6) can be rewritten as

$$\rho C_p \left(\partial_t T + \mathbf{u} \cdot \nabla T\right) = \beta T (\partial_t p + \mathbf{u} \cdot \nabla p) + k \nabla^2 T + \Phi. \tag{34}$$

The terms on the left-hand-side are of order $\rho u_t^2/t^*$, where u_t is the thermal velocity, which is a few hundred m/s at ambient temperature and t^* is the characteristic time scale for the

flow. The terms on the right-hand-side which involve pressure are at most of order $\rho u^{*2}/t^*$, where the characteristic flow velocity u^* is of order cm/s and hence can be safely ignored. The viscous dissipation term Φ is of order $\rho u^{*2}\nu/\ell^{*2}$, where $\nu = \mu/\rho$ is the kinematic viscosity of the fluid and ℓ^* is the characteristic length scale of the flow. Since t^* is at most comparable to the viscous time scale ℓ^{*2}/ν, this term can also be safely ignored [75]. Therefore, the transport of heat is described by an advection-diffusion equation

$$\partial_t T + \mathbf{u} \cdot \nabla T = \alpha \nabla^2 T, \tag{35}$$

where $\alpha = k/\rho C_p$ is the thermal diffusivity

Finally, with the help of (23) the transport equation for the dilute component (12) can also be cast in the form of an advection-diffusion equation

$$\partial_t \rho_r + \mathbf{u} \cdot \nabla \rho_r = D \nabla^2 \rho_r. \tag{36}$$

This equation guarantees the mass conservation for the dilute component locally. As a consequence, the mass of the dilute component is also conserved globally.

Mass conservation of the dominant component d requires a separate equation

$$\int_{\text{gas}} \rho_d dV + m_l \delta_{d,v} = m_d \tag{37}$$

where $\delta_{d,v}$ is the standard Kronecker delta,

$$m_l = \int_{\text{liquid}} \rho_l dV \tag{38}$$

is the mass of the liquid phase, and m_d is its total mass of the dominant component. The Navier-Stokes equation and the incompressibility conditions define the pressure field p up to a constant p_o. The total pressure in the gas phase is

$$p_g = p + p_o, \tag{39}$$

where the pressure offset p_o can be computed from the mass conservation constraint (37) using (13), (14), (15) and (39):

$$p_o = \left[m_d - m_l \delta_{d,v} - \int_{\text{gas}} \frac{p - \rho_r \bar{R}_r T}{\bar{R}_d T} dV \right] / \left[\int_{\text{gas}} \frac{1}{\bar{R}_d T} dV \right]. \tag{40}$$

When the gas is pure vapor, $c_a = 0$, the fields $\mathbf{u}$, p, and T can be found by solving the governing equations (18), (33), and (35), subject to the constraint (40). When the gas phase is a binary mixture, $\mathbf{u}$, p, T, and ρ_r can be found using the governing equations (18), (33), (35) and (40) for the mixture, and the equation (36) for the dilute component, with (16) yielding the solution for the concentration field.

2.6 Boundary Conditions

As Fig. 4 illustrates, the fluid is assumed to be contained in a rectangular test cell with inner dimensions $L \times W \times H$, and thin walls of thickness h_w. Hence, the system of coupled evolution equations for the bulk fields has to be solved in a self-consistent manner, subject to the boundary conditions describing the balance of momentum, heat, and mass fluxes at the liquid-gas interface and at the inner surface of the walls of the cavity.

2.6.1 Liquid-Gas Interface

There are two kinds of boundary conditions at the liquid-gas interface. The first kind is a direct consequence of conservation laws discussed above and can be obtained by integrating (18), (33), (35) or (36) over a small "pillbox" control volume enclosing a portion of the interface. The second type of boundary conditions is obtained using kinetic theory and describes the flux of various quantities caused by deviations from local phase equilibrium at the interface.

2.6.1.1 Local Phase Equilibrium

Local phase equilibrium between the vapor and the liquid phase is established when the temperature of the vapor at the interface is equal to the saturation temperature (at a given temperature) when the chemical potentials of the liquid and vapor phases are equal. This leads to a relationship between saturation temperature and pressure known as the Clausius-Clapeyron equation

$$\ln \frac{p_v}{p_v^0} = \frac{\mathcal{L}}{\bar{R}_v}\left(\frac{1}{T_s^0} - \frac{1}{T_s}\right), \tag{41}$$

where the subscript s denotes the saturation values and T_s^0 is the saturation temperature at the reference vapor pressure p_v^0. Fluids with a higher vapor pressure are usually more volatile, and the vapor pressure is more sensitive to the temperature for fluids with higher latent heat. In the numerical model a generalization (valid over a wider range of temperatures) of (41), known as the Antoine equation

$$\ln p_v = A_v - \frac{B_v}{C_v + T_s} \tag{42}$$

is used, where A_v, B_v, and C_v are empirical coefficients.

The Clausius-Clapeyron equation (41) can be considered a "linearization" of the Antoine equation valid over a small range of temperatures. It is easy to see that

$$p_v^0 = \exp\left(A_v - \frac{B_v}{C_v + T_s^0}\right) \tag{43}$$

and

$$\mathcal{L} = B_v \bar{R}_v \left(\frac{T_s^0}{C_v + T_s^0}\right)^2. \tag{44}$$

For the ranges of temperatures explored in this study, the variation in p_v^0 and $\mathcal{L}$ is negligible and both parameters can be assumed constant. In principle, either (41) or (42) can be used to determine the saturation pressure as a function of temperature. However, to ensure logical consistency in the remainder of this work the Clausius-Clapeyron equation will be used in all analytical calculations, while the Antoine equation will be used to compute the equilibrium value of the vapor pressure p_v^0 and the latent heat $\mathcal{L}$ at the reference temperature T_0 using the relations (43) and (44).

2.6.1.2 Heat and Mass Flux Balance

The heat flux balance across the interface is given by

$$\mathcal{L}J = k_g \partial_n T_g - k_l \partial_n T_l, \tag{45}$$

where $\partial_n = \mathbf{n} \cdot \nabla$ and $\mathbf{n}$ is the unit normal to the interface pointing towards vapor and J is the vapor mass flux density due to phase change (positive for evaporation, negative for

condensation). The mass flux balance on the liquid side of the interface gives

$$u_{l,n} - u_{i,n} = \frac{J}{\rho_l}, \tag{46}$$

where the right-hand-side can be neglected, since $\rho_l \gg \rho_g$. Here and below the index after the comma indicates the component of a vector. On the gas side of the interface, when there is no air, the mass flux balance on the vapor side of the interface is described by a similar relation

$$J = \rho_v(u_{g,n} - u_{i,n}). \tag{47}$$

When the gas is a mixture of air and vapor,

$$J = -D\partial_n\rho_v + \rho_v(u_{g,n} - u_{i,n}), \tag{48}$$

where the first term on the right-hand-side represents the diffusion component, and the second term represents the advection component (referred to as the "convection component" by Wang *et al.* [88]). Since air is noncondensable, its mass flux across the interface is zero, therefore

$$0 = -D\partial_n\rho_a + \rho_a(u_{g,n} - u_{i,n}). \tag{49}$$

For binary diffusion, the diffusion coefficient of vapor through air is the same as that of air through vapor. The densities of vapor and air can be related through the mass conservation and the ideal gas law

$$\frac{\rho_v}{M_v} + \frac{\rho_a}{M_a} = \frac{p_g}{RT}, \tag{50}$$

and their normal gradients can be related by taking the normal gradients on both sides of (50). Since the total pressure is essentially constant, this yields

$$\frac{\partial_n\rho_v}{M_v} + \frac{\partial_n\rho_a}{M_a} = -\frac{p_g}{RT_i^2}\partial_n T_g. \tag{51}$$

Together with (48) and (49) this relation can be used to express J directly in terms of $\partial_n\rho_b$ and $\partial_n T_g$, where $b = a$ or v.

2.6.1.3 Phase Change Models

Several theoretical models have been put forward to describe the mass flux across the liquid-vapor interface due to phase change. By far the most commonly used and widely accepted model is based on the Kinetic Theory of Gases (KTG) [172]. It assumes that the chemical potential and the temperature are continuous across the liquid-vapor interface

$$T_l = T_i = T_v,\tag{52}$$

and predicts that the mass flux across the interface is given by

$$J = \frac{2\chi}{2 - \chi}\sqrt{\frac{1}{2\pi\bar{R}_v}}\left[\frac{p_s(T_i)}{T_i^{1/2}} - \frac{p_v}{T_v^{1/2}}\right],\tag{53}$$

where χ is the accommodation coefficient, which describes the fraction of vapor molecules moving towards the interface that remain at the interface (as opposed to reflecting back into the vapor phase). Unless stated otherwise, $\chi = 1$ is used in this study, since for nonpolar liquids, such as HMDS, the accommodation coefficient is found to be equal (or very close) to unity [173, 174]. With the help of the Clausius-Clapeyron relation (41), (53) can be approximated as [175]

$$J = \Omega(T_i - T_s),\tag{54}$$

where

$$\Omega = \frac{2\chi}{2 - \chi}\sqrt{\frac{1}{2\pi\bar{R}_v}}\frac{p_s\mathcal{L}}{\bar{R}_vT_s^{5/2}}\tag{55}$$

is referred as the interfacial resistance associated with phase change. In this thesis, unless mentioned otherwise, phase change will be described by an alternative form [176] of the expression (53)

$$J = \frac{2\chi}{2 - \chi}\rho_v\sqrt{\frac{\bar{R}_vT_i}{2\pi}}\left[\frac{p_l - p_g}{\rho_l\bar{R}_vT_i} + \frac{\mathcal{L}}{\bar{R}_vT_i}\frac{T_i - T_s}{T_s}\right],\tag{56}$$

which explicitly incorporates the pressure jump (e.g., due to curvature or disjoining pressure) across the interface. Expression (56) involves linearization of (53) and, while it is consistent with the Clausius-Clapeyron relation (41), it is only consistent with the Antoine

equation (42) over the range of temperatures for which the latent heat (44) can be considered constant.

The KTG model is applicable only for relatively small deviations from the state of global thermodynamic equilibrium (i.e., small imposed temperature gradients) and breaks down for larger deviations (larger gradients). Phase change under conditions far from equilibrium can be described more accurately by models that, unlike KTG, allow for a jump in the temperature and chemical potential at the liquid-vapor interface. In particular, the Non-Equilibrium Thermodynamics (NET) model [177] was developed specifically to describe phase change far from equilibrium, but has also been used to explain some nonintuitive observations (e.g., inverted temperature profiles in liquids with large latent heats [178]) in near-equilibrium systems. It predicts the following relations between the mass flux J and the heat flux $q_v = k_v \partial_n T_v$ on the vapor side:

$$\frac{p_s - p_v}{\sqrt{2\pi \bar{R}_v T_l}} = r_{11} J + r_{12} \frac{q_v}{\bar{R}_v T_l}, \tag{57}$$

$$\frac{p_s}{\sqrt{2\pi \bar{R}_v T_l}} \frac{T_l - T_v}{T_l} = r_{21} J + r_{22} \frac{q_v}{\bar{R}_v T_l}, \tag{58}$$

where T_l and T_v are the interfacial temperatures on the liquid and vapor side, respectively, and $p_s(T_l)$ is determined from (42). The dimensionless resistivities r_{ij} are obtained from the Onsager reciprocity relation. If the vapor behaves as an ideal gas with accommodation (condensation) coefficient χ, their values can be obtained using kinetic theory of gases [178]: $r_{11} = \chi^{-1} - 0.40044$, $r_{12} = r_{21} = 0.126$, and $r_{22} = 0.294$.

Another phase change model was derived using Statistical Rate Theory (SRT) [179, 180] to explain measured temperature jumps at water-vapor interfaces during intensive evaporation in the near-absence of noncondensables with and without external temperature gradients [181, 182]. The model is based on the transition probability concept, as defined in quantum mechanics, and uses the Boltzmann definition of entropy to describe irreversible processes far from global thermodynamic equilibrium. SRT predicts the following mass

flux across the interface [182]:

$$J = \frac{2p_s}{\sqrt{2\pi\bar{R}_v T_l}} \left[\frac{p_v - p_s + 2\kappa\sigma}{\rho_l \bar{R}_v T_l} + \frac{p_s}{p_v} - 1 - 2\left(\frac{T_v}{T_l} - 1\right)^2 \right],$$ (59)

where $\kappa = \nabla \cdot \mathbf{n}$ is the interfacial curvature and $p_s(T_l)$ is again determined by (42). SRT, however, does not give a prediction for the heat flux q_v on the vapor side. To complete the system, one additional expression is derived from NET following Bond and Struchtrup [183]. Combining (57) and (58) yields

$$q_v = \frac{p_s \bar{R}_v (r_{11}T_l - r_{21}T_l - r_{11}T_v) + r_{21}p_v \bar{R}_v T_l}{(r_{11}r_{22} - r_{12}r_{21}) \sqrt{2\pi_v \bar{R}_v T_l}}.$$ (60)

The phase change model based on SRT assumes that all molecules from the vapor phase that collide with the liquid-vapor interface are transferred to the liquid phase [180], which is equivalent to setting $\chi = 1$. Furthermore, the cross terms are ignored [183], i.e., $r_{12} = r_{21} = 0$. In order to facilitate comparison between the phase change models based on KTG, NET and SRT, these values will be used for the accommodation coefficient and the cross terms coefficients in the remainder of this study, unless noted otherwise.

2.6.1.4 Boundary Conditions for the Velocity

The boundary conditions for the normal components of the velocity have been discussed in Section 2.6.1.2. The tangential components are considered to be continuous at the liquid-gas interface

$$(\mathbb{1} - \mathbf{nn}) \cdot (\mathbf{u}_l - \mathbf{u}_g) = 0.$$ (61)

The stress (or momentum flux) balance incorporates the viscous drag between the two phases, thermocapillary effects, and the vapor recoil [47]

$$(\mathbf{\Sigma}_l - \mathbf{\Sigma}_g) \cdot \mathbf{n} = \mathbf{n}\kappa\sigma + \nabla_s\sigma + J^2(\rho_l^{-1} - \rho_g^{-1})\mathbf{n},$$ (62)

where $\mathbf{\Sigma}_l$ and $\mathbf{\Sigma}_g$ are the stress tensors on the liquid and gas side of the interface, and

$$\nabla_s = (\mathbb{1} - \mathbf{nn}) \cdot \nabla$$ (63)

40

is the surface gradient.

It is useful to consider the normal and tangential components of the stress balance (62) separately. For the normal component, it is found from (4)

$$\mathbf{n} \cdot \boldsymbol{\Sigma} \cdot \mathbf{n} = -p + 2\mu\mathbf{n}\mathbf{n} : \nabla\mathbf{u}. \tag{64}$$

On the other hand, taking the trace of the identity

$$\nabla\mathbf{u} = \nabla_s\mathbf{u} + \mathbf{n}\mathbf{n} \cdot \nabla\mathbf{u}. \tag{65}$$

yields

$$\nabla \cdot \mathbf{u} = \nabla_s \cdot \mathbf{u} + \mathbf{n}\mathbf{n} : \nabla\mathbf{u}. \tag{66}$$

Therefore, for incompressible flow

$$\mathbf{n}\mathbf{n} : \nabla\mathbf{u} = -\nabla_s \cdot \mathbf{u} \tag{67}$$

and the normal stress balance can rewritten as

$$p_g - p_l = \sigma\kappa + 2(\mu_l - \mu_g)\nabla_s \cdot \mathbf{u}_i + J^2(\rho_l^{-1} - \rho_g^{-1}). \tag{68}$$

In the problem considered here the vapor recoil term is negligible compared with the capillary pressure term and hence will not be included.

For the tangential components of the stress balance it is found

$$(\mathbb{1} - \mathbf{n}\mathbf{n}) \cdot (\boldsymbol{\Sigma}_l - \boldsymbol{\Sigma}_g) \cdot \mathbf{n} = \nabla_s\sigma, \tag{69}$$

or, introducing a tangent vector $\boldsymbol{\tau}$,

$$\boldsymbol{\tau} \cdot (\boldsymbol{\Sigma}_l - \boldsymbol{\Sigma}_g) \cdot \mathbf{n} = \partial_\tau\sigma. \tag{70}$$

where $\partial_\tau = \boldsymbol{\tau} \cdot \nabla$. In this work, surface tension is assumed to be a linear function of temperature, so

$$\nabla_s\sigma = -\gamma\nabla_s T_i, \tag{71}$$

where $\gamma = -\partial\sigma/\partial T$ is the temperature coefficient of surface tension. Hence, the tangential components of stress balance (70) can be rewritten as

$$\mu_l[\partial_n u_{l,\tau} + \partial_\tau u_{l,n}] - \mu_g[\partial_n u_{g,\tau} + \partial_\tau u_{g,n}] = -\gamma\partial_\tau T_i. \tag{72}$$

2.6.2 Inner Surface of the Cavity

Since the thickness (in x extent) of the walls of the cavity is much smaller than that of the liquid and gas layer, one-dimensional conduction through the walls is assumed, yielding an analytical solution for the temperature inside the walls. Using this solution, the following boundary conditions can be applied on the inside of the side walls:

$$
\begin{aligned}
T|_{x=0} &= T_c + \frac{k}{k_w} h_w \partial_n T, \\
T|_{x=L} &= T_h + \frac{k}{k_w} h_w \partial_n T,
\end{aligned}
\tag{73}
$$

where $k = k_g$ ($k = k_l$) above (below) the contact line. For the other (the top, bottom, front and back) walls, heat flux is ignored

$$
\partial_n T = 0 \tag{74}
$$

since adiabatic boundary conditions are typical of most experiments.

Standard no-slip boundary conditions $\mathbf{u} = 0$ for the velocity and, for a binary mixture, no-flux boundary conditions

$$
\partial_n \rho_r = 0 \tag{75}
$$

for the density of the dilute component are imposed on all the walls.

2.6.3 Solution Procedure

The boundary conditions imposed at different boundaries are summarized in Table 1. In order to find numerical solutions, the governing equations (33), (35) and (36) are solved

Table 1: Types of boundary conditions imposed on various boundaries in the numerical implementation of the model.

Field	Types of boundary conditions			
	Interface, vapor side	Interface, liquid side	Hot/Cold walls	Other alone walls
$\mathbf{u}$	Dirichlet	Neumann	Dirichlet	Dirichlet
p	Neumann	Dirichlet	Neumann	Neumann
T	Dirichlet	Neumann	Neumann	Neumann
ρ	Neumann	–	Neumann	Neumann

separately in the two phases. The solution requires that the boundary equations at the liquid-gas interface be separated between the two sides of the interface, while there is some freedom in which boundary conditions are applied on each side. The boundary conditions chosen for these simulations were dictated by the numerical implementation. For instance, temperature continuity (52) was imposed on the vapor side, while the heat flux balance (45) was imposed on the liquid side of the interface.

The nonlinear equations representing the boundary conditions at the interface are coupled and need to be solved simultaneously. During the simulations, the solution of this system of equation is found using Newton iteration with the values of the field at the previous time step used as the initial condition. The boundary conditions and the fields solved for depend on the model and the gas phase composition, which are discussed in detail in the appendix B.2.3.2.

CHAPTER 3

CONVECTION AT ATMOSPHERIC CONDITIONS

Most of the intuition on which the design of current two-phase thermal management devices, such as heat pipes, is based on studies of convection at atmospheric conditions. The strength of the two main forces driving convection, buoyancy and thermocapillarity, is most commonly described in terms of the nondimensional parameters

$$Ra_L = \frac{g\beta_l d_l^4 \Delta T}{\nu_l \alpha_l L} \tag{76}$$

and

$$Ma_L = \frac{\gamma d_l^2 \Delta T}{\mu_l \alpha_l L}, \tag{77}$$

which are known, respectively, as the "laboratory" Rayleigh and Marangoni number. Although it is relatively easy to measure Ma_L in experiments, thermocapillary stress is determined by the interfacial temperature gradient τ, which could be significantly different from the imposed temperature gradient $\Delta T/L$. Hence, more recent studies use instead the "interfacial" Marangoni number

$$Ma_i = \frac{\gamma d_l^2}{\mu_l \alpha_l} \tau. \tag{78}$$

One can similarly define the "interfacial" Rayleigh number

$$Ra_l = \frac{g\beta_l d_l^4 \tau}{\nu_l \alpha_l}. \tag{79}$$

The ratio of the Rayleigh and Marangoni numbers

$$Bo_D = \frac{Ra_L}{Ma_L} = \frac{Ra_l}{Ma_i} = \frac{\rho_l g \beta_l d_l^2}{\gamma} \tag{80}$$

is independent of the applied thermal gradient. It quantifies the relative strength of buoyancy and thermocapillarity and is known as the dynamic Bond number.

Essentially all available experimental evidence suggests that as Ma_i (or Ma_L) increases, the initially steady and uniform flow becomes less stable, leading to the development of a

series of localized convection rolls from the hot end. For small values of the dynamic Bond number ($Bo_D \lesssim 0.2$) when thermocapillarity dominates, hydrothermal waves form at an angle to the direction of the thermal gradient and travel from the cold end towards the hot end [12]. For larger Bo_D, when buoyancy becomes important, a steady pattern develops instead. It features multiple stationary co-rotating convection rolls that align in the transverse direction (at least when the transverse aspect ratio $\Gamma_y = W/d_l$ is not very large). As Ma_i increases further, an oscillatory multicellular state develops with convection rolls near the cold end traveling in the direction opposite to hydrothermal waves and substantially more complicated dynamics near the hot end [1, 9–12].

The problem has also been studied using various theoretical approaches. The majority of numerical studies to date [9, 19–22] have also focused on convection under atmospheric conditions. For the most part, the numerical simulations used a one-sided model that ignored transport in the gas phase, assumed a liquid layer with a flat, non-deformable free surface with adiabatic boundary conditions, and neglected phase change. Li *et al.* [24] have investigated non-adiabatic effects by using Newton's law of cooling at small Biot numbers. While these numerical simulations were able to reproduce many features of the experimental observations, their results have limited applicability. Most important, they fail to account for the effects of volatility, which can be rather significant, especially at reduced pressures.

Analytical solutions were derived for an unbounded uniform return flow [4, 5, 184], also using a one-sided model. These solutions predict rather accurately the steady unicellular flow observed in finite cavities away from the end walls under ambient conditions at low temperature gradients. The transitions between the flow patterns have also been studied using linear stability analysis. Most of the studies again assumed an adiabatic boundary condition at the free surface and failed to predict the correct patterns, particularly, the transitions to steady multicells [14, 15]. It was found that if the adiabatic boundary condition is replaced with Newton's law of cooling [16], a transition to stationary rolls is found for

a range of *Bi* and *Bo*$_D$. However the rolls are longitudinal, rather than transverse. Furthermore, it was shown that, depending on the Prandtl number

$$Pr_l = \frac{\nu_l}{\alpha_l} \tag{81}$$

of the liquid, stationary convection rolls tend to form near the hot (for normal liquids with $Pr_l > 1$) or cold (for liquid metals with $Pr_l < 1$) end wall [17]. Finally, Priede and Gerbeth [18] showed that stationary transverse convection rolls should arise in laterally bounded layers naturally, since traveling waves run into one of the end walls and dissipate before they can be sufficiently amplified as a result of linear instability.

Since none of the theoretical studies described above accounted for the shape of the free surface, the proper thermal boundary conditions at the free surface, or the effect of transport in the gas phase, this study investigated buoyancy-thermocapillary convection under ambient conditions numerically and analytically using a two-sided model. This Chapter describes the results which were originally reported in [185]. Hence, for consistency, we use the material parameters from [185], which are summarized in Table 2. The objectives of this investigation are two-fold: (i) to validate the two-sided model and its numerical implementation and (ii) to determine the validity of the various assumptions made, explicitly or implicitly, by the one-sided models.

3.1   Numerical Results

In all the numerical simulations reported in this work, the initial condition corresponds to both layers at rest, with uniform temperature $T_0 = (T_c + T_h)/2$ (= 293 K in all cases), where T_h and T_c are the temperatures imposed, respectively, on the outer surfaces of the left and the right side wall (cf. Fig. 4). The liquid layer is of uniform thickness (so the liquid-gas interface is initially flat), and the gas layer is a uniform mixture of vapor and air. The partial pressure of the vapor $p_v = p_s(T_0)$ is set equal to the vapor pressure at T_0, calculated from (42), and the partial pressure of air p_a is such that the total pressure p_g is equal to the ambient pressure (1 atm). As the system evolves towards an asymptotic state, the flow

develops in both phases, the interface distorts to accommodate the assigned contact angle at the walls, and gradients in the temperature and vapor concentration are established. The silicone oil (HMDS) wets quartz very well. However, in the numerical simulations the contact angle $\theta \equiv 50°$ (unless noted otherwise) to avoid numerical instabilities.

The wetting of the cavity walls by the liquid leads to the distortion of the free surface which depends on the value of the contact angle (cf. Fig. 5). The curvature of the free surface is the highest near the walls, while away from the walls the interface becomes flat. When the flow is sufficiently slow, the corresponding capillary rise is given by [186]

$$d_c = \sqrt{2} \sin\left(\frac{\pi}{4} - \frac{\theta}{2}\right) l_c, \tag{82}$$

where θ is the contact angle and l_c is the capillary length

$$l_c = \sqrt{\frac{\sigma}{\rho_l g}} \tag{83}$$

which, for HMDS, is equal to 1.45 mm. For $\theta = 50°$ we have $d_c \approx 1$ mm, which is comparable to the thickness $d_l = 2.45$ mm of the flat portion of the liquid layer in the central portion of the cavity.

Since the initial transient state is of secondary interest, the simulation is initially performed on a coarse hexahedral mesh (initially all cells are cubical with side 0.5 mm). In

Table 2: Material properties at the reference temperature $T_0 = 293$ K and pressure $p_g = 1$ atm. The coefficients A_v, B_v, and C_v for the Antoine's equation were taken from Ref. [168].

	liquid	air	vapor
μ (kg/m-s)	4.95×10^{-4}	1.82×10^{-5}	5.84×10^{-6}
ρ (kg/m³)	761.0	1.43	0.28
k (W/(m·K))	0.10	0.03	0.01
β (1/K)	1.34×10^{-3}	3.41×10^{-3}	3.41×10^{-3}
α (m²/s)	9.52×10^{-8}	1.89×10^{-5}	2.71×10^{-5}
σ (N/m)	1.59×10^{-2}		
γ (N/m-K)	7×10^{-5}		
D (m²/s)	2.5×10^{-5}		
$\mathcal{L}$ (J/kg)	2.14×10^{5}		
A_v (Pa)	20.16		
B_v (Pa·K)	2.58×10^{3}		
C_v (K)	-74.71		

order to resolve the fine structure of the various boundary layers, especially in the liquid layer, mesh refinement, which is discussed in B.3.4, is applied when the solution has converged on the current mesh, and the simulation is resumed on the refined mesh, until the results become mesh independent. To ensure that an asymptotic (steady or time-periodic) state is achieved, all the 2D simulations were carried out to a physical time of at least 600 s, while the 3D simulations, which were much more computationally intensive, were carried out to physical times of at least 100 s.

Most of the numerical results presented below were obtained using 2D simulations, which correspond to the vertical mid-plane of the cavity, $y = W/2$, with the physical boundary conditions on the side walls (front and back of the cavity) replaced with periodic boundary conditions for all the fields. A series of simulations were carried out with the same geometry and initial conditions, but with different temperature differences ΔT imposed between the outer surface of the two end walls. As the focus is primarily on the effect of the gas layer, the thickness d_l of the liquid layer (away from the walls) is held fixed. Previous studies show that, at the values of $Bo_D = 0.85$ and $Pr_l = 6.8$ describing this setup, the primary instability is towards a stationary pattern of transverse convection rolls.

3.1.1 Steady Unicellular and Multicellular Flow

For sufficiently low ΔT, the flow reaches a steady state (after an initial transient). Fig. 6 shows the streamlines of this steady flow in both the liquid and the gas phases at several values of ΔT. Closed streamlines near the bottom wall and the interface which extend over
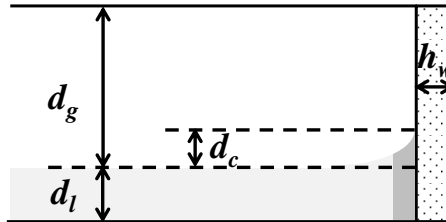
Figure 5: The schematic of the meniscus region near the hot end wall (dotted rectangle on the right). The liquid (light gray) rises near the wall as result of wetting. The dark gray denotes the thermal boundary layer in the liquid.

the entire liquid layer indicate that return flow is observed in the liquid layer. In particular, when $\Delta T = 4$ K, a uniform return-flow basic state is observed in the core region of the flow. The liquid flows from the hot (right) end of the test cell towards the cold (left) end along the free surface, driven by a combination of buoyancy and thermocapillary stresses, with a return flow near the bottom. In the gas layer, thermocapillarity opposes buoyancy, resulting in a large clockwise convective roll in the core region. Buoyancy produces two smaller counterclockwise recirculation rolls in the top corners. Following Riley and Neitzel's terminology, this is called a steady unicellular flow (SUF).

It should be mentioned, however, that a pair of convection rolls always exists near the end walls, a stronger one near the hot end wall and a weaker one near the cold end wall. These convection rolls are driven by buoyancy and are a characteristic feature of convection due to a horizontal temperature gradient. In this case the end walls enhance the convective motion, unlike the case of the vertical temperature gradient where the viscous boundary layers near the end walls suppress convection.

As ΔT increases, additional convection rolls appear starting near the hot end wall. For instance, at $\Delta T = 7$ K four additional convection rolls can be distinguished in the liquid layer near the hot wall. When the temperature difference is increased to $\Delta T = 10$ K, the convection rolls become more pronounced, especially near the hot wall, but the pattern still does not extend across the entire cell. This convective motion starts to affect the temperature field, leading to undulations in the isotherms in the liquid phase (see Fig. 7) near the hot wall reflecting the advection of heat by the convective motion of the fluid. Riley and Neitzel named the pattern with multiple stationary convection rolls a steady multicellular flow (SMC). Deviating from their naming convention and following instead Li *et al.* [1], this flow pattern is defined as partial multicells (PMC) when the convection rolls do not extend over the entire horizontal extent of the system. As ΔT is increased to 15 K, the convective pattern spreads over the entire cell and the convective rolls are clearly distinguishable not only in the liquid, but also in the gas phase. This pattern will be referred to

here as the "true" SMC state. As ΔT is increased further, to 20 K, convection in both layers becomes more vigorous, but the pattern remains stationary.

The temperature field shown in Fig. 7 displays a pronounced asymmetry between the liquid and the gas layer. In the liquid layer the temperature field is affected quite strongly

$\Delta T = 4$ K

$\Delta T = 7$ K

$\Delta T = 10$ K

$\Delta T = 15$ K

$\Delta T = 20$ K
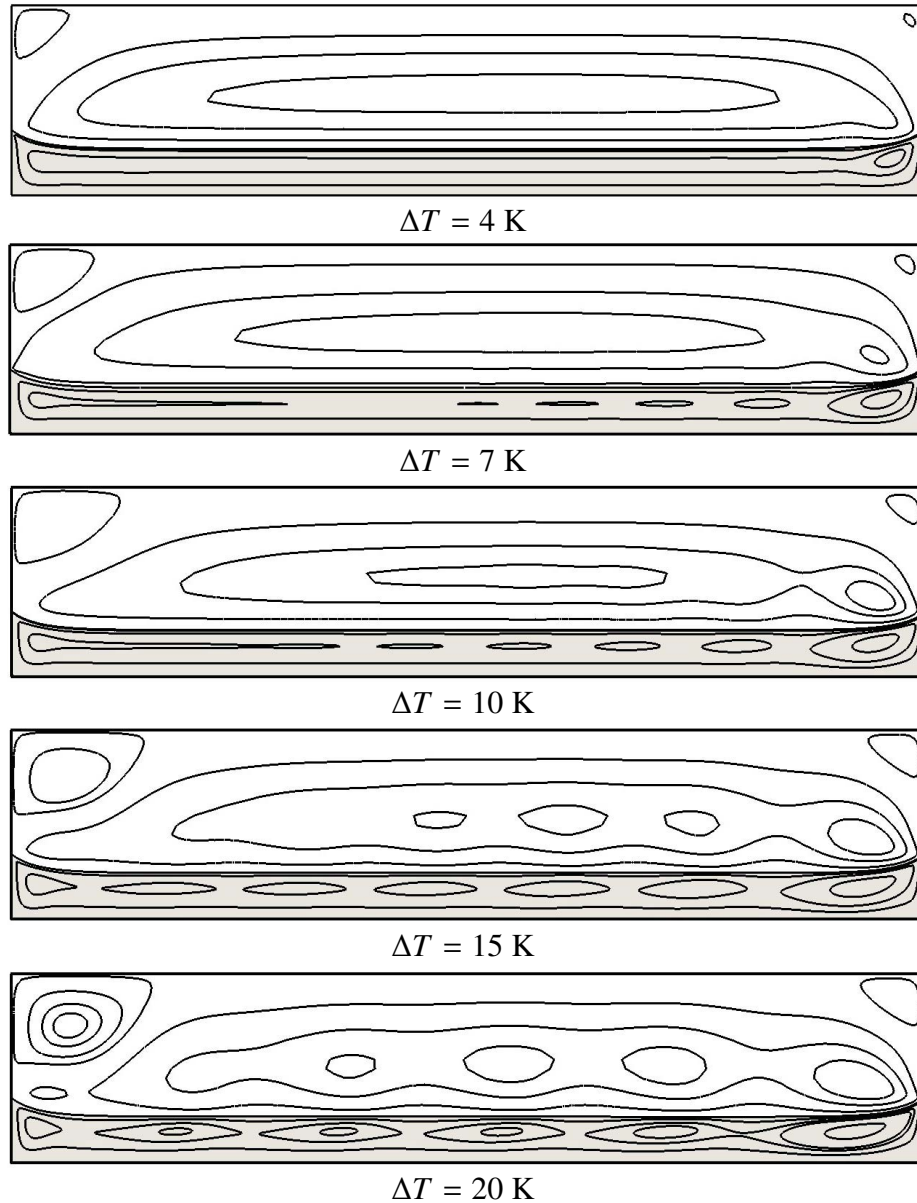
Figure 6: Dependence of the flow field on the imposed temperature difference ΔT. Solid lines represent the streamlines of the flow. Here and below, the gray (white) background indicates the liquid (gas) phase; the hot end wall is on the right, and the cold end wall is on the left.

by the fluid flow. Advection of heat has a progressively stronger effect as ΔT increases, which is expected given the high values of the thermal Péclet number

$$Pe_l = \frac{d_l u_i}{\alpha_l}. \tag{84}$$

At atmospheric conditions $Pe_l \sim 100$ (cf. Appendix A). The high Pe_l also causes thin

$\Delta T = 4$ K, $\delta T = 0.25$ K

$\Delta T = 7$ K, $\delta T = 0.5$ K

$\Delta T = 10$ K, $\delta T = 0.5$ K

$\Delta T = 15$ K, $\delta T = 1$ K

$\Delta T = 20$ K, $\delta T = 1$ K
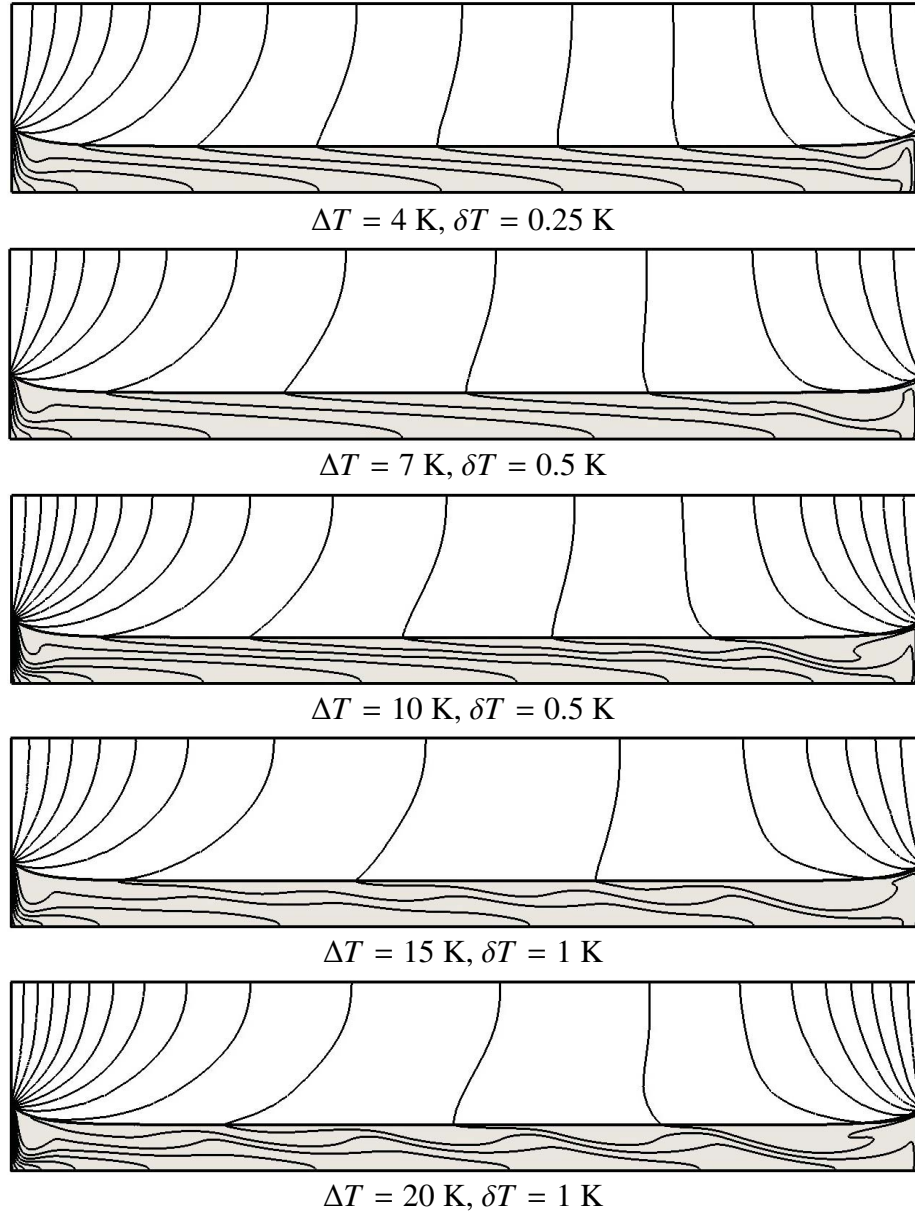
Figure 7: Dependence of the temperature field inside the cavity on the imposed temperature difference ΔT. Solid lines represent the isotherms, with temperature difference δT between them as indicated.

thermal boundary layers to form near both end walls (dark gray in Fig. 5). On the other hand, the temperature field in the gas layer remains qualitatively similar for all ΔT considered here. The temperature varies smoothly in both the horizontal and the vertical direction and is essentially unaffected by the fluid flow, which is consistent with the relatively small values of the thermal Péclet number

$$Pe_g = \frac{l_g u_g}{\alpha_g}, \tag{85}$$

where l_g and u_g are the characteristic length and velocity scales in the gas layer. At atmospheric conditions $u_g = u_i$ and $l_g = d_g = H - d_l$, and $Pe_g \sim 1$ (cf. Appendix A).

The wavelength of the convective pattern appears to grow monotonically with ΔT. The number of convection rolls first increases, as the pattern expands from the hot to the cold end wall, and after the multicellular pattern is established, the number of rolls steadily decreases, until the convection pattern becomes time-dependent at higher ΔT. This trend is consistent with both the experiments of Riley and Neitzel [12] and the numerical simulations of Shevtsova et $al.$ [22].

3.1.2 Oscillatory Multicellular Flow

As ΔT is increased beyond 20 K, the stationary convection pattern is destabilized and the flow becomes unsteady. In particular, for $\Delta T = 30$ K, the flow is time-periodic, with period $\mathcal{T} \approx 3.2$ s. Fig. 8 shows the stream function ψ_l in the liquid layer at different times during one period. Multiple convection rolls are observed, as was the case for the stationary convection rolls at smaller ΔT. However, these convection rolls no longer have a consistent spacing or position over time.

Riley and Neitzel [12] refer to this flow as oscillatory multicells (OMC). The results from these 2D simulations suggest, however, that this term may not be completely accurate, at least over the entire extent of the flow. The flow near the hot end is indeed oscillatory. The roll adjacent to the hot end wall (labeled A in Fig. 8) has both a larger size and greater strength than all other rolls. Starting from the time $t = 0$, roll A grows, mostly in the x

direction during the first half of the period. As it is elongated, a new roll (labeled B) forms at the left edge of roll A around $t = (3/8)\mathcal{T}$. During the second half of the period, roll A starts to shrink, and the new roll B is "pinched off" around $t = (5/8)\mathcal{T}$ and recedes from roll A. The strength or roll B gradually decreases and it then travels back towards
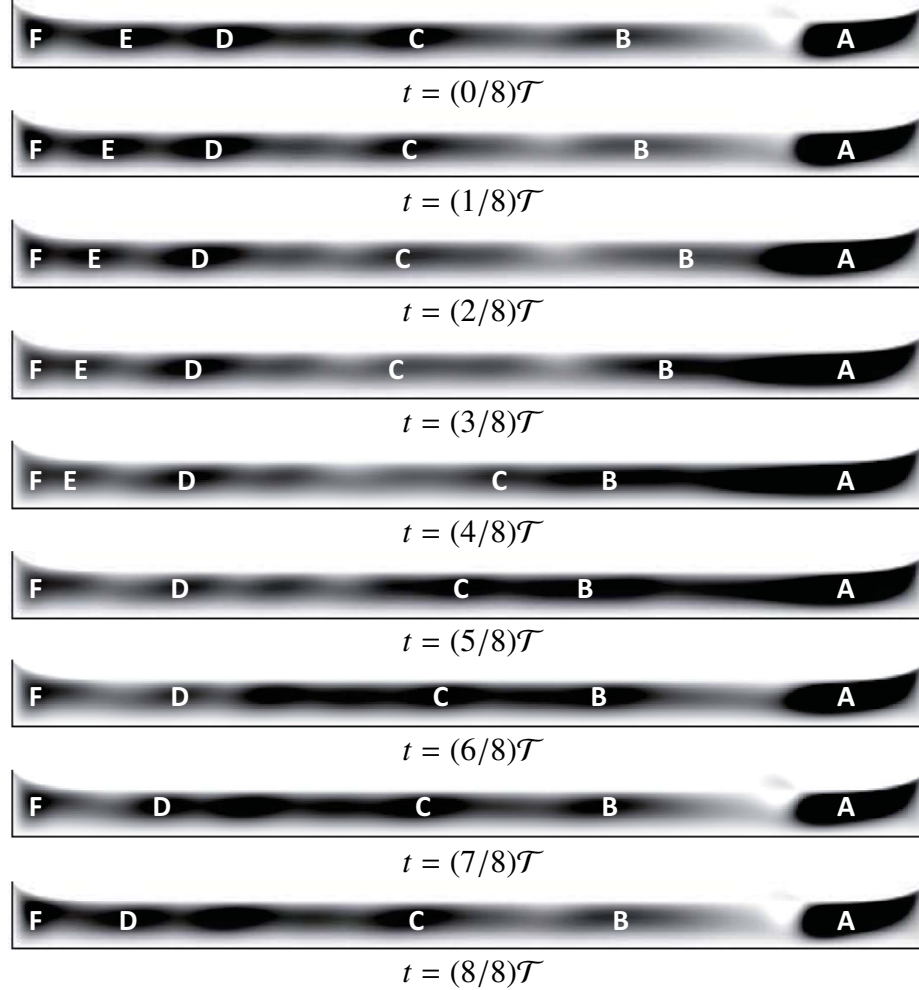
Figure 8: Stream function in the liquid layer at different times during one period of oscillation for $\Delta T = 30$ K. The shaded background represents the value of the stream function ψ_l, with darker color indicating higher values. The time interval between consecutive images is approximately 0.4 s. High-resolution movie showing the evolution of the flow field and the temperature field can be found in the supplemental file of this thesis, and also online at https://youtu.be/nRbag8ADOg0. The movie shows five periods (which corresponds to about 16.4 s). The upper panel shows the temperature T, the middle panel – the stream function ψ, and the lower panel – the magnitude of the velocity $\mathbf{u}$. The standard jet color map is used with blue corresponding to the minima and red – the maxima. The range of variation for T is 289 to 297 K and for $|\mathbf{u}|$ is 0 to 15 mm/s.

roll A, merging with A around $t = (2/8)\mathcal{T}$. This is quite similar to what the numerical simulations of Villers and Platten [9] showed for a liquid layer with a streamwise aspect ratio $\Gamma_x = L/d_l = 9$ substantially smaller than that studied here ($\Gamma_x = 19.8$).

Near the cold end, however, the dynamics are best described as a traveling wave. Several convection rolls appear, two of which are labeled D and E in Fig. 8, traveling to the left, i.e., in the direction opposite to that of hydrothermal waves. Both rolls D and E keep moving towards the stationary roll F adjacent to the cold wall. Around $t = (3/8)\mathcal{T}$ roll E starts to merge with roll F, disappearing around $t = (5/8)\mathcal{T}$. Roll D keeps traveling to the left, taking at $t = (8/8)\mathcal{T}$ the position of roll E at $t = (0/8)\mathcal{T}$, after which the process repeats. It should be noted that both the strength of the rolls and the speed at which they travel towards the cold wall varies considerably during one period.

In the middle of the cell, it is harder to distinguish individual convection rolls. The dynamics are dominated by a roll (labeled C) which nucleates at the right edge of the central region around $t = (4/8)\mathcal{T}$, just to the left of roll B, travels to the left edge of the central region and disappears there around $t = (3/8)\mathcal{T}$. Summing up, it is found that the time-periodic flow is rather complicated, with oscillatory dynamics near the hot end wall, a traveling wave near the cold end wall, and dynamics in the middle which appear to be some sort of mixture of the regimes found near the two end walls.

The flow behavior found in the numerics is qualitatively consistent with the experimental observations of Li *et al.* [1]. Their velocity data also show oscillatory dynamics on one side of the cavity (periodic modulation of the width of the roll nearest the hot wall) and traveling waves on the opposite side (rolls moving towards the cold end wall).

3.2   Comparison with Experiments

In order to directly compare these numerical results with those of other experimental (as well as numerical and analytical) studies, the Marangoni number (78) needs to be determined based on the average interfacial temperature gradient $\bar{\tau}$, which characterizes the

magnitude of thermocapillary stresses. The values of ΔT are not directly comparable due to the presence of the side walls of the cavity in the setup considered here (cf. Fig. 4). As shown in Fig. 9, the interfacial temperature in the core region of the flow varies linearly with position x at lower ΔT, while for higher ΔT there is significant modulation due to convection in the liquid. Hence to calculate the interfacial Marangoni number, a spatially averaged value of the gradient $\bar{\tau}$ is used which corresponds to a linear fit to the graph of $T_i(x)$ excluding a few-mm-wide regions next to the end walls.

As it has been pointed out in numerous previous studies, $\bar{\tau}$ is in many cases quite different from the imposed gradient $\Delta T/L$. As a result, the interfacial Marangoni number Ma_i (78) is often much less than the "laboratory" Marangoni number Ma_L (77) often used in the earlier studies. In the range of ΔT where the flow is steady, $\Delta T/L$ is found to vary as a rational function of $\bar{\tau}$

$$\frac{\Delta T}{L} = \bar{\tau}\frac{1 + a_T\bar{\tau}^2}{1 + b_T\bar{\tau}^2}, \tag{86}$$

where $a_T = 1.1 \times 10^{-3}$ and $b_T = 1.4 \times 10^{-4}$ are the fitting parameters, as Fig. 10 shows. We will denote the solution $\bar{\tau} = \tau_0(\Delta T/L)$. In the limit $\Delta T \to 0$ the fit (86) correctly reproduces
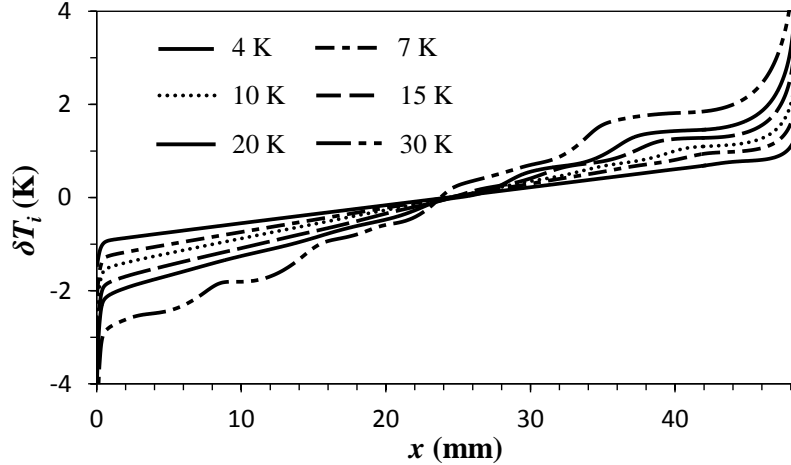
Figure 9: Interfacial temperature for different imposed temperature difference ΔT. To amplify the variation of T_i in the central region of the cell, the variation $\delta T_i = T_i - \langle T_i \rangle_x$ about the average value is plotted with truncated y-axis.

the analytical solution

$$\frac{\Delta T}{L}\bigg|_{\Delta T \to 0} = \left(1 + 2\frac{k_l}{k_w}\frac{h_w}{L}\right)\tau = 1.00368\tau, \tag{87}$$

which describes a conductive profile in the liquid layer.

In terms of the interfacial Marangoni number, the numerical simulations predict the transition from SUF to PMC to occurs at $342 < Ma_i < 460$, the transition from PMC to SMC at $546 < Ma_i < 682$, and the transition from SMC to OMC at $804 < Ma_i < 1096$. Although these values can be compared with experimental results, this comparison is somewhat qualitative, since the actual flow studied in most of the experiments is not strictly identical to that in the 2D simulations presented here. In most studies, the flow cell is open to the surroundings and the liquid is in direct contact with the temperature-controlled end walls, while the simulations assume that the fluid is contained in a sealed thin-walled container (see Fig. 4). Furthermore, variations in the contact angle lead to slight variations in the thickness of the liquid layer and the slope of the free surface near the walls, which affect the relative importance of both buoyancy and thermocapillarity.

Riley and Neitzel [12] used a cavity with a flow Section of length $L = 50$ mm and width $W = 30$ mm and liquid layers ranging in depths d_l from 0.75 mm to 2.5 mm. These
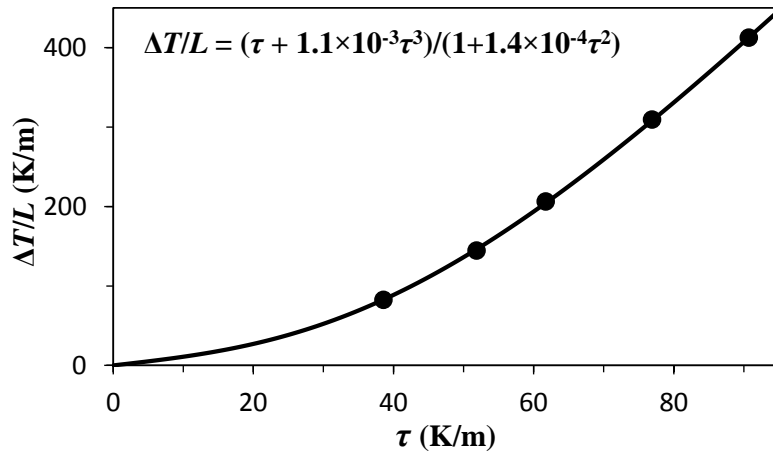
Figure 10: The relation between the gradient τ of the interfacial temperature in the core region of the flow and the imposed temperature gradient $\Delta T/L$. For steady flows ($\Delta T = 4$, 7, 10, 15, 20 K) the dependence can be fitted with extremely high accuracy ($R^2 = 0.9999$) by a low order rational function.

dimensions correspond to the streamwise and spanwise aspect ratios of $12 \leq \Gamma_x \leq 40$ and $20 \leq \Gamma_y \leq 66.7$ (compared with $\Gamma_x = 19.8$ and $\Gamma_y = \infty$ used here), so the geometry of their experiments is perhaps the closest to that represented by the 2D numerical simulations. The working fluid in their experiments was 1 cSt Dow Corning silicone oil with $Pr_l = 13.9$, while the simulation were performed for a substantially more volatile 0.65 cSt silicone oil with $Pr_l = 6.8$.

Fig. 11 (adapted from Ref. [12]) compares the flow regimes observed in the experiment with those found in the simulations. As Ma_i increases, the experimental flow goes through the same sequence of transitions as in the numeric. The critical values of Ma_i for these transitions are, however, different. In particular, in the numerics the transition from SUF to PMC occurs at Ma_i which is noticeably lower than the critical value of about 540 extrapolated from the experimental data. This is consistent with the general trend of the critical Ma_i increasing with Pr_l (for $Pr_l \gtrsim 1$) [18] (also see Fig. 53). Unfortunately, Riley and Neitzel do not report the critical Ma_i for the transition to SMC or OMC for $Bo_D > 0.42$.
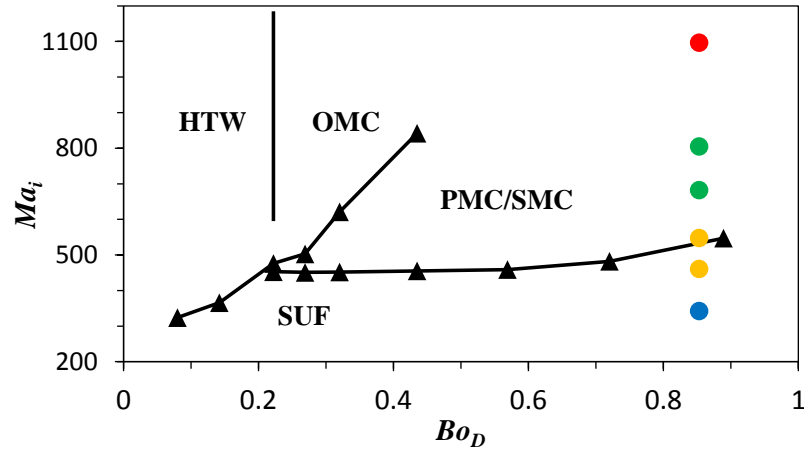
Figure 11: The flow regimes observed for different Bo_D and Ma_i. The lines show transitions between different flow regimes in the experiments of Riley and Neitzel [12]. The labels denote steady unicellular flow (SUF), partial multicellular flow (PMC), steady multicellular flow (SMC), oscillating multicellular flow (OMC) and hydrothermal waves (HTW). The filled circles show the results of the numerical simulations. Blue denotes steady unicellular flow, orange – partial multicellular flow, green – steady multicellular flow, and red – oscillating multicellular flow.

Another useful reference is provided by the experiments of Villers and Platten [9] which used a cavity with a flow Section of length L = 30 mm and width W = 10 mm and a liquid layer thickness 1.70 mm $\leq d_l \leq$ 14.25 mm, corresponding to 2.1 $\leq \Gamma_x \leq$ 17.6 and 0.7 $\leq \Gamma_y \leq$ 5.9. The working fluid was acetone with Pr_l = 4.2. The experimental observations are only classified as either stationary or oscillatory flow, so we can only compare the critical Marangoni numbers for transition from SMC to OMC. Villers and Platten only quote the laboratory Marangoni number (77), so the (Bo_D, Ma_L) plane is used to present the results. As Fig. 12 shows, the transition to OMC occurs at comparable values of Ma_L in the experiment and in the numerics, although, again, quantitative agreement is not expected due to the difference in the values of Pr_l, lateral confinement, and the absence of the containing walls of the test cell in the experiment.

The setup of the experiments of Li *et al.* [1] are the closest to the numerical simulations presented here: the length and height of the cavity are the same, and the working liquid is 0.65 cSt silicone oil, although the properties are not exactly the same. In the experiment the transition from SUF to SMC happens at 260 < Ma_i < 320, the transition from PMC to SMC at 320 < Ma_i < 430, and the transition from SMC to OMC at 750 < Ma_i < 780.
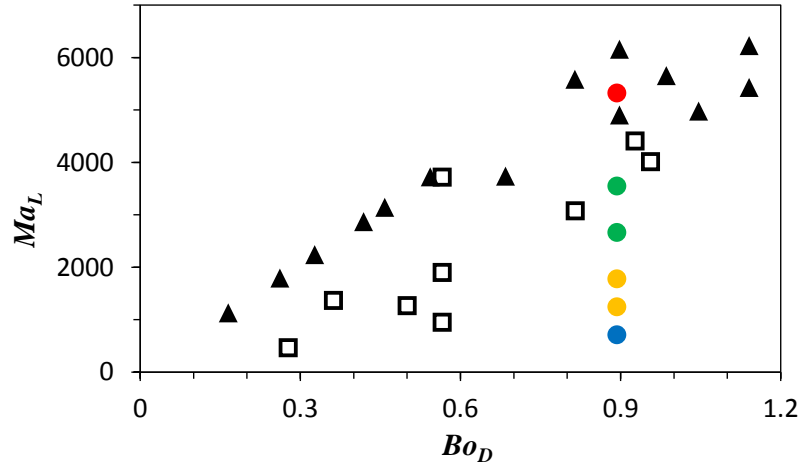
Figure 12: The flow regimes observed for different Bo_D and Ma_L. Filled triangles and open squares represent, respectively, oscillatory and stationary flow patterns observed by Villers and Platten [9]. The filled circles show the results of simulation, with the same notations as in Fig. 11.

All the experimental values are therefore slightly lower than the numerical predictions. Furthermore, for the oscillatory flow, the dynamics of convection rolls in the experiment are very similar to the numerical results. The temporal period of the experimental flow is larger ($\mathcal{T}$ = 5.4 s) than what is found in the numerics ($\mathcal{T}$ = 3.2 s), which is not surprising given the difference in Ma_i (990 in the experiment vs. 1096 in the numerics) and Bo_D (0.74 in the experiment vs. 0.85 in the numerics).

The uncertainty in the fluid properties used in the simulations is likely the main reason for imperfect agreement with the experiments of Li *et al.* [1]. Various experimental studies with 0.65 cSt silicone oil reported different values for the fluid properties. Most notably, the value of the temperature coefficient of surface tension γ reported in the literature ranges between 6.4×10^{-5} N/m-K [187], 8×10^{-5} N/m-K [13, 188], and 8.9×10^{-5} N/m-K [161, 162]. This is a variation of more than 30%, which changes both Ma and Bo_D by the same amount. The more reliable source for the fluid properties [161, 162] is used in later Chapters and leads to better agreement.

The discrepancies may also be due to a number of other reasons. For instance, the experiments have significant lateral confinement, while numerical simulations assume $\Gamma_y = \infty$. The finite width W = 10 mm of the experimental cell used in Ref. [1] (which corresponds to Γ_y of only 4.1) causes a curvature of the free surface in the spanwise direction and a deviation in the layer thickness at the side walls from the transversely flat profile assumed by the numerical simulations. The experiments also show evidence of weak secondary flow in the (y, z) plane which is not present in the numerics and could modify the temperature distribution in the liquid layer. The effects of the contact angle and three-dimensionality of the flow are addressed below in Sections 3.3 and 3.4.

3.3 The Effect of the Interfacial Curvature

Experimental studies of buoyancy-thermocapillary convection used setups that differed in a number of ways. For instance, Villers and Platten [9] and Li *et al.* [1] used liquids that

wetted the flat end (and side) walls, with relatively small contact angles, which produced a curved free surface (cf. Figs. 4 and 5). On the other hand, in the experiments of Riley and Neitzel [12] the interface was pinned to achieve a uniform liquid layer thickness over the entire cavity, which corresponds to a contact angle of 90°. The numerical simulations [9, 19–22] also used a flat and non-deformable interface. In order to investigate how the variation in the contact angle affects the flow, a series of 2D numerical simulations were performed with θ varying between 30° and 90°. The geometry was kept the same as in the previous simulations to facilitate comparison. The temperature difference between the outer surfaces of the two end walls was fixed at $\Delta T = 10$ K for all the cases. This value is reasonably close to the transition from PMC to SMC, making the structure of the flow quite sensitive to variations in any parameters.

$\theta = 30°$, $Ma_i \approx 565$

$\theta = 50°$, $Ma_i \approx 539$

$\theta = 70°$, $Ma_i \approx 535$

$\theta = 90°$, $Ma_i \approx 529$
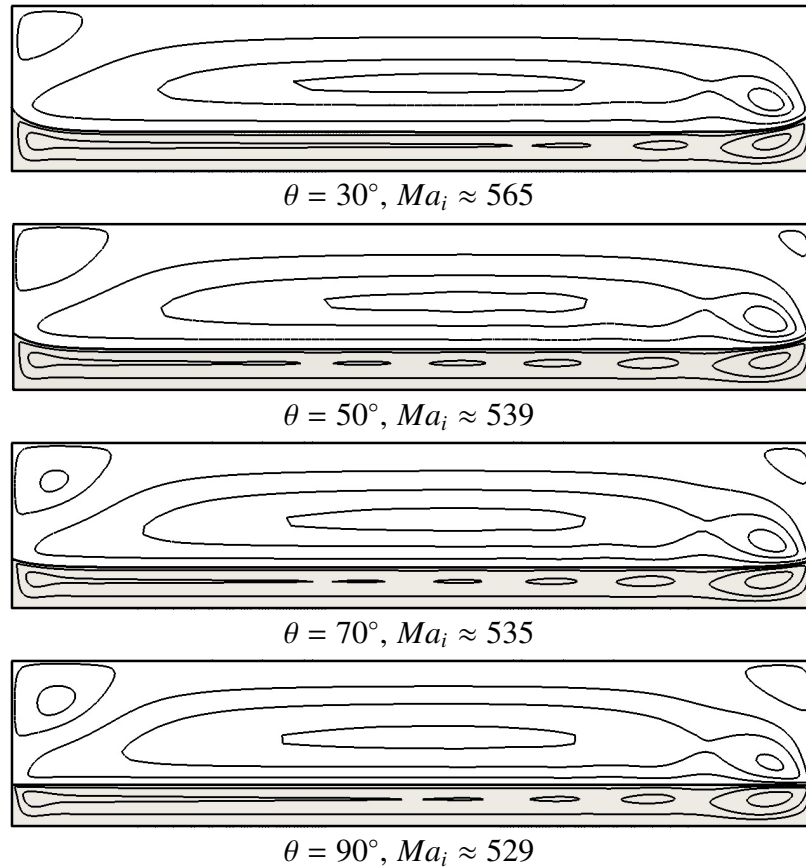
Figure 13: Streamlines of the steady flow for different values of the contact angle θ. $\Delta T = 10$ K and the average thickness of the liquid layer is $d_l \approx 2.5$ mm.

Not surprisingly, the flow is found to depend weakly on the value of θ, even in the core region away from the end walls. For the four values of the contact angle investigated, the flow patterns shown in Fig. 13 are qualitatively similar, although the values of Ma_i are slightly different (due to the change in the thickness of the liquid layer with θ). In the liquid layer, several weak convection rolls can be seen in the core region of the flow. There are four additional rolls for $\theta = 50°$ and $70°$, three for $\theta = 90°$ and two for $\theta = 30°$. In the gas layer, the flow patterns for the four different θ are almost indistinguishable. The temperature field (not shown), is essentially the same in the range of θ considered. In summary, these results suggest that the influence of the contact angle on the flow pattern, both near the end walls and in the core region of the flow, is relatively weak and therefore presumably can only partially account for the discrepancies between the experimental results and numerical predictions.

3.4 Three-Dimensional Effects

The effect of the lateral walls (both the viscous damping of the flow due to the no-slip boundary condition and the variation in the thickness of the liquid layer in the y direction due to the interfacial curvature for $\theta \neq 90°$) can only be understood by performing a full 3D simulation. However, simulating the flow in a cell with the dimensions 48.5 mm $\times$ 10 mm $\times$ 10 mm that was in Ref. [1] proved too time-consuming. Properly resolving the thin boundary layers, despite the use of adaptive mesh refinement, produces more than 10^6 computational cells for 1/8 mm resolution. Matching the resolution of the 2D simulations (which used a mesh with resolution of up to 1/16 mm) would have required over 10^7 computational cells. Therefore, the comparison for the results between 2D and 3D simulations is done for a cavity with inner dimensions of 15 mm $\times$ 5 mm $\times$ 5 mm ($L \times H \times W$), which has the additional benefit of enhancing the confinement effects. The thickness of the liquid layer was set to $d_l = 1.5$ mm, which corresponds to $Bo_D = 0.322$, $\Gamma_x = 10$, and $\Gamma_y = 3.3$. Furthermore, to avoid confusing the effects of lateral confinement with the effects of contact

angle, $\theta \equiv 90°$, which produces an essentially flat free surface.

Two different values of ΔT were considered, corresponding to values where the flow will be in steady unicellular or the steady multicellular regimes. In particular, for $\Delta T = 4$ K (which corresponds to $Ma_i = 298$), a steady unicellular flow is found. Fig. 14 shows this flow in the vertical mid-plane of the 3D cavity which is almost indistinguishable from

(a)

(b)
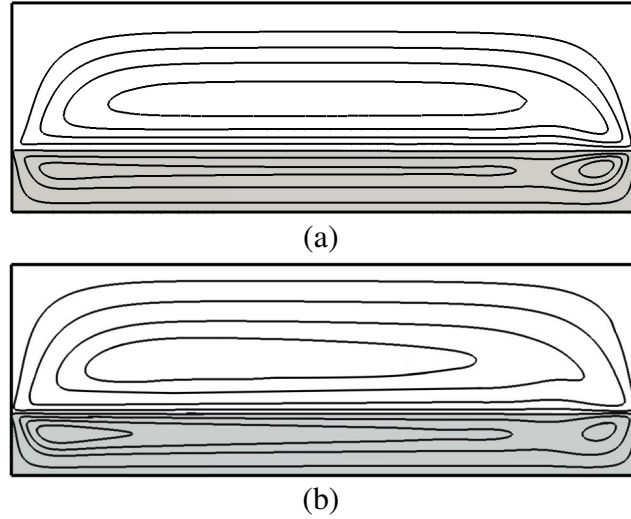
Figure 14: The flow in the vertical plane for $\Delta T = 4$ K. Streamlines of (a) the 2D flow and (b) the 3D flow in the mid-plane ($y = 2.5$ mm) of the cavity are shown.

(a)

(b)
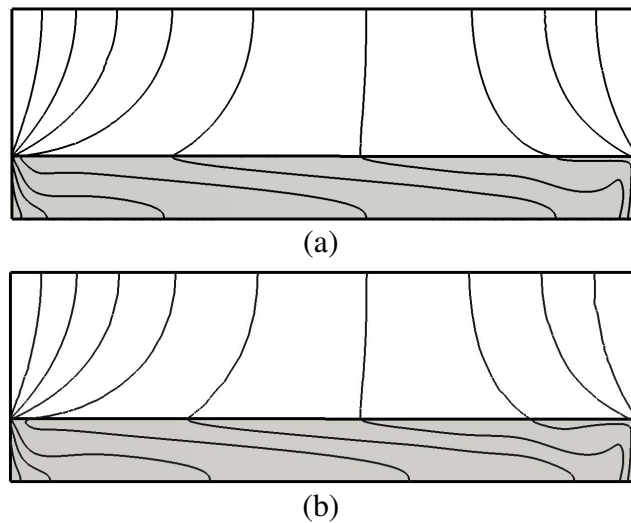
Figure 15: The temperature field in the vertical plane for $\Delta T = 4$ K. Isotherms of (a) the 2D solution and (b) the 3D solution in the mid-plane ($y = 2.5$ mm) of the cavity are shown. The temperature difference between two adjacent isotherms is $\delta T = 0.4$ K.

62

the corresponding 2D flow. Similarly, the temperature field in the mid-plane of the cavity is almost indistinguishable from the 2D solution (see Fig. 15).

In fact, both the flow field and the temperature field are very accurately represented by the 2D solution over most of the cavity interior. As Fig. 16 shows, the 3D and the 2D temperature fields in the liquid are essentially identical in the horizontal plane at $z = 1$ mm passing through the center of the two convection rolls. The vertical component of velocity u_z in that horizontal plane is also essentially the same in 3D and in 2D (see Fig. 17) everywhere except near the side walls, where the 3D velocity vanishes due to no-slip boundary conditions.

For $\Delta T = 20$ K (which corresponds to $Ma_i = 602$), a steady multicellular flow is found. Fig. 18 shows that the flow in the vertical mid-plane of the 3D cavity is again almost indistinguishable from the corresponding 2D flow. The slight difference in the position of convection rolls is due to the weak time dependence of the 3D solution which very slowly approaches a steady flow; the 3D flow structure becomes more similar to the 2D solution at longer times. Similarly, the temperature field in the mid-plane of the cavity is essentially indistinguishable from the 2D solution (see Fig. 19).
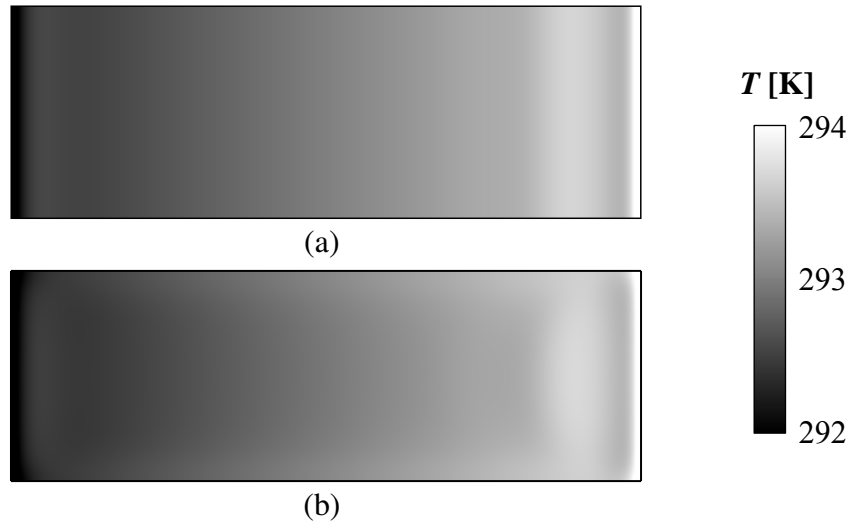
Figure 16: The temperature of the liquid in the horizontal plane $z = 1$ mm for $\Delta T = 4$ K. Shown are (a) the 2D solution and (b) the 3D solution.

However, there are significant differences between the 3D and the 2D solution on either side of the vertical mid-plane, as can be seen in a horizontal cross-section of the cavity. For instance, Fig. 20 shows that the strong modulation (in the x direction) of the 3D temperature field in the mid-plane disappears near the side walls, making the variation essentially monotonic. On the other hand, the vertical component of the 3D velocity field in the horizontal plane (see Fig. 21) shows that convection rolls become strongly distorted. Instead

(a)

(b)

u_z [mm/s]

1.0

0

-1.0
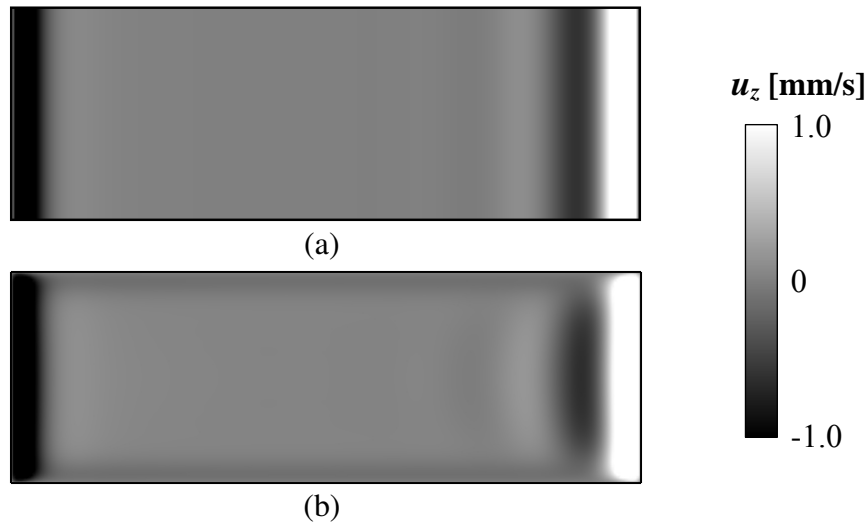
Figure 17: The velocity of the liquid in the horizontal plane $z = 1$ mm for $\Delta T = 4$ K. The vertical component $u_{\tilde{z}}$ is shown for (a) the 2D solution and (b) the 3D solution.

(a)

(b)
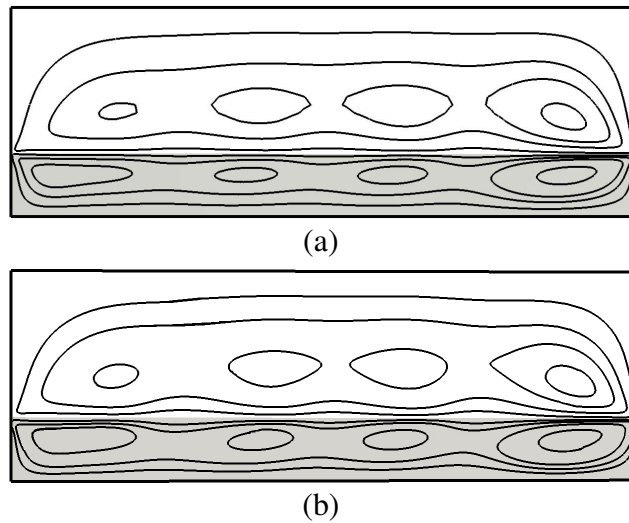
Figure 18: The flow in the vertical plane for $\Delta T = 20$ K. Streamlines of (a) the 2D flow and (b) the 3D flow in the mid-plane ($y = 2.5$ mm) of the cavity are shown.

of tilting, as predicted by 3D linear stability analyses [14, 15], the rolls bend symmetrically to form "chevrons that approach the side walls at the same angle on both sides.

In summary, for $\theta = 90°$, 2D simulations appear to provide a reasonably accurate description (both qualitative and quantitative) of the two-phase flow in the symmetry plane of the flow cell or cavity containing the fluid for a range of applied temperature gradients. For

(a)

(b)
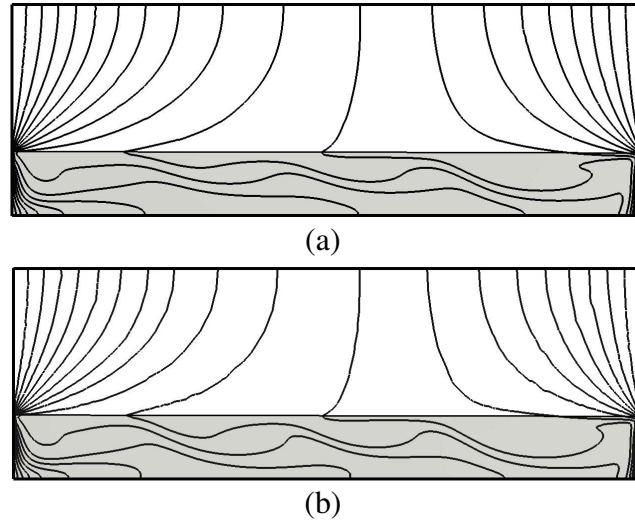
Figure 19: The temperature field in the vertical plane for $\Delta T = 20$ K. Isotherms of (a) the 2D solution and (b) the 3D solution in the mid-plane ($y = 2.5$ mm) of the cavity are shown. The temperature difference between two adjacent isotherms is $\delta T = 1$ K.

(a)

(b)
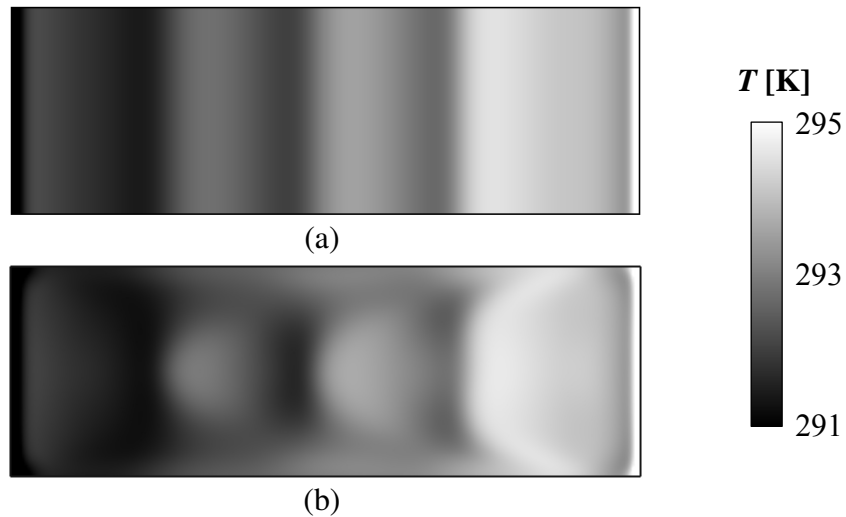
Figure 20: The temperature of the liquid in the horizontal plane $z = 1$ mm for $\Delta T = 20$ K. Shown are (a) the 2D solution and (b) the 3D solution.
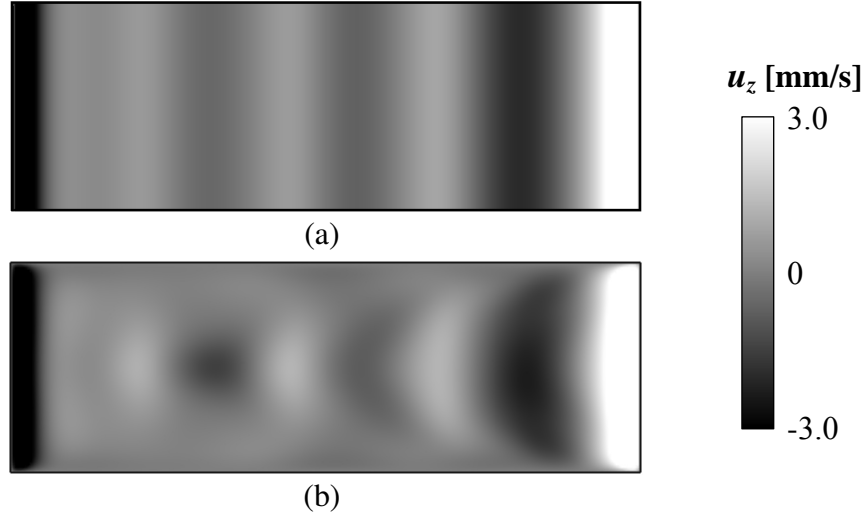
Figure 21: The velocity of the liquid in the horizontal plane $z = 1$ mm for $\Delta T = 20$ K. The vertical component $u_{\tilde{z}}$ is shown for (a) the 2D solution and (b) the 3D solution.

lower ΔT (in the SUF regime) the 2D solution is accurate everywhere except near the side walls. For higher ΔT (in the SMC regime) a fully 3D solution is required to describe the flow on either side of the symmetry plane. It is possible that for small values of θ, the case for most of the experimental studies, the variation of the thickness of the liquid film in the y direction could have a more pronounced effect on the flow structure and stability. Further investigation of this issue was impractical, however, due to the cost of the 3D simulations, each of which took about a month of computational time on a 16-core computer.

3.5 Theoretical Analysis

Many of the numerical results, such as the velocity and temperature fields in the SUF regime away from the end walls, can be validated by comparison with the analytical solutions for the 2D flow in a laterally unbounded layer driven by an imposed temperature gradient τ. In order to reduce the number of parameters, the governing equations are nondimensionalized (where the dimensionless parameters are denoted with a tilde) by introducing the following scales:

Length scale d_l,

66

Time scale d_l^2/ν_l,

Velocity scale ν_l/d_l,

Density scale ρ_l^0,

Pressure scale $\rho_l^0(\nu_l/d_l)^2$,

Temperature scale $\tau d_l = \mu_l \alpha_l M a_i / (\gamma d_l)$.

The dimensionless governing equations for the liquid layer $(-1 < \tilde{z} < 0)$ become

$$\tilde{\nabla} \cdot \tilde{\mathbf{u}}_l = 0,$$

$$\partial_{\tilde{t}} \tilde{\mathbf{u}}_l + \tilde{\mathbf{u}}_l \cdot \tilde{\nabla} \tilde{\mathbf{u}}_l = -\tilde{\nabla} \tilde{p} + \tilde{\nabla}^2 \tilde{\mathbf{u}}_l + Gr_l \tilde{T}_l \hat{z},$$

$$\partial_{\tilde{t}} \tilde{T}_l + \tilde{\mathbf{u}}_l \cdot \tilde{\nabla} \tilde{T}_l = Pr_l^{-1} \tilde{\nabla}^2 \tilde{T}_l, \tag{88}$$

where $\tilde{\mathbf{u}}_l = \mathbf{u}_l d_l / \nu_l$, $\tilde{T}_l = (T_l - T_0)/\tau d_l$, and

$$Gr_l = \frac{Ra_l}{Pr_l} = \frac{g \beta_l d_l^4 \tau}{\nu_l^2}. \tag{89}$$

is the Grashof number. A new coordinate system is defined

$$\tilde{\mathbf{r}} = \frac{\mathbf{r}}{d_l} - \hat{z} - \frac{L}{2d_l} \hat{x}, \tag{90}$$

so that $\tilde{\mathbf{r}} = 0$ in the middle of the liquid-vapor interface. The dimensionless governing equations for the gas layer $(0 < \tilde{z} < \tilde{d}_g)$ are

$$\tilde{\nabla} \cdot \tilde{\mathbf{u}}_g = 0,$$

$$\partial_{\tilde{t}} \tilde{\mathbf{u}}_g + \tilde{\mathbf{u}}_g \cdot \tilde{\nabla} \tilde{\mathbf{u}}_g = -\frac{\rho_l^0}{\rho_g^0} \tilde{\nabla} \tilde{p} + K_\nu \tilde{\nabla}^2 \tilde{\mathbf{u}}_g + (\Xi_T \tilde{T}_g + \Xi_\rho \tilde{\rho}_v) \hat{z},$$

$$\partial_{\tilde{t}} \tilde{T}_g + \tilde{\mathbf{u}}_g \cdot \tilde{\nabla} \tilde{T}_g = K_\alpha \tilde{\nabla}^2 \tilde{T}_g,$$

$$\partial_{\tilde{t}} \tilde{\rho}_v + \tilde{\mathbf{u}}_g \cdot \tilde{\nabla} \tilde{\rho}_v = K_D \tilde{\nabla}^2 \tilde{\rho}_v, \tag{91}$$

where $\tilde{\mathbf{u}}_g = \mathbf{u}_g d_l / \nu_l$, $\tilde{T}_g = (T_g - T_0)/\tau d_l$, $\tilde{\rho}_v = (\rho_v - \rho_v^0)/\rho_l^0$, $\tilde{d}_g = d_g/d_l$, $\rho_g^0 = \rho_a^0 + \rho_v^0$, $K_\nu = \nu_g/\nu_l$, $K_\alpha = \alpha_g/\nu_l$, and $K_D = D/\nu_l$. The equilibrium densities of air and vapor are

$$\rho_v^0 = \frac{p_v^0}{\bar{R}_v T_0},$$

$$\rho_a^0 = \frac{\bar{c}_a}{1 - \bar{c}_a} \frac{p_v^0}{\bar{R}_a T_0} = \frac{\bar{c}_a}{1 - \bar{c}_a} \frac{\bar{R}_v}{\bar{R}_a} \rho_v^0, \tag{92}$$

where p_v^0 is the saturation vapor pressure at the temperature T_0, and the nondimensional parameters

$$\Xi_T = \frac{\beta_g}{\beta_l} Gr_l,$$

$$\Xi_\rho = \frac{g d_l^3}{\nu_l^2} \frac{\rho_l^0}{\rho_g^0} \left(\frac{\bar{R}_v}{\bar{R}_a} - 1 \right) \tag{93}$$

describe the contributions to the buoyancy force in the gas layer due to perturbations in the tempreature and composition of the gas, respectively. While Ξ_T depends on τ (through Gr_l), but not $\bar{c}_a$, Ξ_ρ depends on $\bar{c}_a$ (through ρ_g^0), but not τ.

At the bottom of the liquid layer ($\tilde{z} = -1$) and the top of the gas layer ($\tilde{z} = \tilde{d}_g$), no-slip and adiabatic boundary conditions apply

$$\tilde{\mathbf{u}} = 0,$$

$$\partial_{\tilde{z}} \tilde{T} = 0. \tag{94}$$

At the interface ($\tilde{z} = 0$), the temperature and velocity fields are continuous

$$\tilde{T}_l = \tilde{T}_g = \tilde{T}_i,$$

$$\tilde{\mathbf{u}}_l = \tilde{\mathbf{u}}_g = \tilde{\mathbf{u}}_i. \tag{95}$$

Since $\mu_l \gg \mu_g$ and $d_g > d_l$, the viscous stress in the gas layer can be ignored, yielding a simplified expression for the shear stress balance at the interface

$$\partial_{\tilde{z}} \tilde{u}_{l,x} = -Re_l \partial_{\tilde{x}} \tilde{T}_l, \tag{96}$$

where

$$Re_l = \frac{Ma_i}{Pr_l} = \frac{\gamma d_l^2}{\mu_l \nu_l} \tau, \tag{97}$$

is the Reynolds number.

The heat flux balance (45) at the interface reduces to

$$\partial_{\tilde{z}} \tilde{T}_l = \frac{k_g}{k_l} \partial_{\tilde{z}} \tilde{T}_g - \frac{G_2}{Ma_i} \tilde{J}, \tag{98}$$

where $k_g = (1 - \bar{c}_a)k_v + \bar{c}_a k_a$ and $\tilde{J} = J d_l/(D\rho_l^0)$ is the dimensionless mass flux. The dimensionless combination

$$G_2 = \frac{\mathcal{L} D \gamma d_l}{\nu_l \alpha_l k_l},$$ (99)

or more precisely the ratio G_2/Ma_i, describes the relative magnitude of the latent heat released (absorbed) at the interface due to condensation (evaporation) compared with the vertical heat flux in the liquid layer due to conduction.

The mass flux balance at the gas side of the interface for the vapor (48) and the non-condensable gas (49) in dimensionless form gives

$$\tilde{J} = -\partial_{\tilde{z}}\tilde{\rho}_v + \tilde{\rho}_v \tilde{u}_{g,z},$$

$$0 = -\partial_{\tilde{z}}\tilde{\rho}_a + \tilde{\rho}_a \tilde{u}_{g,z}.$$ (100)

By eliminating $\tilde{u}_{g,z}$ from these two equations with the help of (50), the mass flux $\tilde{J}$ can be related to the gradients of the vapor density and gas temperature

$$\tilde{J} = -\frac{1}{\bar{c}_a}\partial_{\tilde{z}}\tilde{\rho}_v - \frac{1}{\bar{c}_a}\frac{\tau d_l}{T_0}\frac{\rho_v^0}{\rho_l^0}\partial_{\tilde{z}}\tilde{T}_g,$$ (101)

where $\rho_v^0 = p_s(T_0)/(\bar{R}_v T_0)$ is the vapor density which corresponds to the saturation pressure at the reference temperature T_0. Since $\tau d_l \ll T_0$ as well as $\rho_v^0 \ll \rho_l^0$, the last term on the right-hand-side of (101) is negligibly small compared to the first one and will not be considered further. Finally, at the top of the gas layer, mass flux vanishes

$$\partial_{\tilde{z}}\tilde{\rho}_r = 0.$$ (102)

For the base return flow (SUF) at atmospheric conditions, since the phase change is negligible away from the end walls, it is assumed that $\tilde{J} = 0$, which is also one of the assumptions made in one-sided models. This leads to a number of simplifications. In particular, (100) and (101) require that $\tilde{u}_{l,z} = \tilde{u}_{g,z} = 0$ and $\partial_{\tilde{z}}\tilde{\rho}_v = 0$ at the interface. Furthermore, solutions should satisfy the adiabatic boundary conditions at the free surface, $\partial_{\tilde{z}}\tilde{T}_l = \partial_{\tilde{z}}\tilde{T}_g = 0$.

In order to satisfy the incompressibility condition, stream functions are introduced in both layers, such that

$$\tilde{\mathbf{u}}_l = (\partial_{\tilde{z}}\tilde{\psi}_l, 0, -\partial_{\tilde{x}}\tilde{\psi}_l),$$

$$\tilde{\mathbf{u}}_g = (\partial_{\tilde{z}}\tilde{\psi}_g, 0, -\partial_{\tilde{x}}\tilde{\psi}_g). \tag{103}$$

Eliminating the pressure, the governing equations (88) for the liquid layer can be rewritten as

$$(\partial_{\tilde{t}} - \tilde{\nabla}^2 + \partial_{\tilde{z}}\tilde{\psi}_l\partial_{\tilde{x}} - \partial_{\tilde{x}}\tilde{\psi}_l\partial_{\tilde{z}})\tilde{\nabla}^2\tilde{\psi}_l + Gr_l\partial_{\tilde{x}}\tilde{T}_l = 0,$$

$$\partial_{\tilde{t}}\tilde{T}_l + \partial_{\tilde{z}}\tilde{\psi}_l\partial_{\tilde{x}}\tilde{T}_l - \partial_{\tilde{x}}\tilde{\psi}_l\partial_{\tilde{z}}\tilde{T}_l - Pr_l^{-1}\tilde{\nabla}^2\tilde{T}_l = 0. \tag{104}$$

For the gas layer they are rewritten as

$$(\partial_{\tilde{t}} - K_\nu\tilde{\nabla}^2 + \partial_{\tilde{z}}\tilde{\psi}_g\partial_{\tilde{x}} - \partial_{\tilde{x}}\tilde{\psi}_g\partial_{\tilde{z}})\tilde{\nabla}^2\tilde{\psi}_g + \Xi_T\partial_{\tilde{x}}\tilde{T}_g + \Xi_\rho\partial_{\tilde{x}}\tilde{\rho}_v = 0,$$

$$\partial_{\tilde{t}}\tilde{T}_g + \partial_{\tilde{z}}\tilde{\psi}_g\partial_{\tilde{x}}\tilde{T}_g - \partial_{\tilde{x}}\tilde{\psi}_g\partial_{\tilde{z}}\tilde{T}_g - K_\alpha\tilde{\nabla}^2\tilde{T}_g = 0,$$

$$\partial_{\tilde{t}}\tilde{\rho}_v + \partial_{\tilde{z}}\tilde{\psi}_g\partial_{\tilde{x}}\tilde{\rho}_v - \partial_{\tilde{x}}\tilde{\psi}_g\partial_{\tilde{z}}\tilde{\rho}_v - K_D\tilde{\nabla}^2\tilde{\rho}_v = 0. \tag{105}$$

The corresponding boundary conditions on $\tilde{\psi}$ can be easily obtained from those for $\mathbf{u}$. At the bottom of the liquid layer and the top of the gas layer

$$\tilde{\psi} = 0,$$

$$\partial_{\tilde{x}}\tilde{\psi} = \partial_{\tilde{z}}\tilde{\psi} = 0 \tag{106}$$

and at the interface

$$\tilde{\psi}_l = \tilde{\psi}_g = 0,$$

$$\partial_{\tilde{z}}\tilde{\psi}_l - \partial_{\tilde{z}}\tilde{\psi}_g = 0,$$

$$\partial_{\tilde{z}}^2\tilde{\psi}_l + Re_l\partial_{\tilde{x}}\tilde{T}_l = 0. \tag{107}$$

3.5.1 Fluid Flow and Temperature in the Liquid Layer

Solutions are obtained for a horizontal flow where both $\tilde{\psi}_l$ and $\tilde{\psi}_g$ are functions of $\tilde{z}$ alone and

$$\tilde{T}_l = \tilde{x} + \tilde{\theta}_l(\tilde{z}), \tag{108}$$

where $\tilde{\theta}_l(0) = 0$ such that $T_i = T_0$ at $x = 0$. In this case the governing equations (104) are reduced to

$$-\tilde{\psi}_l'''' + Gr_l = 0,$$
$$Pr_l\tilde{\psi}_l' - \tilde{\theta}_l'' = 0, \tag{109}$$

where prime stands for the derivatives with respect to the $\tilde{z}$ coordinate.

Solving the evolution equations (109) subject to the boundary conditions at the bottom and the free surface of the liquid layer, one finds the steady state solutions for the stream function

$$\tilde{\psi}_l = Re_l\left[-\frac{\tilde{z}(\tilde{z}+1)^2}{4} + Bo_D\frac{\tilde{z}(\tilde{z}+1)^2(2\tilde{z}-1)}{48}\right]\hat{x}, \tag{110}$$

velocity

$$\tilde{\mathbf{u}}_l = Re_l\left[-\frac{(\tilde{z}+1)(3\tilde{z}+1)}{4} + Bo_D\frac{(\tilde{z}+1)(8\tilde{z}^2+\tilde{z}-1)}{48}\right]\hat{x}, \tag{111}$$

and temperature field

$$\tilde{T}_l = \tilde{x} + Ma_i\left[-\frac{\tilde{z}^2(3\tilde{z}^2+8\tilde{z}+6)}{48} + Bo_D\frac{\tilde{z}^2(8\tilde{z}^3+15\tilde{z}^2-10)}{960}\right] \tag{112}$$

describing the SUF regime. These solutions agree with the analytical solutions originally obtained by Birikh [4] and later rederived by Kirdyashkin [5] and Villers and Platten [184] using a one-sided model that ignores the effects of the gas phase.

Returning to dimensional units, we find that the flow velocity at the interface can be written in the form

$$u_i = u_T + u_B, \tag{113}$$

where

$$u_T = \frac{1}{4} \frac{v_l}{d_l} \frac{Ma_i}{Pr_l} = \frac{1}{4} \frac{\gamma d_l}{\mu_l} \tau \qquad (114)$$

is the contribution due to thermocapillary stresses and

$$u_B = \frac{1}{48} \frac{v_l}{d_l} \frac{Ra_l}{Pr_l} = \frac{1}{48} \frac{\beta_l \rho_l g d_l^3}{\mu_l} \tau, \qquad (115)$$

is the contribution due to buoyancy. Note that, according to (114) we have $Re_l = 4u_T d_l / v_l$.

As Fig. 22 illustrates, the numerical results and the analytical solutions are in excellent agreement for moderate temperature differences $\Delta T = 4$ K and $\Delta T = 7$ K at which
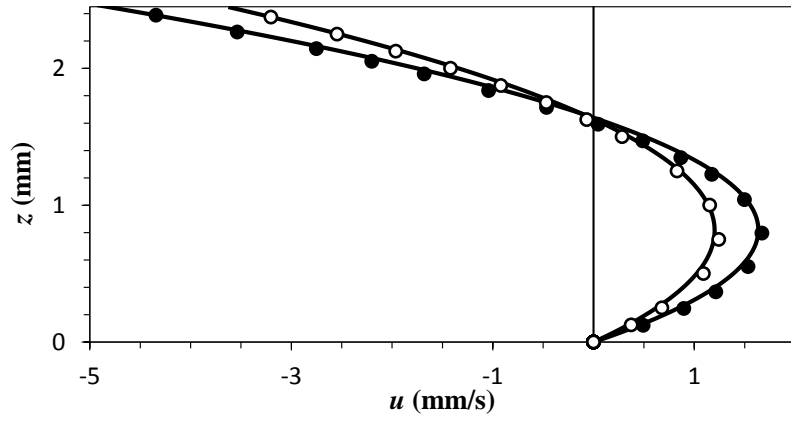
(a)
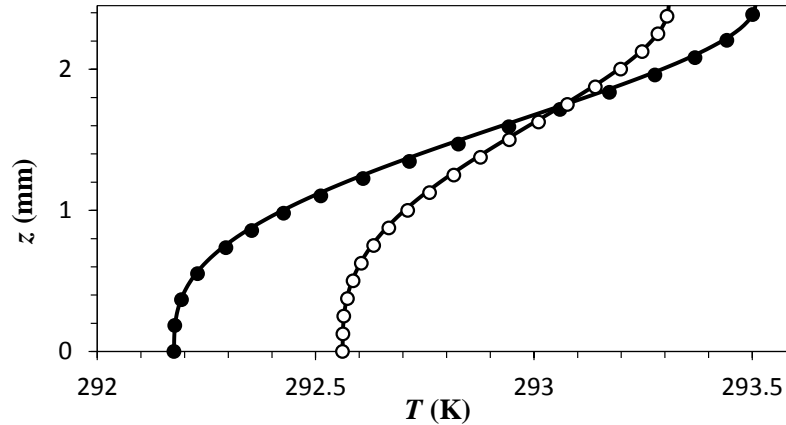
(b)

Figure 22: Vertical profiles of the horizontal velocity $u_{l,x}$ (a) and temperature T_l (b) in the liquid layer in the middle of the cell, $x = L/2$. Open and close circles correspond to numerical results for $\Delta T = 4$ K and $\Delta T = 7$ K, respectively; solid lines show the theoretical predictions.

72

unicellular flow is found in the middle of the test cell. In particular, the predicted flow velocity is in reasonably good agreement with experimental measurements despite the slight difference in the applied ΔT and the numerics being restricted to 2D: The analytical solution (111) predicts the maximal and minimal values of $u_{l,x}$ to be $u_{\min} = -3.6$ mm/s and $u_{\max} = 1.2$ mm/s for $\Delta T = 4$ K and $d = 2.45$ mm (which corresponds to $Ma_i = 342.3$ and $Bo_D = 0.85$), while experimental observations [1] give $u_{\min} = -3.7$ mm/s and $u_{\max} = 1.3$ mm/s for $\Delta T = 3.8$ K and $d_l = 2.5$ mm (which corresponds to $Ma_i = 370$ and $Bo_D = 0.89$).

The assumption that the interfacial temperature varies linearly in the core region of the flow has been widely used in previous studies without much justification, both for deriving the solutions (111) and (112) for the return flow underlying the stability analyses [14,16,18] as well as in models of the adiabatic Section of heat pipes [61, 189, 190], which assume unidirectional flow in the liquid phase. However, the validity of this assumption cannot be established by a one-sided model which ignores the transport in the gas phase. In fact, when $\bar{c}_a$ becomes sufficiently low, the interfacial temperature profile becomes nonlinear, as will be shown in Chapter 5. Proper justification of the linearity assumption requires showing that it is consistent with a steady-state solution of the transport equations in the gas phase which satisfies all of the boundary conditions at the free surface.

3.5.2 Fluid Flow, Temperature, and Composition in the Gas Layer

The solutions for the gas velocity, temperature, and vapor density in the core region can be found in the same way the solutions (111) and (112) were obtained in the liquid phase. The solution for $\tilde{\rho}_v$ at the interface is first derived, however, before deriving the solution in the bulk. The equilibrium vapor density is a function of the saturation temperature. Using the Clausius-Clapeyron relation and the ideal gas law it is found

$$\partial_x \rho_v = \left(1 - \frac{\bar{R}_v T_s}{\mathcal{L}}\right) \frac{\mathcal{L} p_v}{\bar{R}_v^2 T_s^3} \partial_x T_s.$$ (116)

Since the interface is flat, there is no pressure jump, and $p_g = p_l$. Furthermore, there is no phase change, $J = 0$, so $T_s = T_i$ according to (56) and $\partial_x T_s = \tau$. For $\tau x \ll T_0$, T_i can be

replaced with the reference temperature T_0. Nondimensionalizing (116) therefore yields

$$\partial_{\tilde{x}}\tilde{\rho}_v = \tilde{\varrho} \equiv \frac{1 - \upsilon}{\upsilon}\frac{\rho_v^0}{\rho_l^0}\frac{d_l\tau}{T_0} = (1 - \upsilon)(1 - c_a)\frac{G_1}{G_2}Ma_i, \tag{117}$$

where we introduced two new nondimensional combinations:

$$\upsilon = \frac{\bar{R}_v T_0}{\mathcal{L}}, \tag{118}$$

which quantifies the relative magnitude of latent heat compared with thermal energy, and

$$G_1 = \frac{\mathcal{L}^2 Dp_g}{\bar{R}_v^2 T_0^3 k_l} = \upsilon^{-2}\frac{Dp_g}{T_0 k_l}, \tag{119}$$

which describes the relative magnitude of the latent heat released (absorbed) at the interface due to condensation (evaporation) compared with the horizontal heat flux in the liquid layer due to conduction. Since $\rho_v = \rho_v^0$ at $T = T_0$,

$$\tilde{\rho}_v = \tilde{\varrho}\tilde{x}, \tag{120}$$

at the interface. In dimensional units, $\rho_v = \rho_v^0 + \varrho x$, where

$$\varrho = \frac{\rho_l^0}{d_l}\tilde{\varrho} = \frac{1 - \upsilon}{\upsilon}\frac{\rho_v^0}{T_0}\tau. \tag{121}$$

For solutions where $\tilde{\psi}_g$, $\tilde{\theta}_g$, and $\tilde{\rho}_v$ only depend on $\tilde{z}$, (105) can be reduced to

$$-\tilde{\psi}_g'''' + \Xi_T + \Xi_\rho\tilde{\varrho} = 0,$$

$$\tilde{\psi}_g' - K_\alpha\tilde{\theta}_g'' = 0,$$

$$\tilde{\psi}_g' - K_D\tilde{\rho}_v'' = 0. \tag{122}$$

Solving these equations subject to the boundary conditions at the interface and the top wall of the cell stated previously yields the steady state solutions for the nondimensional velocity

$$\tilde{\mathbf{u}}_g = -\mathcal{R}\left[\frac{(\tilde{z} - \tilde{d}_g)(3\tilde{z} - \tilde{d}_g)}{4\tilde{d}_g^2} + \mathcal{B}\frac{(\tilde{z} - \tilde{d}_g)(8\tilde{z}^2 - \tilde{d}_g\tilde{z} - \tilde{d}_g^2)}{48\tilde{d}_g^3}\right]\hat{x}, \tag{123}$$

temperature

$$\tilde{T}_g = \tilde{x} - \frac{\mathcal{R}}{K_\alpha} \left[\frac{\tilde{z}^2(3\tilde{z}^2 - 8\tilde{d}_g\tilde{z} + 6\tilde{d}_g^2)}{48\tilde{d}_g^2} + \mathcal{B}\frac{\tilde{z}^2(8\tilde{z}^3 - 15\tilde{d}_g\tilde{z}^2 + 10\tilde{d}_g^3)}{960\tilde{d}_g^3} \right], \tag{124}$$

and vapor density of the gas

$$\tilde{\rho}_v = \tilde{\varrho}\tilde{x} - \tilde{\varrho}\frac{\mathcal{R}}{K_D} \left[\frac{\tilde{z}^2(3\tilde{z}^2 - 8\tilde{d}_g\tilde{z} + 6\tilde{d}_g^2)}{48\tilde{d}_g^2} + \mathcal{B}\frac{\tilde{z}^2(8\tilde{z}^3 - 15\tilde{d}_g\tilde{z}^2 + 10\tilde{d}_g^3)}{960\tilde{d}_g^3} \right]. \tag{125}$$

The parameters $\mathcal{R}$ and $\mathcal{B}$ are analogous to the Reynolds number and the dynamic Bond number, but incorporate the properties of both fluid layers:

$$\mathcal{R} = Re_l\left(1 + \frac{Bo_D}{12}\right) + \frac{\tilde{d}_g^3}{12K_v}(\Xi_T + \Xi_\rho\tilde{\varrho}),$$

$$\mathcal{B} = -\frac{\tilde{d}_g^3}{\mathcal{R}K_v}(\Xi_T + \Xi_\rho\tilde{\varrho}). \tag{126}$$

Note that the form of the analytical solutions (111)-(112) and (123)-(125) is different compared with Ref. [185] because the buoyancy force caused by the variation in the composition of the gas is explicitly taken into account in this analysis, and the different choice of the origin of the coordinate system.

Since both T_g and p_g are essentially constant (the variation in T_g over the core region of the flow is about 0.4% for $\Delta T = 4$ K, while the pressure drop due to viscous effects is negligible compared with ambient pressure), the concentration field is essentially proportional to the vapor density, so that (125) yields:

$$c_v = \frac{\bar{R}_v T_g}{p_g}\rho_v = \frac{\bar{R}_v T_g}{p_g}(\rho_v^0 + \rho_l^0\tilde{\rho}_v) \tag{127}$$

or, after setting $T_g \approx T_0$,

$$c_v = 1 - c_a \approx 1 - \bar{c}_a + \varsigma x + \hat{c}_v(z), \tag{128}$$

where $\hat{c}_v(z)$ is the vertical concentration profile which corresponds to the second term on the right-hand-side of (125) and the horizontal concentration gradient $\varsigma = \partial_x c_v = -\partial_x c_a$ is given (again with the help of Clausius-Clapeyron relation) by

$$\varsigma = \frac{1 - \bar{c}_a}{\upsilon}\frac{\tau}{T_0} = \frac{1 - \bar{c}_a}{1 - \upsilon}\frac{\rho_l^0}{\rho_v^0}\frac{\tilde{\varrho}}{d_l}. \tag{129}$$

In particular, at the interface (128) reduces to

$$c_v \approx 1 - \bar{c}_a + \varsigma x, \tag{130}$$

Note that the relation (129) between the concentration gradient ς and the temperature gradient τ holds for all the regimes, not just SUF.

Solutions (123)-(125) are valid in a region of length L, provided T_i and c_a do not vary significantly about their averages T_0 and $\bar{c}_a$, respectively. This requires

$$\tau L \ll T_0,$$

$$\varsigma L \ll \bar{c}_a. \tag{131}$$

Both of these conditions are in fact satisfied, and consequently the interfacial temperature gradient τ is indeed constant when $\bar{c}_a$ is sufficiently large (e.g., at atmospheric conditions)

(a)

(b)

(c)
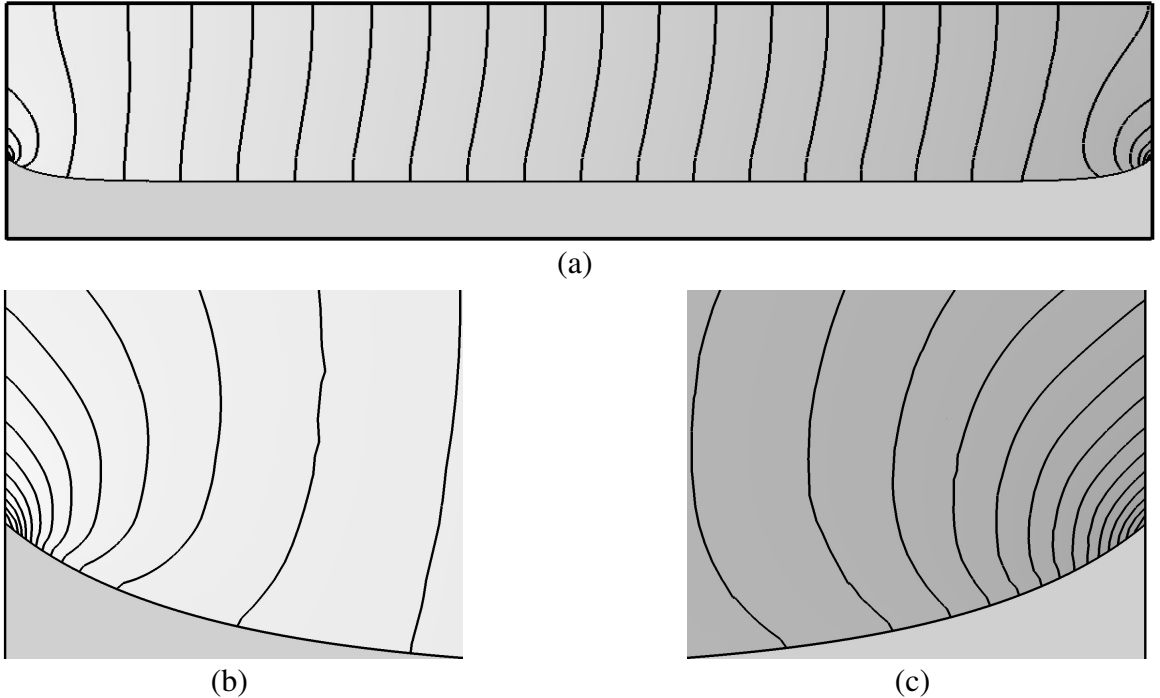
Figure 23: Vapor concentration c_v in the gas phase for $\Delta T = 4$ K. Entire cell (a) and the blow-ups of the 3 mm-wide regions near the contact line at the cold end wall (b) and near the contact line at the hot end wall (c). The difference between adjacent level sets is $\delta c = 0.02\%$ in (a) and $\delta c = 0.01\%$ in (b) and (c). Darker shade indicates higher concentration, ranging from 3.82% to 4.46% in the gas phase. The concentration field is not defined in the liquid phase.

and ΔT is sufficiently small. This assumption is not valid, however, both at larger ΔT when convection rolls appear (cf. Figs. 6 and 7) and at smaller $\bar{c}_a$, as will be shown in Chapter 5. Indeed, the numerical solution for a small $\Delta T = 4$ K and large $\bar{c}_a = 0.96$ shown in Fig. 23(a) has precisely the form (128) in the core region of the flow, where J is negligibly small and the no-flux boundary condition for ρ_v at the interface is justified. The numerical solution for the temperature (cf. Fig. 7), however, deviates noticeably from the analytical solution (124) even for $\Delta T = 4$ K, which corresponds to the SUF regime. There are two reasons for this discrepancy. First, the boundary conditions for the temperature at the end walls impose a large gradient in both the horizontal and the vertical direction, modifying the temperature profile considerably compared with the analytical solution for a laterally unbounded layer. Second, the thermal diffusivity α_g is four times the molecular diffusivity D (at atmospheric conditions the Lewis number is $Le = \alpha_g/D = 2.93$), so the temperature disturbance extends considerably further away from the end walls for the temperature field, compared with the concentration field, as Fig. 7 illustrates. Hence, due to the relatively small aspect ratio of the gas layer ($\Gamma_{x,g} = L/d_g = 6.4$) the end wall effects cause a substantial perturbation of the temperature field even in the core region, which is not the case for the density and concentration fields.

3.6   End Wall Effects

Near the end walls the assumptions and approximations valid in the core region break down and T_i is no longer a linear function of x. Indeed, as Fig. 9 shows, the interfacial temperature changes very quickly near the end walls. In fact, the corresponding thermal boundary layers account for a significant fraction of the imposed temperature difference ΔT. The remainder of the temperature drop takes place inside the end walls, as can be seen in Fig. 24. For these flow parameters, the variation in T_i over the core region of the flow (roughly τL), the temperature drop across the thermal boundary layers, and that inside the end walls (in the regions wetted by the liquid), are all comparable.

As shown in Fig. 24, the inner endwall temperature varies significantly with height, reflecting the variation in the temperature drop δT across the walls (the difference between the solid and the dashed line in Fig. 24). This temperature drop is negligible where the wall is in contact with the gas for which $k_w \gg k_g$, but quite large below the contact line, since k_w is comparable to k_l. The largest temperature drop is at the contact line, where heat conduction through the wall is balanced not only by the heat conduction through the liquid, but also by the heat released or absorbed as a result of phase change at the interface. It should be pointed out, however, that the there is also a strong asymmetry between the two end walls: the temperature drop below the contact line is relatively uniform along the hot wall, but varies by an order of magnitude (between 0.2 K and 2.5 K) along the cold end wall. This asymmetry is due to the structure of the thermal boundary layers. The boundary layer thickness decreases with z at the cold end wall, but increases with z at the hot end wall due to the opposite direction of the flow (down along the cold endwall, up along the hot endwall).

Since the endwalls are fairly thin, heat conduction is effectively one-dimensional. Hence,
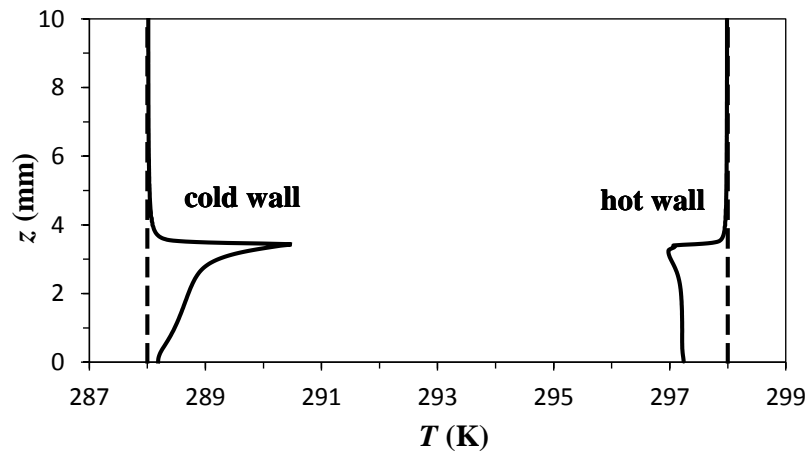
Figure 24: Solid lines represent temperature distribution along the inner surfaces of the end walls, dashed lines represented the temperature imposed on the outer surfaces of the end walls, which are $T_c = 288$ K and $T_h = 298$ K at the cold and the hot end wall, respectively, corresponding to $\Delta T = 10$ K.

the temperature drop δT across each endwall can be directly related to the heat flux distribution across the endwall, $q_w = k_w \delta T / h_w$. Our results illustrate the pitfalls of the simplified models (e.g., for describing condensation) that relate phase change to the imposed heat flux. Both the spatial variation in q_w and the asymmetry between the two endwalls clearly demonstrate that the heat flux cannot be imposed externally. Instead, it has to be computed using the solution of the proper transport equations.

3.7 Validity of the One-Sided Models

Previous studies based on one-side models used a number of assumptions, some of which were poorly justified. For example, the interface was assumed rigid and, in most cases, flat; the phase change was neglected; and either adiabatic thermal boundary conditions or Newton's law of cooling were used. In this Section, the two-sided model which describes momentum, heat, and mass transport in both phases, as well as the phase change across the entire interface, is used to validate the assumptions underlying one-sided models.

3.7.1 Interface Shape

Most existing one-sided models assume that the interface is flat and nondeformable in the core region. The flow in the liquid layer can, in principle distort the free surface. The relative importance of gravity, viscous, and inertial effects relative to surface tension is described, respectively, by the Bond number

$$Bo = \frac{\rho_l g d_l^2}{\sigma} = \frac{d_l^2}{l_c^2}, \tag{132}$$

the capillary number

$$Ca = \frac{\mu_l u_i}{\sigma}, \tag{133}$$

and the Weber number

$$We = Re_l Ca. \tag{134}$$

The characteristic values of these parameters in this study are $Bo = 3$, $Ca = 0.0002$, and $We = 0.01$. Since both Ca and We in this problem are much smaller than unity while Bo

is $O(1)$, the distortion of the interface due to the viscous and inertial effects associated with the flow should be negligible and the surface shape should be determined by the balance of gravity and capillarity alone.

To verify this, we computed the curvature κ of the interface numerically. Fig. 25 shows κ nondimensionalized by the thickness d_l of the liquid layer, for the 2D numerical simulation with $\Delta T = 20$ K. The relatively high curvature near the end walls is caused by the distortion of the interface due to the deviation of the contact angle from 90°. At this high temperature gradient the interface in the core region of the flow is not perfectly flat: the sign of the curvature oscillates, indicating a stationary surface wave caused by the convection rolls in the liquid layer. However, the amplitude of these oscillations is quite small, $\kappa d_l = O(We)$, so the interface can indeed be considered essentially flat (and rigid) in the core region (roughly 8 mm $\lesssim x \lesssim$ 40 mm).

3.7.2 Phase Change

Existing one-sided models also ignore phase change at the interface, which is justified for non-volatile liquids with low vapor pressures, such as decane, but certainly not for volatile liquids, such as acetone or low-viscosity silicone oils. In order to determine whether phase change can indeed be ignored, a nondimensional mass flux $\bar{J} = J/J^*$ is computed, where
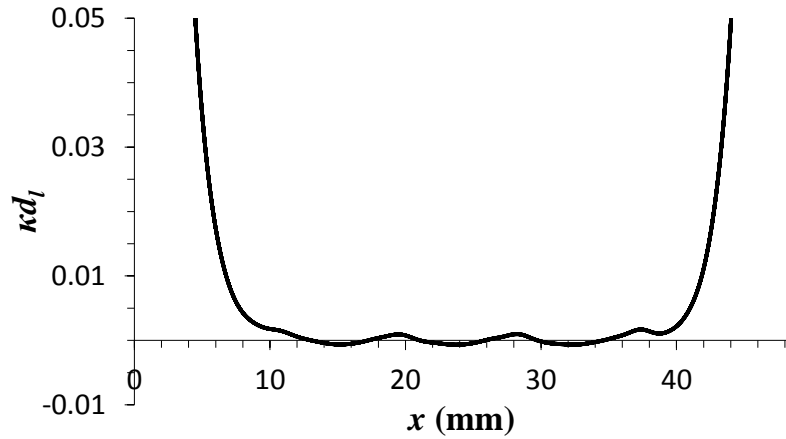
Figure 25: Nondimensional curvature of the liquid-vapor interface for $\Delta T = 20$ K. The variation in the sign reflects the distortion of the interface due to convection in the liquid layer. The vertical range has been truncated to amplify the variation in the core region.

J^* is taken equal to the characteristic mass flux

$$J^* = \rho_l u_i \qquad (135)$$

in the liquid layer based on the tangential component of the velocity at the interface u_i (113).

As shown in Fig. 26, for the volatile silicone oil considered in this Chapter, the phase change is localized to the boundary layers near the end walls. For $\Delta T = 4$ K, when the flow is SUF, the mass flux across the interface due to phase change in the core region of

(a)

(b)   (c)
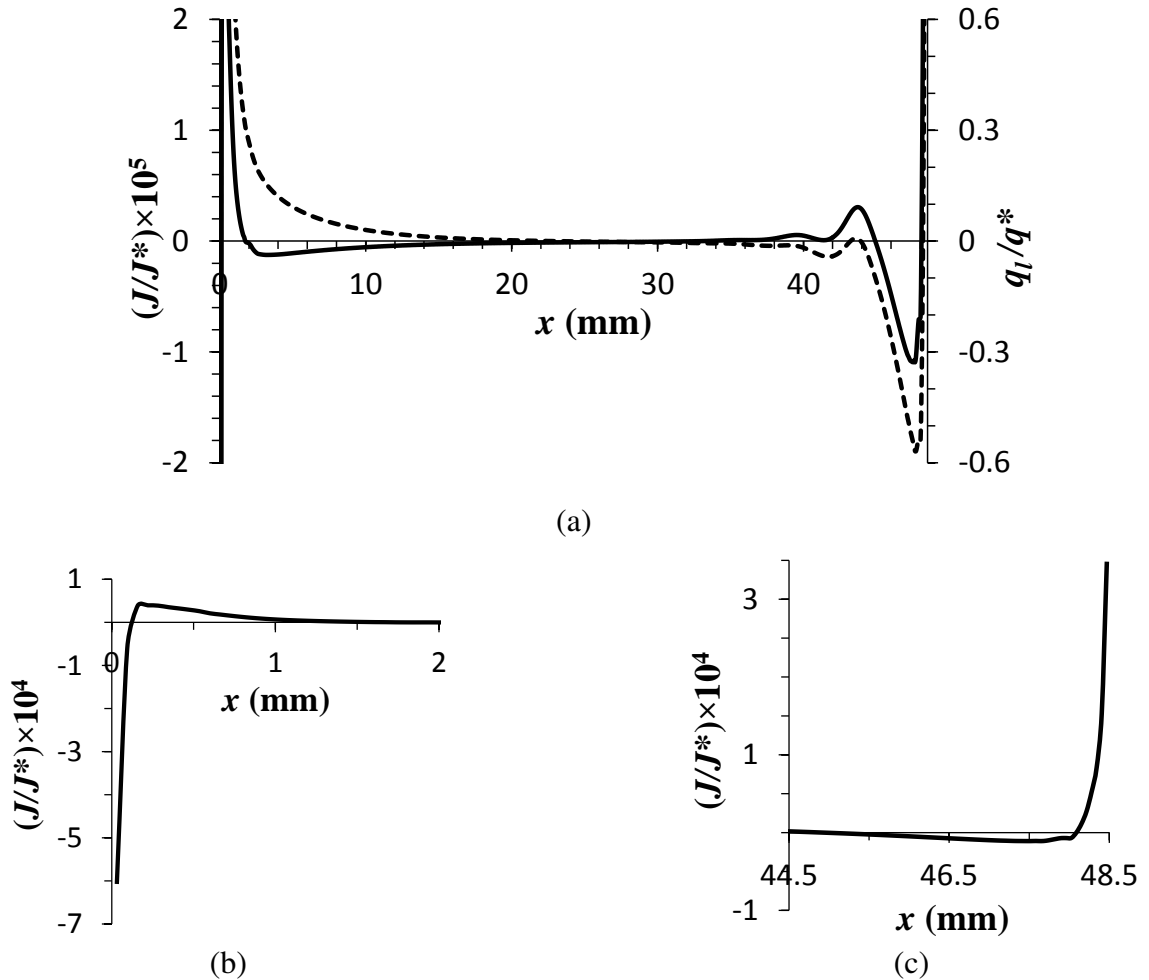
Figure 26: Nondimensional mass flux $\bar{J}$ (solid line) and nondimensional heat flux $\bar{q}_l$ in the liquid towards the interface (dashed line) for unicellular flow, $\Delta T = 4$ K. In (a) the vertical range has been truncated to amplify the variation in the core region of the flow. Panels (b) and (c) show the variation of the mass flux over its entire range near the end walls.

the flow is indeed negligibly small compared to J^*. Moreover, as shown in Fig. 27, as ΔT increases and the flow transitions to SMC and OMC, the mass flux J is still negligible compared to J^*, although it increases significantly and develops modulations corresponding to the convection rolls in the liquid layer. Therefore, it is reasonable to assume that phase change does not significantly affect the *mass* flux in the liquid at ambient conditions. This, however, does not mean that phase change does not affect the *heat* flux inside (or between) the two layers.

3.7.3 Newton's Law of Cooling

Instead of the proper heat flux balance (45), most one-sided models use either Newton's law of cooling

$$\partial_n T_l = -Bi \frac{T_i - T_0}{d_l}, \tag{136}$$

where Bi is the Biot number, or treat the interface as adiabatic, which is a special case of (136) with $Bi = 0$. For the adiabatic boundary condition at the bottom of the liquid layer, the analytical solutions derived in Section 3.5 are only valid if the normal component of the heat flux $q_l = -k_l \partial_n T_l$ in the liquid at the interface also vanishes, which corresponds to the limit $Bi = 0$. In order to check whether q_l is negligibly small, a nondimensional heat flux
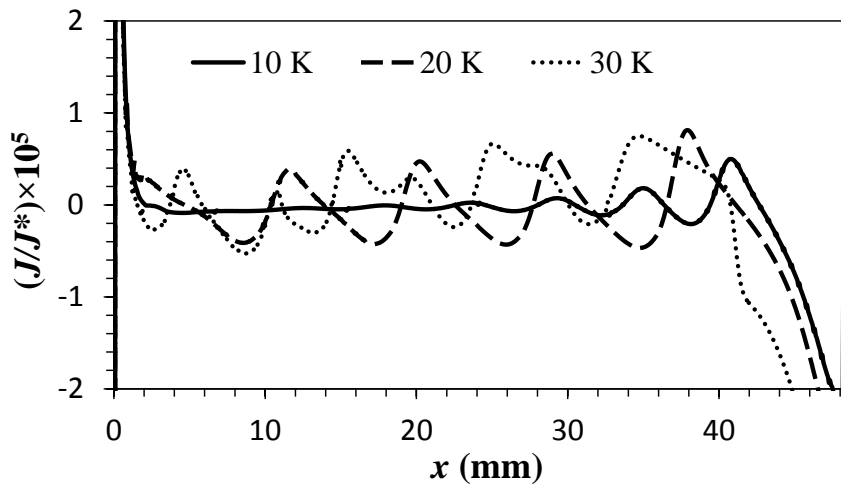
Figure 27: Nondimensional mass flux $\bar{J}$ for different ΔT. The vertical range has been truncated to amplify the variation in the core region of the flow. The flow at $\Delta T = 30$ K is time-periodic; a particular (representative) time instance is shown.

$\bar{q}_l = q_l/q^*$ is computed, where q^* is the conductive heat flux through the liquid layer along the z direction,

$$q^* = k_l \frac{\delta T}{d_l}, \tag{137}$$

where $\delta T = T|_{z=d_l} - T|_{z=0}$ is the characteristic temperature difference across the liquid layer (e.g., $\delta T = 0.75$ K for $\Delta T = 4$ K). Again, Fig. 26 shows that q_l is small compared to q^* in the core region of the flow (3% or less), mostly justifying the use of the adiabatic boundary condition at the interface away from the end walls. Moreover, a high degree of correlation between $\bar{J}$ and $\bar{q}_l$ is found. Indeed, this is to be expected, since by ignoring the heat conduction in the gas phase (45) can be reduced to $q_l \approx \mathcal{L}J$. However, there are regions near the end walls where the heat flux $q_g = k_g \partial_n T_g$ in the gas phase cannot be ignored, as is typically done in one-sided models, even at atmospheric conditions.

Furthermore, a closer inspection of Fig. 26 shows a rather counter-intuitive result. There is a region near the cold wall (0.1 mm < x < 1.8 mm) where the liquid evaporates ($J > 0$), and another region near the hot wall (45 mm < x < 48.1 mm) where the vapor condenses ($J < 0$). Everywhere else the sign of J is as one would expect. For instance, vapor condenses immediately next to the cold wall (0 mm < x < 0.1 mm) and liquid evaporates immediately next to the hot wall (48.1 mm < x < 48.5 mm). Our intuition, however, is shaped primarily by cases involving thin films, where heat is transported through the liquid by conduction: when the wall temperature is higher (lower) than the local saturation temperature T_s, so is the interfacial temperature T_i, and one expects evaporation (condensation). In this particular geometry, one expects condensation near a cold wall (where the wall temperature is lower than T_s) and evaporation near a hot wall (where the wall temperature is higher than T_s). Indeed, this is what is found very close to the end walls (within 0.1-0.4 mm). A little further away, heat transport is dominated by advection, not conduction (as the shape of the isotherms in Fig. 7 clearly illustrates), and T_i can easily become higher (lower) than T_s near a cold (hot) wall. As it turns out, this is exactly what happens.

As mentioned previously, there is a high degree of correlation between J and q_l, so it

is natural to expect that it is the heat flux in the liquid (towards or away from the interface, depending on the local flow field) that controls the sign of J. In order to see how the flow in the liquid affects the phase change at the interface, it is instructive to compare the flow field, the temperature field, the normal heat flux, and the mass flux for the case $\Delta T = 20$ K (which corresponds to the SMC regime). As Fig. 28 shows, in the presence of convection rolls neither the heat fluxes at the two sides of the interface nor the mass flux (which is proportional to the latent heat associated with phase change, $\mathcal{L}J = q_m = q_g + q_l$) are negligible even in the core region of the flow. Both J and q_l are modulated by convection in the liquid, with the minima of J and q_l located above the rolls and the maxima located between the rolls, while the heat flux q_g in the gas phase is considerably smaller (although still non-negligible). In particular, q_l can be as high as 10% of q^* and q_g as high as 5% of q^* in the core region of the flow, illustrating the breakdown of the adiabatic boundary condition in the multicellular regime, even at atmospheric conditions.

The same relation applies to the rolls adjacent to the end walls. In particular, a region of condensation is found above, and a narrow region of evaporation to the right of, the roll adjacent to the hot end wall for both $\Delta T = 20$ K and $\Delta T = 4$ K. The roll adjacent to the cold end wall is too weak to drive condensation right above it. However, the flow near the stagnation point at the contact line is fast enough at all ΔT to invert the sign of q_l and cause evaporation in a narrow region close to the cold wall. Right at the contact line the velocity vanishes and q_l becomes negative, producing an even narrower region of condensation.

3.8   Discussion

Comparison of the numerical results with the experimental data and analytical solutions helps validate the two-side numerical model which accounts for momentum, mass, and heat transport in both phases and phase change along the entire interface. At atmospheric conditions, as Ma_i increases (while $Bo_D = O(1)$ is fixed), the flow in the liquid layer transitions from the base return flow (SUF) to stationary multicells (PMC and SMC) and then

oscillatory multicells (OMC). These results are consistent with the existing experimental studies, and the critical values of the Marangoni number are similar to those found in the experiments, although there are noticeable quantitative differences due to the differences between the numerical simulations and experiments. It was found that the geometric effects – specifically the curvature of the free surface due to wetting of the cavity walls by the fluid and the confinement effect of the side walls – have a weak effect on the convection pattern, at least in the symmetry plane of the cavity. Therefore the most likely reason for the discrepancies between the numerics and the experiment is the uncertainty in the values of various material parameters. Moreover, the vertical profiles of velocity and temperature
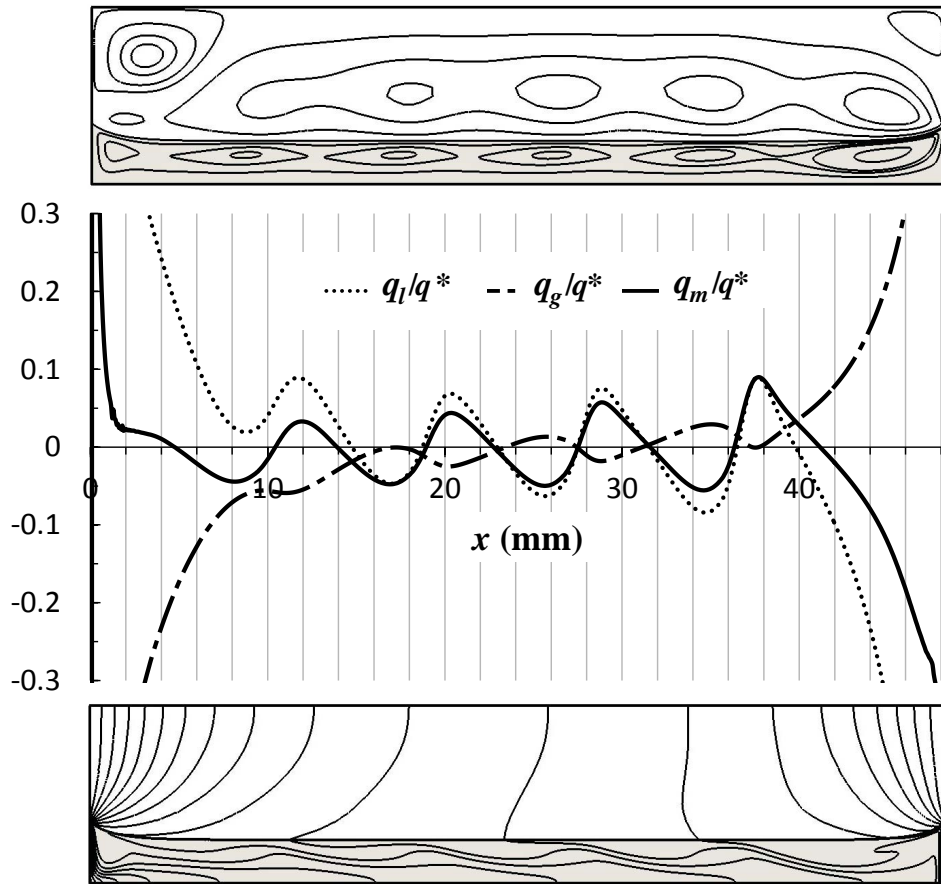
Figure 28: Flow structure, heat flux, and temperature field for the case when $\Delta T = 20$ K. The middle panel shows the (nondimensionalized) conductive heat flux at the liquid side $q_l = -k_l \partial_n T_l$, the vapor side $q_g = k_g \partial_n T_g$, and the heat flux associated with phase change, $q_m = \mathcal{L}J = q_l + q_g$. The vertical range has been truncated to amplify the variation in the core region of the flow.

85

in the core region of flow where SUF is observed are compared with the analytical solutions for base return flow and the results show good agreement.

Theoretical analysis of the unbounded base return flow has been extended to the gas layer, and the self-consistent analytical solutions of the two-phase flow suggest that the transport in the gas phase has a significant effect on the flow in the liquid phase. The interfacial temperature gradient τ is controlled by the density and concentration gradient of vapor in the gas phase (129). In particular, the assumption of a linear interfacial temperature profile used in one-sided models can be justified by showing its consistency with the solutions of transport equations in the gas phase. This assumption is only valid at low ΔT and high $\bar{c}_a$. Furthermore, the value of $\bar{\tau}$ is a free parameter, in confined systems, $\bar{\tau}$ should be determined by matching this solution in the core region of flow with that in the regions near the end walls, where phase change cannot be neglected.

Various assumptions used in one-sided models have been validated using this two-sided model. It was found that in the SUF regime, the assumptions of flat interface, negligible phase change and heat flux through the interface, and the linear interfacial temperature are in general satisfied in the core region of the flow, but not near the end walls. Actually, a counter-intuitive effect was found near the end walls which has never been previously observed either in experiments or in numerical simulations using one-sided models: there is a region of evaporation close the cold end wall and a region of condensation near the hot end wall. This effect can be explained by advective heat transport in the liquid layer. When additional convection rolls appear in the core region of the flow and advective heat transport becomes progressively stronger, the heat flux through the interface can no longer be ignored even in the core region of flow, and Newton's law of cooling breaks down. This suggests that one-sided models might be reasonably accurate for describing the base flow (in SUF regime), which corresponds to low ΔT and high $\bar{c}_a$. However, the results based on one-sided models are not quantitatively accurate at high ΔT when the transport in the gas phase becomes more important. Furthermore, at low $\bar{c}_a$, the assumption of a linear

interfaical temperature profile breaks down and a two-sided model should be used.

CHAPTER 4

CONVECTION UNDER PURE VAPOR

As noted previously, many of the assumptions underlying current models of two-phase cooling devices are based on assumptions that have been justified, at least to some extent, under atmospheric conditions when the gas phase is dominated by noncondensables (air). On the other hand, it is well known that noncondensables significantly impede phase change and hence degrade the thermal performances of two-phase cooling devices [191]. Hence, their optimal operating conditions correspond to the opposite limit, when noncondensables are nearly absent and the gas phase is dominated by the coolant vapor. Recent experimental studies [1] showed that the flow of the liquid confined in the sealed cavity shown in Fig. 4 changes drastically when most of the air is removed. In particular, convection patterns are strongly suppressed as the total pressure p_g, and hence the average concentration $\bar{c}_a$ of noncondensables decreases, while the flow speed in the liquid layer unexpectedly remains essentially the same for a range of p_g varying by more than two orders of magnitude, from atmospheric pressure $p_{atm} = 101$ kPa down to $p_g = 5$ kPa, which is just above the fluid saturation pressure.

This counterintuitive result cannot be explained using a one-sided model, and illustrates the limitations of an approach that ignores transport in the gas phase. Furthermore, it shows that the results obtained under ambient conditions, when air dominates, cannot be extrapolated to the opposite limit when vapor dominates, which is the more relevant situation for thermal management applications. A few theoretical studies [49, 50, 82, 90, 91] have considered the vapor-dominated limit. However, these studies used very restrictive assumptions and/or a very crude description of one of the two phases, and shed little light on the two-phase flow driven by a combination of buoyancy and thermocapillary stresses.

Hence, this chapter details the predictions of the two-sided transport model of two-phase flow in the limit when there are no noncondensables in the gas phase, i.e., $\bar{c}_a = 0$.

The same fluid properties are used in this chapter as those used in the air-dominated limit to facilitate comparison with the air-dominated limit (see Table 2). As discussed in Chapter 3, the contact angle has a minor effect on the shape of the free surface and the flow everywhere except very near the contact lines, and the 2D approximation provides reasonably accurate results in the vertical mid-plane $y = W/2$ of the cavity. Therefore the 2D flow in that mid-plane will be considered in this chapter and the contact angle $\theta \equiv 50°$. The results discussed in most of this chapter were also reported in [192].

4.1   Fluid Flow and Temperature Fields

To study how the flow in both layers changes with the applied temperature difference, simulations were performed for values of ΔT ranging from 10 K to 30 K using the KTG expression for the evaporation/condensation mass flux (56) with accommodation coefficient $\chi = 1$. Over this range of ΔT under atmospheric conditions, the flow is found to transition from steady unicellular to steady multicellular to oscillatory convection, as discussed in Chapter 3. In the absence of noncondensables, at otherwise identical conditions, the flow was found to reach steady state for all of these values of ΔT. The corresponding streamlines in both the liquid and the vapor phase are shown in Fig. 29. The flow in the liquid layer is markedly different under vapor ($\bar{c}_a = 0$) and under air ($\bar{c}_a = 0.96$). Under air the flow in the central region of the cell is best described as a horizontal return flow with multiple embedded convection rolls whose strength increases with ΔT (see Fig. 6). In this case thermocapillarity is the dominant driving force [185]. The flow under vapor, however, is dominated instead by two counterclockwise convection rolls, a larger one near the cold wall and a smaller one near the hot wall; and this flow structure remains qualitatively the same as ΔT increases. The flow is much stronger near the end walls than that in the central region, suggesting that the main driving force in buoyancy, *vs.* thermocapillarity.

The flows in the vapor phase also differ at $\bar{c}_a = 0$ and 0.96. Under air a (clockwise) recirculation flow is found in the vapor phase, which mirrors the flow in the liquid phase. It

is driven primarily by thermocapillarity, with buoyancy driving counterclockwise recircu-
lation in the top corners. Under vapor, the flow in the vapor phase becomes unidirectional,
where the liquid evaporates near the hot wall, and the resultant vapor flows from the hot
wall to the cold wall and condenses there. Again, increasing ΔT has essentially no effect on
the structure of the flow field. The observation from the numerics that the convection pat-
tern is independent of the applied temperature difference, at least qualitatively, is consistent
with experimental results of Li *et al.* [1] which show that transitions from steady unicellu-
lar to steady multicellular to oscillatory convection observed under atmospheric conditions
disappear when (most of) the air is removed.

Table 3 summarizes the average interfacial velocities predicted by the numerical model
(along with the analytical estimates derived below) for different values of ΔT. Not only
are the flow patterns under air and under vapor significantly different, but the magnitudes
of the velocity are quite different as well. While the flow is relatively fast under air (the
largest interfacial velocity is of order 1 cm/s), the largest interfacial velocity is reduced to

$\Delta T = 10$ K

$\Delta T = 20$ K

$\Delta T = 30$ K
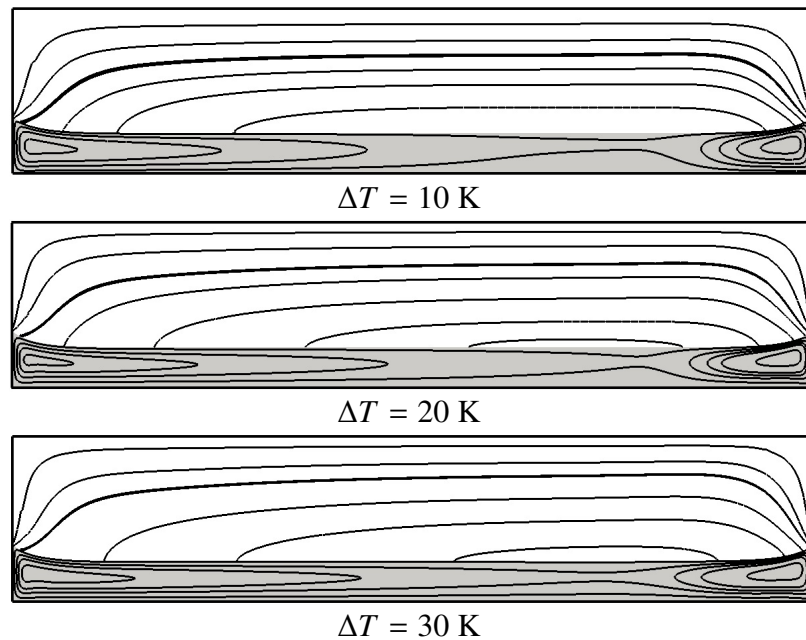
Figure 29: Streamlines of the flow under pure vapor for different ΔT. The contact angle
is $\theta = 50°$. As usual, the gray (white) background indicates the liquid (gas) phase; the hot
end wall is on the right, and the cold end wall is on the left.

Table 3: The spatial average of the interfacial velocity $\langle |\mathbf{u}_i| \rangle_x$ and the estimates of thermo-capillary and buoyancy contributions based on (114) and (152). A time-averaged value is given for the time-periodic flow under air at $\Delta T = 30$ K.

ΔT	under vapor			under air		
	$\langle |\mathbf{u}_i| \rangle_x$	u_B	u_T	$\langle |\mathbf{u}_i| \rangle_x$	u_B	u_T
(K)	(mm/s)	(mm/s)	(mm/s)	(mm/s)	(mm/s)	(mm/s)
10	0.5	1.3	0.002	6	1.3	5.3
20	0.9	2.6	0.005	9.4	2.6	7.8
30	1.1	3.8	0.007	11.6	3.8	10.7

a few mm/s under vapor. In order to understand this rather significant reduction in the flow velocity it is helpful to compare the temperature fields in the two cases.

Figure 30 shows the isotherms for both cases when applied temperature difference is $\Delta T = 10$ K. Under air, the temperature changes gradually between the hot end and the cold end in both phases. Under vapor, the isotherms are clustered near the hot and cold end walls, indicating the existence of thin thermal boundary layers along the end walls, and the temperature is nearly constant over the central region (i.e., most) of the cell. Moreover, the temperature is essentially constant along the entire interface. This suggests that thermo-capillarity is significantly reduced under vapor. Indeed, for a liquid in equilibrium with its vapor, the interfacial temperature is set by the saturation temperature, which depends only on the *absolute* pressure. Since the latter is effectively constant, the interfacial temperature

(a)

(b)
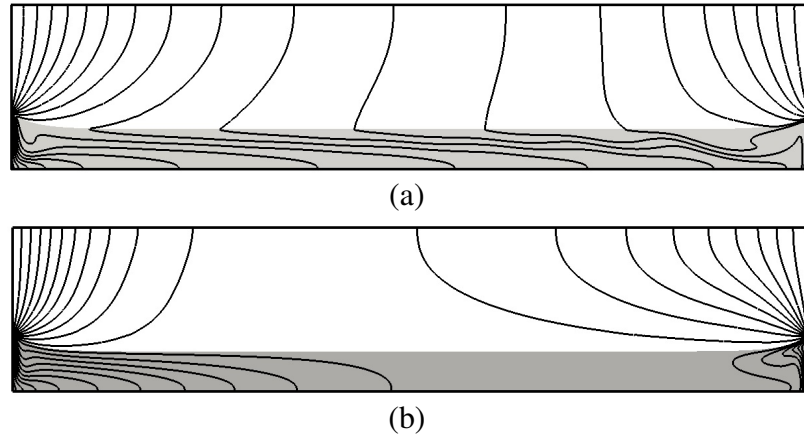
Figure 30: Temperature field for the steady-state flows (a) under air and (b) under vapor. In both cases $\Delta T = 10$ K. The temperature difference between adjacent isotherms is 0.5 K.

must also be nearly constant, as discussed in more detail next.

4.2 Theoretical Analysis

The numerical results presented above can be understood qualitatively, and in some cases even quantitatively, by identifying the key physical processes in various regions of the flow. This allows the comprehensive model presented in Chapter 2 to be simplified to a form where approximate solutions or, at least, reasonable estimates for various fluxes and variations, can be derived for the $\bar{c}_a = 0$ limit considered here.

4.2.1 Interfacial Temperature

The variation of the temperature at the interface between the liquid and the gas phase T_i (about its average value $\langle T_i \rangle_x \approx T_0$) is shown in Fig. 31. When the system is under air at atmospheric pressure, $T_i(x)$ is a nearly periodic modulation about a linear profile over most of the interface, as observed, for instance, in the experiments of Riley and Neitzel [12]. The modulation corresponds to the advection of heat by convective flow and the average interfacial temperature gradient $\bar{\tau}$ is comparable to the imposed temperature gradient $\Delta T/L$. In the absence of air, the interfacial temperature becomes essentially constant. The value of $\bar{\tau}$, and the corresponding thermocapillary stresses, decrease by three orders of magnitude, compared with the values found under air at the same ΔT.

This drastic reduction in the magnitude of $\bar{\tau}$ can be explained by a simple argument. In the absence of noncondensables, the diffusion of vapor does not inhibit phase change, so the interfacial temperature should be very close to the saturation temperature due to the large value of the latent heat in (56). On the other hand, T_s is a function of the vapor pressure p_v, which is nearly constant. Hence T_s is nearly constant, and so is T_i.

A quantitative estimate for the variation of T_i in the two limits can be obtained by a straightforward analysis of the theoretical model. Using (56) the interfacial temperature

can be written as

$$T_i \approx T_s + \underbrace{\frac{2-\chi}{2\chi}\sqrt{\frac{2\pi}{\bar{R}_v T_s}}\frac{\bar{R}_v T_s^2}{\rho_v \mathcal{L}}J}_{T_p} - \underbrace{\frac{T_s}{\rho_l \mathcal{L}}(p_l - p_v)}_{T_c}. \tag{138}$$

The variation $\Delta T_i \sim \bar{\tau}L$ in the interfacial temperature over the central portion of the cell is then the sum of the contributions describing the variations ΔT_s, ΔT_p, and ΔT_c, or the three terms on the right hand side of (138). These terms describe the effect of variation in the saturation pressure, phase change, and interfacial curvature, respectively.

First consider the last term, ΔT_c. Since the fluid velocities are very low, the pressure jump across the interface is determined by the Young-Laplace pressure $|p_l - p_v| \approx \kappa\sigma$,
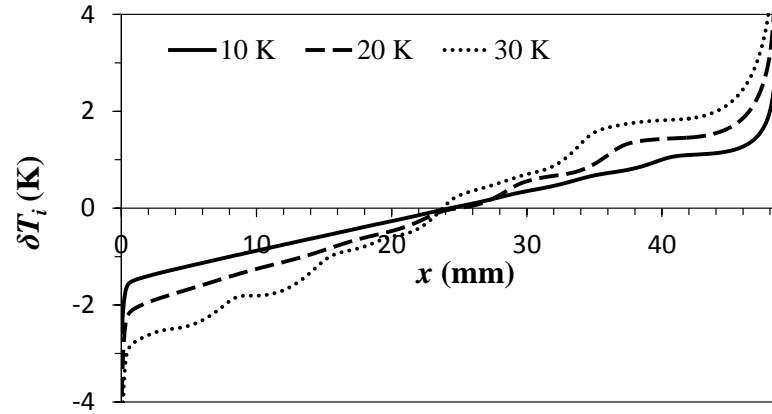
(a)
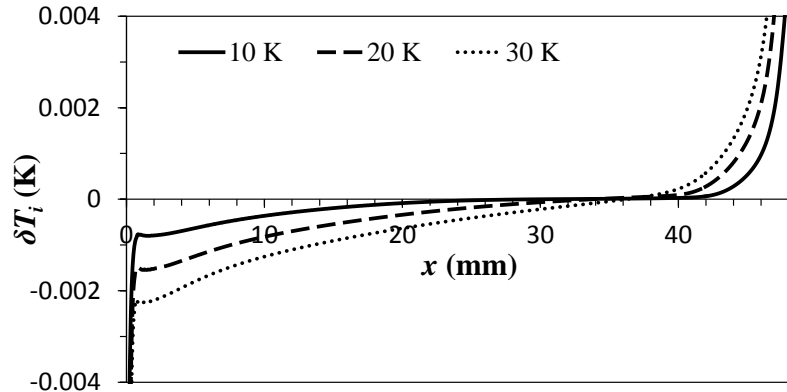
(b)

Figure 31: Interfacial temperature (a) under air and (b) under vapor. To amplify the variation of T_i in the central region of the cell the variation $\delta T_i = T_i - \langle T_i \rangle_x$ about the average value is plotted with truncated the y-axis.

where the largest curvature of the interface is comparable to the inverse of the capillary length scale l_c (83). Furthermore, $T_s \approx T_0$, so the temperature variation due to the curvature of the interface is

$$\Delta T_c \sim \frac{T_0}{\mathcal{L}} \sqrt{\frac{\sigma g}{\rho_l}} \approx 2 \times 10^{-5} \text{ K}, \tag{139}$$

irrespective of the presence or absence of noncondensables.

The magnitude of the temperature variation ΔT_p due to the latent heat absorbed or released at the interface is controlled by the variation in the mass flux ΔJ, which describes the phase change at the interface. In the absence of noncondensables, the amount of latent heat absorbed (released) at the interface, and therefore the rate of phase change, in the region adjacent to the hot (cold) end wall is only constrained by heat conduction. Since k_w is substantially higher than both k_g and k_l, thermal resistance of the walls can be ignored. Furthermore, since $k_l \gg k_g$, heat conduction through the gas can also be ignored. The relevant length scale is the thickness of the liquid layer d_l and the relevant temperature scale is $\Delta T/2$. Ignoring the negligible heat flux in the gas phase and using (45) therefore leads to the following estimate:

$$\Delta J \sim \frac{k_l}{\mathcal{L}} \frac{\Delta T}{2d_l}. \tag{140}$$

Substituting the fluid properties from Table 2 gives $\Delta J \sim 10^{-3}$ kg/(m^{2}s) for $\Delta T = 10$ K, which is consistent with the variation in J across the core region of the flow obtained in the numerical simulations (cf. Fig. 32(b)). With the typical choice $\chi = 1$ (for a nonpolar liquid)

$$\Delta T_p \sim \frac{2-\chi}{2\chi} \sqrt{\frac{2\pi}{\bar{R}_v T_0}} \frac{\bar{R}_v T_0^2}{\rho_v \mathcal{L}} \Delta J \tag{141}$$

yields $\Delta T_p \sim 8 \times 10^{-4}$ K.

When the gas phase is dominated by noncondensables (air), phase change is suppressed, since vapor has to diffuse towards/away from the interface. In this case the mass flux across the interface is limited by diffusion and the variation in the mass flux can be estimated as

$$\Delta J \sim D\,|\partial_n \rho_v| \sim D\frac{\Delta \rho_v}{2d_l}, \tag{142}$$

where $\Delta\rho_v$ is the variation of the vapor density, which can be estimated from the equilibrium values of the vapor pressure at T_h and T_c. With the help of (14) and (41) it is found that

$$\Delta\rho_v \sim \frac{\partial\rho_v}{\partial p_v}\frac{\partial p_v}{\partial T}\Delta T \sim \frac{\mathcal{L}p_v}{\bar{R}_v^2 T_0^3}\Delta T, \tag{143}$$

and therefore

$$\Delta J \sim D\frac{\mathcal{L}p_v}{\bar{R}_v^2 T_0^3}\frac{\Delta T}{2d_l}. \tag{144}$$

For $\Delta T = 10$ K this estimate gives $\Delta J \sim 7\times10^{-4}$ kg/(m^{2}s). A more accurate estimate can be obtained by using the variation of temperature along the interface $\Delta T_i \approx \bar{\tau}L$ instead of ΔT in (144), which gives a slightly lower value $\Delta J \sim 2\times10^{-4}$ kg/(m^{2}s) that is in better agreement with the numerical result (cf. Fig. 32(a)). However, for the purposes of estimating ΔT_i the former, less accurate, estimate is sufficient and gives $\Delta T_p \sim 5\times10^{-4}$ K.
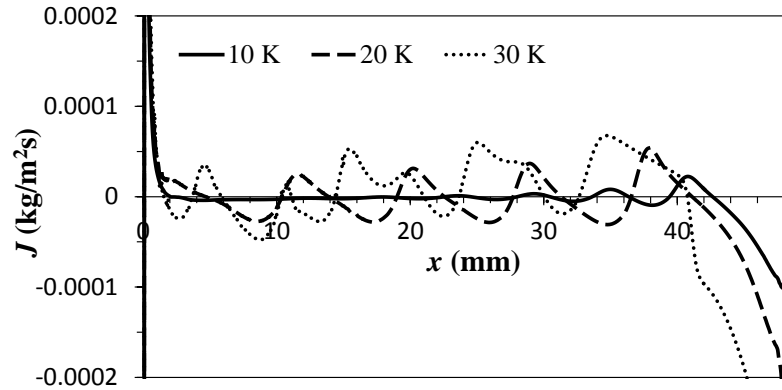
(a)
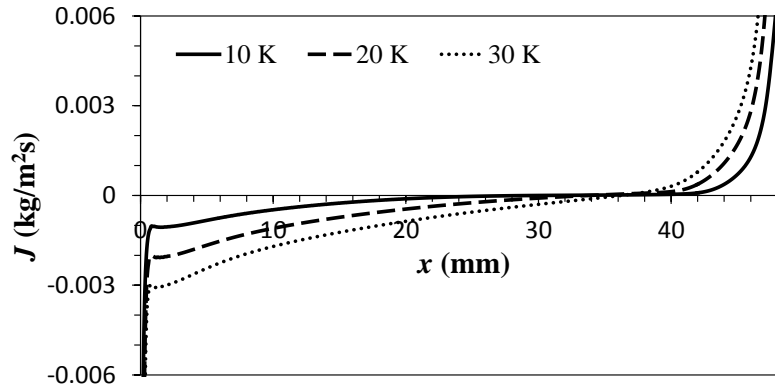
(b)

Figure 32: Mass flux for different ΔT (a) under air and (b) under vapor. The y-axis is truncated so that the details of the variation in the core region of the flow can be seen.

Finally, the magnitude of the variation in the saturation temperature ΔT_s is controlled by the variation of the vapor pressure Δp_v, which differs greatly in the two limits considered here. When the gas phase is pure vapor, the vapor pressure is equal to the absolute pressure in the gas phase. The variation of the absolute pressure along the liquid-gas interface can be estimated using the pressure drop for the flow of viscous vapor. The flow has an approximately Poiseuille profile between the two large parallel planes formed by the top wall and the liquid-vapor interface, with the separation equal to the vapor layer thickness d_g. The vapor speed is much larger than that of the liquid-vapor interface, so both planes can be assumed stationary. The volumetric flow rate per unit width (in the y direction) can be estimated by integrating the phase change mass flux over the region of intense evaporation (which has a width of order d_l) $\dot{Q} \sim \Delta J d_l / \rho_v$ yielding

$$\Delta p_v \sim 12 \frac{\mu_v \dot{Q} L}{d_g^3} \sim 12 \frac{\mu_v d_l L}{\rho_v d_g^3} \Delta J, \tag{145}$$

which together with (14) and (41) gives

$$\Delta T_s = \frac{\partial T_s}{\partial p_v} \Delta p_v \sim 12 \frac{\mu_v d_l L T_0}{\rho_v^2 d_g^3 \mathcal{L}} \Delta J. \tag{146}$$

Using the estimate (140) for ΔJ gives $\Delta T_s \sim 3 \times 10^{-7}$ K.

In the limit where noncondensables are dominant, the vapor pressure is equal to the partial pressure instead of the absolute pressure. With the help of (14), (41) and (143) it is found

$$\Delta T_s = \frac{\partial T_s}{\partial p_v} \frac{\partial p_v}{\partial \rho_v} \Delta \rho_v \sim \frac{\bar{R}_v T_0^2}{\mathcal{L} p_v} \bar{R}_v T_0 \frac{\mathcal{L} p_v \Delta T}{\bar{R}_v^2 T_0^3} = \Delta T, \tag{147}$$

so that, in this case, it is the imposed temperature difference ΔT instead that sets the scale for the variation in T_s.

Table 4 summarizes the estimates that quantify the contributions of these various physical effects to the variation in the interfacial temperature. Clearly, the dominant physical effect is different for the two limiting cases considered here. Under pure vapor, $\Delta T_s \ll \Delta T_c \ll \Delta T_p$, so that the variation in T_i is mainly due to the latent heat released or absorbed at the interface. However, despite the absence of noncondensables that suppress

Table 4: Estimates of how various physical effects contribute to the variation in the interfacial temperature T_i, for $\Delta T = 10$ K.

	ΔT_s (K)	ΔT_p (K)	ΔT_c (K)	ΔT_i (K)
under vapor	3×10^{-7}	8×10^{-4}	2×10^{-5}	8×10^{-4}
under air	10	5×10^{-4}	2×10^{-5}	10

phase change, this is a fairly weak effect: the resulting variation $\Delta T_i \approx \Delta T_p$ is almost four orders of magnitude less than the imposed temperature difference ΔT. Under air, $\Delta T_c \ll \Delta T_p \ll \Delta T_s$, so that the variation in T_i is mainly due to the variation of the saturation temperature, $\Delta T_i \approx \Delta T_s \sim \Delta T$. Both estimates are in good agreement with the numerical results presented in Fig. 31.

4.2.2 Thermal Boundary Layer Thickness

The analysis presented above gives an estimate for the interfacial temperature variation in the core region of the flow. However, as Fig. 31 illustrates, the interfacial temperature varies much more rapidly near the end walls than in the central portion of the cell, changing by $\delta T_i = O(\Delta T)$ across very thin interfacial thermal boundary layers. The thickness δx of these boundary layers can be estimated using an energy balance [193]. Since the contact lines correspond to the stagnation points of the flow, the heat transport in the boundary layers is dominated by conduction and, since $k_g \ll k_l$ both under vapor and under air, the heat flux balance (45) can be simplified, yielding

$$\mathcal{L} J_b = k_g \partial_n T_g - k_l \partial_n T_l \approx k_l \frac{\delta T_b}{\delta x_i}, \qquad (148)$$

where $\delta T_b = T_i^{in} - T_i^{out}$ is the interfacial temperature variation across the boundary layers, and J_b is the mass flux within the boundary layers. Here the superscripts "in" and "out" denote the values on the inside and on the outside, respectively, of the thermal boundary layer. The mass flux J_b can be estimated by ignoring the first (curvature) term on the right-hand-side of (56), so

$$J_b \approx \frac{2\chi}{2 - \chi} \sqrt{\frac{\bar{R}_v T_i^{in}}{2\pi}} \left(\frac{\rho_v \mathcal{L}}{\bar{R}_v T_i^{in}} \frac{T_i^{in} - T_s^{in}}{T_s^{in}} \right). \qquad (149)$$

The saturation temperature is essentially constant across the boundary layer, $T_s^{in} \approx T_s^{out}$. Furthermore, the mass flux is much smaller outside of the boundary layers, $T_s^{out} \approx T_i^{out}$. Therefore, $T_i^{out} \approx T_s^{in}$. Combining with (148) and (149) this yields an estimate of the interfacial thermal boundary layer thickness

$$\delta x_i \sim \frac{2-\chi}{2\chi} \sqrt{\frac{2\pi}{\bar{R}_v T_i^{in}}} \left(\frac{k_l \bar{R}_v T_i^{in} T_s^{in}}{\rho_v \mathcal{L}^2} \right) \sim \frac{d_l}{K}, \tag{150}$$

where K is the "non-equilibrium parameter"

$$K = \frac{2\chi}{2-\chi} \sqrt{\frac{\bar{R}_v T_0}{2\pi}} \frac{\rho_v \mathcal{L}^2 d_l}{k_l \bar{R}_v T_0^2} \tag{151}$$

introduced by Burelbach *et al.* [194], which defines the ratio of the latent heat flux at the interface to the conductive heat flux in the liquid. For the conditions of the present study $K = 6.8 \times 10^3$, so $\delta x \sim 0.37 \ \mu$m, which is two orders of magnitude less than the spatial resolution of the finest computational mesh used here, explaining the singular behavior of J and T_i in the vicinity of the contact lines.

It should be noted that the bulk thermal boundary layers *inside* the liquid layer that were discussed in Chapter 3 are much thicker. The thickness of the bulk thermal boundary layers is determined by the balance of advection and conduction, which gives an estimate $\delta x_b = (d_l + d_c)/Pe_l \sim 35 \ \mu$m for the largest ΔT considered here, a value comparable to the spatial resolution of the numerical simulations.

4.2.3 Interfacial Flow Speed

The magnitude of the flow velocity at the interface (113) for different $\bar{c}_a$ can be estimated from the analytical solution (111) for the uniform flow in an unbounded fluid layer [4, 5, 184]. However, in the present case it is more appropriate to express the contribution due to buoyancy in terms of the laboratory, *vs.* interfacial, Rayleigh number

$$u_B = \frac{1}{48} \frac{\nu_l}{d_l} \frac{Ra_L}{Pr_l} \approx \frac{1}{48} \frac{\beta_l \rho_l g d_l^3}{\mu_l L} \Delta T. \tag{152}$$

While in a laterally unbounded layer both u_T and u_B are controlled by the interfacial temperature gradient τ, in a laterally bounded layer, close to the walls (where u_i is maximum

under air) u_B is instead controlled by the imposed temperature difference ΔT, which sets the vertical temperature variation in the liquid layer under both air and vapor. For the range of ΔT considered here, the relation between τ and ΔT is not straightforward. For instance, under air the relationship is nonlinear (86). Furthermore, while u_T is sensitive to the presence of noncondensables, u_B is not. The ratio of the two velocities is

$$\frac{u_T}{u_B} \approx 12 \frac{L\bar{\tau}}{\Delta T} Bo_D^{-1}, \tag{153}$$

where the dynamic Bond number $Bo_D = 0.86$ for the liquid layer of thickness $d_l = 2.45$ mm considered here.

The values of various nondimensional parameters are summarized in Table 5. Under air $L\bar{\tau}/\Delta T$ varies from about 0.2 to 0.3 for ΔT between 10 K and 30 K, so the flow is dominated by thermocapillary, $u_i \approx u_T$. Under vapor $L\bar{\tau}/\Delta T \ll 1$, so the flow is dominated by buoyancy, $u_i \approx u_B$ and should be slower by a factor of 3 to 4, compared with the flow at the same ΔT under air. Overall, these estimates are consistent with the numerical results presented in Table 3, although the numerically computed flow speeds under vapor are found to be even smaller than u_B, since the flow profile differs substantially from the analytical solution on which the estimate (113) is based (the flow is substantially slower than u_B far from the end walls).

4.2.4 Newton's Law of Cooling

The numerical results presented in Section 3.7 show that Newton's law of cooling (136) at the interface completely breaks down under air. In particular, for SUF, the assumption of

Table 5: The values of nondimensional parameters for the numerical solutions under vapor and under air.

	under vapor			under air		
ΔT (K)	10	20	30	10	20	30
$Ra_L \times 10^{-3}$	1.6	3.2	4.7	1.6	3.2	4.7
Ma_i	0.22	0.48	0.72	547	804	1096
$L\bar{\tau}/\Delta T$	1.3×10^{-4}			0.3	0.22	0.2

an adiabatic interface ($Bi = 0$) is not valid near the end walls (although it might be justified for the regions away from the end walls); for SMC and OMC, this assumption breaks down over the entire interface.

Under pure vapor, assuming the heat conduction in the gas layer can be ignored, the heat flux balance relation (45) reduces to

$$\mathcal{L}J \approx -k_l \partial_n T_l. \tag{154}$$

Furthermore, ΔT_c and ΔT_s are negligible compared to ΔT_p, so $T_c \approx 0$ and $T_s \approx T_0$ in (138), which yields Newton's law of cooling (136) with

$$Bi \approx K. \tag{155}$$

Figure 33 shows the local Biot number computed from the numerical solutions in the two limits. The local values of Bi under pure vapor are indeed comparable to the theoretical estimate (155) over the entire x interval. In contrast, under air Bi varies significantly, and even changes sign, indicating that there is no direct correlation between the deviation of the interfacial temperature from a constant reference value and the normal component of the temperature gradient in the liquid layer. While it is known that the Biot number generally depends on the horizontal wave-number of convective motions [195], the convective patterns at $\Delta T \lesssim 20$ K appear reasonably monochromatic (see Fig. 6), so such significant variation in Bi is a nontrivial result.

It should be noted that the "non-equilibrium parameter" (151) also determines how much the interfacial temperature T_i can deviate from the local saturation temperature T_s. Ignoring the term T_c in (138) and using the estimate (140) for the mass flux J we quickly find that, regardless of $\bar{c}_a$,

$$|T_i - T_s| \lesssim \frac{\Delta T}{K} \sim 10^{-3} \text{ K}. \tag{156}$$

4.3 Comparison of Different Phase Change Models

The analysis of the KTG-based model shows that significant gradients in interfacial temperature can only be established when noncondensables impede the transport of vapor from the hot end to the cold end of the cell. Hence, when air is removed completely from the test cell, thermocapillary stresses are dramatically suppressed, and the interfacial flow speed decreases significantly. However, the experiments show the observed flow speed under almost pure vapor (when most of the air has been removed) are comparable to, and near the cold end even slightly higher than, those under air [1]. Since buoyancy is unaffected by the presence of noncondensables, this implies that the thermocapillary stresses and hence the interfacial temperature gradient $\bar{\tau}$ in the experiment should be essentially the same at

(a)

(b)
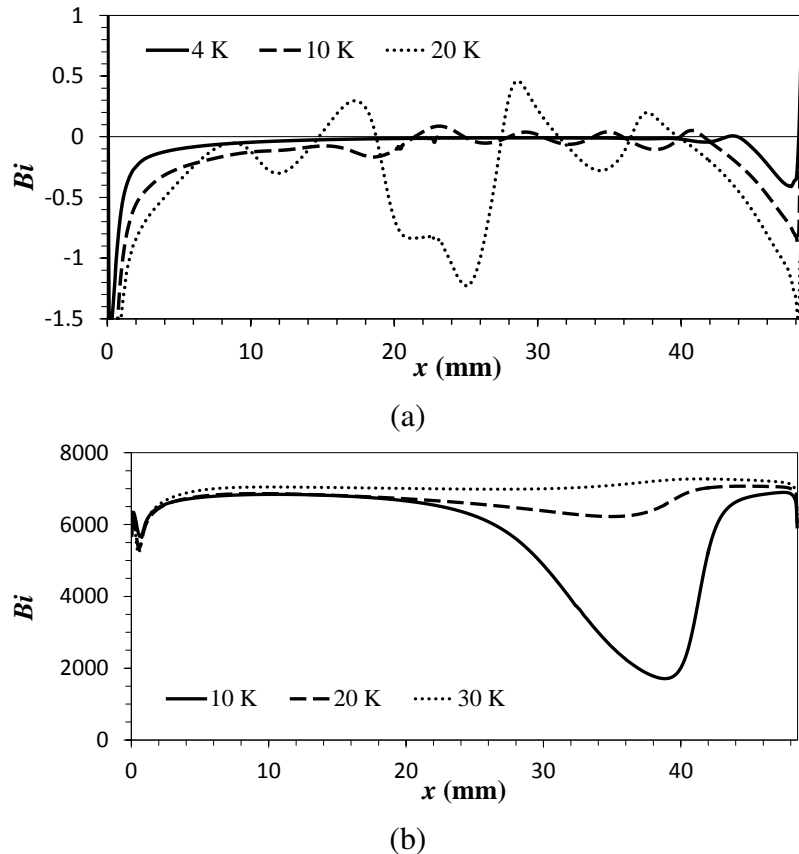
Figure 33: Local Biot number computed using (281) for different ΔT (a) under air and (b) under vapor. Under vapor T_0 is set as the interfacial temperature at the point where $\partial_n T_l = 0$, while under air $T_0 = (T_c + T_h)/2$. The vertical range in (a) is truncated to amplify the variation in the core region of the flow.

atmospheric conditions and when most of the air has been removed.

There could be several explanations for this discrepancy. The possibility that even a small amount of noncondensables could have an unexpectedly strong effect on the flow will be considered in Chapter 5. In this chapter two of other potential explanations for the unexpected dependence of the interfacial temperature gradient on $\bar{c}_a$ will be investigated. First, the temperature across the interface may not necessarily be continuous under intense phase change. Second, it is possible that the value of the accommodation coefficient for silicone oil, which is not well established, could differ substantially from unity.

The predictions of KTG could possibly break down under intense phase change, so a different theoretical model may be required to describe phase change in the (near) absence of noncondensables. Indeed, SRT and NET predict a temperature jump across the liquid-vapor interface, which could, in principle, lead to a variation in the temperature of the liquid that exceeds the variation in the temperature of the gas at the interface, and hence produce stronger thermocapillary stresses. Some experimental studies report temperature jumps across the interface as high as 3 K for unforced evaporation and as high as 10-20 K for evaporation of heated layers of water [182, 196, 197].

These three different models of phase change were therefore used to compute the steady-state flow under vapor for $\Delta T = 10$ K below. For KTG and NET, the accommodation coefficient is set as unity ($\chi = 1$), following the vast majority of theoretical studies
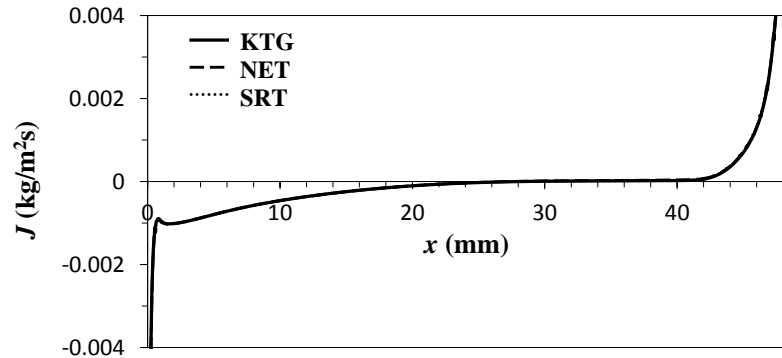
Figure 34: Mass flux for $\Delta T = 10$ K. The vertical range is truncated to amplify the variation in the core region of the flow.

102

of nonpolar liquids. The corresponding mass flux J is shown in Fig. 34. Quite interestingly, the spatial profile of J is independent of the choice of the model — the three curves are indistinguishable. The temperature profiles on the liquid side of the interface shown in Fig. 35(a) are also very similar for all three models. Most importantly, the results of all three models are consistent with the estimates derived in the previous section. In other words, all three models unequivocally predict that the thermocapillary stresses should essentially disappear when the noncondensables are removed from the cell.

As expected, NET and SRT both predict that the temperature field is not continuous across the interface. Fig. 36 shows the temperature jump between the liquid and the vapor side of the interface, $T_l - T_g$, computed numerically for these two phase change models
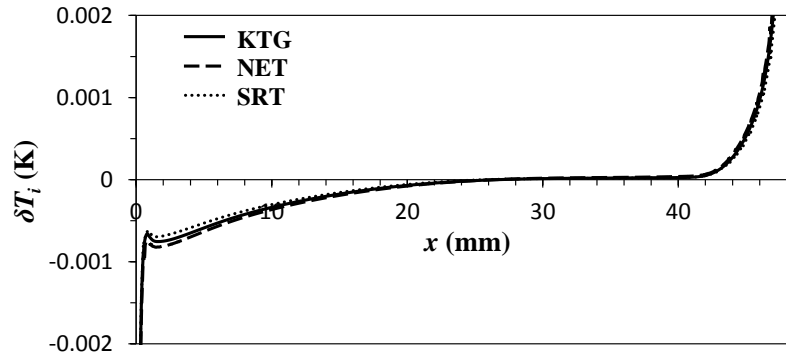
(a)
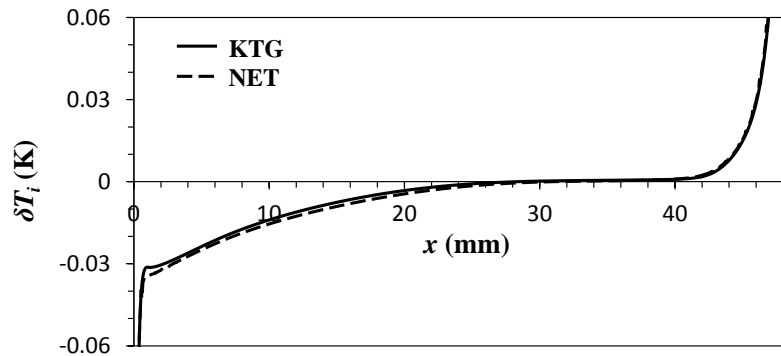
(b)

Figure 35: Interfacial temperature profile for $\Delta T = 10$ K. To amplify the variation of T_i in the core region of the flow, the deviation $\delta T_i = T_i - \langle T_i \rangle_x$ above the average value (on the liquid side for NET and SRT) is plotted with truncated the y-axis.. The accommodation coefficient is $\chi = 1$ in (a) and 0.05 in (b).

with and without the cross terms. NET and SRT produce essentially identical profiles, with the largest temperature jump occurring at the cold (hot) wall where vapor condenses (liquid evaporates) and reaches values of 0.3 K (-0.3 K), or about 3% of the applied temperature difference $\Delta T = 10$ K. The typical values in the core region of the flow are much smaller (less than 0.1%), so away from the contact lines the temperature can be considered continuous across the liquid-vapor interface.

When the cross terms are ignored, the temperature jump varies monotonically between the two end walls. On the other hand, when the cross terms are taken into account, the temperature jump profile becomes non-monotonic, with $T_l > T_g$ in a narrow region near the

(a)

(b)
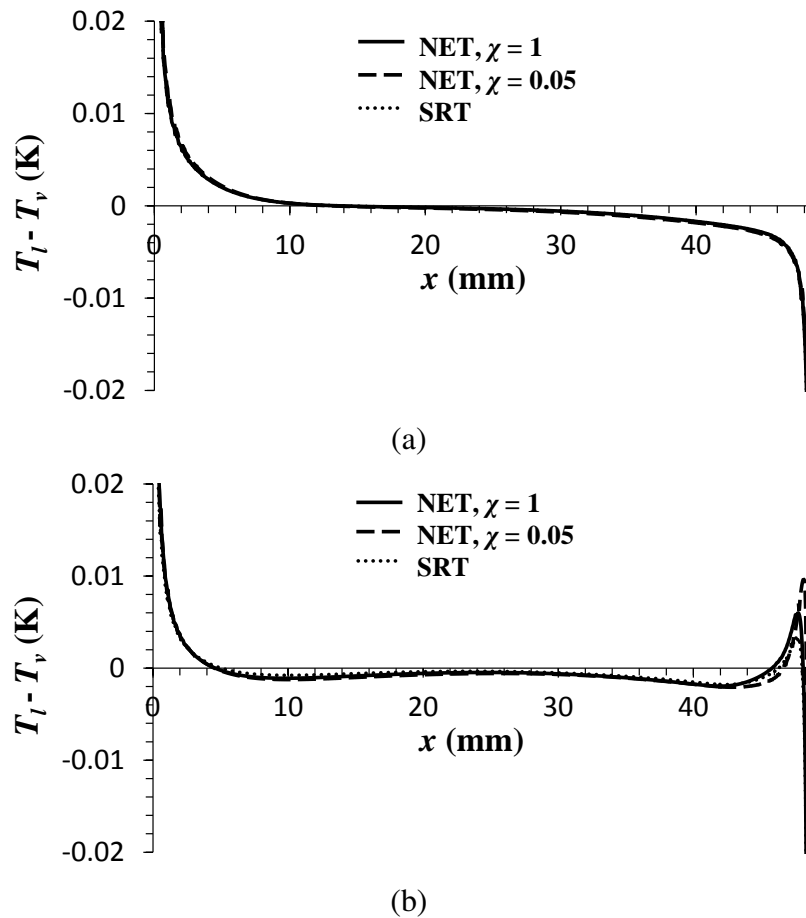
Figure 36: Temperature jump across the interface predicted by NET and SRT without (a) and with (b) the cross terms, for $\Delta T = 10$ K. The vertical range is truncated to amplify the variation in the core region of the flow.

hot end wall. These results are consistent with the relation (58) shared by the two models, which predicts that when $r_{21} = 0$ the temperature jump is proportional to the monotonically varying heat flux q_v (not shown). When $r_{21} \neq 0$, $T_l - T_g$ depends on both q_v and J, which typically have opposite signs, explaining the loss of monotonicity.

The variation in the vapor temperature along the interface far exceeds that in the liquid, although both are substantially less than the imposed temperature difference ΔT. This means that KTG provides a reasonably accurate description of the phase change process and the temperature can be assumed to be continuous across the interface without introducing significant error.

4.4   Dependence on the Accommodation Coefficient

Another possible explanation for the discrepancy between the model predictions and the experimental observations is that the assumed value of the accommodation coefficient χ is incorrect. As discussed earlier, $\Delta T_i \approx \Delta T_p$ under vapor. Assuming that the mass flux J is independent of the details of the phase change model (and, in particular, the choice of χ), from (141) it follows that

$$\Delta T_i \propto f(\chi) = \frac{2}{\chi} - 1 \tag{157}$$

for small values of χ. While there are no reliable values for the accommodation coefficient reported in the literature for 0.65 cSt silicone oil, values as low as 10^{-2} have been reported for water [182, 198, 199]. The numerical simulations were therefore repeated for $\chi = 0.05$, which is most likely much less than the actual value for the silicone oil (which is a non-polar liquid), to quantify the dependence of the results on the accommodation coefficient. According to (157), this should increase ΔT_i by a factor of $(2\chi^{-1} - 1) \approx 40$.

The results of numerical simulations presented in Fig. 37 show that the mass flux J is indeed independent not only of the choice of the phase change model, but also of the value of χ, at least over this range of accommodation coefficients. This result can be easily rationalized by generalizing the argument which lead to the relation (140) between the overall

variation ΔJ and the heat flux through the liquid layer. In the absence of noncondensables the heat flux through the gas layer is negligibly small, while the interfacial temperature is effectively constant. Under these conditions, thermocapillarity is negligible and the flow in the liquid layer is governed solely by buoyancy. This flow, along with the heat conduction through the liquid, determines the temperature distribution, and hence the conductive heat flux $k_l \partial_n T_l \approx \mathcal{L} J$, along the entire interface.

Fig. 35(b) compares the interfacial temperature T_i computed using KTG and NET for $\chi = 0.05$. The interfacial temperature profiles remain similar, even for this value of χ. As expected, the interfacial temperature variation ΔT_i increases significantly as χ decreases from unity to 0.05. To quantify the changes in the interfacial temperature associated with
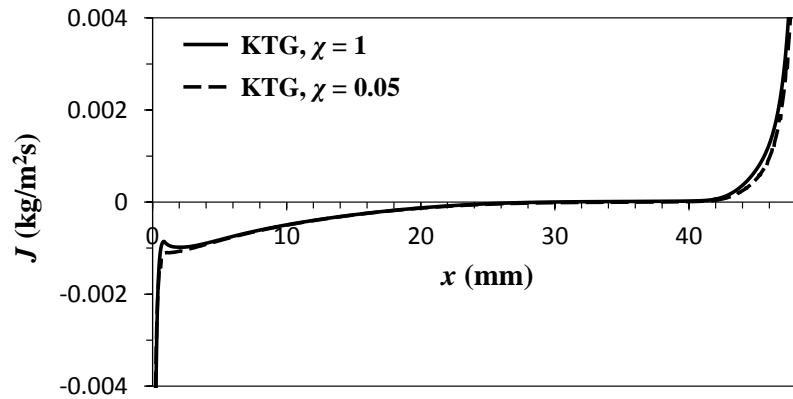
(a)
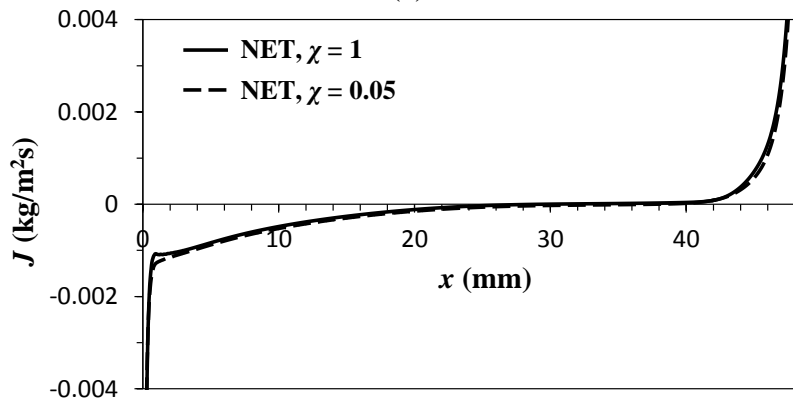
(b)

Figure 37: Mass flux using for different values of the accommodation coefficient for (a) KTG and (b) NET. In both cases $\Delta T = 10$ K and the vertical range is truncated.

the changes in the accommodation coefficient, the data from Fig. 35 were replotted in Fig. 38, which shows the temperature variation $\delta T_i = T_i - \langle T_i \rangle_x$ about the mean rescaled by the dimensionless factor $f(\chi)$. The scaled interfacial temperature profiles are essentially independent of both the choice of model and the value of χ. This means that ΔT_i does indeed scale with $f(\chi)$, as predicted previously. While ΔT_i increases as χ decreases, in order to achieve ΔT_i of order ΔT, the value of χ has to be reduced to about 10^{-4} which, for silicone oil, appears unphysical. Hence, the only logical conclusion is that an improper choice of the value of the accommodation coefficient also fails to account for the discrepancy between theoretical predictions and experimental observations.

Finally, while the value of the accommodation coefficient does affect the variation of T_i *along* the interface, it has almost no effect on the temperature jump $T_l - T_g$ *across* the
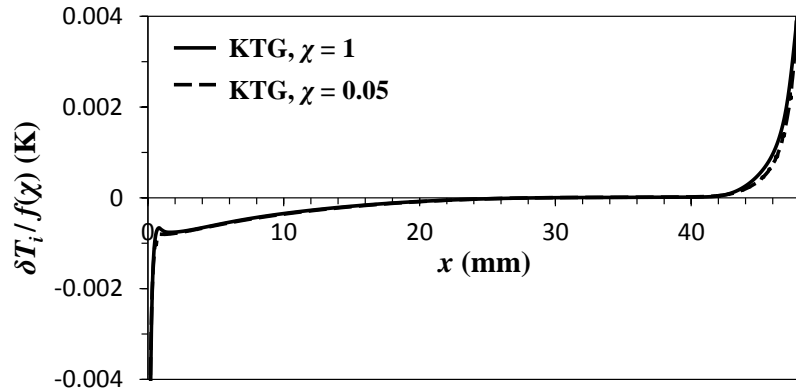
(a)
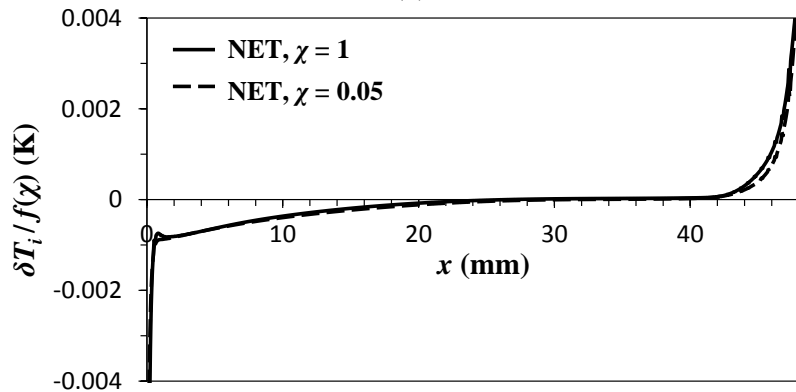
(b)

Figure 38: Scaled interfacial temperature profiles for (a) KTG and (b) NET. In both cases $\Delta T = 10$ K and the vertical range is truncated.

interface. As Fig. 36 illustrates, the temperature jump is independent of the value of χ along the entire interface when the cross terms are ignored. Including the cross terms in the phase change model leads to a very weak dependence on χ, which is constrained to a narrow region near the hot end wall (where evaporation is significant).

4.5 Discussion

Comparison of the results presented in Chapters 3 and 4 shows that the presence of non-condensable gases has a profound effect on the fluid flow and heat and mass transfer. For example, the convection patterns in the range of ΔT considered here are completely different. Moreover, the flow speed is also significantly reduced in the system under pure vapor. It is found that the difference is due to the thermocapillary stresses which essentially disappear in the absence of air. In both cases, the interfacial temperature is determined by the saturation temperature, with a small deviation (of order 10^{-3} K) due to the latent heat released/absorbed at the interface as a result of phase change. When the gas phase is dominated by air, as the concentration gradient is set up along the interface, the gradient in the saturation temperature is comparable to the imposed temperature gradient, and the flow is primarily driven by thermocapillary stresses. When the air is completely removed, the concentration gradient disappears, thermocapillarity becomes negligible, and the flow is driven primarily by buoyancy.

While the numerical simulations are qualitatively consistent with the theoretical analysis, there is discrepancy in the flow speed between the numerical predictions and the experimental observations [1]. Some potential reasons have been investigated and it was found that neither the temperature jump across the interface, which is predicted by some phase change models, nor the dependence of the interfacial temperature on the accommodation coefficient were sufficient to explain the discrepancy. A more careful examination of the experimental conditions shows that although most of the air was removed from the system, there are still a small amount of air estimated to be around 14%. To better understand the

effect of residual noncondensables on the heat and mass transport in confined and sealed two-phase flows of volatile fluids, the case of low, but nonzero, $\bar{c}_a$ will be considered in the next Chapter.

Two-phase cooling devices in practice are never completely free of noncondensables during operations. Their optimal operating conditions are much closer to the limit considered in this Chapter (two-phase flow under pure vapor) than the limit considered in Chapter 3 (two-phase flow under atmospheric conditions). The significant differences we discovered between these two limits illustrate the danger of extrapolating the results and intuition obtained under atmospheric conditions and applying them to models of cooling devices. For instance, the assumption used by most heat pipe models that phase change is negligible in the "adiabatic" region holds under atmospheric conditions, but breaks down completely under pure vapor (and, as we show in the next Chapter, for low $\bar{c}_a$ in general).

CHAPTER 5

CONVECTION AT REDUCED PRESSURES

Chapters 3 and 4 describe buoyancy-thermocapillary convection in a layer of volatile liquid subject to a horizontal temperature gradient at atmospheric conditions and under pure vapor, respectively. Recent fundamental studies of this problem were mainly motivated by applications to thermal management. Although the ideal operating conditions for two-phase cooling devices such as thermosyphons, heat pipes, and heat spreaders corresponds to the pure vapor case, noncondensables, such as air, tend to dissolve in liquids and be adsorbed into solids, and removing them completely is usually neither feasible, nor practical. Hence, the liquid almost always remains in contact with a mixture of its own vapor and some, usually small, amount of air. As the results of Chapter 4 indicate, noncondensables can have a rather significant effect on heat and mass flow, even in small amounts. Hence the limit when the gas mixture is dominated by the vapor, but nonetheless contains a (small) nonzero amount of noncondensables, should be investigated separately.

The effect of noncondensables on some aspects of heat/mass transfer in two-phase systems has been studied previously. For example, the effect of noncondensables on the filmwise condensation of vapors in simple geometries (i.e., thin liquid layers of condensate on flat or cylindrical surfaces) is reasonably well understood [109, 110]. However, there are few theoretical studies that have considered transport in a whole closed system [49, 50, 82, 90, 91], specifically the effects of noncondensables on evaporation and transport of vapor from the hot to the cold side. The experimental study of Li *et al.* [1] appears to be the only investigation to date of the effect of noncondensables on the flow in the entire liquid layer. In particular, these experiments show that, at relatively small imposed temperature gradients, the flow structure and speeds remain essentially the same as the air concentration decreases from 96% (ambient conditions) to 14%, which corresponds to a reduction by more than two orders of magnitude in the partial pressure of air. The theoretical

analysis presented in the previous chapters cannot explain this observation.

To better understand the effect of noncondensables on heat and mass transport in volatile fluids in confined and sealed geometries, we next consider the limit of the two-sided model described in Chapter 2 where vapor and air are the dominant and dilute components, respectively (the opposite case was considered in Chapter 3). Although the 0.65 cSt silicone oil, hexamethyldisloxane, is still the working fluid, the fluid properties have been updated in this chapter based on more recent values from the literature [161, 162], and so some of the material parameters differ from those used in Chapters 3 and 4. The updated properties of the working fluid are summarized in Table 6. The liquid film thickness is still d_l = 2.45 mm, and the corresponding values of the Prandtl and dynamic Bond numbers are Pr_l = 9.19 and Bo_D = 0.67. Since the flow in the vertical mid-plane at atmospheric conditions was found to be essentially 2D and the contact angle had little effect, the flow is assumed to be 2D in this Chapter as well, and the contact angle is fixed at $\theta = 50°$. This Chapter includes the results that were reported in [200].

Table 6: Material properties of pure components (HMDS, air) at the reference temperature T_0 = 293 K [161, 162].

	liquid	vapor	air
μ (kg/(m·s))	5.27×10^{-4}	5.84×10^{-6}	1.81×10^{-5}
ρ (kg/m^3)	765.5	0.27	1.20
β (1/K)	1.32×10^{-3}	3.41×10^{-3}	3.41×10^{-3}
k (W/(m·K))	0.110	0.011	0.026
C_p (J/(kg·K))	1914	1482	1004
α (m^2/s)	7.49×10^{-8}	2.80×10^{-5}	2.12×10^{-5}
D (m^2/s)	-	1.46×10^{-4}	5.84×10^{-6}
σ (N/m)	1.58×10^{-2}		
γ (N/(m·K))	8.9×10^{-5}		
$\mathcal{L}$ (J/kg)	2.25×10^{5}		
A_v (Pa)	20.90		
B_v (Pa·K)	2.96×10^{3}		
C_v (K)	-58.05		

5.1 Solutions in the Bulk

In order to investigate the effect of noncondensables on the flow, numerical simulations were performed for ΔT varying between 0.01 K and 30 K and $\bar{c}_a$ varying between 0 (pure vapor) and 0.96 (atmospheric pressure). The numerical model employed in Chapters 3 and 4 was used at the limits $\bar{c}_a \geq 0.85$ and $\bar{c}_a = 0$, respectively. In the vapor-dominated limit $0 < \bar{c}_a \leq 0.16$ a revised version of the model from Chapter 3 was used, with the transport equation (36) describing the concentration of air, *vs.* vapor, as was the case in Chapter 3.

5.1.1 Flow Field

The dependence of the flow on the imposed temperature gradient was previously discussed in Chapters 3 and 4. The results discussed here focus instead upon how the flow depends on the concentration of noncondensables at a fixed $\Delta T = 10$ K. In particular, Fig. 39 shows the streamlines of the flow in both the liquid and the gas phases. At atmospheric conditions, $\bar{c}_a = 0.96$ (or 96% air), an oscillatory multicellular flow (OMC) is found with convection rolls covering the entire liquid layer. The amplitude of oscillation, however, is extremely small, so the flow can effectively be considered steady. The reduction in the range of ΔT values where OMC flow occurs, compared with the value (almost 30 K) reported in Chapter 3, is due to the difference in the material parameters (cf. Tables 2 and 6).

As the average air concentration decreases, convection rolls gradually weaken and disappear, starting near the cold end wall. This can be seen already at $\bar{c}_a = 0.85$, where a steady multicellular flow (SMC) is found. When the concentration of air decreases to 16% ($\bar{c}_a = 0.16$), the flow is instead steady unicellular flow (SUF), and all of the convection rolls disappear except for two rolls, one near each end walls. In the central region of the liquid layer, there is a horizontal return flow (corresponding to the analytical solution (111)) with the same profile across any vertical cross section. Finally, as $\bar{c}_a$ decreases to 8% or less, the horizontal flow speed becomes nonuniform, with a pronounced minimum forming around $x \approx 38$ mm. The flow at these low, but nonzero, values of $\bar{c}_a$ is *qualitatively* similar to that found under pure vapor (cf. Fig. 29).

$\bar{c}_a = 0$ (0% air)

$\bar{c}_a = 0.04$ (4% air)

$\bar{c}_a = 0.08$ (8% air)

$\bar{c}_a = 0.16$ (16% air)

$\bar{c}_a = 0.85$ (85% air)

$\bar{c}_a = 0.96$ (96% air)
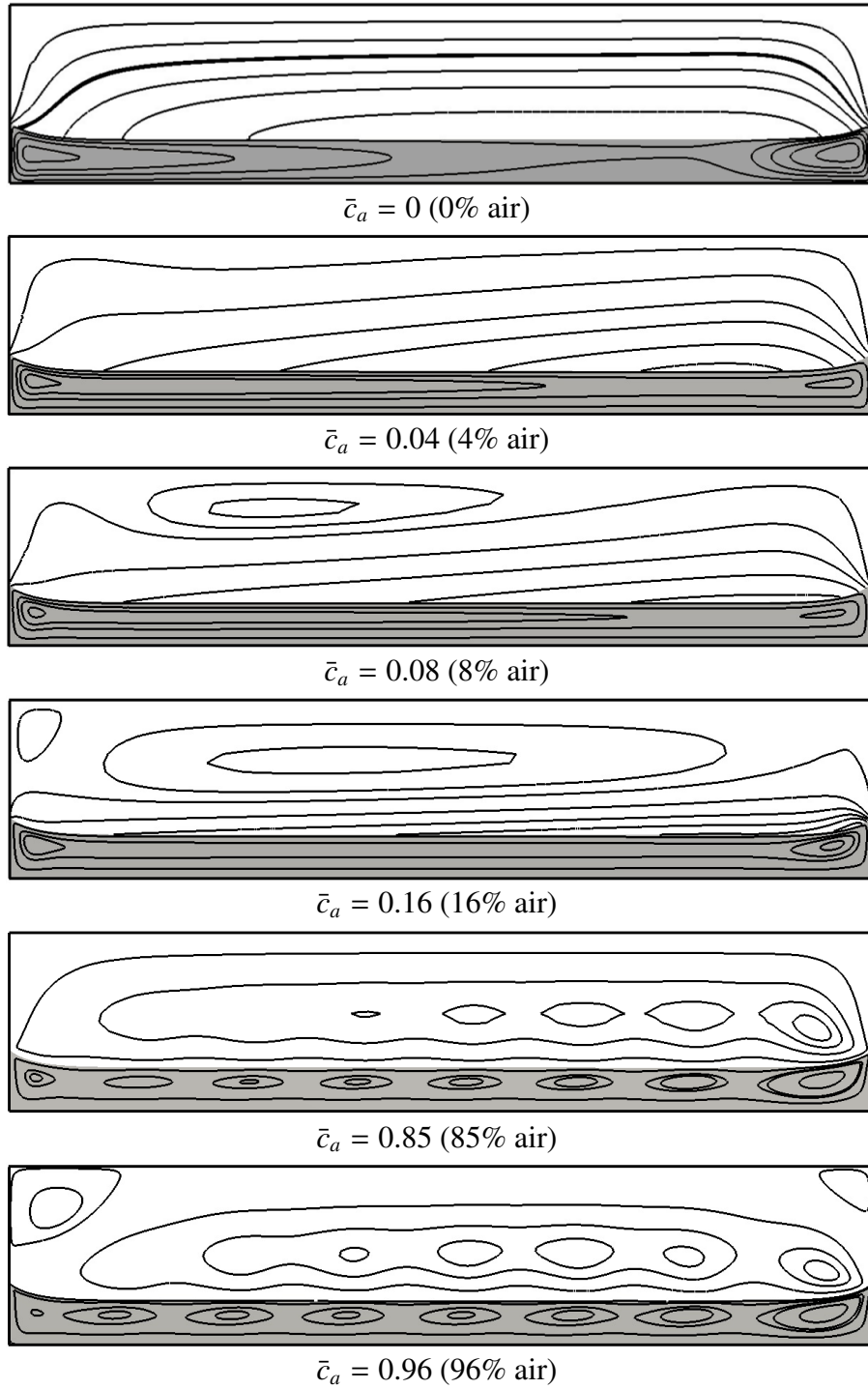
Figure 39: Streamlines of the flow (solid lines) at different average concentrations of air $\bar{c}_a$. The temperature difference is $\Delta T = 10$ K. As usual, the gray (white) background indicates the liquid (gas) phase; the hot end wall is on the right, and the cold end wall is on the left.

The flow in the gas phase is not directly observable in experiment, so numerical simulation is, at present, the only way to describe the transport of vapors. Two features of this flow are noteworthy. First of all, as $\bar{c}_a$ decreases, the global flow structure gradually changes. At (near-) atmospheric conditions ($\bar{c}_a \geq 0.85$) a return flow is found with the gas (mostly noncondensables) flowing from the hot to the cold wall along the free surface and in the opposite direction along the top of the cavity, with almost all streamlines closed. In the (near-) absence of air ($\bar{c}_a \leq 0.04$), however, the flow is unidirectional, with the gas (mostly vapor) flowing from the hot to the cold end wall. At intermediate concentrations ($\bar{c}_a = 0.08$ and 0.16), the velocity field exhibits features of both types of flows: there is a region of recirculation (closed streamlines) near the top of the cavity, but most of the streamlines originate and terminate on the interface, as one would expect for a gas mixture dominated by vapor. Second, at (near-) atmospheric conditions local convection rolls are also found in the gas phase. They are located directly above their corresponding convection rolls in the liquid phase for $\bar{c}_a$. This reflects the dominant role of interfacial processes in destabilization of the uniform return flow and the emergence of convection pattern. Moreover, there are no convection rolls in the gas phase when there is steady unicellular flow in the liquid layer.

5.1.2 Temperature Field

Figure 40 shows the temperature fields corresponding to the flow fields from Fig. 39. The temperature field in the gas phase is qualitatively similar for all $\bar{c}_a$, but in the liquid it depends noticeably on $\bar{c}_a$. At intermediate values of $\bar{c}_a$ (here 0.08 and 0.16) the temperature in the central portion of the liquid layer has a profile consistent with the analytical solution in the SUF regime (112) which, in dimensional form, can be rewritten as

$$T = \tau x + \hat{T}(z), \tag{158}$$

where $\hat{T}(z)$ describes the vertical profile. A qualitatively similar state is also found at (near-) atmospheric conditions in the SUF regime, i.e., $\Delta T \lesssim 3$ K (not shown). For $\bar{c}_a \geq 0.85$

$\bar{c}_a = 0$ (0% air)

$\bar{c}_a = 0.04$ (4% air)

$\bar{c}_a = 0.08$ (8% air)

$\bar{c}_a = 0.16$ (16% air)

$\bar{c}_a = 0.85$ (85% air)

$\bar{c}_a = 0.96$ (96% air)
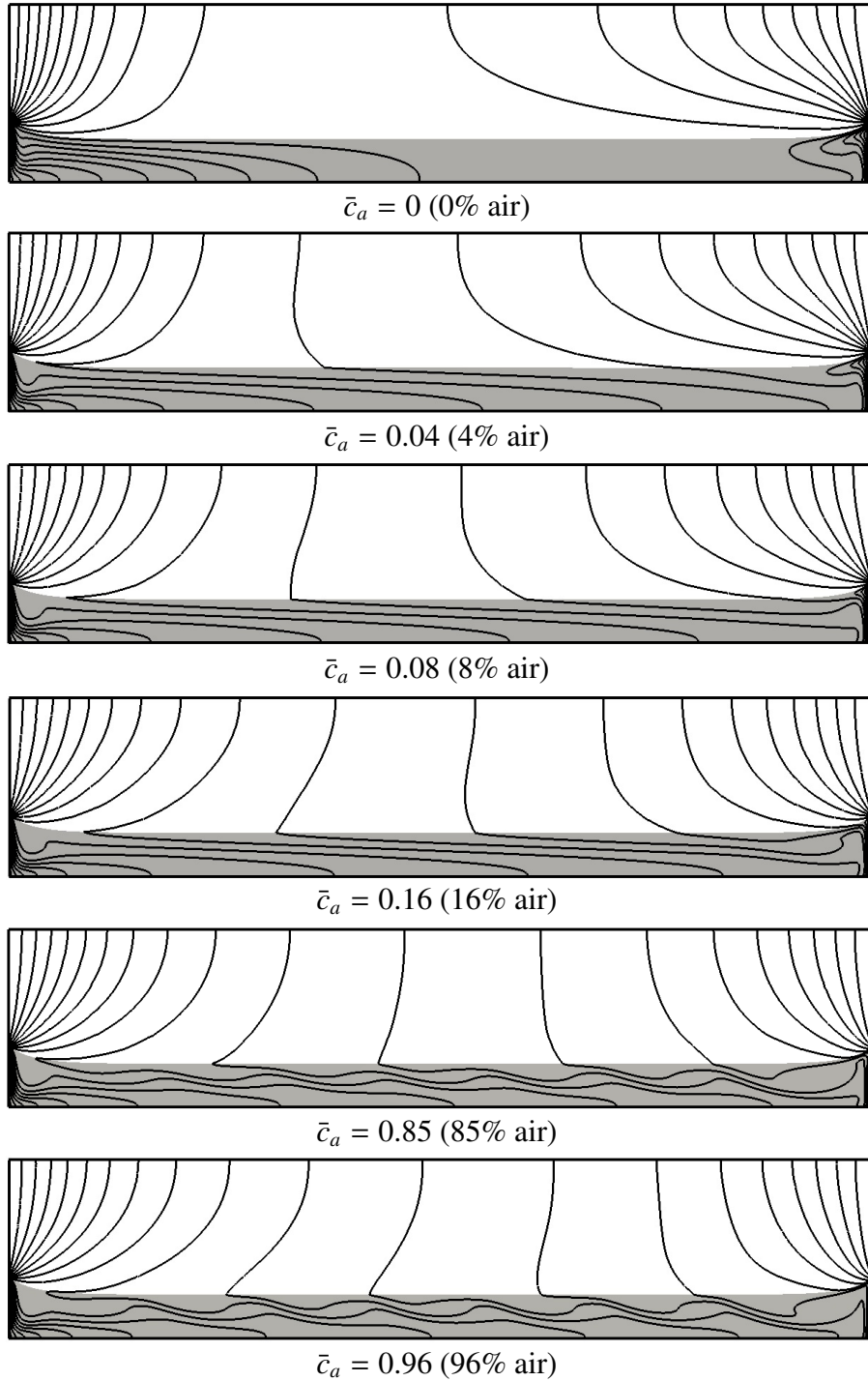
Figure 40: The temperature field inside the cavity at different average concentrations of air $\bar{c}_a$. The temperature difference is $\Delta T = 10$ K and the difference between adjacent isotherms (solid lines) is 0.5 K.

(and $\Delta T = 10$ K), the temperature field displays a noticeable modulation about the profile (158) caused by the advection of heat by the flow. For $\bar{c}_a \lesssim 0.16$ the periodic modulation

115

disappears due to the absence of convection rolls.

Some qualitative features of the temperature field, on the other hand, are independent of $\bar{c}_a$. For instance, the isotherms show strong clustering in the liquid phase near both end walls, indicating the formation of thermal boundary layers. In contrast, no thermal boundary layers form near the end walls in the gas phase. Instead, the temperature field appears to be fairly insensitive to the fluid flow and is dominated by heat conduction, which seems odd, given that thermal conductivity k_g of the gas is considerably smaller than thermal conductivity k_l of the liquid. However, in steady state the temperature field is actually controlled by the thermal diffusivity α, which is much larger in the gas than in the liquid (see Table 6) due to their vastly different densities, which explains why conduction dominates. Similar observations were made in Chapter 3, where it was pointed out that the differences between the two layers can be traced to the values of Péclet numbers $Pe_l \gg 1$, and $Pe_g = O(1)$.

5.1.3 Concentration Field

While the liquid phase is a simple fluid, the gas phase is a binary fluid, except for the pure vapor case $\bar{c}_a = 0$. The concentration field in the gas phase for different $\bar{c}_a$ is shown in Fig. 41. The concentration of air decreases with x for all $\bar{c}_a$, which is consistent with the air being swept by the flow of vapor towards the cold end wall. For $\bar{c}_a \geq 0.85$, c_a varies within a small range about its average. The horizontal concentration profile is linear near the top of the cavity, while near the interface significant spatial modulation about the linear profile is observed, which is caused by advection of the gas mixture by the convective flow.

As $\bar{c}_a$ decreases, the range of c_a increases. For instance, at $\bar{c}_a = 0.16$, the maximum value of c_a is more than double the minimum value. At this and other intermediate values of $\bar{c}_a$, the concentration field in the central region of the cavity has a linear (in the horizontal direction) profile, similar to the temperature field in the liquid layer,

$$c_a = -\varsigma x + \hat{c}_a(z), \tag{159}$$

116

where ς is the interfacial concentration gradient given by (129) and $\hat{c}_a(z) = 1 - \hat{c}_v(z)$ is the vertical concentration profile.

For $\bar{c}_a \lesssim 0.08$, the horizontal concentration gradient ς is no longer constant and its magnitude decreases with x, while the air concentration at the hot end wall is a small fraction of $\bar{c}_a$. At the same time, the vertical concentration profile $\hat{c}_a(z)$ becomes essentially flat in the central portion of the cavity.

5.1.4 Flow Regimes

The flow regimes found in the numerical simulations for different ΔT and $\bar{c}_a$ are summarized and compared with the experimental observations of Li *et al.* [1] in Fig. 42. Instead of the dimensional parameter ΔT, the results are presented in terms of the interfacial Marangoni number Ma_i which depends on the spatial average of the interfacial temperature gradient τ. Overall, the two sets of results are found to be in good agreement, which suggests that the model captures the salient physical processes. The flow fields shown in Fig. 39 illustrate all the qualitatively different regimes except for PMC, which features multiple convection rolls that do not extend all the way to the cold end wall. While this regime, which occurs between SUF and SMC [1], is expected to be found for $\Delta T = 10$ K at intermediate values of $\bar{c}_a$, the numerical model based on a dilute approximation is not expected to produce accurate predictions when the concentrations of air and vapor are comparable. Nevertheless, the PMC state is indeed found at higher $\bar{c}_a$ and lower ΔT, as shown in Fig. 42.

In fact, for $\bar{c}_a \geq 0.85$ all four flow regimes are found, from SUF at low ΔT to OMC at high ΔT. Both experiments and numerics show that a reduction in the concentration of noncondensables increases the threshold (critical Ma_i) for transition between different flow regimes. As a result, not all flow regimes are found at lower $\bar{c}_a$. For instance, at $\bar{c}_a \leq 0.16$ and $\Delta T \leq 30$ K only the SUF state is found in the numerics. In the experiment only the SUF and PMC states are found at $\bar{c}_a = 0.14$, with the latter only occurring at the largest $\Delta T \gtrsim 11$ K.

$\bar{c}_a = 0.01, \delta c_a = 0.001, 0.002 < c_a < 0.026$

$\bar{c}_a = 0.04, \delta c_a = 0.004, 0.011 < c_a < 0.081$

$\bar{c}_a = 0.08, \delta c_a = 0.005, 0.032 < c_a < 0.134$

$\bar{c}_a = 0.16, \delta c_a = 0.005, 0.094 < c_a < 0.220$

$\bar{c}_a = 0.85, \delta c_a = 0.00125, 0.822 < c_a < 0.863$

$\bar{c}_a = 0.96, \delta c_a = 0.0004, 0.952 < c_a < 0.963$
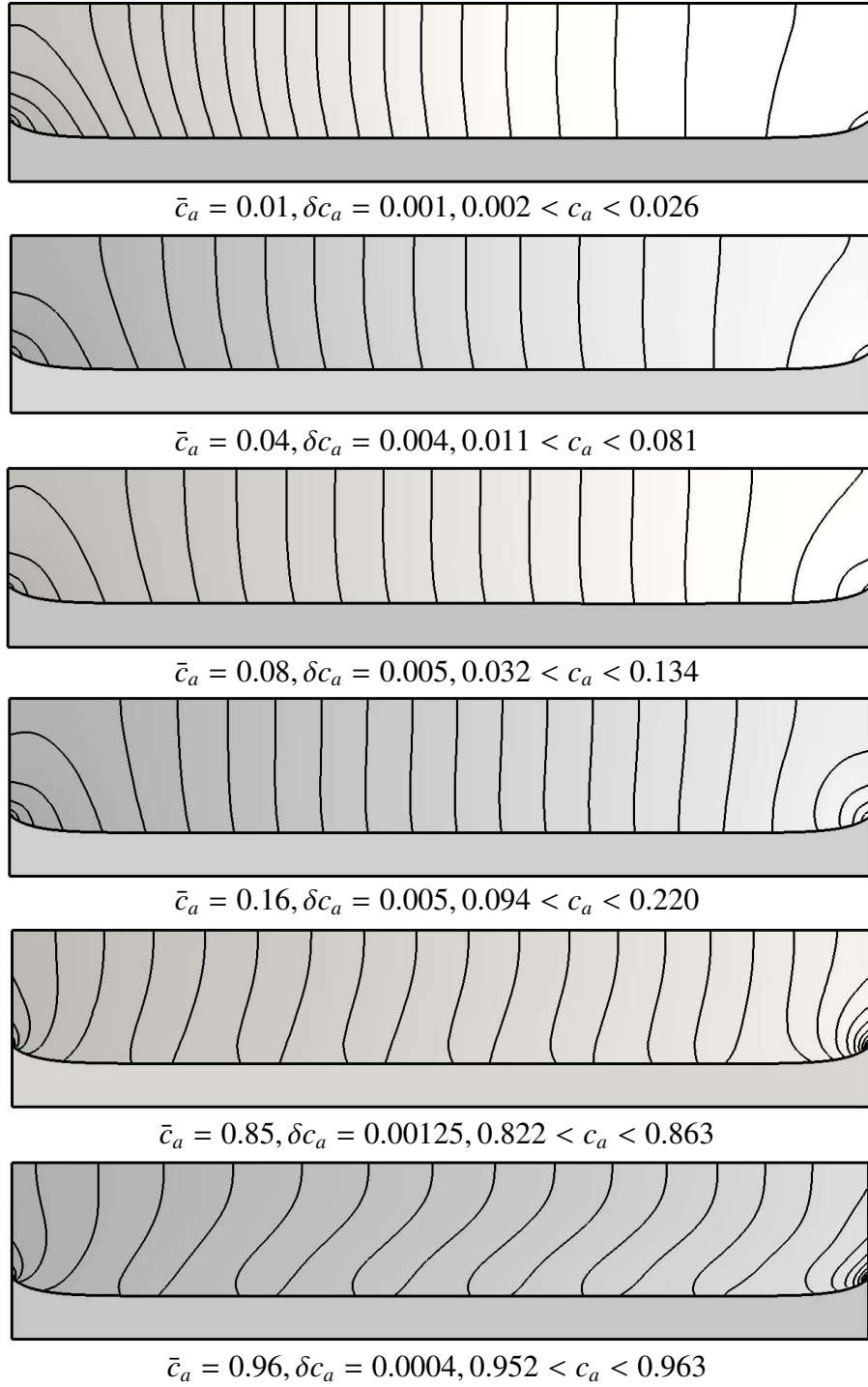
Figure 41: Air concentration c_a in the gas phase for $\Delta T = 10$ K and different $\bar{c}_a$. δc_a denotes the interval between adjacent level sets. In the gas phase, darker shade indicates higher air concentration. In the liquid phase, the concentration field is not defined.

At atmospheric conditions the thresholds for transition from SUF to PMC ($Ma_i \approx 390$) and from SMC to OMC ($Ma_i \approx 780$) are very similar in the experiment and numerics, however the transition from PMC to SMC occurs in the numerics at a higher Marangoni number ($Ma_i \approx 600$) compared with the experiment (where it happens at $Ma_i \approx 430$). One reason for this discrepancy is the different value of the contact angle (in the numerics $\theta = 50°$, while in the experiment $\theta \approx 0°$), which as shown in section 3.3, does affect the flow pattern. Another potential reason is the assumption of the model that condensation does not occur on the cold end wall. In the experiment a significant fraction of the vapor likely condenses on the cold end wall, forming a thin film that drains towards the liquid layer. This can noticeably enhance condensation at all $\bar{c}_a$. As a result, the same values of ΔT can correspond to different Ma_i in the experiment and numerics. Finally, Ma_i is estimated
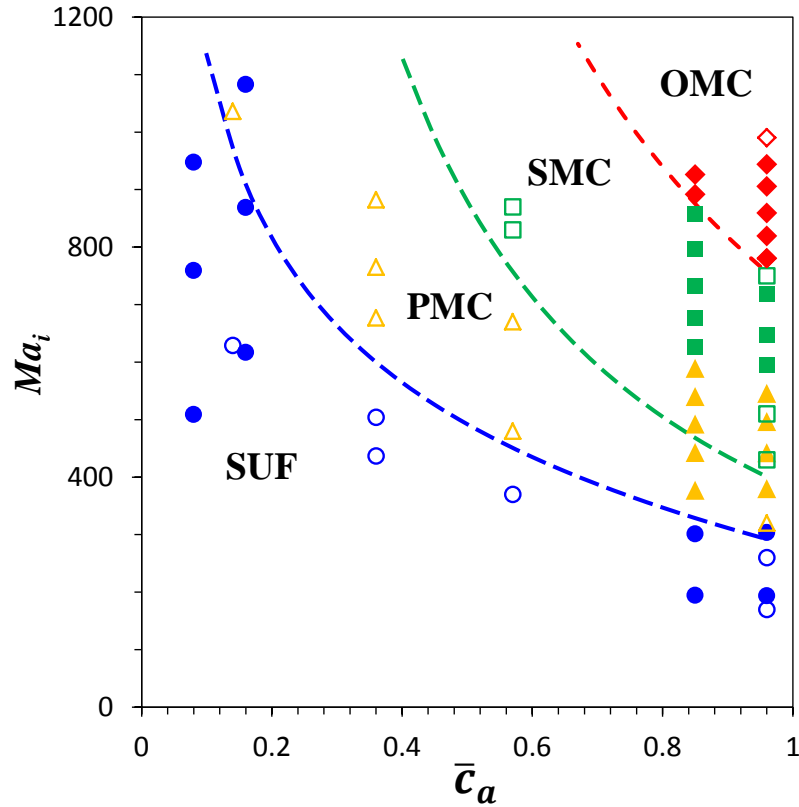
Figure 42: Flow regimes: SUF (○), PMC (△), SMC (□), and OMC (◇). Open symbols correspond to experimental results of Li *et al.* [1] and filled symbols – to numerical results from this study. Dashed lines show the approximate positions of the boundaries between different regimes based on the experimental results.

in the experiments by curve-fitting the spatially-averaged liquid-phase velocity profile (in the presence of convection rolls) to the analytical solution (applicable in the absence of convection rolls), and the accuracy of this estimated Ma_i remains undetermined.

The changes in the structure of the flow found at a fixed $\Delta T = 10$ K as $\bar{c}_a$ increases are qualitatively similar to the changes found at atmospheric conditions ($\bar{c}_a = 0.96$) as ΔT increases [1, 185]. Hence, it seems likely that the same physical mechanism is responsible for the destabilization of the uniform return flow found in the SUF regime in both cases (this will be discussed in detail in the next Chapter). In order to better understand the structure and stability of the flow as a function of ΔT and $\bar{c}_a$, the next Section considers the interfacial profiles of the velocity, temperature, and concentration fields, as well as the mass flux J describing the intensity of phase change at the interface.

5.2 Solutions at the Interface

The flow in the bulk is significantly affected by the conditions at the interface. Thermo-capillarity, which is the dominant force at $Bo_D = O(1)$ and $\bar{c}_a = O(1)$, is caused by the interfacial temperature gradient τ. Since $T_i \approx T_s$ (156), where T_s is a function of p_v and hence c_a, the flow is effectively controlled by the concentration profile at the interface. In this Section the temperature, velocity distribution, as well as the phase change mass flux and concentration distribution along the interface are discussed in more detail.

5.2.1 The Temperature and Velocity Profiles

First, consider the interfacial temperature T_i. Fig. 43(a) shows interfacial temperature profiles for different $\bar{c}_a$ (and fixed $\Delta T = 10$ K). In all cases, the most significant feature is that T_i varies essentially linearly with distance across almost the entire interface, with significant deviations from linearity only near the end walls (i.e., in the regions where thermal boundary layers form in the liquid). At intermediate values of $\bar{c}_a$, the interfacial temperature gradient τ outside the boundary layers can be considered to be constant (cf. Fig. 43(b)). For $\bar{c}_a \gtrsim 0.85$, the temperature profile oscillates sinusoidally about the average value $\bar{\tau}$ with

a period set by the wavelength λ of the convective pattern. For $\bar{c}_a \lesssim 0.08$, on the other hand, the gradient τ slowly (and monotonically) decreases with x.

At atmospheric pressure, $\bar{\tau}$ is comparable to the imposed temperature gradient $\Delta T/L$. However, as the concentration of air decreases, $\bar{\tau}$ also decreases and in the absence of air ($\bar{c}_a = 0$), the interfacial temperature becomes essentially constant, with $\bar{\tau}$ decreasing by three orders of magnitude, compared with the values found at atmospheric conditions at
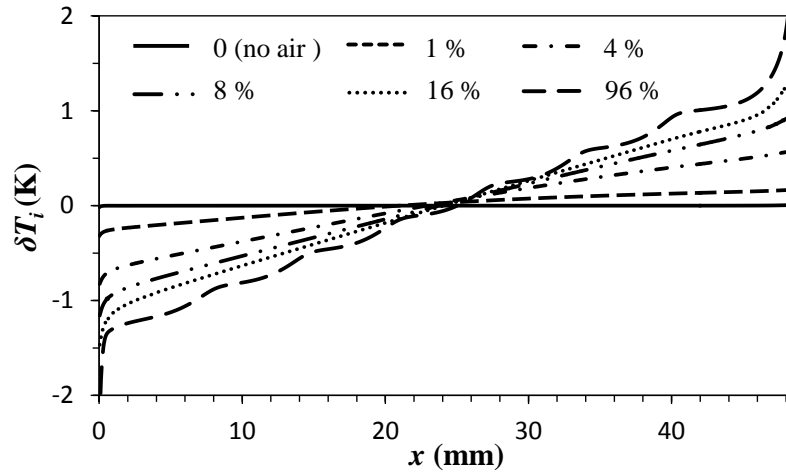
(a)
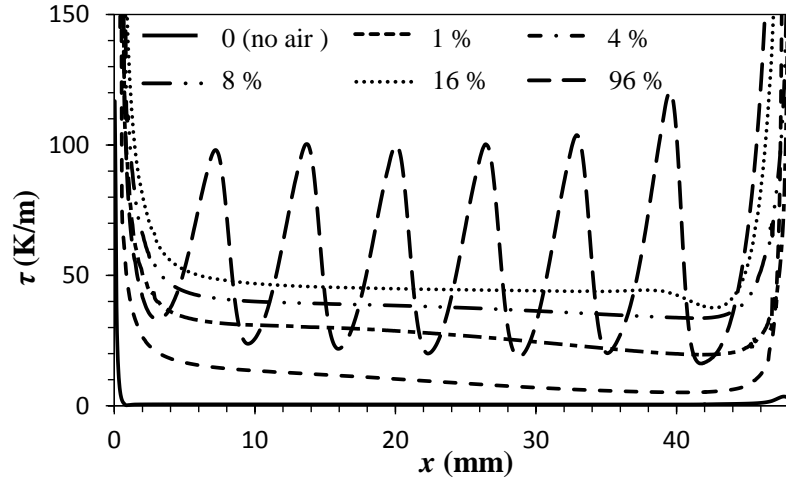
(b)

Figure 43: Interfacial temperature profile (a) and the interfacial temperature gradient $\tau = \partial_x T_i$ (b) for different average concentrations of air $\bar{c}_a$ and $\Delta T = 10$ K. To amplify the variation of T_i in the central region of the cavity, the variation $\delta T_i = T_i - \langle T_i \rangle_x$ about the average is plotted in (a) and the y-axis is truncated in both panels.

the same ΔT (cf. Chapter 5). The relation between τ and c_a will be discussed in more detail at the end of this Section.

The interfacial velocity profiles u_i for different $\bar{c}_a$ are shown in Fig. 44 and can be interpreted with the help of the analytical solution (113) for a steady return flow in an unbounded liquid layer driven by a constant temperature gradient $\bar{\tau}$. The relative strength of buoyancy and thermocapillarity is described by the ratio of u_B and u_T (153). These two forces are of equal strength, $u_T = u_B$, at the critical air concentration $\bar{c}_a^{(1)}$ such that $\bar{\tau}(\bar{c}_a^{(1)}) = \tau^*$, where

$$\tau^* = \frac{Bo_D}{12}\frac{\Delta T}{L}. \tag{160}$$

Based on the numerical results at $\Delta T = 10$ K and $Bo_D = 0.67$, $0.01 < \bar{c}_a^{(1)} < 0.02$.

When $\bar{c}_a > \bar{c}_a^{(1)}$ the flow is driven mainly by thermocapillarity and the analytical solution (113) accurately describes the velocity field in the SUF regime. In this limit the interfacial flow velocity is determined by the interfacial temperature gradient, $u_i \approx u_T \propto \tau$, even locally, as long as τ varies slowly with x. In particular, u_i exhibits spatial modulation reflecting spatial modulation in τ at higher $\bar{c}_a$, when the flow is in the PMC or SMC regime. As Fig. 43(b) shows, $\bar{\tau}$ changes relatively little as $\bar{c}_a$ decreases from 0.96 to 0.16 and its magnitude remains comparable to (about a quarter of) $\Delta T/L$. Correspondingly, the average
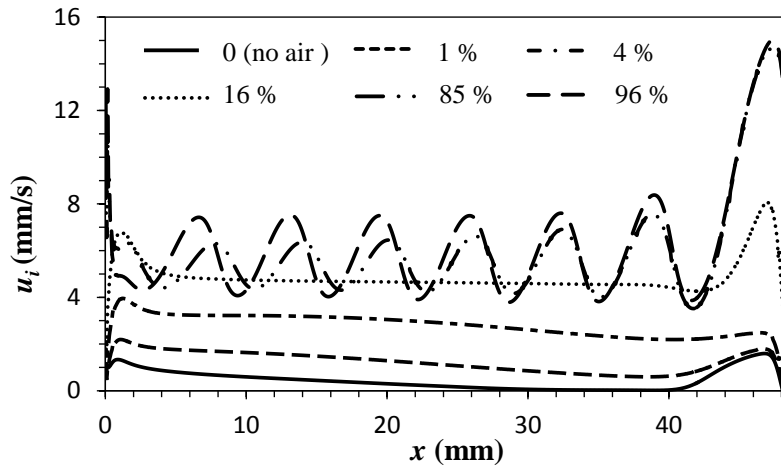
Figure 44: Interfacial velocity for different average concentrations of air $\bar{c}_a$ and $\Delta T = 10$ K.

flow velocity remains essentially independent of $\bar{c}_a$ in this range of concentrations, as Fig. 44 illustrates. This explains the puzzling experimental observation [1] that the interfacial velocity remains almost unchanged across much of the interface when the concentration of air decreases from 0.96 to 0.14. In fact, the numerical simulations show that the interfacial velocity a few mm away from the cold end wall even increases slightly as $\bar{c}_a$ decreases from 0.96 to around 0.16, which is also in agreement with experimental observations.

For $\bar{c}_a < \bar{c}_a^{(1)}$, the buoyancy force becomes dominant, the analytical solution (113) breaks down completely, and the flow field is described by two large convection rolls driven by buoyancy, with pronounced maxima near the two end walls. The flow in this limit is *quantitatively* similar to that found under pure vapor (cf. Fig. 29) and should correspond to the limit of infinite Bo_D at atmospheric conditions (when buoyancy again dominates over thermocapillarity). Hence, the effect of reducing $\bar{c}_a$ from the atmospheric value 0.96 to that corresponding to pure vapor ($\bar{c}_a = 0$) is analogous to increasing the dynamic Bond number from its reference value to infinity.

5.2.2 Mass Flux Due to Phase Change

While the concentration of noncondensables affects the velocity profile only indirectly, it has a direct, and rather dramatic, effect on the phase change at the interface. The mass
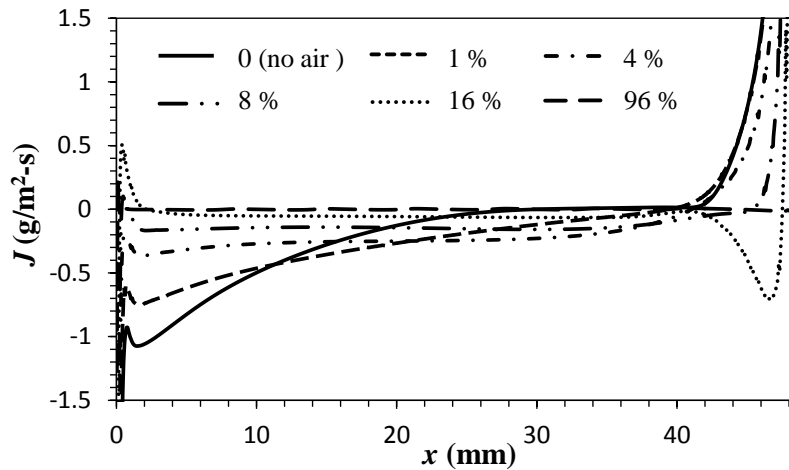
Figure 45: Mass flux due to phase change at the interface at different average concentrations of air and $\Delta T = 10$ K, with truncated y-axis.

flux distribution along the interface, which characterizes the intensity of phase change, is shown in Fig. 45. At atmospheric conditions ($\bar{c}_a = 0.96$), phase change is negligible over almost the entire interface, as transport of the vapor away from, or towards, the interface is severely restricted by diffusion through air. The phase change is only non-negligible very near the contact lines, with the liquid evaporating near the hot end wall ($J > 0$) and the vapor condensing near the cold end wall ($J < 0$).

As expected, decreasing the air concentration enhances phase change near the end walls. However, the phase change (based on mass flux J) is significant along the entire interface for $\bar{c}_a \lesssim 0.16$. In particular, at $\bar{c}_a = 0.16$ there is a wide region near the hot end wall where $J < 0$ (i.e., the vapor condenses) and a narrower region with $J > 0$ (i.e., the liquid evaporates) near the cold end wall. This somewhat paradoxical result is due to advection, as discussed earlier in Chapter 3.

As the concentration of air is reduced further, the region of condensation expands and eventually (for $\bar{c}_a \lesssim 0.04$) extends to cover about 80% of the entire interface. Although the maximum values of J are still found next to the end walls (phase change is most intense in the contact line regions at all $\bar{c}_a$), phase change along the rest of the liquid-vapor interface becomes non-negligible. As $\bar{c}_a \to 0$, the mass flux J smoothly approaches the profile found in the limit of pure vapor. Similarly, the fluid flow and temperature fields in both the bulk and at the interface smoothly approach those for pure vapor (cf. Chapter 4).

The results for low $\bar{c}_a$ have serious implications for modeling heat pipes, which typically assume that phase change takes place only in the "evaporator" and the "condenser" regions, which are separated by a large "adiabatic" section where phase change is negligible and the temperature profile is linear [61, 189, 190]. Although the liquid flow in this model is not representative of heat pipes (see Section 5.3 for an in-depth discussion), the temperature profile and the flow in the gas phase is, so these numerical results should still be relevant to heat pipes. In practice, noncondensables are mostly evacuated from heat pipes to enhance phase change and the associated latent heat flux. The above results suggest, however, that

in this limit there is no "adiabatic" region, since the temperature profile is not linear, and phase change is non-negligible, away from the heated/cooled end walls. The models of heat pipes which ignore phase change in the "adiabatic" region appear to be based on results from experiments performed under atmospheric conditions; hence, these results are unlikely to provide an accurate description of heat and mass flow at reduced pressures.

Quantifying the net amount of phase change (and the associated latent heat) requires some care as J is not a monotonic function of x for all $\bar{c}_a$. For instance, at higher $\bar{c}_a$ some of the evaporation (condensation) near the hot (cold) end wall is offset by the condensation (evaporation) just a few mm away. At lower $\bar{c}_a$ phase change is not even localized near the end walls. To account for the non-monotonic nature of $J(x)$, the characteristic mass flux J_v (across a vertical cross-section of the cavity) will be used, which is chosen as the maximum

$$J_v = \max_x I(x) \qquad (161)$$

of the (properly normalized) net mass flux $I(x)$ along a portion of the interface between 0 and x,

$$I(x) = \frac{1}{d_g} \left| \int_0^x J \sqrt{1 + (dz/dx)^2}\, dx \right|, \qquad (162)$$

where $I(L) = 0$ in steady state due to mass conservation.

If phase change occurs for the most part in the contact line regions, $I(x)$ should be essentially constant over the entire "adiabatic" region and the mass flux of vapor across
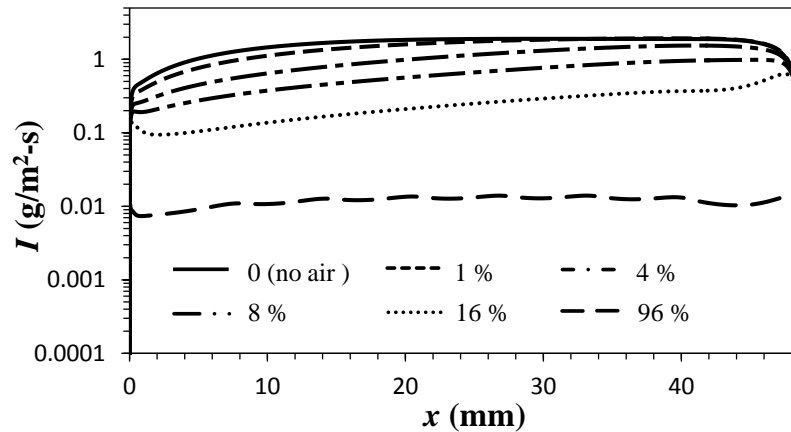
Figure 46: Integrated mass flux I at different average concentrations of air and $\Delta T = 10$ K.

any vertical cross-section in that region would be equal to J_v. As Fig. 46 shows, $I(x)$ varies most rapidly near the contact lines where phase change is most intense for all $\bar{c}_a$. For $\bar{c}_a = 0.96$, aside from some weak modulation due to convection rolls, $I(x)$ is indeed essentially constant across most of the interface. However, for $\bar{c}_a \lesssim 0.16$, I varies significantly (by almost an order of magnitude) outside of the contact line regions, and so the "adiabatic" region disappears at reduced noncondensables concentrations.

The characteristic mass flux J_v is shown as a function of the average concentration of noncondensables in Fig. 47. As expected, J_v is a monotonically decreasing function of $\bar{c}_a$ (i.e., noncondensables do suppress phase change). J_v does not vary noticeably for $\bar{c}_a$ below about 1%, which suggests that noncondensables essentially do not impede the flow of vapor once $\bar{c}_a$ is below some critical value. Increasing $\bar{c}_a$ to about 0.08 (which corresponds to 1.5% mass fraction of air) halves J_v, compared with the pure vapor case, at which point the adverse role of noncondensables is evident, as they significantly reduce the phase change and the latent heat contribution to the heat flux. For reference, for filmwise condensation of steam, the condensation rate is halved at an air mass fraction of 0.5% [109]. At ambient conditions J_v decreases by more than two orders of magnitude compared with the pure vapor case, which illustrates the kind of improvement in the heat flux that can be achieved by evacuating noncondensables from heat pipes and other similar passive thermal management devices.

5.2.3 The Concentration Profile

The relative role of advection and diffusion to mass transport in the gas layer is defined by the mass Péclet number

$$Pe_m = \frac{u_g l_g}{D},\tag{163}$$

where $l_g = d_g$ is the relevant length scale and the characteristic velocity u_g is determined by the interfacial velocity (113) at high $\bar{c}_a$, and by the mass flux $\mathbf{J}_v \approx \rho_v \mathbf{u}_g$ instead at low $\bar{c}_a$. Since $D \propto 1/p_g \propto 1 - \bar{c}_a$, while u_g does not vary significantly with $\bar{c}_a$, the Péclet

number is largest at atmospheric conditions and quickly decreases as $\bar{c}_a$ is reduced (cf. Appendix A). As illustrated by the concentration fields in Fig. 41, advection dominates at atmospheric conditions. However, for $\bar{c}_a \lesssim 0.85$, Pe_m becomes less than unity, and mass diffusion becomes the dominant tranport mechanism. In this range of $\bar{c}_a$, the concentration (and hence density) gradient in the central portion of the cavity is nearly horizontal due to the large aspect ratio of the gas layer, so vapor flux from the hot side to the cold side can be considered essentially one-dimensional. Hence, the variation of the mass flux with both x and z direction in the central portion of the cavity can be ignored, yielding

$$\mathbf{J}(x, z) \approx -J_v \hat{\mathbf{x}}, \tag{164}$$

where

$$J_v \approx \frac{1}{\bar{c}_a} D \partial_x \rho_v = \frac{D}{\bar{c}_a \bar{R}_v T} \partial_x p_v, \tag{165}$$

in agreement with the well-known result for condensation of vapor on a cold surface [96]. J_v can be related to the average interfacial temperature gradient $\bar{\tau}$ using the Clausius-Clapeyron equation and the fact that the interfacial temperature is essentially equal to the saturation temperature:

$$J_v \approx \frac{1 - \bar{c}_a}{\bar{c}_a} \frac{\mathcal{L} D p_g}{\bar{R}_v^2 T_0^3} \bar{\tau} = \frac{1 - \bar{c}_a}{\bar{c}_a} G_1 \frac{k_l}{\mathcal{L}} \bar{\tau}. \tag{166}$$
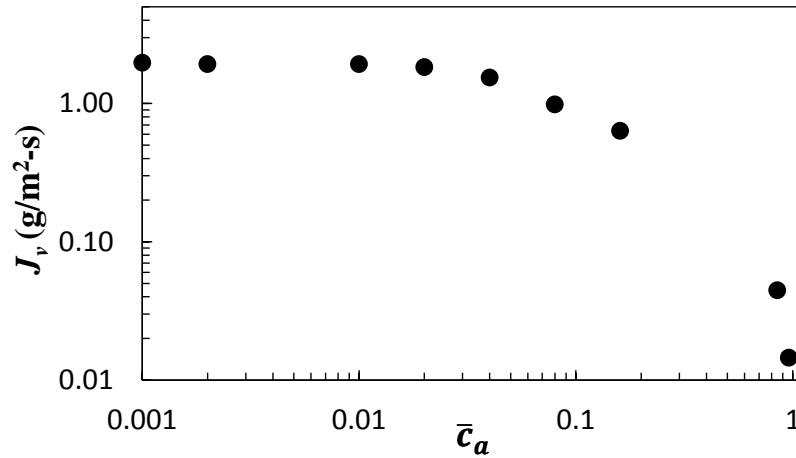
Figure 47: Characteristic mass flux J_v as a function of the average concentration of air at $\Delta T = 10$ K.

Note that, according to (32), the product Dp_g is independent of p_g (and hence $\bar{c}_a$), while $|T - T_0| \ll T_0$, so the combination

$$\xi = \frac{\bar{R}_v T_0}{D p_g} \tag{167}$$

is only a function of T_0 and can be considered a constant which has the same value in all the cases considered in this study. Since the total pressure $p_g = p_a + p_v$ is essentially constant, (165) can be rewritten as

$$\xi J_v p_a \approx \partial_x p_v = -\partial_x p_a, \tag{168}$$

integration of which yields the spatial profile of the partial pressure of noncondensables at the interface

$$p_a \approx \frac{\bar{c}_a}{1 - \bar{c}_a} \frac{\xi J_v L}{1 - e^{-\xi J_v L}} p_v^0 e^{-\xi J_v x}, \tag{169}$$

where p_v^0 is the saturation pressure of vapor at T_0. And since $p_a/c_a = p_g = p_v^0/(1 - \bar{c}_a)$, the concentration of noncondensables is given by

$$c_a \approx \bar{c}_a \frac{\xi J_v L}{1 - e^{-\xi J_v L}} e^{-\xi J_v x}. \tag{170}$$

The nonlinear profile of $c_a(x)$ reflects the accumulation of noncondensables near the cold end wall when $\xi J_v L \gtrsim 1$ (at low $\bar{c}_a$). As the combination $\xi J_v L$ decreases below unity (at high $\bar{c}_a$), the concentration profile becomes linear:

$$c_a \approx \bar{c}_a \left[1 + \xi J_v \left(\frac{L}{2} - x \right) \right]. \tag{171}$$

The transition from a linear to an exponential profile should occur when $\xi J_v(\bar{c}_a) L \approx 1$, which corresponds to the critical concentration $\bar{c}_a^{(2)}$ close to 0.08 for the system considered here. The numerical results for the (normalized) air concentration at the interface are in very good agreement with the analytical prediction (170), as shown in Fig. 48. The concentration of air indeed has an exponential profile for $\bar{c}_a \leq 0.08$, with the maximum at the cold end wall, $x = 0$. For $\bar{c}_a \geq 0.16$, however, the concentration profile becomes essentially linear in x both along the interface and in the bulk.

It should be pointed out that the derivation of the concentration profile (170) does not hold at near-atmospheric conditions, where advection is nonnegligible and, as a result, c_a depends on both x and z coordinates. However, in this limit the vapor concentration profile $c_v = 1 - c_a$ can be computed analytically in the SUF regime (cf. Eq. (128)). In particular, at the interface one again finds a linear concentration profile (130), so (170) in fact holds in the entire range of $\bar{c}_a$. (For consistency, it should also be noted that $x = 0$ is redefined to occur in the middle of the cavity when deriving (128) and (130).)

Since the interfacial temperature gradient τ is related to the interfacial concentration gradient $\varsigma = -\partial_x c_a$ locally via (129), for $\bar{c}_a \gtrsim \bar{c}_a^{(2)}$

$$\tau(x) \approx \bar{\tau} = \frac{\bar{c}_a}{1 - \bar{c}_a} \upsilon T_0 \xi J_v, \tag{172}$$

i.e., τ should become independent of x. For $\bar{c}_a \lesssim \bar{c}_a^{(2)}$ the τ-profile should become exponential according to (170):

$$\frac{\tau}{\bar{\tau}} \approx \frac{c_a}{\bar{c}_a} \approx \frac{\xi J_v L}{1 - e^{-\xi J_v L}} e^{-\xi J_v x}. \tag{173}$$

Both predictions are in agreement with the numerical results shown in Fig. 43(b) in the SUF regime away from the end walls (i.e., when and where the vapor flow is essentially
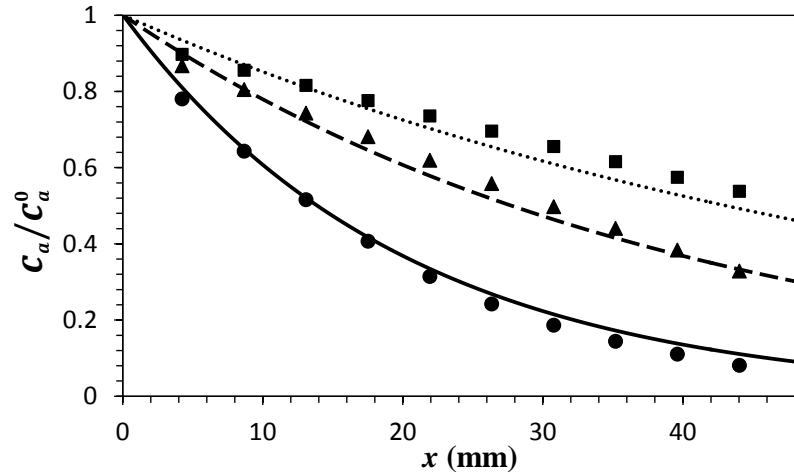
Figure 48: Normalized air concentration at different average concentrations of air $\bar{c}_a$ and $\Delta T = 10$ K. Numerical and analytical results are represented by symbols and lines, respectively: $\bar{c}_a = 0.001$ (● and solid line), $\bar{c}_a = 0.08$ (▲ and dash line) and $\bar{c}_a = 0.16$ (■ and dot line).

one-dimensional, so the above simplified description applies).

When $\bar{c}_a = \bar{c}_a^{(2)}$, the characteristic length scale on which the concentration gradient varies coincides with the length L of the cavity. Therefore this critical concentration also determines the transition between different scaling behaviors of J_v and $\bar{\tau}$ with $\bar{c}_a$. For $\bar{c}_a > \bar{c}_a^{(2)}$, the mass flux of vapor is constrained mainly by the diffusion of vapor through the air, so that J_v increases as $\bar{c}_a$ decreases, while $\bar{\tau}$ remains approximately constant. For $\bar{c}_a < \bar{c}_a^{(2)}$, phase change is not significantly impeded by the noncondensables, so J_v is instead constrained by heat conduction through the liquid layer (see Section 5.3.1 for an in-depth discussion) and hence becomes essentially independent of $\bar{c}_a$ (cf. Fig. 47), while $\bar{\tau}$ becomes proportional to $\bar{c}_a$ according to (166). This is consistent with the main conclusion of Chapter 4 that thermocapillary stresses essentially disappear when noncondensables are completely removed.

The numerical results for the interfacial temperature gradient $\bar{\tau}$ over a wide range of ΔT can be reasonably well approximated by the empirical correlation

$$\frac{\bar{\tau}(\bar{c}_a)}{\bar{\tau}(\bar{c}_a^a)} \equiv R_{\bar{\tau}}(\bar{c}_a) = \left(a_c \bar{c}_a^{-1} + b_c\right)^{-1}, \tag{174}$$
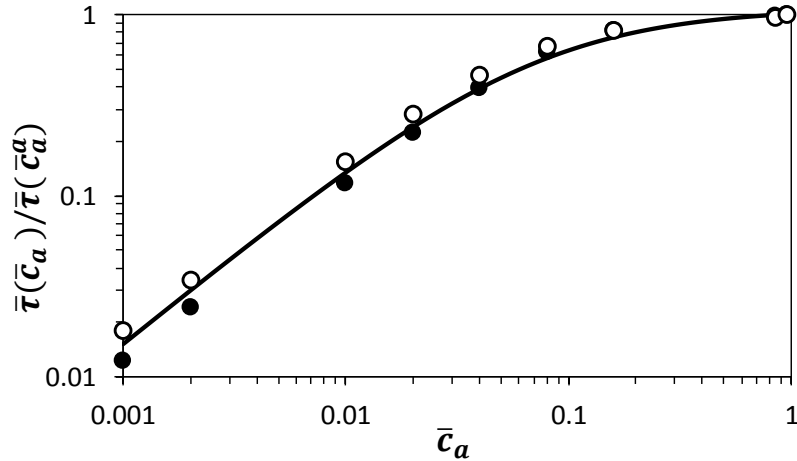
Figure 49: The dependence of the average temperature gradient $\bar{\tau}$ on the average concentrations of air $\bar{c}_a$. The temperature gradient has been normalized by its value at the average concentration of air $\bar{c}_a^a$ at atmospheric conditions. Filled and open circles show the numerical results at $\Delta T = 4$ K and $\Delta T = 10$ K, respectively. Solid line represents the fitting function (174), where $R^2 = 0.9928$

where $a_c = 0.065$ and $b_c = 0.921$ are the fitting parameters and $\bar{c}_a^a = 0.96$ is the average concentration of air at atmospheric conditions (cf. Fig. 49). For $Bo_D = 0.67$, the predicted critical concentration $\bar{c}_a^{(2)} = a_c/b_c \approx 0.07$ agrees with the numerical results, as $\bar{c}_a^{(2)}$ corresponds to the cross-over in the scaling of both the mass flux J_v (cf. Fig. 47) and the temperature gradient $\bar{\tau}$ (cf. Fig. 49). It is also supported by the experimental results of Li *et al.* [1] which show that $\bar{\tau}$ remains almost independent of $\bar{c}_a$ for $\bar{c}_a \gtrsim 0.14$.

The relation (174) can be used to determine the threshold values of the air concentration that define transitions between the flow regimes at a fixed ΔT. For instance, combining (174) and (160) yields the concentration

$$\bar{c}_a^{(1)} = a_c \left[\bar{\tau}(\bar{c}_a^a) \left(\frac{Bo_D}{12} \frac{\Delta T}{L} \right)^{-1} - b_c \right]^{-1} \tag{175}$$

where thermocapillarity and buoyancy are of equal importance. For $\Delta T = 10$ K and $Bo_D = 0.67$, $\bar{c}_a^{(1)} \approx 0.016$, which is consistent with the numerical results reported in Section 5.2.1.

5.3 Mass and Heat Fluxes

In this section, the simplified analytical model developed above is used to describe the effect of the liquid layer thickness on the mass and heat flux in confined two-phase flows as well as predict the performance of simple thermal management devices. For a sealed cavity, the net steady-state mass flux of liquid and vapor along the direction of the applied temperature gradient is zero. However, the characteristic mass flow rate in the gas layer $\dot{m}_v$ and the liquid layer $\dot{m}_l$ can vary significantly depending upon the flow conditions. The intensity of phase change can therefore be characterized by the ratio $\dot{m}_v/\dot{m}_l$.

5.3.1 Mass Flux of Vapor

At relatively high $\bar{c}_a$, phase change is constrained mainly by diffusion of vapor from the hot to the cold side of the cavity. The mass flux of vapor J_v is given by (166), so the corresponding mass flow rate can be found by integrating J_v across a vertical cross section

of the gas layer:

$$\dot{m}_v = Wd_gJ_v = \frac{1 - \bar{c}_a}{\bar{c}_a}\frac{Wk_lG_1}{\mathcal{L}}\bar{\tau}d_g, \tag{176}$$

where W is the width of the cavity (cf. Fig. 4). Since $\dot{m}_v \propto J_v$, its dependence on $\bar{c}_a$ can be determined from the data shown in Fig. 47. In particular, since $\bar{\tau}$ is essentially constant for relatively high values of $\bar{c}_a$, (176) gives $\dot{m}_v \propto (1 - \bar{c}_a)/\bar{c}_a$, so the mass flux increases monotonically as $\bar{c}_a$ decreases.

At small $\bar{c}_a$ (more precisely, for $\bar{c}_a < \bar{c}_a^{(2)}$), which is the limit at which two-phase cooling devices typically operate, $\bar{\tau} \propto \bar{c}_a$ according to (173), so $\dot{m}_v$ approaches a constant value, $\dot{m}_v^0$. In this limit phase change is not impeded by the noncondensables, but is constrained by heat conduction, so we can use the estimate (140) to determine $\dot{m}_v^0$. The mass flow rate of vapor can be obtained by integrating the mass flux J over the portion of the interface (of area $\sim Wd_l$) where most of the evaporation (or condensation) occurs, yielding an estimate

$$\dot{m}_v^0 \sim Wd_l\Delta J = \varphi_c \frac{Wk_l\Delta T}{\mathcal{L}}, \tag{177}$$

where φ_c is a geometrical coefficient that describes the heat conduction through the wedge of liquid bounded by the free surface and one of the end walls, and therefore depends on the contact angle. For the system considered in this study, $\varphi_c \approx 3$ at $\theta = 50°$ and $\Delta T = 10$ K. It should be emphasized that (177) is only an estimate, and should be used with care. For instance, since $\dot{m}_v \to \dot{m}_v^0$ in the limit $\bar{c}_a \to 0$, one finds that $\varphi_c \propto L\bar{\tau}/\Delta T$ which, strictly speaking, is not a constant and decreases by a factor of four when ΔT increases from 0 K to 10 K (cf. Fig. 10).

5.3.2 Thick Liquid Layers

The characteristic mass flow rate $\dot{m}_l$ in the liquid layer depends on the flow regime. In thicker layers featuring a return flow, $\dot{m}_l$ can be estimated by integrating the mass flux in the direction of the temperature gradient using the analytical solution (111) for the return base flow

$$\dot{m}_l = \rho_lW\int_{u_{l,x}>0}u_{l,x}dz \approx \left(\frac{1}{27} + \frac{5}{972}Bo_D\right)\alpha_l\rho_lMa_iW. \tag{178}$$

As discussed in Section 5.2.1, the analytical solution (111) and hence (178) for the mass flow rate in the liquid layer is only valid at $\bar{c}_a \geq \bar{c}_a^{(1)}$, when the flow is driven by both thermocapillarity and buoyancy.

Equations (177) and (178) can be used to find the upper limit for the ratio $\dot{m}_v/\dot{m}_l$, yielding

$$\frac{\dot{m}_v}{\dot{m}_l} \approx \varphi_c \left(\frac{1}{27} + \frac{5}{972} Bo_D \right)^{-1} \frac{Pr_l E}{Ma_i}, \tag{179}$$

where

$$E = \frac{k_l \Delta T}{\rho_l \nu_l \mathcal{L}} \tag{180}$$

is the evaporation number introduced by Burelbach $et\ al.$ [194] which defines the ratio of the evaporative time scale (i.e., how long it would take for a liquid layer to completely evaporate) to the viscous time scale. In this study $\dot{m}_v/\dot{m}_l \ll 1$ (for example, $\dot{m}_v/\dot{m}_l \approx 8 \times 10^{-3}$ at $\Delta T = 10$ K and $Bo_D = 0.67$), which means that the net flux is essentially zero even in the liquid layer, justifying the assumption of a return flow. This is consistent with the numerical results (cf. Fig. 6).

The heat flux between the hot and the cold end walls is due to conduction and advection through the liquid and the gas layers, as well as latent heat associated with phase change. The heat flow rate due to conduction is simply

$$Q^c \approx W(d_l k_l + d_g k_g)\bar{\tau} \propto \bar{\tau}. \tag{181}$$

Since $\dot{m}_v \ll \dot{m}_l$, the heat flow rate due to advection is confined almost entirely to the liquid layer

$$Q^a \approx W \frac{k_l}{\alpha_l} \int_0^{d_l} T_l u_{l,x} dz, \tag{182}$$

and depends on the flow regime. For a return flow in the SUF regime, Q^a can be estimated using the analytical solutions (112) and (111), giving

$$Q^a \approx A Ma_i^2 W d_l k_l \bar{\tau} \tag{183}$$

where

$$A = \frac{19Bo_D^2 + 252Bo_D + 864}{1451520}.$$ (184)

The heat flow rate due to phase change is related to the mass flow rate of vapor

$$Q^p = \dot{m}_v \mathcal{L}.$$ (185)

Since the estimate (183) is valid at $\bar{c}_a \gtrsim \bar{c}_a^{(1)}$ when the flow is driven by both thermocapillarity and buoyancy, the mass flow rate is given by (176), yielding

$$Q^p = W\frac{1 - \bar{c}_a}{\bar{c}_a}G_1 k_l d_g \bar{\tau}$$ (186)

The relative contributions of phase change and conduction to the heat transport are therefore given by the ratio

$$\frac{Q^p}{Q^c} = \frac{1 - \bar{c}_a}{\bar{c}_a}\frac{\tilde{d}_g k_l}{k_l + \tilde{d}_g k_g}G_1.$$ (187)

In this study, due to the relatively high latent heat and volatility of the silicone oil, the phase change contribution is non-negligible even at atmospheric conditions ($\bar{c}_a = 0.96$), where $Q^p/Q^c = 0.30$. The ratio quickly increases ($Q^p/Q^c \approx 1$ already at $\bar{c}_a = 0.88$), and phase change becomes the dominant heat transfer mechanism, as $\bar{c}_a$ decreases.

The relative contributions of phase change and advection to the heat transport are given by the ratio

$$\frac{Q^p}{Q^a} \approx \frac{1 - \bar{c}_a}{\bar{c}_a}\frac{G_1 \tilde{d}_g}{AMa_i^2}.$$ (188)

For liquid layers with fixed thickness d_l and fixed ΔT, this ratio becomes a function of the concentration of noncondensables $\bar{c}_a$. It is the largest at atmospheric conditions, when the flow speed is the largest, while phase change is greatly suppressed. As $\bar{c}_a$ decreases, the flow speed decreases, while phase change is enhanced, and so the contribution of phase change becomes more important. In this study, at $\Delta T = 10$ K and $d_l = 2.45$ mm, $Q^p/Q^a \approx 10^{-3}$ at atmospheric conditions, so advection dominates phase change. At $\bar{c}_a \approx 0.1$, $Q^p/Q^a \approx 1$, and phase change becomes the dominant heat transfer mechanism for $\bar{c}_a < 0.1$.

The relative contributions of phase change and advection also depend on ΔT and d_l. Although the dependence on the thickness of the liquid layer will be considered in Section 5.3.3, d_l is instead assumed to be constant here. When $\bar{c}_a$ is also constant, $Q^p/Q^a \propto \tau^{-2}$, so that advection dominates when ΔT is large, and phase change dominates when ΔT is small. We already know that phase change dominates at low $\bar{c}_a$ when $\bar{\tau}$ is also small, regardless of ΔT. Advection can dominate only at high $\bar{c}_a$. For instance, at atmospheric conditions and $d_l = 2.45$ mm, $Q^p/Q^a < 1$ when $\Delta T > 0.1$ K . To summarize, $Q^p \gg Q^c \gg Q^a$ for small $\bar{c}_a$. For large $\bar{c}_a$, the dominant heat transfer mechanism depends on the applied temperature difference: when ΔT is small, $Q^c > Q^p \gg Q^a$, while when ΔT is large, $Q^a \gg Q^c > Q^p$.

5.3.3 Thin Liquid Layers

The transport model for the gas layer that has been developed and validated in this chapter can be applied to modeling two-phase thermal management devices, such as heat pipes employing wicks or microchannels. To illustrate this, consider the limit $d_l \to 0$ of the two-layer system discussed previously. For $Bo_D \lesssim 1$, the second term in (179) can be neglected. Furthermore, $Ma_i \propto d_l^2$, so as the thickness of the liquid layer decreases, $\dot{m}_v/\dot{m}_l$ should rapidly increase (assuming $\Delta T/\bar{\tau}$ does not vary significantly with d_l). For instance, at $\Delta T = 10$ K the magnitudes of $\dot{m}_v$ and $\dot{m}_l$ become comparable when d_l decreases to about 0.2 mm. This, of course, is a fairly crude estimate, since (179) is based on the assumption of a return flow, which breaks down when $\dot{m}_v$ becomes comparable to $\dot{m}_l$. As d_l decreases further, capillary pressure becomes the dominant mechanism driving the flow in the liquid layer, (179) breaks down completely, and one should expect $\dot{m}_v \approx \dot{m}_l$ and the flow in both the liquid and the gas layer to become unidirectional. This limit is more relevant to the regime in which heat pipes operate.

The capillary pressure can be related to the interfacial temperature using the mass flux expression (53). Neglecting the left-hand-side yields

$$p_c = p_l - p_g = \rho_l \mathcal{L} \left| 1 - \frac{T_i}{T_s} \right|. \tag{189}$$

135

Since the gas pressure p_g is essentially constant in the (thick) vapor layer, the difference in the capillary pressure between the cold end and the hot end can be related to the temperature variation

$$\Delta p_c \approx \rho_l \mathcal{L} \frac{\Delta T_i}{T_s} \approx \rho_l \mathcal{L} \frac{\Delta T}{T_0}. \tag{190}$$

For a circular capillary of diameter d_l, the largest capillary pressure that can be produced by the meniscus at the hot end is $\kappa \sigma$, where the curvature is $\kappa = 2/(d_l/2)$. At the cold end, where condensate can completely flood the wick, the interface can be considered nearly flat, so that

$$\Delta p_c = 4 \frac{\sigma}{d_l}. \tag{191}$$

Equating (190) and (191) gives the critical diameter

$$d_l^c = \frac{4\sigma}{\rho_l \mathcal{L}} \frac{T_0}{\Delta T}. \tag{192}$$

For a typical $\Delta T = 10$ K, $d_l^c = 0.01$ μm $= 10$ nm. For $d_l < d_l^c$ the capillary pressure is given by (190), while for $d_l > d_l^c$, which is the usual case, the capillary pressure is given by (191).

Assuming the liquid flows through a single pore of length of L and uniform transverse dimension $d_l \ll L$, we can assume that the flow is fully developed. The mass flow rate in the liquid phase driven by the capillary pressure drop Δp_c is

$$\dot{m}_l^1 = \varphi_l \frac{d_l^4 \Delta p_c}{\nu_l L}, \tag{193}$$

where φ_l is a geometrical prefactor which describes the cross sectional shape of the pore (for instance, $\varphi_l = \pi/128$ for a pore with circular cross section). For a single layer of pores in the wick (note that the result can easily be generalized to an arbitrary number of layers), the number of pores, per width W of the cavity in the spanwise direction, is roughly W/d_l, so the net flux is

$$\dot{m}_l \approx \frac{W}{d_l} \dot{m}_l^1 = \varphi_l \frac{W d_l^3 \rho_l \mathcal{L}}{\nu_l L} \frac{\Delta T}{T_0} \tag{194}$$

when $d_l < d_l^c$, while for $d_l > d_l^c$

$$\dot{m}_l \approx 4\varphi_l \frac{W d_l^2 \sigma}{\nu_l L}. \tag{195}$$

136

Naively, one would expect that the same results, with a somewhat different $\varphi_l = O(1)$ will be obtained if the closed pores were replaced with open microchannels of width d_l, as is often the case in a micro heat pipe. However, since the microchannels are open, phase change will take place along the entire length of the device and, as our analysis of the convection problem showed, there will be no adiabatic region and the capillary force will be opposed by the thermocapillary stresses at the free surface. Furthermore, the temperature profile will be exponential, rather than linear, as is assumed in standard models of heat pipes. In the limit of highly conductive walls, the temperature difference between the two ends of the device is approximately ΔT, so (173) reduces to

$$\tau \approx \frac{\xi J_v \Delta T}{1 - e^{-\xi J_v L}} e^{-\xi J_v x} \tag{196}$$

with $\bar{\tau} \approx \Delta T / L$. As (196) shows, the highest temperature gradient

$$\tau_{\max} \approx \frac{1 - \bar{c}_a}{\bar{c}_a} \upsilon^{-1} \frac{\Delta T}{T_0} \frac{\Delta T}{L} \tag{197}$$

will develop near the cold end. The balance of thermocapillary and capillary forces for the liquid in the microchannel of width (and depth) d_l requires

$$d_l \gamma \tau = d_l^2 \frac{\Delta p_c}{L}. \tag{198}$$

Since $\tau_{\max} \propto \bar{c}_a^{-1}$, thermocapillary forces will overcome the capillary pressure near the cold end for $\bar{c}_a \lesssim \bar{c}_a^{(3)}$, where

$$\bar{c}_a^{(3)} = \frac{\gamma}{\upsilon \Delta p_c} \frac{\Delta T}{T_0} \frac{\Delta T}{d_l} \geq \frac{\gamma \Delta T}{4 \upsilon \sigma} \frac{\Delta T}{T_0}, \tag{199}$$

blocking the flow of coolant from the "condenser" back to the "evaporator". However, the critical concentration of noncondensables at which this happens is relatively low (e.g., $\bar{c}_a^{(3)} = 0.007$ at $\Delta T = 10$ K for HMDS). For $\bar{c}_a \gtrsim \bar{c}_a^{(3)}$ thermocapillarity can be ignored, so micro-heat pipes can be analyzed in the same way as macro-heat pipes with a wick.

In the limit of low $\bar{c}_a$ ($\bar{c}_a \leq \bar{c}_a^{(2)}$), the conditions at which two-phase cooling devices typically operate, the mass flow rate in the gas phase is constrained either by the heat

conduction through the liquid layer (177) or by the viscosity of the liquid flowing through the wick, yielding (194) or (195). Since $\dot{m}_l$ increases monotonically with d_l, another critical value d_l^h can be found by equating (177) and (195), which yields

$$d_l^h = \left(\frac{\varphi_c}{4\varphi_l} \frac{k_l \nu_l L \Delta T}{\mathcal{L}\sigma} \right)^{1/2}. \tag{200}$$

For a typical $\Delta T = 10$ K we find $d_l^h = 17.8$ μm, which is three orders of magnitude larger than d_l^c. The mass flow rate is controlled by conduction of heat through the liquid when $d_l > d_l^h$ (the solid green line in Fig. 50) and by the viscosity of the liquid flowing through the wick or microchannels when $d_l < d_l^h$ (the solid red line). In particular, assuming the pores of the wick have a constant cross section, d_l^h determines the smallest diameter yielding the maximal heat flux. The largest diameter is controlled by the hydrostatic pressure $\Delta p_g = \rho_l g L$. To ensure the flow in the wick does not depend on the orientation of $\mathbf{g}$, one should have $\Delta p_c \gg \Delta p_g$, so that

$$d_l \ll d_l^m = \frac{4\sigma}{\rho_l g L} = \frac{4 l_c^2}{L}. \tag{201}$$

For $L = 48.5$ mm, we find $d_l^m \approx 170$ μm.

In the limit of small d_l the heat flow rate due to conduction is given by (181) with $d_l = 0$. The heat flow rate due to phase change is given by (185), where the mass flow rate of vapor
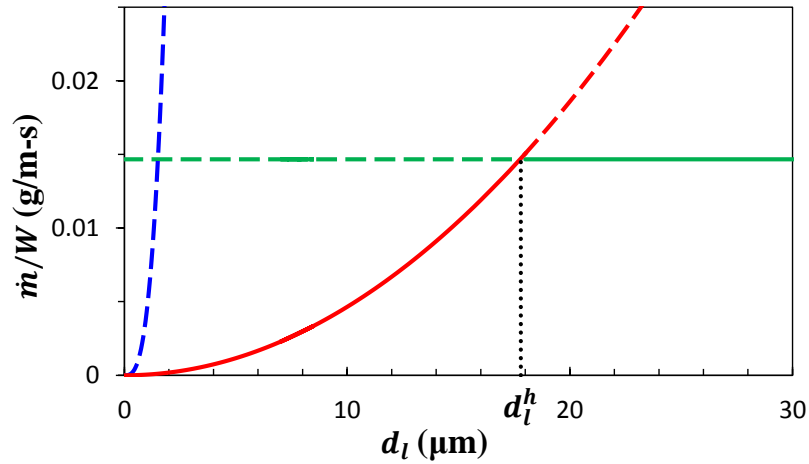
Figure 50: The dependence of the mass flow rate per unit width $\dot{m}/W$ on the pore diameter d_l at $\Delta T = 10$ K, $\varphi_c = 3$, and $\varphi_l = \pi/128$. The green, blue and red line represent the results predicted by (177), (194), and (195), respectively.

$\dot{m}_v = \dot{m}_l = \dot{m}$ can be estimated using (177) for $\bar{c}_a \lesssim \bar{c}_a^{(2)}$, yielding

$$Q^p = \dot{m}\mathcal{L} \sim W\varphi_c k_l \Delta T. \tag{202}$$

Since the liquid layer is very thin, and assuming the wick is made of a highly conductive material, $k_w \gg k_l$, the temperature profile in both the liquid and gas layer would be essentially the same, $T_l(x) \approx T_g(x)$, so the heat flow rate due to advection in both layers can be estimated as

$$Q^a \approx -\dot{m}\Delta C_p T_0, \tag{203}$$

where $\Delta C_p = C_{p,l} - C_{p,g}$ is the difference betweem the specific heat of the liquid and the gas (cf. Table 6). Since in general $\Delta C_p > 0$, advection actually carries heat in the reverse direction, from the cold end towards the hot end.

Finally, the heat conduction is negligible at low $\bar{c}_a$, so the net heat flow rate is given by

$$Q \approx Q^p + Q^a = \dot{m}[\mathcal{L} - \Delta C_p T_0]. \tag{204}$$

For the liquid considered here

$$\left|\frac{Q^a}{Q^p}\right| = \frac{\Delta C_p T_0}{\mathcal{L}} = 0.57, \tag{205}$$

so Q^a and Q^p are quite comparable and, therefore, the difference between $C_{p,l}$ and $C_{p,g}$ substantially reduces the heat flux due to phase change. In comparison, for water $|Q^a/Q^p| = 0.25$, so the difference in the heat capacities of the two phases has a substantially smaller effect.

We can thus obtain the theoretical maximum heat transfer coefficient for a heat pipe (with microchannels of uniform cross-section or with a wick featuring pores with a uniform diameter)

$$h = \frac{Q}{Wd_g\Delta T} \approx \varphi_c \frac{k_l}{d_g}\left[1 - \frac{\Delta C_p T_0}{\mathcal{L}}\right], \tag{206}$$

which is limited by the practical minimum value of d_g. As d_g decreases, the pressure drop Δp_g across the gas layer increases. This pressure drop is related to $\dot{m}$ via a relation similar

to (193):

$$\dot{m} = \varphi_g \frac{W d_g^3 \Delta p_g}{v_g L}, \tag{207}$$

where $\varphi_g = O(1)$ is a geometric factor describing the cross-section of the cavity through which the gas flows. We should have $\Delta p_g \ll \Delta p_c$ which, assuming $\varphi_g \approx \varphi_l$, requires

$$\frac{d_g^3}{d_l^3} \gg \frac{v_g}{v_l}. \tag{208}$$

Taking, for instance, $d_g = 2(v_g/v_l)^{1/3} d_l$, we find

$$h \approx \frac{\varphi_c}{2} \left(\frac{v_l}{v_g} \right)^{1/3} \frac{k_l}{d_l} \left[1 - \frac{\Delta C_p T_0}{\mathcal{L}} \right], \tag{209}$$

with the maximum achieved at $d_l = d_l^h$. Interestingly, even though phase change is the dominant heat transfer mechanism, the heat transfer coefficient for a given d_l turns out to be controlled primarily by the thermal conductivity k_l, vs. the latent heat $\mathcal{L}$, of the working liquid. In particular, for the silicone oil considered here, $h \approx 1.2 \times 10^3$ W/(m^{2}K). For water (with the same $d_l = d_l^h = 17.8$ μm) one finds a higher value $h \approx 4.5 \times 10^3$ W/(m^{2}K). For reference, the corresponding value for solid copper of the same thickness L is 8×10^3 W/(m^{2}K). Moreover, Mozumder *et al.* [201] found $h \approx 4 \times 10^3$ W/(m^{2}K) for a miniature heat pipe with 5 mm diameter and 150 mm length, with water as a working fluid. The result (209) also does not explicitly depend on the length L of the cavity, although it does depend on the pore diameter d_l the minimal value of which does depend on both L and the latent heat $\mathcal{L}$ through (200). The heat transfer coefficient can also be increased significantly by making the pore cross-section nonuniform, but a detailed discussion of this is beyond the scope of this thesis.

5.4 Discussion

By investigating buoyancy-thermocapillary convections while varying the average concentration of noncondensables (air) in the gas phase from that corresponding to ambient conditions to zero, when the gas phase becomes a pure vapor, it was found that the (average)

composition of the gas phase has a crucial impact on the fluid flow and the transport of heat and mass. The numerical results show that as the average concentration $\bar{c}_a$ of air decreases from $\bar{c}_a^a = 0.96$ to $\bar{c}_a^{(2)} \approx 0.07$, the interfacial temperature gradient $\bar{\tau}$ remains almost constant, hence the thermocapillary stresses and the average flow speed remain essentially the same. These numerical results are consistent with the experimental observations of Li *et al.* [1]. On the other hand, as $\bar{c}_a$ decreases below $\bar{c}_a^{(1)} \approx 0.016$, the interfacial temperature gradient and the associated thermocapillary stresses essentially vanish, and the flow again becomes independent of the concentration of noncondensables, according to the numerics. Such low concentrations are not easily accessible in experiment, so no comparison can be made in this limit.

In order to understand these results, a simplified analytical model of the gas layer was developed by assuming the mass transport of the vapor through the gas is essentially one-dimensional (along the direction of the applied temperature difference) and diffusion-dominated. In this approximation, the concentration profile $c_a(\mathbf{x})$ can be computed analytically as a function of the characteristic mass flux J_v of vapor, with the analytical prediction showing good agreement with numerical results in the entire range of $\bar{c}_a$ and for all ΔT at which the flow is in the SUF regime. This simplified model helps untangle the interdependence of the fluid flow, temperature, and concentration fields inherent in the full two-sided model presented in Chapter 2. Specifically, it is found that the concentration profile that is set up by the mass transport in the gas phase determines the interfacial temperature profile which, in turn, determines the interfacial velocity profile and the flow fields in both the liquid and the gas layer.

Unlike the full two-sided model which can only be solved numerically, the simplified transport model makes analytical prediction feasible. In particular, it predicts that $\bar{\tau}$ exhibits different scaling behavior with $\bar{c}_a$, with different ranges of $\bar{c}_a$. When the average air concentration is relatively high, $\bar{c}_a \gtrsim \bar{c}_a^{(2)}$, the vapor mass flux J_v is constrained by the diffusion of vapor through the gas phase, and the interfacial temperature profile is predicted

to be linear, with slope $\bar{\tau}$ weakly dependent on $\bar{c}_a$. When $\bar{c}_a \lesssim \bar{c}_a^{(2)}$, the mass flux J_v is constrained by the heat conduction through the liquid layer and becomes weakly dependent on $\bar{c}_a$. In this limit, the temperature profile is predicted to be exponential, with the average slope $\bar{\tau} \propto \bar{c}_a$. Consequently, thermocapillary stresses decrease significantly as $\bar{c}_a$ decreases, leading to the decrease in the flow speed and noticeable change in the base flow profile. For $\bar{c}_a \lesssim \bar{c}_a^{(1)}$ thermocapillary stresses become negligible, the flow is driven primarily by the buoyancy force which is $\bar{c}_a$-independent, and the flow profile changes substantially.

Unlike the base flow itself, the stability of the flow is strongly affected by the presence of noncondensables, regardless of their concentration. As $\bar{c}_a$ decreases, the flow stability is enhanced, with critical Marangoni numbers for transitions between different flow regimes increasing rather significantly. In fact, at sufficiently low $\bar{c}_a$ flow transitions disappear completely, with steady unicellular flow observed for all applied temperature gradients studied here. While numerical simulations describe the change in flow stability, they do not explain what drives this change. Hence, in order to better understand the flow stability, a linear stability analysis of the problem was performed which includes the effect of heat and mass transport in the gas layer, as well as the phase change at the interface. The results will be presented in the next Chapter.

Although the flow in the relatively thick liquid layer investigated in this study is quite different from the liquid flows typical in thermal management applications, the transport of heat and mass through the gas layer and across the interface are nevertheless quite similar. Therefore, the transport model for the gas phase can be extended to two-phase evaporative cooling devices such as heat pipes that employ wicks or microchannels of various geometries. As shown in this Chapter, the mass flow rate $\dot{m}_v$ of vapor in the heat pipe is constrained by either (rarely) the viscosity of the liquid flowing through the wick (or microchannels) or (much more commonly) by the heat conduction through the liquid layer. By comparing different constraints on $\dot{m}_v$, the optimal value for the size of a pore in the wick (or the diameter of a microchannel) can be calculated analytically. The optimal pore/microchannel

size was found to depend on the properties of the fluid, the geometry of the flow, and the imposed temperature difference.

The transport model for the gas phase shows that while heat pipes employing wicks with closed pores can be treated by partitioning them into "evaporator," "condenser," and "adiabatic" sections, for heat pipes employing microchannels such a partition is invalid. In particular, the model predicts that while lowering the concentration of noncondensables suppresses thermocapillary stresses over most of the free surface, these stresses are actually enhanced near the cold end. In particular, for $\bar{c}_a < \bar{c}_a^{(3)}$ thermocapillary stresses are predicted to block the flow of coolant out of the *condenser*. This is notably different from film dry-out, which has been predicted to occur in the *evaporator* at higher $\bar{c}_a$.

The model also allows an analytical calculation of the heat flow rate. Heat pipes operate optimally in the limit $\bar{c}_a \lesssim \bar{c}_a^{(2)}$, where $\dot{m}_v$ is heat conduction-limited. In this limit the heat transport is dominated by advection and the latent heat associated with phase change at the liquid-vapor interface. While phase change transfers the heat from the hot end towards the cold end, advection in general transfers the heat in the opposite direction. The model shows that the ratio Q^a/Q^p of the two contributions to the heat flux is proportional to the ratio of the difference ΔC_p between the heat capacity of the working fluid in its liquid and vapor form to the latent heat $\mathcal{L}$. When the product $\Delta C_p T_0$ is comparable to $\mathcal{L}$, advection has a strong adverse effect on thermal performance, a fact that appears to have been strongly under-appreciated to date.

The thermal performance of a particular heat pipe can be conveniently described using the heat transfer coefficient, which can also be computed analytically using the simplified model of the two phases. The analytical expression for the heat transfer coefficient provides a simple way both for evaluating different heat pipe designs and for choosing an optimal working fluid. Surprisingly, it was found that while the optimal pore size depends on multiple material parameters of the working fluid (its thermal conductivity, latent heat, viscosity, and surface tension), the heat transfer coefficient is controlled primarily by the ratio of

thermal conductivity of the liquid to the pore size. The concentration of noncondensables appears to have a minor effect on the thermal performance below $\bar{c}_a^{(2)}$ (i.e., below 7% for HMDS), although for water noncondensables have been predicted to affect condensation even at concentrations as low as 0.5% [109].

CHAPTER 6

LINEAR STABILITY ANALYSIS

To date, only one study presented a linear stability analysis of pattern formation in buoyancy-thermocapillary convection which correctly predicts the formation of a stationary pattern at $Bo_D = O(1)$. This study by Priede and Gerbeth [18] is, however, based on a one-layer model where phase change is neglected and the free surface is considered adiabatic. While this description may be acceptable for nonvolatile liquids or at high concentrations of noncondensables, it fails to describe volatile liquids at lower concentrations of noncondensables. This chapter therefore describes a more general linear stability analysis that also accounts for heat and mass flux across the interface associated with phase change. In order to avoid dealing with the boundary conditions near the end or side walls, the horizontal liquid layer and the gas layer above the liquid are both assumed to be laterally infinite, with constant thicknesses d_l and d_g, respectively. The interface is assumed to be flat and non-deformable. Finally, the base flow (SUF) is assumed to correspond to a mean horizontal temperature gradient τ.

6.1 Governing Equations and the Base Solution

The governing equations for both layers have been presented in Chapter 2 and in nondimensional form in Chapter 3. While the nondimensional equations (88) for the liquid layer can be used without modification, several approximations will be made in the treatment of heat and mass transport on the gas side in order to obtain a tractable problem which can generate useful physical insights. The relative contribution of advection and diffusion to the mass transport in the gas layer is described by the mass Péclet number (163). Since the relevant length scale here is the wavelength of the convective pattern, which is comparable to the depth of the liquid layer, it reduces to $Pe_m = d_l u_g / D$. Its largest values are achieved at atmospheric conditions, when D is the smallest and $u_g = u_i$. For the problem

investigated here, the transition happens at around $\Delta T = 4$ K when $Pe_m \approx 1$ at atmospheric conditions. While this means that diffusion dominates advection only at length scales below d_l, dropping the advective term in the transport equation (36) should not affect the results dramatically. The relative contributions of advection and conduction to the heat transport in the gas layer is described by the thermal Péclet number (85) which reduces to $Pe_g = d_l u_i / \alpha_g$. We find $Pe_g \approx 0.4$ at $\Delta T = 4$ K, so the advective contribution can also be ignored in the transport equation (35).

The relevant time scale for temperature equilibration in the gas layer is $t_g^t = d_l^2 / \alpha_g = 0.3$ s and the time scale for composition equilibration is $t_g^m = d_l^2 / D = 1$ s. In the liquid layer the time scale for momentum equilibration is $t_l^\nu = d_l^2 / \nu_l = 9$ s, while the time scale for temperature equilibration is $t_l^t = d_l^2 / \alpha_l = 83$ s. Since the gas layer is characterized by much faster relaxation rates than the liquid layer, the time dependence in the gas phase can be neglected, with the dynamics of perturbation in the gas phase slaved to those in the liquid phase. As a result, the advection-diffusion equations (91) for the heat and mass transport in the gas layer are reduced to the much simpler Laplace equations, which can be solved analytically:

$$\nabla^2 T_g = 0,$$

$$\nabla^2 \rho_r = 0, \tag{210}$$

where T_g is the dimensionless gas temperature, ρ_r is the dimensionless density of the dilute component.

It should be noted that neglecting the time-varying dynamics of the gas phase changes neither the critical Marangoni number nor the critical wavelength for stationary instabilities, so this simplification is justified if the transition thresholds are the only parameters of interest.

The base solution (110)-(112) describing the core region of the liquid layer in the SUF

regime was derived in Chapter 3 and will be reproduced here for convenience:

$$\tilde{\psi}_{l0} = Re_l\left[-\frac{\tilde{z}(\tilde{z}+1)^2}{4} + Bo_D\frac{\tilde{z}(\tilde{z}+1)^2(2\tilde{z}-1)}{48}\right]\hat{x},$$

$$\tilde{T}_{l0} = \tilde{x} + Ma_i\left[-\frac{\tilde{z}^2(3\tilde{z}^2+8\tilde{z}+6)}{48} + Bo_D\frac{\tilde{z}^2(8\tilde{z}^3+15\tilde{z}^2-10)}{960}\right]. \tag{211}$$

The base solution describing the core region of the gas layer satisfying the equations (210) can be obtained by setting $\mathcal{R} = 0$ in (124)-(125) which is equivalent to setting $\mathbf{u}_g = 0$ and yields solutions that are independent of $\tilde{z}$ and vary linearly with $\tilde{x}$:

$$\tilde{T}_{g0} = \tilde{x},$$

$$\tilde{\rho}_{v0} = \tilde{\varrho}\tilde{x}. \tag{212}$$

6.2 Boundary Conditions for the Perturbations

Although adiabatic boundary conditions apply for the base state, perturbations in the (interfacial) temperature will give rise to a nonzero heat and mass flux across the interface and, consequently, in the gas phase. Perturbed solutions can be written in the form of Fourier integrals

$$\tilde{\psi}_l = \tilde{\psi}_{l0} + \int_{-\infty}^{\infty} \tilde{\psi}_{lq}(\tilde{z})e^{iqx+\sigma_q t}dq,$$

$$\tilde{T}_l = \tilde{T}_{l0} + \int_{-\infty}^{\infty} \tilde{\theta}_{lq}(\tilde{z})e^{iqx+\sigma_q t}dq,$$

$$\tilde{T}_g = \tilde{T}_{g0} + \int_{-\infty}^{\infty} \tilde{\theta}_{gq}(\tilde{z})e^{iqx+\sigma_q t}dq,$$

$$\tilde{\rho}_v = \tilde{\rho}_{v0} + \int_{-\infty}^{\infty} \tilde{\rho}_{vq}(\tilde{z})e^{iqx+\sigma_q t}dq, \tag{213}$$

where $q = k + is$ is the complex wavenumber, $\sigma_q = \alpha_q + i\omega_q$ is the growth rate, $\tilde{\psi}_{lq}(\tilde{z})$, $\tilde{\theta}_{lq}(\tilde{z})$, $\tilde{\theta}_{gq}(\tilde{z})$ and $\tilde{\rho}_{vq}(\tilde{z})$ define the vertical profile for the perturbations of stream function $\tilde{\psi}_l$, liquid temperature $\tilde{T}_l$, gas temperature $\tilde{T}_g$, and vapor density $\tilde{\rho}_v$ for the mode defined by the wavenumber q, respectively. Here the vapor is assumed to be dilute in the gas phase $(\rho_r = \rho_v)$.

The temperature perturbation in the gas phase $\tilde{\theta}_{gq}$ satisfies (210), which requires

$$\tilde{\theta}''_{gq} = q^2 \tilde{\theta}_{gq}, \tag{214}$$

where the temperature is continuous across the interface

$$\tilde{\theta}_{gq}(0) = \tilde{\theta}_{lq}(0) = \tilde{\theta}_{iq}, \tag{215}$$

and the boundary condition at the top of the gas layer is adiabatic

$$\tilde{\theta}'_{gq}(\tilde{d}_g) = 0. \tag{216}$$

The solution is

$$\tilde{\theta}_{gq}(\tilde{z}) = \frac{\cosh\left[q(\tilde{z} - \tilde{d}_g)\right]}{\cosh\left(q\tilde{d}_g\right)} \tilde{\theta}_{iq}. \tag{217}$$

The evolution equation and the boundary conditions for the perturbation in the vapor density $\tilde{\rho}_{vq}$ are analogous and give

$$\tilde{\rho}_{vq}(\tilde{z}) = \frac{\cosh\left[q(\tilde{z} - \tilde{d}_g)\right]}{\cosh\left(q\tilde{d}_g\right)} \tilde{\rho}_{viq}, \tag{218}$$

where $\tilde{\rho}_{viq}$ is determined by the perturbations in the vapor pressure at the interface, which can be related to the perturbations in the interfacial temperature via the Clausius-Clapeyron relation which expresses local phase equilibrium

$$\tilde{\rho}_{viq} = \tilde{\varrho}\tilde{\theta}_{iq}. \tag{219}$$

Fourier transforming (101) yields

$$\tilde{J}_q = -\frac{1}{\bar{c}_a}\tilde{\rho}'_{vq}(0), \tag{220}$$

where $\tilde{J}_q$ is the Fourier coefficient of $\tilde{J}(x)$ (recall that the base solution is $\tilde{J} = 0$). Subtracting the base solutions from the heat balance (98), Fourier transforming the result, and using (220) gives the following relation

$$\tilde{\theta}'_{lq}(0) = \frac{k_g}{k_l}\tilde{\theta}'_{gq}(0) + \frac{1}{\bar{c}_a}\frac{G_2}{Ma_i}\tilde{\rho}'_{vq}(0). \tag{221}$$

With the help of (217), (218), and (219) this can rewritten in the form of Newton's law of cooling

$$\tilde{\theta}'_{lq}(0) = -Bi_q \tilde{\theta}_{lq}(0) \tag{222}$$

where we introduced a wavenumber-dependent analogue of the Biot number

$$Bi_q = q \tanh\left(q\tilde{d}_g\right) \left[\frac{k_g}{k_l} + \frac{1 - \bar{c}_a}{\bar{c}_a}(1 - \upsilon)G_1\right], \tag{223}$$

which will be subsequently called the Biot *coefficient* to emphasize the fact that it is a function of q and $\bar{c}_a$, *vs.* a constant. The prefactor $\tanh(q\tilde{d}_g)$ describes the effect of the finite thickness of the gas layer. For $d_g \gg d_l$, this prefactor approaches unity and (223) reduces to the expression derived by Chauvet *et al.* [128] for the stability of a volatile liquid layer in the presence of a *vertical* temperature gradient. It should be noted that the Biot coefficient (223) is different from, and unrelated to, the Biot number (155) that characterizes the deviation of the interfacial temperature from the average temperature T_0.

When the dilute component is air, rather than vapor, the disturbance in the mass flux can be expressed as

$$\tilde{J}_q = -\frac{1}{\bar{c}_a}\tilde{\rho}'_{vq}(0) = \frac{\bar{R}_a}{\bar{R}_v}\frac{1}{\bar{c}_a}\tilde{\rho}'_{aq}(0), \tag{224}$$

where the disturbance in the air density ρ_{aq} satisfies the same equation, and therefore has the same form, as the disturbance in the vapor density

$$\tilde{\rho}_{aq}(\tilde{z}) = \frac{\cosh\left[q(\tilde{z} - \tilde{d}_g)\right]}{\cosh\left(q\tilde{d}_g\right)}\tilde{\rho}_{aiq}. \tag{225}$$

The interfacial disturbances $\tilde{\rho}_{aiq}$ and $\tilde{\rho}_{viq}$ can be related, since the total pressure is essentially constant,

$$\tilde{\rho}_{aiq} = -\frac{\bar{R}_v}{\bar{R}_a}\tilde{\rho}_{viq}. \tag{226}$$

Substituting (225), (226) and (219) into (224), the same relation is obtained between $\tilde{J}_q$ and $\tilde{\theta}_{gq}$, and thus (222) remains true for any $\bar{c}_a$.

6.3 Evolution Equations for the Perturbations

By linearizing the governing equations (104) around the base state (211), the evolution equations for the perturbations $\tilde{\psi}_{lq}$ and $\tilde{\theta}_{lq}$ in the liquid are

$$(d_{\tilde{z}}^2 - q^2)^2 \tilde{\psi}_{lq} + iqC_1(\tilde{z})Re_l\tilde{\psi}_{lq}'' - iqC_2(\tilde{z})Re_l\tilde{\psi}_{lq} - iqGr_l\tilde{\theta}_{lq} = \sigma_q(d_{\tilde{z}}^2 - q^2)\tilde{\psi}_{lq},$$

$$Pr_l^{-1}(d_{\tilde{z}}^2 - q^2)\tilde{\theta}_{lq} + iqC_1(\tilde{z})Re_l\tilde{\theta}_{lq} - iqC_3(\tilde{z})Ma_i\tilde{\psi}_{lq} - \tilde{\psi}_{lq}' = \sigma_q\tilde{\theta}_{lq}. \tag{227}$$

where

$$C_1(\tilde{z}) = \frac{(\tilde{z}+1)(3\tilde{z}+1)}{4} - Bo_D\frac{(\tilde{z}+1)(8\tilde{z}^2 + \tilde{z} - 1)}{48},$$

$$C_2(\tilde{z}) = q^2 C_1(\tilde{z}) + \frac{3}{2} - Bo_D\frac{8\tilde{z}+3}{8},$$

$$C_3(\tilde{z}) = \frac{\tilde{z}(\tilde{z}+1)^2}{4} - Bo_D\frac{\tilde{z}(\tilde{z}+1)^2(2\tilde{z}-1)}{48}. \tag{228}$$

This is a system of ODEs which is fourth order with respect to $\tilde{\psi}_{lq}$ and second order with respect to $\tilde{\theta}_{lq}$ and hence needs a total of six boundary conditions. These boundary conditions are:

$$\tilde{\psi}_{lq}(-1) = 0,$$

$$\tilde{\psi}_{lq}'(-1) = 0,$$

$$\tilde{\theta}_{lq}'(-1) = 0. \tag{229}$$

at the bottom of the liquid layer and

$$\tilde{\psi}_{lq}(0) = 0,$$

$$\tilde{\psi}_{lq}''(0) = -iqRe_l\tilde{\theta}_{lq}(0), \tag{230}$$

$$\tilde{\theta}_{lq}'(0) = -Bi_q\tilde{\theta}_{lq}(0) \tag{231}$$

at the free surface.

The corresponding boundary value problem was solved using function **bvp5c** in Matlab 2013a. This function takes a system of first order ODEs as input, so the higher order ODEs

(227) are converted to a system of six first order ODEs

$$y_1' = y_2,$$

$$y_2' = y_3,$$

$$y_3' = y_4,$$

$$y_4' = C_4(\tilde{z})y_1 + C_5(\tilde{z})y_3 + iGr_l q y_5,$$

$$y_5' = y_6,$$

$$y_6' = C_6(\tilde{z})y_1 + Pr_l y_2 + C_7(\tilde{z})y_5, \tag{232}$$

where $y_1 = \tilde{\psi}_{lq}$, $y_5 = \tilde{\theta}_{lq}$, and

$$C_4(\tilde{z}) = -iGr_l \frac{q^3(\tilde{z}+1)(8\tilde{z}^2 + \tilde{z} - 1)}{48} - iGr_l q \frac{8\tilde{z}+3}{8}$$
$$+ iRe_l \frac{q^3(\tilde{z}+1)(3\tilde{z}+1) + 6q}{4} - q^2(q^2 + \sigma_q),$$

$$C_5(\tilde{z}) = iGr_l \frac{q(\tilde{z}+1)(8\tilde{z}^2 + \tilde{z} - 1)}{48} - iRe_l \frac{q(\tilde{z}+1)(3\tilde{z}+1)}{4} + 2q^2 + \sigma_q,$$

$$C_6(\tilde{z}) = i Ma_i Pr_l q C_3(\tilde{z}),$$

$$C_7(\tilde{z}) = -i Ma_i q C_1(\tilde{z}) + \sigma_q Pr_l + q^2. \tag{233}$$

Respectively, the boundary conditions become

$$y_1(-1) = 0,$$

$$y_1(0) = 0,$$

$$y_2(-1) = 0,$$

$$y_3(0) + iq Re_l y_5(0) = 0,$$

$$y_6(-1) = 0,$$

$$y_6(0) + Bi_q y_5(0) = 0. \tag{234}$$

The critical values for Ma_i and the wavenumber $k = 2\pi d_l/\lambda$ describing the transition to PMC or SMC state correspond to a stationary instability with $\alpha_q = \omega_q = 0$. The boundary conditions in this problem are of the "enhancing" type [202], so the pattern emerges near

the end walls at a smaller value of Ma_i than in the core region of the flow, away from the

end walls (cf. Section 3.1.1). The perturbation is always $O(1)$ at $x = L$ due to the presence

of a convection roll that exists for all ΔT near the hot end wall. Hence, below the critical

value of Ma_i, the imaginary part of the wavenumber q defines the spatial attenuation of the

perturbation (or the number of convection rolls that can be detected in the liquid layer). In

this analysis, $s_{\mathrm{PMC}} = 2d_l/\lambda$ for the transition from SUF to PMC (which corresponds to one

extra roll). For systems with a small aspect ratio, $s_{\mathrm{SMC}} = 2/\Gamma_x$ for the transitions from PMC

to SMC (which corresponds to convection rolls filling the entire liquid layer) but, since in

this study $\Gamma_x \approx 20$ is quite large, $s_{\mathrm{SMC}} = 0$ will be used instead.

6.4   Comparison with Experimental and Numerical Results

Previous theoretical studies focused mainly on the dependence of the critical Marangoni

number Ma_i on the dynamic Bond number Bo_D and the Prandtl number Pr_l characterizing

the liquid layer. In this Section linear stability analysis will also be used to investigate how

both the critical Ma_i and the critical wavelength $\lambda = 2\pi d_l/k$ depend on the concentration of

noncondensables $\bar{c}_a$. The linear stability predictions will also be compared with available

experimental and numerical data.

Riley and Neitzel [12] determined how both the critical Ma_i and the critical wavelength

λ corresponding to the onset of steady multicells (SMC) depended upon the dynamic Bond

number Bo_D for a 1 cSt silicone oil with $Pr_l = 13.9$. In their study, the transition threshold

for SMC is identified as the instance when multiple convection rolls appear near the hot end

wall, but do not extend all the way to the cold end wall, which is a fairly vague definition

that could span a range of Ma_i. In this study, following Li *et al.* [1], the onset of partial

multicells (PMC) is defined as the instance when the convection roll near the hot end splits

into two, while the onset of SMC is defined as the instance when multiple convection rolls

cover the entire liquid layer (which can be infinite along the streamwise direction). There-

fore, in order to compare the predictions of linear stability analysis with the experimental

data, critical values for the onset of both PMC and SMC were calculated using $Pr_l = 13.9$, which matches the working fluid used in the experiments. Other material parameters of the liquid that were not reported in Ref. [12] were taken from Ref. [203]. Since no data have been found for the material properties of the vapor, the vapor properties were assumed to be the same as those of the 0.65 cSt silicone oil [161, 162]. This should only have a minor effect on the results—since the 1 cSt silicone oil is not particularly volatile (vapor pressure $p_v = 0.5$ kPa at $T = 298$ K), the properties of the gas phase are essentially those of air ($\bar{c}_a = 0.995$ at atmospheric conditions).
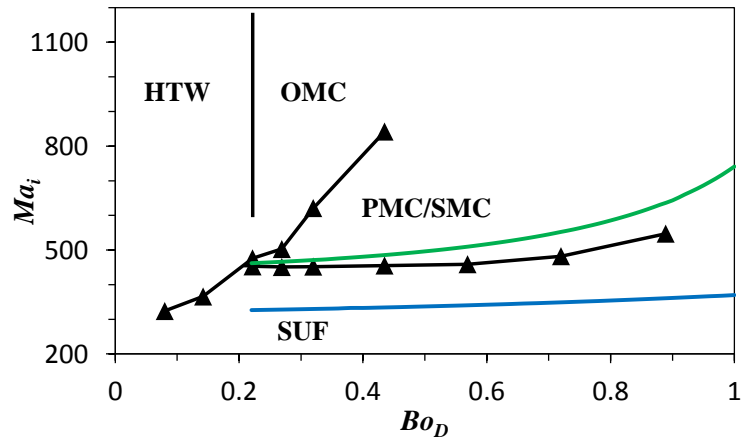
(a)
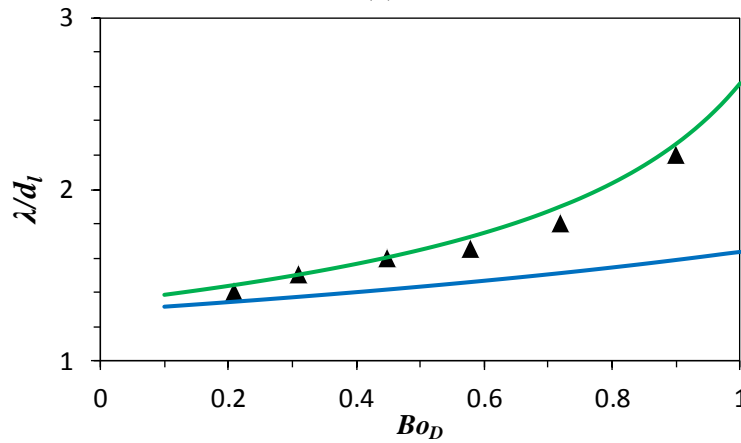
(b)

Figure 51: The critical Marangoni number (a) and the critical wavelength (b). Experimental results obtained by Riley and Neitzel [12] are shown as black filled symbols and lines, the predictions of the linear stability for transition to the PMC and SMC states are shown as blue and green lines, respectively.

153

As shown in Fig. 51, both the critical Ma_i and the critical wavelength observed in the experiments are bracketed by the theoretical values corresponding to the onset of PMC and SMC, and are closer to the SMC boundary. Indeed, Riley and Neitzel's supporting figures show the presence of multiple convection rolls at the critical Ma_i, so their threshold values should be closer to the SMC threshold than the PMC threshold predicted by this linear stability analysis.

Next, how do the critical Ma_i and the wavelength λ for the onset of the PMC and
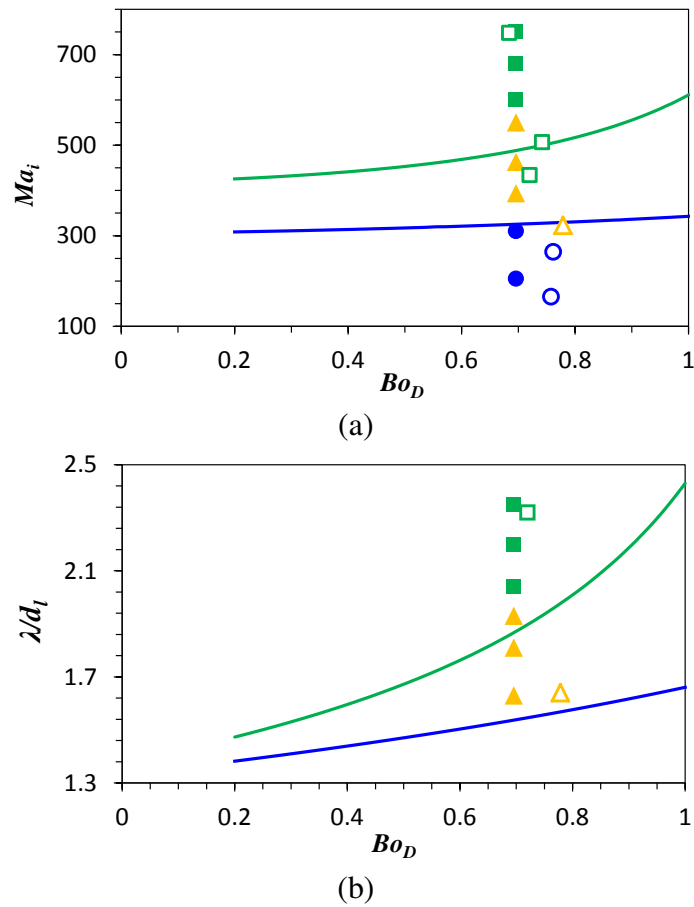
Figure 52: The critical Marangoni number (a) and the critical wavelength (b) for onset of the PMC and SMC states in the system considered in this work (at $Pr_l = 9.17, \bar{c}_a = 0.96$) as a function of the dynamic Bond number Bo_D. The blue solid line corresponds to onset of the PMC state, the green solid line corresponds to onset of the SMC state. The notations for flow regimes are the same as those in Fig. 42: SUF (o), PMC ($\triangle$), SMC ($\square$), and OMC ($\diamond$). Open symbols correspond to experimental results of Li *et al.* [1] and filled symbols – to numerical results from this study.

SMC states depend on various parameters in this flow? Linear stability calculations were performed using the material parameters listed in Table 6 to facilitate direct comparison with the results of numerical simulations reported in Chapter 5 and experimental data of Li *et al.* [1].

The predicted dependence on dynamic Bond number at atmospheric conditions $\bar{c}_a = 0.96$ and $Pr_l = 9.19$ is shown in Fig. 52. Similar to the case of the $Pr_l = 13.9$ liquid, the critical values of Ma_i and λ increase monotonically with Bo_D over the range where a stationary pattern is found. This increase in Ma_i can be easily understood by noting that buoyancy has a stabilizing effect on the flow, since the temperature increases, and hence the density of the liquid decreases, with height.

(a)

(b)
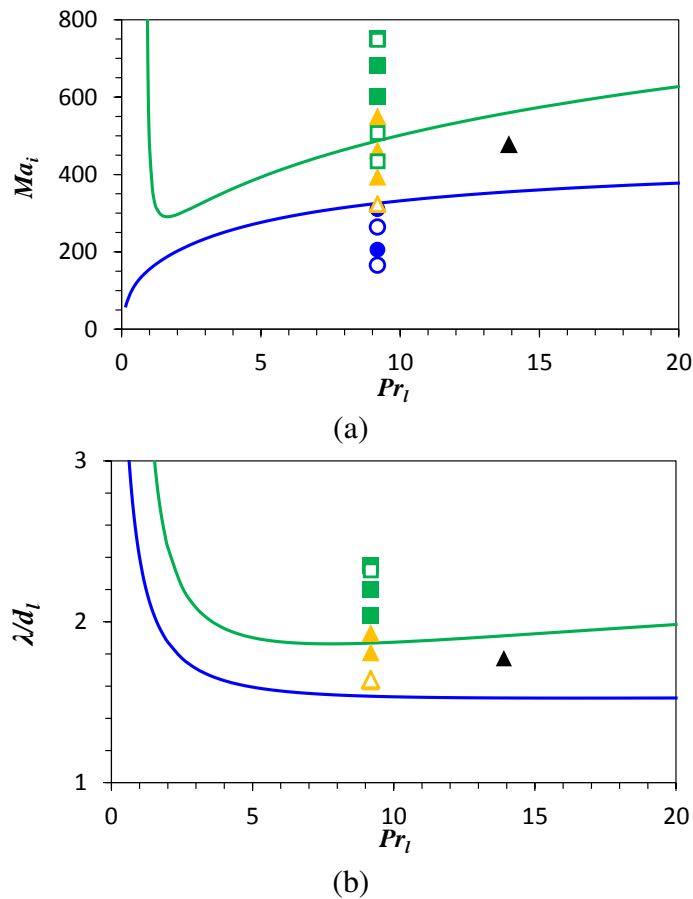
Figure 53: The critical Marangoni number (a) and the critical wavelength (b) for onset of the PMC and SMC states in the system considered in this work (at $Bo_D = 0.67$, $\bar{c}_a = 0.96$) as a function of the Prandtl number Pr_l. The notations are the same as those in Fig. 52.

The dependence of Ma_i and λ on the Prandtl number of the liquid, again at atmospheric conditions $\bar{c}_a = 0.96$ and $Bo_D = 0.67$, is shown in Fig. 53. For the onset of PMC, the critical Ma_i increases monotonically with Bo_D, and the critical wavelength λ decreases monotonically with Bo_D. For the onset of SMC, the critical Ma_i quickly decreases for small Pr_l, reaching a minimum at $Pr_l \approx 1.6$, and then gradually increases, in qualitative agreement with the results obtained by Priede and Gerbeth [18] for their one-sided model with an adiabatic interface. With the exception of liquid metals, Ma_i can be considered a monotonically increasing function of Pr_l over the entire range o f Pr_l corresponding to liquids. The dependence of the critical wavelength on the Prandtl number is however nonmonotonic: λ decreases until it reaches a minimum at $Pr_l \approx 8$, then slowly increases with Pr_l. Unlike the critical Ma_i, the critical λ is almost insensitive to the changes in Pr_l, for both the PMC and the SMC threshold over the relevant range of Pr_l.

While most of the previous studies only investigated convection patterns at atmospheric
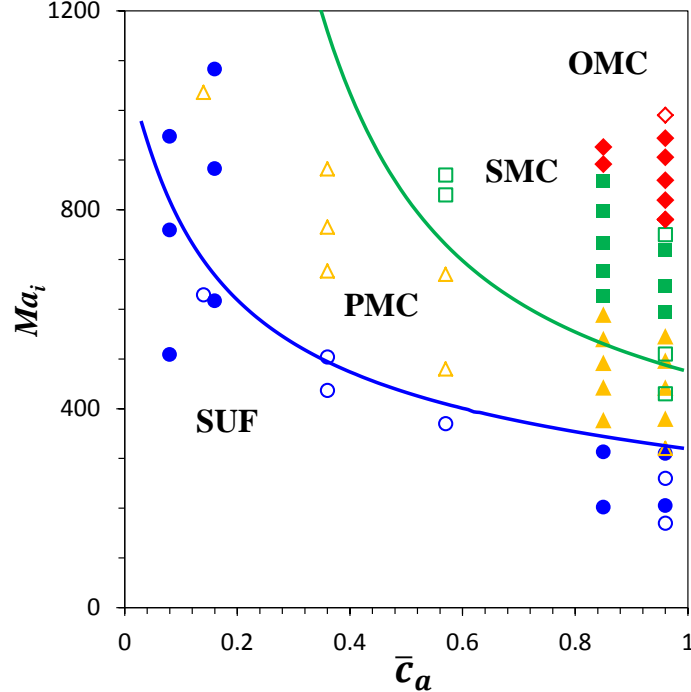
Figure 54: The critical Marangoni number for onset of the PMC and SMC states in the system considered in this work (at $Pr_l = 9.19, Bo_D = 0.67$) as a function of the average concentration of noncondensables $\bar{c}_a$. The notations are the same as those in Fig. 52.

156

conditions, the present model extends the analysis to arbitrary compositions of the gas phase by explicitly including the heat and mass transport through the gas phase. The dependence of the critical Ma_i on the average concentration $\bar{c}_a$ of noncondensables at $Pr_l = 9.17$ and $Bo_D = 0.67$ is shown in Fig. 54. The predicted critical Ma_i increases rather significantly as $\bar{c}_a$ decreases from atmospheric values to values where the gas is dominated by the vapor, *vs.* air. This is consistent with both experimental and numerical results, as summarized in Table 7.

When the gas phase is dominated by air ($\bar{c}_a = 0.96, 0.85$), the predictions of linear stability analysis for the onset of PMC are within the transition range found in the numerical simulations, while the predicted threshold of SMC is lower by about 20 % compared with that found in the numerical simulations. When the vapor is dominant ($\bar{c}_a \leq 0.16$), the numerical simulations always find SUF, even when Ma_i is larger than the threshold value predicted by the linear stability analysis. Since the model on which the numerical simulations are based is only valid in the dilute approximation, no results are available for

Table 7: Critical Ma_i predicted by the linear stability analysis for the onset of PMC state (a) and SMC state (b) at different average air concentration $\bar{c}_a$, at $Pr_l = 9.17$ and $Bo_D = 0.67$. Available numerical and experimental data are included which specifies the range when transitions occur.

$\bar{c}_a$	Linear Stability Analysis	Numerics	Experiments
0.96	325	303-379	264-323
0.85	344	301-377	-
0.56	411	-	366-478
0.34	503	-	504-677
0.11	748	-	629-1036

(a)

$\bar{c}_a$	Linear Stability Analysis	Numerics	Experiments
0.96	487	546-594	323-434
0.85	523	589-627	-
0.56	702	-	667-827

(b)

comparison at intermediate air concentrations. The predictions of the linear stability analysis are in better agreement with the experimental data, although the predicted thresholds for the onset of PMC and SMC states at atmospheric conditions are higher by about 20% than those found in experiment.

The dependence of the critical wavelength on $\bar{c}_a$ shows a trend similar to Ma_i: λ is found to decrease as $\bar{c}_a$ increases (cf. Fig. 55). For small $\bar{c}_a$, λ becomes comparable to the length L of the cavity. These predictions are also in reasonable agreement with both numerical and experimental results [204]. When the gas phase is dominated by air ($\bar{c}_a = 0.96, 0.85$), linear stability analysis underpredicts the critical wavelengths for both the PMC and SMC states by about 6% compared with the values found in the numerical simulations. When the gas phase is dominated by the vapor, the numerical simulations predict that the base state is stable at all ΔT, so no numerical data are available for comparison at low $\bar{c}_a$. Nevertheless, the linear stability predictions are in good agreement with the experimental data.
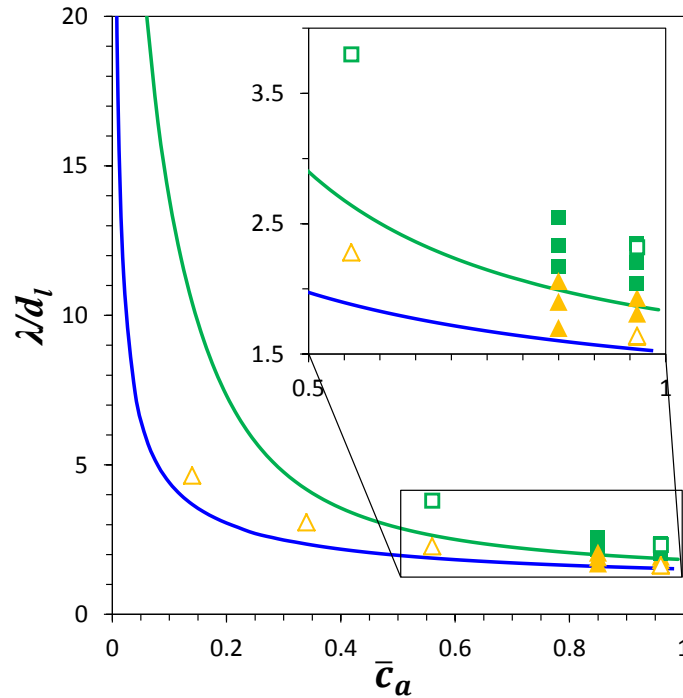
Figure 55: The critical wavelength for onset of the PMC and SMC states in the system considered in this work (at $Pr_l = 9.19$, $Bo_D = 0.67$) as a function of the average concentration of noncondensables $\bar{c}_a$. The notations are the same as those in Fig. 52.

The linear stability analysis assumes a flat interface and will therefore break down for $\lambda \gg 1$, when the thickness of the liquid layer should have significant variations, even in an unbounded layer. So the theoretical predictions at low $\bar{c}_a$ (and also at low Pr_l) are unlikely to be very accurate. Furthermore, at low $\bar{c}_a$ ($\bar{c}_a \lesssim \bar{c}_a^{(2)}$), the interfacial temperature profile in the SUF state is not a linear function of position, and so the analytical solution for the base flow is not valid.

In order to quantify the effect of the gas phase on the flow stability, the predictions of the linear stability analysis are compared for two cases: (i) when the mass and heat transport through the gas phase are accounted for through the boundary condition (223); and (ii)

(a)

(b)
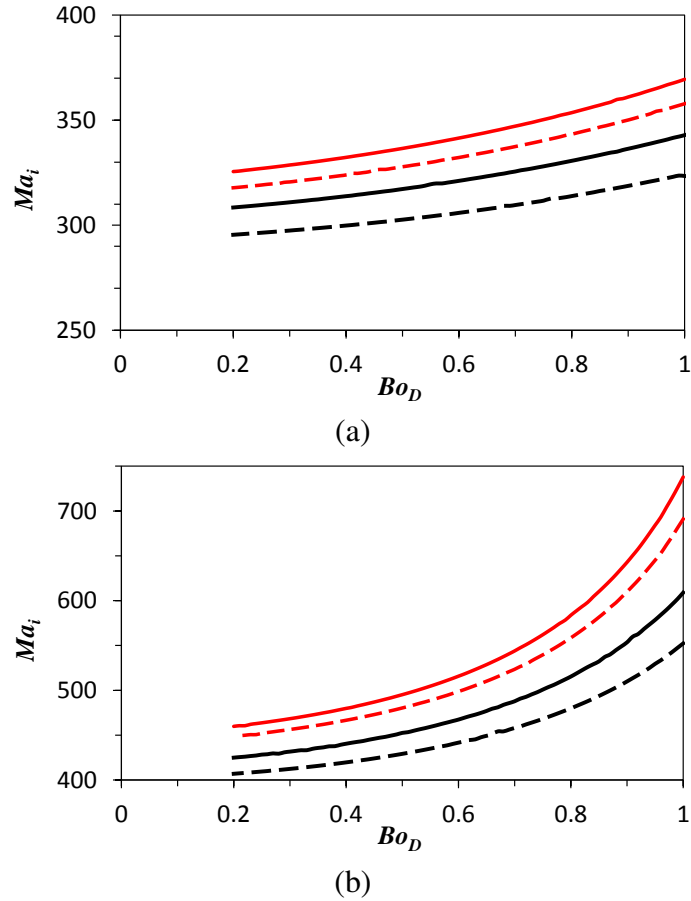
Figure 56: The critical Marangoni number for the onset of PMC state (a) and SMC state (b) at atmospheric conditions. Black color represent the 0.65 cSt silicone oil at $Pr_l = 9.17$, $\bar{c}_a = 0.96$, red color represent the 1 cSt silicone oil at $Pr_l = 13.9$, $\bar{c}_a = 0.995$. Solid lines represent results with $Bi = Bi_q$, dashed lines represent results with $Bi = 0$.

when that transport is completely ignored and the adiabatic boundary condition ($Bi = 0$) is used, as is the case for the analysis by Priede and Gerbeth [18] based on the one-sided model. These two cases will be compared at atmospheric conditions when the difference should be the smallest, for flow in both the 1 cSt silicone oil used by Riley and Neitzel [12] and the 0.65 cSt silicone oil used in this study. As shown in Fig. 56, the critical Ma_i for case (i) is always higher than that for case (ii). In other words, the transport of heat and mass through the gas phase delays the transition. Since 0.65 cSt silicone oil is more volatile than 1 cSt silicone oil, the difference between the two cases is larger for the 0.65 cSt silicone oil. For example, at $Bo_D = 0.69$, the critical Ma_i for onset of the PMC state is greater by 3% for the 1 cSt silicone oil, and by 5% for the 0.65 cSt silicone oil.

Despite this difference, at atmospheric pressure the adiabatic boundary condition could be considered a reasonable assumption. Indeed, at atmospheric conditions, phase change is greatly suppressed, so the effect of vapor transport through the gas phase is relatively minor. The effect of heat transport is also relatively small, since the thermal conductivity of both liquids is greater than that of air. However, as $\bar{c}_a$ decreases and phase change is enhanced, the predictions of the one-sided model become progressively less accurate. In particular, it completely fails to describe the dependence of the critical Ma_i on the concentration of noncondensables, because heat and mass transport through the gas phase, and their dependence on the concentration of noncondensables, are completely ignored.

6.5 Discussion

Although the linear stability analysis of the two-sided model presented above neglected advection in the gas phase, its predictions for the onset of the PMC and SMC states are in reasonable agreement with the reported numerical results and experimental data. In particular, the linear stability analysis correctly predicts that the transitions between different flow regimes are delayed (i.e., shifted towards higher Ma_i) when the concentration of noncondensables decreases, although quantitative agreement is not expected at low $\bar{c}_a$ when

both the assumption of a flat interface breaks down and the analytical solution describing the SUF regime becomes invalid. Despite these limitations, the agreement found at higher $\bar{c}_a$ confirms the validity of the assumptions made in the linear stability analysis, suggesting that it captures most, if not all, of the essential physical processes governing the flow stability for volatile liquids driven by a horizontal temperature gradient.

The discrepancies between the linear stability analysis and the numerical results are likely caused by insufficient spatial resolution. While adaptive mesh refinement produces a fairly fine mesh (with a minimum dimension of 0.0625 mm) in the liquid phase and near the end walls, a coarser mesh was used in the core region of the gas phase. Discrepancies between the linear stability analysis and the experimental results are likely due to the curvature of the free surface. The liquid rises at the end walls and side walls, increasing the thickness of the liquid layer there from d_l to $d_l + d_c$. The capillary rise d_c given by (82) can be as large as the capillary length $l_c = 1.45$ mm, which is $0.6 d_l$ where $d_l = 2.45$ mm. Since the Marangoni number is a quadratic function of the thickness of the liquid layer, its average value in the experiments could be significantly greater than that given by the thickness d_l of the liquid layer at the mid-plane of the cavity.

In this problem, buoyancy plays a stabilizing role. Hence, the instability leading to the formation of convection rolls is driven primarily by thermocapillary stresses, which depend on the interfacial temperature gradient. The fluctuations in the interfacial temperature are affected significantly by the heat and mass flux through the gas phase, which can be described using the Biot coefficient Bi_q as a function of both the wavenumber q and the average concentration of noncondensables $\bar{c}_a$. The first term in the square brackets in (223) describes the effect of conductive heat transport through the gas layer, and reflects the dependence of thermal conductivity of the gas phase on the gas composition, while the second term describes the effect of the latent heat released or absorbed at the interface as a result of phase change, and reflects the variation in the diffusive transport of vapor through the gas phase, which also depends on the gas composition. Both heat and mass transport

161

through the gas phase suppress the fluctuations in the interfacial temperature.

To better understand the relative impact of the heat and mass transfer on stability, it is instructive to compare the trends and characteristic magnitudes of the two terms in (223). For the 0.65 cSt silicone oil used in this study, as $\bar{c}_a$ decreases, the first term decreases slightly (thermal conductivity of the vapor is somewhat smaller than that of the air), but the second term increases significantly as phase change is enhanced. At atmospheric conditions, the heat flux in the gas phase has a slightly larger effect (the magnitudes of the first and second terms in the square brackets are 0.23 and 0.16, respectively). The mass flux becomes dominant when $\bar{c}_a < 0.94$ (e.g., for $\bar{c}_a = 0.1$, the magnitudes of the first and second terms in the square brackets are 34.1 and 0.11, respectively). In fact, the second term diverges as $\bar{c}_a \to 0$, which, according to (222), implies that the temperature fluctuations at the interface vanish and the critical Ma_i diverges. This is consistent with the analysis presented in Chapter 4 which shows that the interface becomes essentially isothermal under pure vapor.

Therefore, the increase in the critical Ma_i with decreasing $\bar{c}_a$ is due primarily to the enhancement of phase change, which increases the amount of latent heat released/absorbed by the warmer/cooler regions of the interface, thereby suppressing the fluctuations in the interfacial temperature gradient. The composition of the gas phase has a more significant effect on flow stability than on the base flow itself. As discussed in Chapter 5, the concentration of noncondensables has a relatively weak effect on the base flow, since the average interfacial temperature gradient $\bar{\tau}$, which determines the thermocapillary stresses and hence the speed of the base flow, is almost insensitive to $\bar{c}_a$ above $\sim 0.1\%$.

Since the heat and mass transport through the gas phase significantly affect the flow stability, one-sided models, which neglect these effects, cannot accurately predict the transition thresholds for volatile fluids. As discussed previously, even at atmospheric conditions, when phase change is strongly suppressed, one-sided models with the adiabatic boundary

condition underestimate the critical Ma_i corresponding to the transition thresholds (by 3-5%, compared with the two-phase models considered in this study). At reduced pressures, heat and mass transport through the gas phase are significantly enhanced, and one-sided models lead to wrong results as they completely fail to describe these effects.

A number of nondimensional parameters have been introduced by other linear stability studies of convective flows. In particular, in their analysis of pure Marangoni (thermocapillary) instability in volatile fluids subjected to a *vertical* temperature gradient, Burelbach *et al.* [194] introduced two nondimensional parameters, the evaporation number E (180), which defines the ratio of the evaporative time scale (how long it would take for a liquid to completely evaporate) to the viscous time scale, and the "non-equilibrium parameter" K (151), which defines the ratio of the latent heat flux at the interface to the conductive heat flux in the liquid. A version of the Biot coefficient (223) that describes the limit $d_g \gg d_l$ appears in the recent – correct – stability analysis of that problem [128]. Quite importantly, neither E nor K appear in the proper linear stability analysis of convection in volatile fluids, whether the temperature gradient is vertical as in [128] or horizontal as in the present study; both parameters fail to account for the transport (of either heat or mass) in the gas phase.

Mercier and Normand [16] referred to the Biot number

$$Bi_c = \frac{k_g d_l}{k_l d_g} \tag{235}$$

based on conduction in the two layers in their analysis of buoyancy-thermocapillary convection driven by a horizontal temperature gradient, but did not use it explicitly and instead warned, as pointed out by Normand *et al.* [195], that the Biot number should depend on the wavenumber for convective flows. Indeed, if we were to ignore phase change, and consider an infinitely thick gas layer, the expression (223) would reduce to

$$Bi_q = q\frac{k_g}{k_l} = 2\pi\frac{k_g d_l}{k_l \lambda}, \tag{236}$$

which is similar to (235) in form, but includes wavenumber dependence. The combination (235) also does not account for the transport of mass (in response to phase change) and

is therefore unsuitable for volatile fluids. In summary, the Biot coefficient Bi_q (223), as defined here, is required to characterize convection in volatile fluids.

CHAPTER 7

CONCLUSIONS AND RECOMMENDATIONS

The studies of buoyancy-capillary convection in volatile liquids driven by a horizontal temperature gradient, almost all of which previously considered only atmospheric conditions, were extended in this thesis to reduced pressures. This thesis work, which is hence more relevant for thermal management applications, used a combination of numerical simulations and analytical techniques. The main conclusions and contributions of this work, as well as recommendations for future studies are presented below.

7.1   Summary

In order to improve our fundamental understanding of the confined two-phase flow, which is important for designing advanced thermal management devices, this thesis work focused on extending the previous fundamental studies of buoyancy-thermocapillary convection in volatile fluids to arbitrary concentration of noncondensables. Although this type of convection has been studied extensively at atmospheric conditions using one-sided models, there has been little justification provided for neglecting the transport in the gas phase and across the interface for *volatile* fluids. Therefore the main question is, "Under what conditions can one-sided models provide an accurate description of two-phase flow of volatile fluids? Alternatively, "When is a two-sided model required?

In order to answer either of these questions, it is important to determine the role played by the transport in the gas phase and across the interface in this problem using a two-sided model. Hence, as a part of this thesis work, a comprehensive two-sided model of confined two-phase flows of a simple volatile fluid was developed, which accounts for momentum, mass, and heat transport in both phases, as well as phase change along the entire interface. This model is quite complicated since the fluid flow, temperature field, and concentration field are all interdependent, and hence requires the use of numerical simulations. The model

was therefore implemented numerically using the open source CFD package OpenFOAM and validated by experimental data.

This numerical model was used to investigate buoyancy-thermocapillary convection in the experimental system described in Li *et al.* [1], where a layer of volatile silicone oil was contained in a sealed cavity under a mixture of noncondensables (air) and vapor, with the *average* air concentration $\bar{c}_a$ varying from that corresponding to atmospheric conditions to zero, in which case the gas phase becomes a pure vapor. The two-sided model produced a number of profound and unexpected results.

In particular, three different theoretical models of phase change based on Kinetic Theory of Gases (KTG), Statistical Rate Theory (SRT), and Non-equilibrium Thermodynamics (NET) were compared. For an accommodation coefficient of unity (for nonpolar liquids), the predictions of all three models are in good quantitative agreement. When the accommodation coefficient is less than unity (for polar liquids), only KTG and NET are valid, and the predictions of these two models are in quantitative agreement. Although both SRT and NET predict a temperature jump across the liquid-vapor interface, this temperature jump is found to have a negligible effect on the interfacial temperature, and hence on the thermocapillary stresses and the flow. Therefore, any of these three phase change models can be used to accurately model convection in volatile fluids.

Furthermore, it was found that heat and mass transport in the gas phase play a crucial role in this problem. For relatively thin layers (characterized by $Bo_D = O(1)$), the flow is driven primarily by thermocapillary stresses, which arise in response to the imposed interfacial temperature gradient, over a wide range of $\bar{c}_a$. Under typical experimental conditions the total pressure is essentially constant in the gas layer while, for volatile fluids, the interfacial temperature is essentially equal to the saturation temperature. The latter is determined by the vapor (partial) pressure which, in turn, is a function of the composition of the gas phase described by the local air concentration c_a. And, since the local gas composition is controlled by the mass transport through the gas phase, this transport essentially governs

166

the fluid flow.

This result illustrates a dramatic contradiction between the predictions of a proper two-sided model and the conventional modeling approach based on one-sided models, which assumes that the gas layer plays a negligible role in the problem. Specifically, it was found that one-sided models are only reasonably accurate for describing the case where there is a uniform return flow away from the end walls, where the assumptions of a flat interface, negligible phase change and heat flux through the interface, and linearly varying interfacial temperature profile are all valid. Moreover, in confined systems, the interfacial temperature gradient $\bar{\tau}$ is a free parameter and should be determined by matching the solution in the core region of flow with that near the end walls, where the above assumptions fail (e.g., phase change cannot be neglected for volatile fluids even under atmospheric conditions), and so a two-sided model is still required for an accurate description of the entire flow.

Furthermore, the assumption of a linearly varying interfacial temperature profile that is used in one-sided models is not always valid. In fact, the justification of this assumption for volatile fluids requires a two-sided model. This work therefore extended the theoretical analysis of the base return flow in an unbounded liquid layer [4] to the gas phase, yielding an analytical description of the temperature and velocity field in both phases, and the composition field in the gas phase. The analytical solution for the two-phase flow shows that the assumption of a constant interfacial temperature gradient can be justified by verifying its consistency with the solution of transport equations in the gas phase at high $\bar{c}_a$.

However, the assumption of a linearly varying interfacial temperature profile breaks down at low $\bar{c}_a$. This breakdown can be explained using a simplified analytical model of transport in the gas phase. The obtained analytical solution for the concentration field c_a is valid over the entire range of $\bar{c}_a$, and shows that the concentration and the interfacial temperature profiles in general vary exponentially with the coordinate along the temperature gradient direction, with the maximum at the cold end and the minimum at the hot end of the cavity. When $\bar{c}_a \lesssim \bar{c}_a^{(2)}$ (where $\bar{c}_a^{(2)} = 0.07$ for HMDS), the characteristic length scale

over which the concentration gradient varies becomes smaller than the length of the cavity L and the interfacial temperature profile starts to deviate significantly from a linearly varying profile. So one-sided models can no longer accurately describe the flow, even at low temperature differences ΔT.

While one-sided models are reasonably accurate for describing the flow at low ΔT for $\bar{c}_a \gtrsim \bar{c}_a^{(2)}$, they fail to describe the flow stability behavior at higher ΔT over the entire range of $\bar{c}_a$. Even at atmospheric conditions, the heat transport through the gas phase is non-negligible when additional convection rolls appear in the core region of flow, and one-sided models are unable to accurately predict this behavior. As $\bar{c}_a$ decreases, the flow becomes more stable, with substantial increase in the critical Ma_i for transitions between different flow regimes. Again, the one-sided models completely fail to predict this trend.

To describe the physical mechanisms responsible for suppressing the transitions, linear stability analysis of the two-sided model was performed, accounting for the heat and mass transport in the gas phase. In this problem, buoyancy plays a stabilizing role, with the instability leading to the formation of convection rolls driven primarily by thermocapillary stresses. Both the conductive heat flux and the latent heat released/absorbed due to condensation/evaporation at the interface help damp the perturbations in the interfacial temperature and the associated thermocapillary stresses, and therefore enhance the flow stability. In particular, it was found that the increase in the critical Ma_i with decreasing $\bar{c}_a$ is mostly due to the enhancement in phase change and the associated latent heat released or absorbed at the interface.

The linear stability analysis of the two-sided model suggests that the heat and mass transport through the gas phase have a significant effect upon the flow stability and cannot, in general, be neglected. The wavenumber-dependent Biot coefficient Bi_q, which describes the effect of transport in the gas phase, shows that one-sided models are only valid when the thermal conductivity of the liquid is much higher than that of the gas, $k_g \ll k_l$, and phase change is negligible, $(1 - \upsilon)(1 - \bar{c}_a)/\bar{c}_a < G_1^{-1}$. In fact, the second of these two conditions

is never met when $\bar{c}_a \to 0$, hence a two-sided model is required for a proper description of the flow at high ΔT and low $\bar{c}_a$.

As discussed in the introduction, the main motivation for the present study was initially the applications of two-phase flows to thermal management. On the other hand, due to its fundamental nature, the focus of this work is on a canonical problem whose geometry is at best qualitatively similar to that describing two-phase thermal management devices. However, the transport through the gas layer and across the interface is quite similar for a variety of geometries relevant to two-phase thermal management devices, and therefore, the improved fundamental understanding of transport in both phases resulting from this work should provide useful insights for modeling of evaporative two-phase cooling devices.

The capillary limit that constrains the liquid flow through the wick or microchannels has always been believed to be the major factor in designing heat pipes. However, the constraints imposed by the mass transport through the gas phase and the heat transport through the liquid phase can also be important and hence need to be taken into account. In particular, it is well known that noncondensable gases have a significant impact on the diffusion of vapor and, consequently, on phase change. The mass flow rate of vapor $\dot{m}_v$ increases significantly as $\bar{c}_a$ decreases from the value $\bar{c}_a^a$ at atmospheric pressure to $\bar{c}_a^{(2)}$. The simplified transport model of the gas phase shows that phase change becomes essentially independent of $\bar{c}_a$ below $\bar{c}_a^{(2)}$ and the mass flux is instead limited by heat conduction. This indicates that the benefit of decreasing $\bar{c}_a$ becomes small at sufficiently small $\bar{c}_a$.

Heat pipes have been traditionally modeled by separating their interior into three parts: the "evaporator," the "condenser," and the "adiabatic" regions, ignoring phase change in the adiabatic region, and assuming a linear temperature profile. This is justified for macroscale heat pipes which use wicks with closed pores to drive the liquid from the condenser to the evaporator, since there is no free surface in the adiabatic region. However, the theoretical analysis presented in this work clearly shows that heat pipes featuring open microchannels, e.g., micro-heat pipes, cannot be partitioned in this way, since in the limit where these

devices operate optimally ($\bar{c}_a < \bar{c}_a^{(2)}$) the phase change is non-negligible over the entire heat pipe and the temperature profile is nonlinear. Furthermore, at very low concentrations of noncondensables ($\bar{c}_a < \bar{c}_a^{(3)}$), the model suggests that thermocapillary stresses block the flow of coolant out of the condenser. This shows that, contrary to the naive expectation, it is actually counterproductive to decrease $\bar{c}_a$ too much in terms of thermal transport, and hence a heat pipe using microchannels should have the best performance for $\bar{c}_a^{(3)} < \bar{c}_a < \bar{c}_a^{(2)}$.

Based on the capillary limit and the heat conduction limit, the simplified transport model is able to predict the optimal value for the size of a pore in the wick (or the size of a microchannel). Moreover, it produces an analytical prediction for the heat flow rate and the heat transfer coefficient h. The analytical results provide a simple way both for evaluating different heat pipe designs and for choosing an optimal working fluid. Specifically, it was found that while the optimal pore size depends on multiple material parameters of the working fluid (namely its thermal conductivity, latent heat, viscosity, and surface tension), the heat transfer coefficient h is controlled primarily by the ratio of the thermal conductivity of the liquid to the pore size. In other words, it is the heat conduction limit, rather than the capillary limit, that ultimately defines the performance of a heat pipe. Furthermore, a working fluid with a smaller difference ΔC_p between the heat capacity of its liquid and vapor phase is preferred. Advection of heat has an adverse effect, which could be significant when the product $\Delta C_p T_0$ is comparable to the latent heat $\mathcal{L}$.

7.2 Main Contributions of This Work

The contributions of this thesis work to the fundamental understanding of two-phase flows of volatile fluids include:

1. Development of a simplified analytical description of two-dimensional flow in a layer of liquid under a mixture of its vapor and noncondensable gases, such as air, in confined geometries.

2. Demonstration that transport in the gas phase essentially controls the convection in

the liquid phase and can only be neglected in certain specific and limited cases (e.g., when the flow regime is SUF at high $\bar{c}_a$).

3. Discovery that the heat and mass transport through the gas layer have a crucial effect on the stability of the flow in the liquid layer.

4. Demonstration that different phase change models produce virtually indistinguishable predictions, despite the differences in their assumptions regarding the existence of a temperature jump at the interface.

5. Development of a numerical code based upon an open source CFD package, Open-FOAM, which can be used for fundamental studies of thermocapillary-buoyancy convection.

The contributions of this thesis work to the modeling of evaporative two-phase cooling devices include:

1. Development of a simple transport model for heat pipes with wicks and micro-heat pipes that can analytically predict the heat flux and heat transfer coefficient.

2. Prediction of the optimal size for the pores of the wick (or width of the microchannels) based on the constraints imposed by the capillary forces (capillary limit) and the conduction of heat through the liquid (conduction limit).

3. Discovery that there is no "adiabatic" region in micro-heat pipes at low concentrations of noncondensables, which requires a new modeling approach for such devices.

4. Prediction of the range of concentrations of noncondensables beyond which the thermal performance of evaporative cooling devices will be constrained by either the diffusion of coolant vapor through the gas (diffusion limit) or by thermocapillary forces (thermocapillary limit).

171

7.3 Open Questions

The analysis presented in this thesis uncovered a number of open questions that should be addressed in the future:

1. The interfacial temperature gradient is an important variable for the study of buoyancy-thermocapillary convection, since it determines almost everything in this problem, including the mass and heat transport, and all of the fields in the bulk of both layers. For a fixed (confined) geometry and working fluid, the average interfacial temperature gradient $\bar{\tau}$ becomes a function of the applied temperature difference ΔT and the average concentration of noncondensables $\bar{c}_a$. In this study, the dependence on these two parameters was described using an empirical correlation (174) based on the numerical simulations. In principle, it is desirable to find an analytical expression instead for τ from first principles, which should also determine how it depends on the geometry and material parameters.

2. The structure of the thin thermal boundary layers near the end walls and especially near the contact lines (the micro region) clearly play an important role in heat transport. The temperature field and the fluid flow in the micro region are coupled to each other and must be resolved in order to compute the interfacial temperature and the flow away from the end walls (in the macro region). Due to limited computational resources and the large disparity in the length scales, the numerical simulations in this study were able to resolve the macro region, but not the micro region of the interface. As a result, the numerical solutions for the mass flux and the interfacial temperature display a singular behavior in the vicinity of the contact lines. In order to resolve these fields near the contact line, the wedge-shaped micro region should be modeled analytically, with the solutions in the micro and macro regions matched in the overlap region, like in matched asymptotic expansions. While some solutions for the flow and/or temperature in a wedge are available [205–210], the problem where

172

the two fields are coupled through the boundary condition at the free surface remains unsolved.

3. Due to the extreme computational effort required by full 3D simulations, this thesis work made only a limited effort to consider the effect of the lateral walls in a smaller cavity with a contact angle of 90°. Although the flow in the central vertical plane of the 3D cavity agreed reasonably well with that obtained by the 2D simulations, noticeable deviations from the 2D solution were found on either side of the central plane when additional convection rolls appeared in the bulk flow. 3D numerical simulations become essential when the width W of the cavity becomes much larger that the liquid layer thickness since in this case lateral walls provide little confinement. 3D simulations also become necessary when W is comparable to the layer thickness and the contact angle is different from 90° due to the variation in the layer thickness in the spanwise direction.

4. The numerical simulations in this study accounted for the transport of momentum, heat, and mass in both phases and phase change across the interface. In particular, heat and mass transport in the gas phase due to both advection and diffusion were considered. However, in the linear stability analysis, heat and mass transport in the gas phase due to advection were neglected. Although this is a reasonable assumption for the system in this study as both Pe_g and Pe_m are typically small, it may not be a good assumption for other fluids or other geometries. Therefore linear stability analysis presented in this study should be further extended (or at least verified) by considering the advection of heat and mass in the gas phase.

5. A general analytical model has been developed in this work for predicting the optimal pore size and the heat transfer coefficient of a heat pipe with a wick. While this model should also be qualitatively accurate for a micro-heat pipe, more accurate description is required to obtain quantitatively accurate predictions. In particular, the capillary

pressure that drives the flow of liquid is determined by the shape of the grooves and the wetting properties of the working fluid. Moreover, since the microchannels are open to the gas phase, thermocapillary stresses and the viscous drag exerted by the gas phase could become important in certain limiting cases, and should be considered in analyzing the flow of liquid through the microchannels. There has been some modeling along these lines by other researchers [190, 211], although the thermal boundary conditions assumed in those studies are not realistic.

APPENDIX A

DIMENSIONLESS PARAMETERS

All the dimensionless parameters that have been introduced in the previous chapters are listed in Table 8. The values are calculated based on the geometry (cf. Fig. 4) and the fluid (cf. Table 6) used in this study, assuming the thickness of the liquid layer d_l = 2.45 mm, the contact angle $\theta = 50°$, and ΔT = 10K.

The values for the dimensionless parameters both at atmospheric conditions and under pure vapor are reported. While some dimensionless parameters are independent of the concentration of noncondensables $\bar{c}_a$, others could vary significantly with $\bar{c}_a$. This is because $\bar{c}_a$ affects the material parameters of the gas phase, and more importantly, the mass transport in the gas phase and hence the interfacial temperature gradient τ.

The velocity scales depend on $\bar{c}_a$ and could be different in the two phases. For the thermal Péclet number of the liquid phase Pe_l (84), velocity scale is chosen as the interfacial velocity u_i (113). At atmospheric conditions, the liquid flow is driven primarily by thermocapillary stresses and $u_i = u_T + u_B$. Under pure vapor, thermocapillarity essentially vanishes and $u_i \approx u_B$. For the thermal Péclet number Pe_g (85) and mass Péclet number of the gas phase Pe_m (163), the velocity scale u_g also depends on $\bar{c}_a$. At atmospheric conditions, the gas flow is driven primarily by thermocapillary stresses and $u_g = u_T + u_B$. Under pure vapor, the gas flow becomes unidirectional and u_g can be determined by the mass flow rate of the vapor $\dot{m}_v$. For thick layers under pure vapor, $\dot{m}_v = \dot{m}_v^0$ (177), and

$$u_g = \frac{\dot{m}_v}{\rho_g W d_l} = \frac{\varphi_c k_l \Delta T}{\rho_g d_l \mathcal{L}}. \tag{237}$$

Furthermore, for the linear stability analysis discussed in Chapter 6, the relevant length scale l_g in the gas phase is the wavelength for the convective pattern, which is comparable to the thickness of the liquid layer, therefore $l_g = d_l$. The corresponding values for Pe_g and Pe_m are presented in the parentheses in the following table, which differ by a factor of $\tilde{d}_g = 3.08$ compared with the values based on $l_g = d_g$.

Table 8: Dimensionless parameters and their values at atmospheric conditions and under pure vapor, at d_l = 2.45 mm, θ = 50° and ΔT = 10K. The material parameters corresponds to those in Tables 6.

Dimensionless parameter	At atmospheric conditions	Under pure vapor
Pr_l	9.17	
Ra_L	1.9×10^3	
Ma_L	2.8×10^3	
G_1	4.11	
υ	0.067	
Ξ_T	143	
Bo_D	0.67	
Bo	2.85	
Γ_x	19.8	
Γ_y	4.08	
Γ_g	6.42	
$\tilde{d}_g$	3.08	
K	6.8×10^3	
E	9.3×10^{-3}	
Ma_i	758	0.41
Pr_g	0.71	0.79
Re_l	82.6	4.4×10^{-2}
Re_g	14.2	4.3×10^{-3}
Ra_l	506	0.27
Ra_g	28.5	5.5×10^{-3}
Gr_l	55.2	3.0×10^{-2}
Gr_g	40.1	7.0×10^{-3}
Pe_l	228	38.8
Pe_g	3.03 (0.99)	1.98 (0.64)
Pe_m	9.03 (2.93)	0.37 (0.12)
Ca	1.9×10^{-4}	1.0×10^{-7}
We	1.6×10^{-2}	4.6×10^{-9}
G_2	5.0×10^7	1.3×10^9
K_ν	17.9	31.5
K_α	25.3	40.0
K_D	8.5	212.1
Ξ_ρ	-1.3×10^8	-7.1×10^8
$\mathcal{R}$	84.8	85.8
$\mathcal{B}$	3.21	1.80
Bi_c	0.075	0.032

APPENDIX B

NUMERICAL IMPLEMENTATION

The mathematical model described in Chapter 2 has been numerically implemented by adapting an open-source general-purpose CFD package OpenFOAM [212] to solve the governing equations in both 2D and 3D geometries. OpenFOAM uses the finite volume method [213, 214] to convert the partial differential equations into a set of algebraic equations on discrete control volumes. The discretization is based on the integral form of the governing equations, where Gauss' theorem is used to rewrite the volume integrals of the terms involving various derivatives as the surface integrals of the corresponding fluxes, ensuring that the conservation laws are satisfied both locally and globally. Another advantage of the finite volume method is that it is easy to apply on unstructured meshes.

The moving mesh method [147–155] (also known as moving mesh interface tracking method) is used to describe the motion of the free surface. The domain occupied by each phase (liquid, gas) is represented by a separate computational mesh and the interface between the two phases is represented by a set of mesh faces that divide the two domains. As interface changes shape, the mesh at the interface follows its motion, with the mesh on each side of the interface deforming accordingly. The governing equations are solved separately in each domain, subject to the boundary conditions imposed at the free surface as well as the boundaries of each domain that correspond to the inner surfaces of the walls of the container. Although the moving mesh methods are not the most convenient for simulating flows with interfaces that experience large deformation or changing topology, for flows with moderate interface deformation, they provides a very accurate description of the interface position and shape and therefore simplify the implementation of the boundary conditions at the interface, especially those involving surface tension.

This chapter describes the numerical implementation of the mathematical model. It
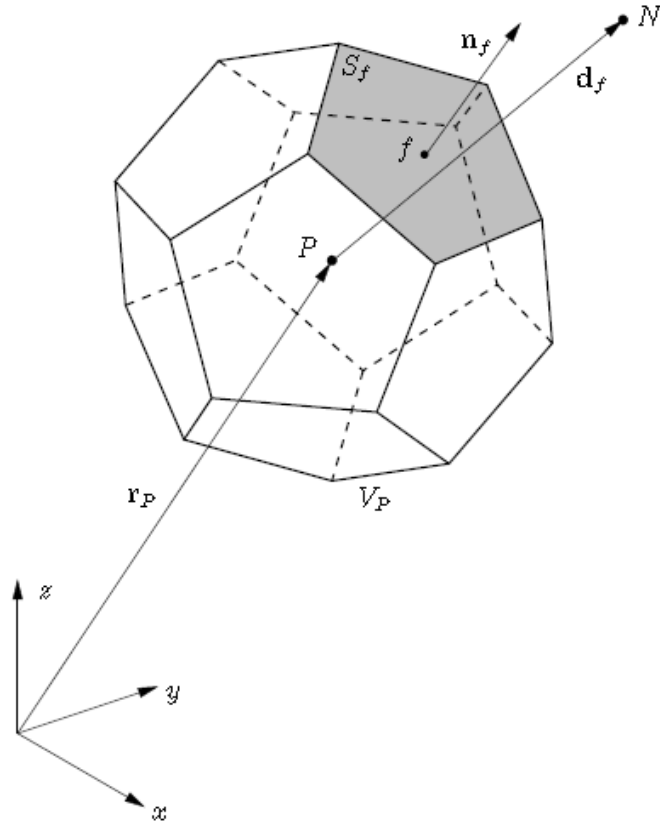
Figure 57: Sketch of the control volume (from [155]).

gives the background on the finite volume method, including the discretization of the solution domain and the governing equations. Then it describes the moving mesh methods and, in particular, the implementation of phase change and thermocapillary stresses. In the end, it describes the procedure for solving the discretized governing equations numerically.

B.1   Finite Volume Method

The finite volume method includes the discretization of the solution domain, the discretization of the governing equations, and the boundary conditions. Each of these are discussed in more detail below.

B.1.1 Discretization of the Solution Domain

Discretization of the solution domain includes the temporal discretization (if required) and spatial discretization. The temporal discretization is straightforward: for a transient problem, the time domain $[0, T]$ is divided into a set of finite time steps or time intervals Δt, which could vary during the numerical simulation. The spatial discretization can be performed in different ways, where the spatial domain V is divided into a set of finite control volumes ΔV, or computational cells, which fill the entire spatial domain without overlapping each other.

The complete computational mesh, which represents the spatial domain occupied by the fluid, is formed by the internal field which is represented by the computational cells, and the boundary fields which are usually represented by a set of cell faces that coincide with the boundaries of the spatial domain. As shown in Fig. 57, each computational cell is bounded by a set of cell faces, which can be generated using a set of cell vertex points.

The mesh generates the discretization of the physical fields, material parameters, etc. In particular, the cell-centered values correspond to the centroids of the cells $\mathbf{r}_P$, which are defined so that

$$\int_v (\mathbf{r} - \mathbf{r}_P)\, dV = 0, \tag{238}$$

while face-centered values correspond to the centers of the cell faces $\mathbf{r}_f$, which are defined so that

$$\int_f \left(\mathbf{r} - \mathbf{r}_f\right) dS = 0. \tag{239}$$

Finally, the edge-centered values correspond to the middle of the edges. For instance, the discretizations of boundary fields, such as the interfacial temperature, use face-centered values, while edge-centered values of the interfacial temperature are used to compute the temperature gradients which determine thermocapillary stresses.

B.1.2 Discretization of the Equations

The governing equations, written in the form of partial differential equations here, are discretized into a set of algebraic equations. For a divergence-free velocity field, transport equations for a tensorial field ϕ can be written in the form

$$\underbrace{\partial_t(\rho\phi)}_{\text{time derivative}} + \underbrace{\nabla \cdot (\rho\mathbf{u}\phi)}_{\text{advection term}} - \underbrace{\nabla \cdot (\Gamma\nabla\phi)}_{\text{diffusion term}} = \underbrace{S_\phi}_{\text{source term}}, \tag{240}$$

where ρ is the density, $\mathbf{u}$ is the velocity, and Γ is the diffusivity. The discretization of a transport equation using the finite volume method is based on the integral form of that equation, where integrals over the volume V of a cell for the terms involving spatial derivatives can be written as a sum of the integrals over the surfaces S that bound the cell based on the Gauss' theorem

$$\int_V (\nabla \otimes \phi)\, dV = \int_S (\mathbf{n} \otimes \phi)\, dS, \tag{241}$$

where $\mathbf{n}$ is the unit outward normal vector, and the symbol $\otimes$ defines a tensor product, such that $\nabla \otimes \phi$ can represent various derivatives including the divergence $\nabla \cdot \phi$, the gradient $\nabla\phi$, and the curl $\nabla \times \phi$.

The surface integral on the right-hand-side of (241) can then be estimated based on the surface fields ϕ_f, which are either specified directly or are approximated using the values specified at the neighboring cell centroids via different numerical schemes [213, 214], including central differencing (CD), which is second order accurate but unbounded; upwind differencing (UD), which guarantees boundedness but is first order accurate; and blended differencing (BD), which preserves boundedness with reasonable accuracy. The discretization of different terms is discussed in more detail below.

B.1.2.1 Divergence

The integral of a divergence term over a control volume can be rewritten as a sum of the surface integrals, following Gauss' theorem (241),

$$\int_V (\nabla \cdot \phi)\, dV = \int_S (\mathbf{n} \cdot \phi)\, dS \approx \sum_f \mathbf{S}_f \cdot \phi_f, \tag{242}$$

180

where $\mathbf{S}_f = \mathbf{n}S_f$ is the outward pointing surface area vector, and ϕ_f is the surface field which is either specified or evaluated based on the face interpolation as discussed above.

B.1.2.2 *Gradient*

There are different discretization schemes for the gradient terms. For the cell-centered gradient, Gauss's theorem (241) leads to

$$\int_v (\nabla\phi)\, dV = \int_s (\mathbf{n}\phi)\, dS \approx \sum_f \mathbf{S}_f \phi_f. \qquad (243)$$

Alternatively, the cell-center gradient can be evaluated by the least squares method [215], which determines the gradient by minimizing the weighted errors for estimating cell-centered values of ϕ at all the cells neighboring the control volume based on the gradient and the value of ϕ at the center of the control volume.

Face-normal component of the gradient $\mathbf{n}\cdot\nabla_f\phi$ also requires discretization. For orthogonal meshes where grid lines are perpendicular at the intersection, the vector $\mathbf{d} = \mathbf{r}_P - \mathbf{r}_N$ connecting the centroids of two connecting cells is normal to the cell face that is shared by the two cells, therefore the corresponding face-normal gradient can be estimated as

$$\mathbf{n}\cdot\nabla_f\phi = \frac{\phi_N - \phi_P}{|\mathbf{d}|}, \qquad (244)$$

where ϕ_P and ϕ_N are the values at the centroids P and N of the two connecting cells. For non-orthogonal meshes, the discretization for the face-normal gradient is augmented to take into account for both the orthogonal contribution and the non-orthogonal contribution [216].

B.1.2.3 Advection Term

The volume integral of the advection term $\nabla \cdot (\rho \mathbf{u} \phi)$ from (240) is discretized using Gauss's theorem (241)

$$
\begin{aligned}
\int_v \nabla \cdot (\rho \mathbf{u} \phi)\, dV &= \int_s (\mathbf{n} \cdot \rho \mathbf{u} \phi)\, dS \\
&\approx \sum_f \mathbf{S}_f \cdot (\rho \mathbf{u})_f\, \phi_f \\
&= \sum_f \rho \dot{V}_f \phi_f,
\end{aligned}
\tag{245}
$$

where

$$
\dot{V}_f = \mathbf{S}_f \cdot \mathbf{u}_f
\tag{246}
$$

is the volume flux through the cell face f.

B.1.2.4 Diffusion Term

The volume integral of the diffusion term $\nabla \cdot (\Gamma \nabla \phi)$ from (240) can be discretized as

$$
\begin{aligned}
\int_v \nabla \cdot (\Gamma \nabla \phi)\, dV &= \int_s (\mathbf{n} \cdot \Gamma \nabla \phi)\, dS \\
&\approx \sum_f \mathbf{S}_f \cdot \Gamma_f \nabla_f \phi,
\end{aligned}
\tag{247}
$$

where the normal face gradient $\mathbf{S}_f \cdot \nabla_f \phi$ is estimated based on the cell-center values, as discussed in section B.1.2.2.

B.1.2.5 Source Term

In general, the source term $\mathcal{S}_\phi$ from (240) can be a function of ϕ. To facilitate the linearization of the transport equation, which will be discussed below in B.1.4, the source term is typically linearized before the discretization

$$
\mathcal{S}_\phi = \mathcal{S}_i \phi + \mathcal{S}_{ii},
\tag{248}
$$

where both $\mathcal{S}_i$ and $\mathcal{S}_{ii}$ can depend on ϕ. The discretization is hence

$$
\int_v \mathcal{S}_\phi dV \approx \mathcal{S}_i \phi V_P + \mathcal{S}_{ii} V_P.
\tag{249}
$$

182

The time derivative $\partial_t(\rho\phi)$ in (240) can be discretized using the difference between the "new" values at the next time step, $\phi^n \equiv \phi(t + \Delta t)$, the "old" values at the previous time step, $\phi^o \equiv \phi(t)$, and sometimes the "old-old" values at the time step before the previous one, $\phi^{oo} \equiv \phi(t - \Delta t)$. In this study the second-order accurate backward differencing scheme [217] is used, hence

$$\int_v \partial_t(\rho\phi)dV \approx \frac{3(\rho\phi V)_P^n - 4(\rho\phi V)_P^o + (\rho\phi V)_P^{oo}}{2\Delta t}. \tag{250}$$

Alternatively, other numerical schemes [213, 214] can be specified with an input file in OpenFOAM [212].

B.1.3 Discretization in Time

For a transient problem, the spatial derivatives, discussed in Sections B.1.2.1 through B.1.2.5, also need to be discretized in time. In general, following (241), the spatial derivatives are discretized as

$$\begin{aligned}
\int_v (\nabla \otimes \phi)\, dV &= \int_s (\mathbf{n} \otimes \phi)\, dS \\
&\approx \sum_f \mathbf{S}_f \otimes \phi_f,
\end{aligned} \tag{251}$$

thus, to leading order in Δt,

$$\int_t^{t+\Delta t} \left[\int_v (\nabla \otimes \phi)\, dV \right] dt \approx \left[\sum_f \mathbf{S}_f \otimes \phi_f \right]^i \Delta t. \tag{252}$$

where i denotes the time step n, o and oo.

There are different ways of estimating (252) that can be specified in the numerical code, depending upon the choice of the time when ϕ is evaluated [213, 214]. In this study the implicit Euler method is used, which corresponds to setting $i = n$. It is a first-order accurate, unconditionally stable and guarantees boundedness.

B.1.4 Linearization of the Transport Equation

With the discretization discussed in B.1.2 and B.1.3, the integral form of the general transport equation (240) for the control volume V_P

$$\underbrace{\int_t^{t+\Delta t}\left[\int_{V_P}\partial_t(\rho\phi)dV\right]dt}_{\text{time derivative}} + \underbrace{\int_t^{t+\Delta t}\left[\int_{V_P}\nabla\cdot(\rho\mathbf{u}\phi)\,dV\right]dt}_{\text{advection term}} - \underbrace{\int_t^{t+\Delta t}\left[\int_{V_P}\nabla\cdot(\Gamma\nabla\phi)\,dV\right]dt}_{\text{diffusion term}}$$

$$= \underbrace{\int_t^{t+\Delta t}\left[\int_{V_P}\mathcal{S}_\phi dV\right]dt}_{\text{source term}}$$

(253)

can be discretized as

$$\frac{3(\rho\phi V)_P^n - 4(\rho\phi V)_P^o + (\rho\phi V)_P^{oo}}{2\Delta t} + \sum_f \mathbf{S}_f^n\cdot(\rho\mathbf{u})_f^n\,\phi_f^n - \sum_f \mathbf{S}_f^n\cdot\Gamma_f^n\nabla_f^n\phi$$

$$= \mathcal{S}_i^n\phi_P^n V_P^n + \mathcal{S}_{ii}^n V_P^n.$$

(254)

based on (250), (245), (247) and (249), where the backward differencing scheme is used for the time derivatives and the implicit Euler scheme for the time discretization of the spatial terms.

Discretization converts the partial differential equation (253) into a set of algebraic equations for the values ϕ_P^n of the field ϕ at each computational mesh cell

$$\mathcal{A}_P\phi_P^n + \sum_N \mathcal{A}_N\phi_N^n = \mathcal{B}_P,$$

(255)

where $\mathcal{A}_P$ includes all the coefficients corresponding to ϕ_P^n, which show up in the time derivative, the advection and diffusion term, and the linear part for the source terms at the new (current) time step; $\mathcal{A}_N$ includes all the coefficients corresponding to the values ϕ_N^n at the neighboring cells, which show up in the advection and diffusion term at the new time step. The summation is done over all the neighboring cells that share a face with the cell P. On the other hand, $\mathcal{B}_P$ includes the rest of the terms contained in the time derivatives that involve neither ϕ_P^n nor ϕ_N^n as well as the advection and diffusion terms evaluated at the previous time step(s) and the constant source terms.

The system of algebraic equations (255) can be written as

$$[\mathcal{A}]^n [\phi]^n = [\mathcal{B}], \tag{256}$$

where $[\mathcal{A}]^n$ is a sparse matrix with the diagonal coefficients $\mathcal{A}_P$ and off-diagonal coefficients $\mathcal{A}_N$, $[\phi]^n$ is the vector consisting of the values ϕ_P^n the field ϕ takes at the cell centroids of the entire mesh at the new time step, while $[\mathcal{B}]$ is a vector consisting of $\mathcal{B}_P$. This system (256) can be solved using different numerical algorithms [214, 218, 219], including both direct methods and iterative methods. When the matrix $[\mathcal{A}]^n$ is large and sparse, it is usually more efficient to use iterative methods.

The transport equations for the momentum, temperature and density are all discretized using the above procedure and solved together with the continuity equation. The velocity and pressure are strongly coupled with each other, while they are relatively weakly coupled with the temperature and the density field. Therefore an iterative method is used to compute the velocity and pressure. The details of the procedure are discussed below in Section B.3.

B.1.5 Discretization of the Boundary Conditions

In order to close the problem, making it well-defined, boundary conditions need to be specified on all the boundaries, including the free surface. Additionally, initial conditions also need to be specified for the transient problem. Discretization requires, as discussed in the section B.1.2, either the values or the gradients of a field at the cell surfaces. Therefore, as shown in Fig. 58, when the cell face b lies on a boundary, the value and the gradient at the boundary face b are required and need to be prescribed. Two types of boundary conditions are used in this study and will be discussed below.

B.1.5.1   Dirichlet Boundary Conditions

Dirichlet boundary conditions prescribe the values ϕ_f of a field on the boundary faces. When the face gradient on the boundary face ($\nabla_f \phi$) is needed, it can be interpolated using
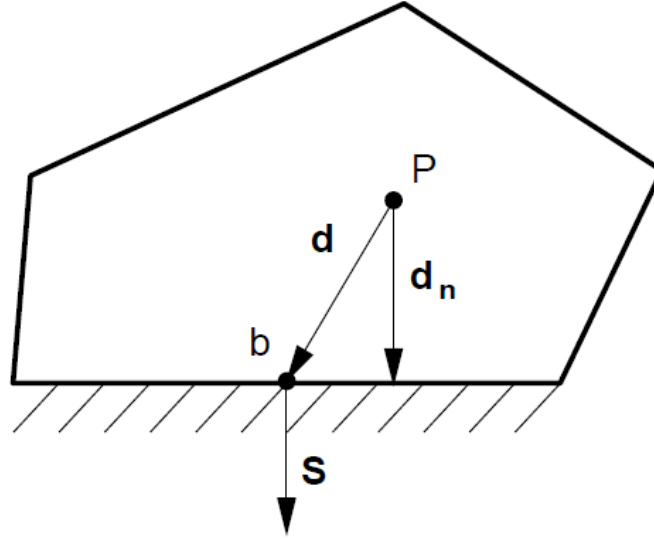
Figure 58: Sketch of the control volume with a boundary face (from [220]). P and b represent the centroids of the control volume and the boundary face, respectively. $\mathbf{S}_f$ represents the face area normal vector. $\mathbf{d}$ represents the distance vector from the cell centroid to the face centroid, while $\mathbf{d}_n$ represent the normal distance vector from the cell centroid to the boundary face, which is parallel to $\mathbf{S}_f$.

the value ϕ_b at the boundary face and the value ϕ_P at the cell centroid,

$$\mathbf{n}_f \cdot (\nabla_f \phi)_b = \frac{\phi_b - \phi_P}{|\mathbf{d}_n|}, \tag{257}$$

where $|\mathbf{d}_n|$ is the normal distance between the cell centroid P and the boundary face f.

B.1.5.2 Neumann Boundary Conditions

Neumann boundary conditions prescribe the gradient $g_b = \mathbf{n}_f \cdot (\nabla_f \phi)_b$ of the variable normal to the boundary at the boundary face. When the value ϕ_f at a cell face is needed, it can be extrapolated using the value ϕ_P at the corresponding cell centroid and the gradient g_b,

$$\phi_b = \phi_P + |\mathbf{d}_n| g_b \tag{258}$$

The discretizations (257) and (258) at the boundaries are second-order accurate when the prescribed boundary conditions, either ϕ_b or g_b are constant along the face. They are only first-order accurate when the prescribed boundary conditions vary along the face and the mesh is non-orthogonal. The correction for the non-orthogonal contribution can be introduced to improve the accuracy [216, 220].
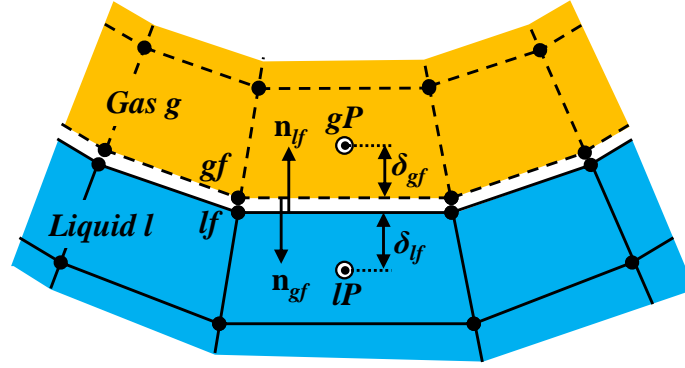
Figure 59: Sketch of the interface with mesh boundaries. lf and gf represent the geometrically identical cell faces at the liquid and the gas side of the interface, with the corresponding normal vector $\mathbf{n}_{lf}$ and $\mathbf{n}_{gf}$. lP and gP represent the cell centroids of the corresponding mesh cells, δ_{lf} and δ_{gf} represent the normal distances between the cell centroids and the cell faces at the interface.

B.2 Moving Mesh Method

In order to simulate two-phase flows, the moving mesh finite volume method is used in this study. As shown in Fig. 59, each phase (liquid or gas) is represented by a separate computational mesh, while the interface between the two phases is represented by two geometrically identical surfaces, which serve as the boundary surfaces for the two phases. In this study, the two boundary surfaces at the interface are discretized in the same way, i.e., for each boundary cell face lf for the liquid phase, there is a corresponding geometrically identical boundary cell face gf for the gas phase.

The transport equations are solved separately on the moving meshes representing both phases, while appropriate boundary conditions are specified on both sides of the interface, coupling the transport in, and the dynamics of, the two phases. In addition, fluid flow and phase change cause movement of the liquid-gas interface and the corresponding distortion of the computational meshes in such a way that cell faces lf an gf always lie at the interface.

B.2.1 Finite Volume Method on the Moving Mesh

To express the transport equations on a moving control volume, the velocity relative to the moving mesh should be used in the advection term. The transport equations are modified based on (240),

$$\underbrace{\partial_t(\rho\phi)}_{\text{time derivative}} + \underbrace{\nabla \cdot [\rho(\mathbf{u} - \mathbf{u}_s)\phi]}_{\text{advection term}} - \underbrace{\nabla \cdot (\Gamma\nabla\phi)}_{\text{diffusion term}} = \underbrace{S_\phi}_{\text{source term}}, \tag{259}$$

where $\mathbf{u}$ is the velocity of the fluid flow and $\mathbf{u}_s$ is the velocity of the mesh or, after this equation has been discretized, the velocity of the centers of the cell faces bounding the control volume (computational cell). Specifically, (245) is generalized to

$$\begin{aligned}
\int_v \nabla \cdot [\rho(\mathbf{u} - \mathbf{u}_s)\phi]\, dV &= \int_s [\mathbf{n} \cdot \rho(\mathbf{u} - \mathbf{u}_s)\phi]\, dS \\
&\approx \sum_f \left(\rho\mathbf{S}_f \cdot \mathbf{u}_f - \rho\mathbf{S}_f \cdot \mathbf{u}_s\right]\phi_f \\
&= \sum_f (\dot{m}_f - \rho\dot{V}_f)\phi_f,
\end{aligned} \tag{260}$$

where $\dot{m}_f = \rho\mathbf{S}_f \cdot \mathbf{u}_f$ is the mass flux through the cell face f, and $\dot{V}_f = \mathbf{S}_f \cdot \mathbf{u}_s$ is the face volume flux due to the motion of the cell face f. While the mass flux satisfy the mass conservation, the face volume flux must satisfy space conservation [221]

$$\partial_t \int_v dV - \int_s \dot{V}_f = 0. \tag{261}$$

at the discrete level to avoid introducing artificial mass sources [221–223]. In this study, backward differencing scheme is used, and (261) is discretized as

$$\frac{3V_p^n - 4V_p^o + V_p^{oo}}{2\Delta t} - \sum_f \dot{V}_f^n \approx 0. \tag{262}$$

Therefore the face volume flux can be calculated from the volume change of a mesh cell ΔV_P between consecutive time steps, which can be decomposed into a set of volumes ΔV_f swept by each cell face f (that bound the mesh cell) during its movement from the old location to the new location

$$\Delta V_P^n = V_p^n - V_p^o = \sum_f \Delta V_f^n. \tag{263}$$

Combing (262) and (263), the face volume flux through the cell face f

$$\dot{V}_f^n = \frac{3}{2}\frac{\Delta V_f^n}{\Delta t} - \frac{1}{2}\frac{\Delta V_f^o}{\Delta t}.$$

(264)

B.2.2 Mesh Motion Solver

A polyhedral vertex-based mesh motion solver [224] is used in this study to update the computational mesh corresponding to the fluid flow by updating the positions of all the cell vertices of the mesh. The movement of the internal mesh is updated based on the movement of the interface.

B.2.2.1 Movement of the Surface Mesh at the Interface

The displacement of the interface needs to be computed, before the rest of the mesh on both sides can be updated. As shown in Fig. 59, the interface is represented by two sets of geometrically identical cells faces, one for each phase. Therefore, only the displacement of the surface mesh on one side (the liquid side, in this study) needs to be determined. The next mass flux through a cell face lf on the liquid side of the interface should be consistent with the mass flux due to phase change

$$\dot{m}_{lf} - \rho_l \dot{V}_{lf} = J.$$

(265)

The face volume flux at the cell face lf, $\dot{V}_{lf}^i$, should satisfy (265), otherwise, the following correction

$$\dot{V}_{lf}' = \dot{V}_{lf} - \dot{V}_{lf}^i = \frac{\dot{m}_{lf} - J}{\rho_l} - \dot{V}_{lf}^i$$

(266)

is required for the face volume flux and the interface needs to be moved accordingly. At each time step, the interface and then entire mesh are updated based on the results from last time step. The physical fields are updated afterwards without updating the mesh, then (265) is usually not satisfied. Therefore iteration is required, and this is referred as the outer iteration, which will be discussed in details in Sec. B.3.3.

In order to update the position of the interface, the displacement of each vertex on the interface (interface points) needs to be specified so that the required correction of face

189
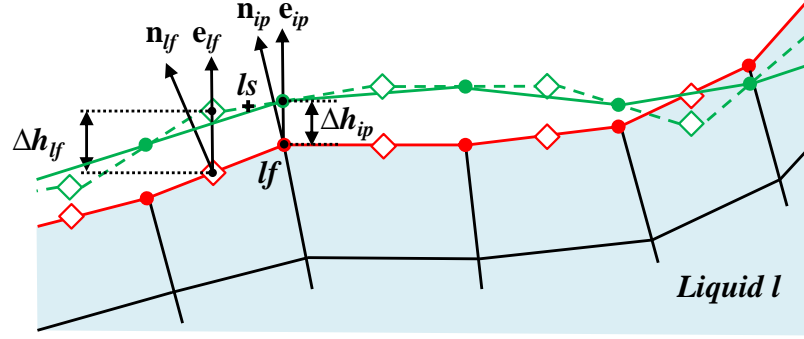
Figure 60: Sketch of the movement of the interface. $\diamond$ represents the control point defined for cell face lf, $\bullet$ represents the interface point, and $+$ presents the point ls calculated based on the neighboring control points. The solid lines connecting the interface points present the interface, the dash lines connecting the control points represent the control point plane, while the red and green color corresponds to the old and new iterations, respectively. Δh_{lf} and Δh_{ip} represent the displacements of the control points and the interface point, while $\mathbf{e}_{lf}$ and $\mathbf{e}_{ip}$ represent the direction vectors for these displacements correspondingly. $\mathbf{n}_{lf}$ and $\mathbf{n}_{ip}$ are the normal vectors of the interface and the control point place.

volume flux $\dot{V}'_{lf}$ is satisfied. This study follows a procedure proposed by Muzaferija and Peric [225] and modified by Tukovic and Jasak [155], where control points are introduced to the interface. As shown in Fig. 60, the control point (represented by the diamond symbol) is introduced to each cell face at the liquid side of the interface, which is typically chosen as the centroid of the cell face initially.

The displacement of the control point in the direction $\mathbf{e}_{lf}$ is

$$\Delta h_{lf} = \frac{\Delta V'_{lf}}{S_{fl} \mathbf{n}_{lf} \cdot \mathbf{e}_{lf}}, \tag{267}$$

where $\mathbf{n}_{lf}$ is the normal vector of the cell face lf, and $\mathbf{e}_{lf}$ is an arbitrary unit vector which defines the control point displacement direction. In this study, $\mathbf{e}_{lf}$ is chosen as the normal vector $\mathbf{e}_{lf}$ from the previous iteration. $\Delta V'_{lf}$ is the volume swept by the cell face lf during its movement from the old position to the new position, and is calculated based on the correction for face volume flux $\dot{V}'_{lf}$. For the backward differencing scheme

$$\Delta V'_{lf} = \frac{2}{3} \dot{V}'_{lf} \Delta t. \tag{268}$$

190

Therefore the new position of the control point can be specified with the position vector

$$\mathbf{r}_{lf}^k = \mathbf{r}_{lf}^{k-1} + \Delta h_{lf}\mathbf{e}_{lf}, \tag{269}$$

where k represents the number of iterations.

Afterwards each interface point (represented by the dot in Fig. 60) is moved onto a control point plane (represented by the dash line in Fig. 60) laid over the corresponding control points. The displacement of the interface point in the direction $\mathbf{e}_{ip}$ is

$$\Delta h_{ip} = \frac{\mathbf{n}_{ip} \cdot (\mathbf{r}_{ls} - \mathbf{r}_{ip}^k)}{\mathbf{n}_{ip} \cdot \mathbf{e}_{ip}}, \tag{270}$$

where $\mathbf{n}_{ip}$ is the normal vector of the control point plane, and $\mathbf{e}_{ip}$ is an arbitrary unit vector which defines the interface point displacement direction. In this study, $\mathbf{e}_{ip}$ is parallel to $\mathbf{e}_{lf}$. $\mathbf{r}_{ip}^k$ is the position vector for the interface point from the previous iteration, while $\mathbf{r}_{ls}$ is the position vector for a point ls on the control point plane that is calculated based on the corresponding control points

$$\mathbf{r}_{ls} = \frac{\sum_{lf} w_{lf}^2 \mathbf{r}_{lf}}{\sum_{lf} w_{lf}^2}, \tag{271}$$

where the summation is performed over all the neighboring control points to the interface point, and the weighing factor w_{lf} is the inverse distance from the control point to the interface point [155].

Therefore the new position of the interface point is

$$\mathbf{r}_{ip}^k = \mathbf{r}_{ip}^{k-1} + \Delta h_{ip}\mathbf{e}_{ip}. \tag{272}$$

For the interface points that lie on the wall boundary ipb, the mirror control points lfm are introduced in order to determine the control point plane. As shown in Fig. 61, a virtual symmetry plane sP is defined based on the specified normal vector $\mathbf{n}_b$, hence the position of the mirror control point is

$$\mathbf{r}_{lfm} = \mathbf{r}_{lf} - 2(\mathbf{r}_{lf} - \mathbf{r}_{ipb}^k) \cdot \mathbf{n}_b\mathbf{n}_b, \tag{273}$$

where $\mathbf{r}_{lf}$ specifies the position of the control point for the cell face at the boundary. Then the position of the interface point at the boundary is also moved to the control point plane defined by the corresponding control points and the mirror control points using (272).

Moreover, the contact angle for the liquid phase at the solid wall can be specified by adjusting the mirror control points and hence the control point plane defined by the control points and the corresponding mirror control points. As shown in Fig 61, when the surface normal of the virtual symmetry plane $\mathbf{n}_b$ is parallel to the surface normal on the solid wall $\mathbf{n}_w$ (c.f. Fig 61(a)), the control point plane (represented by the dash line) is perpendicular to the solid wall, therefore enforcing the contact angle $\theta = 90°$. When the normal vector $\mathbf{n}_b$ is defined at an angle θ to $\mathbf{n}_w$ (c.f. Fig 61(b)), the control point plane will be at the angle θ to the wall as well, hence enforcing the specified contact angle θ as the interface points at the boundary are updated.
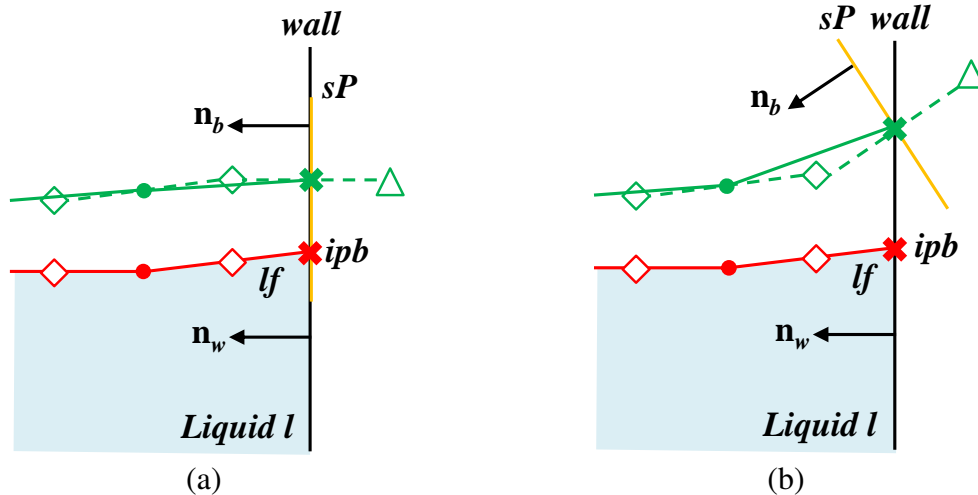
Figure 61: The interface at the solid boundary. ◇ represents the control point, △ represents the mirror control point, ● represents the internal interface point, and × represents the interface point at the solid boundary. The solid lines connecting the interface points present the interface, the dash lines connecting the control points represent the control point plane, while the red and green color corresponds to the old and new iterations, respectively. The black solid line represents the solid wall with the wall normal vector $\mathbf{n}_w$, and the orange solid line represents the virtual symmetry plane sP defined by the normal vector $\mathbf{n}_b$.

The polyhedral vertex-based mesh motion solver [224] is used in this study. The displacement of all the internal vertices is determined by solving the discretized mesh motion equations subject to the motion of the cell faces lying at the interface, while preserving the topology of the mesh. Either the algebraic mesh motion equation or the Laplace equation with constant or variable diffusivity is chosen as the motion equations. The computational mesh is updated iteratively as the position of all the mesh vertices $\mathbf{r}_p$ are updated based the solution of the velocity $\mathbf{u}_p$ at all the vertices

$$\mathbf{r}_p^k = \mathbf{r}_p^{k-1} + \mathbf{u}_p \Delta t. \tag{274}$$

The movement of the computational mesh is coupled with the fluid flow and heat and mass transport, iteration is hence required within each time step so that the computational mesh and the dependent variables are consistent, this will be discussed later in B.3.

B.2.3 Boundary Conditions at the Interface

Appropriate boundary conditions, which are discussed in 2.6.1, need to be discretized and specified at both sides of the interface before the transport equations are discretized and solved for in each phase. While the discretization of the boundary conditions at the solid walls are straightforward, as discussed in B.1.5, the discretization of the boundary conditions at the interface are less easy and is discussed below.

B.2.3.1 Discretization at the Interface

The interface is discretized into a set of geometrically identical mesh cell faces on either side of the interface, the dependent variables at the interface are stored at the center of the cell faces, denoted with the subscript lf or gf, on either the liquid or the gas side, while the dependent variables for the corresponding control volumes are stored at the cell centroid, denoted with the subscript lP or gP.

The normal component of the surface gradient of the tensorial field ϕ is estimated using

193

one sided first order approximation

$$\mathbf{n}_{gf} \cdot \nabla\phi_{gf} \approx \frac{\phi_{gP} - \phi_{gf}}{\delta_{gf}}$$

$$\mathbf{n}_{lf} \cdot \nabla\phi_{lf} \approx \frac{\phi_{lP} - \phi_{lf}}{\delta_{lf}},$$

(275)

where $\mathbf{n}_{lf} = -\mathbf{n}_{gf}$, which are the outward pointing normal vector of cell face lf and gf, respectively, and δ_{lf} and δ_{gf} represent the normal distance between the cell centroid (lP and gP) and the cell faces (lf and gf) on either side of the interface.

The surface derivatives are estimated using the surface Gauss's integral theorem

$$\int_s (\nabla_s \otimes \phi)\, dS = \int_l (\mathbf{t} \otimes \phi)\, dL - \int_s (\kappa\mathbf{n} \otimes \phi)\, dS,$$

(276)

where κ is the surface curvature, $\mathbf{t}$ represents the unit vector normal to the boundary of the surface and tangential to the surface, $\mathbf{n}$ represents the unit outward pointing normal vector at the surfaces, and the symbol $\otimes$ represents the tensor products and therefore $\nabla \otimes \phi$ represents respective derivatives, including the divergence $\nabla \cdot \phi$ and the gradient $\nabla\phi$.

The line integral can be approximated by the sum on all the edges of the surface, and the surface integral can be approximated using the values at the cell face centroid, therefore the surface divergence on surface f can be discretized as

$$\nabla_s \cdot \phi = \frac{1}{S_f} \sum_e (\mathbf{t}_e \cdot \phi_e)\, L_e - \kappa_f\mathbf{n}_f \cdot \phi_f,$$

(277)

and the surface gradient can be discretized as

$$\nabla_s\phi = \frac{1}{S_f} \sum_e (\mathbf{t}_e\phi_e)\, L_e - \kappa_f\mathbf{n}_f\phi_f,$$

(278)

where ϕ_e is evaluated at the edge e of the cell surface, from the interpolation between the cell surface and the neighboring cell surface that shares the edge e; the normal vector to the edge $\mathbf{t}_e$ is approximated as

$$\mathbf{t}_e = \frac{\mathbf{e} \times (\mathbf{n}_i + \mathbf{n}_j)}{|\mathbf{e}||\mathbf{n}_i + \mathbf{n}_j|},$$

(279)

where $\mathbf{e}$ is the vector connecting the vertices i and j of the edge e, $\mathbf{n}_i$ and $\mathbf{n}_j$ are the unit normal vectors at the vertices, and κ_f is the average surface curvature of the cell face.

The unit normal vector $\mathbf{n}_i$ at the vertex i is estimated as the normal vector of a least squares biquadratic surface, which is fitted through the set of vertices that belongs to the faces sharing the vertex i, and passes through the vertex i. The average surface curvature κ_f is estimated from the normal component of the surface tension

$$\kappa_f = \frac{\mathbf{n}_f \cdot \sum_e (\mathbf{t}_e \sigma_e) L_e}{\sigma_f S_f} \tag{280}$$

B.2.3.2 *Interface Iteration*

Most of the boundary conditions at the interface are coupled with each other and need be solved at the same time, which is essentially a problem of solving a set of equations $\mathcal{F}(\mathbf{x}) = 0$, where $\mathbf{x}$ is a vector which consist of all the unknowns. Newton iteration is used to find the solutions for this set of equations, by finding successive better approximation of the solutions (or roots). The differences between the two successive approximations can be estimated by

$$\mathcal{J}_F|_{\mathbf{x}=\mathbf{x}(n-1)} [\mathbf{x}(n) - \mathbf{x}(n-1)] = \mathcal{F}(\mathbf{x}(n-1)), \tag{281}$$

where $\mathcal{J}_F = \frac{\partial \mathcal{F}}{\partial \mathbf{x}}$ is the Jacobian matrix, and the initial guess $\mathbf{x}_0$ correspond to the equilibrium state, for example, $J(0) = 0$, $T_l = T_v = T_i = T_s$, *etc.*. This iteration at the interface is converged after the norm of the residual $\mathcal{F}(\mathbf{x}(n))$ is smaller than the prescribed criteria.

As discussed in 2.6.1, the equations and the corresponding unknowns are different for different conditions and with different phase change models. The vapor pressure is not updated during the iteration at the interface and the value is obtained from the previous outer iteration.

When the gas phase is pure vapor, and KTG model is used for predicting the phase change, the unknown vector is

$$\mathbf{x} = \begin{bmatrix} J, & T_i, & T_s, & V_{ni}, & \rho_v \end{bmatrix}^T, \tag{282}$$

where $V_{ni} = \mathbf{n} \cdot (\mathbf{u}_g - \mathbf{u}_i)$ is the normal component of the velocity relative to the interface at the gas side. The correspond set of equations consist of (56), (45), (237), (42) and (14).

When the gas phase is pure vapor, and NET model is used for predicting the phase change, the unknown vector is

$$\mathbf{x} = \begin{bmatrix} J, & T_l, & T_v, & T_s, & V_{ni}, & \rho_v \end{bmatrix}^T,$$ (283)

and the correspond set of equations consist of (57), (58), (45), (237), (42) and (14).

When the gas phase is pure vapor, and SRT model is used for predicting the phase change, the unknown vector is

$$\mathbf{x} = \begin{bmatrix} J, & T_l, & T_v, & T_s, & V_{ni}, & \rho_v \end{bmatrix}^T,$$ (284)

and the correspond set of equations consist of (59), (60), (45), (237), (42) and (14).

When the gas phase is a binary mixture, and KTG model is used for predicting the phase change, the unknown vector is

$$\mathbf{x} = \begin{bmatrix} J, & T_i, & T_s, & V_n, & \rho_d, & \mathbf{n} \cdot \nabla \rho_v^n, & \mathbf{n} \cdot \nabla \rho_a^n \end{bmatrix}^T,$$ (285)

and the correspond set of equations consist of (56), (45), (48), (49), (42), (51) and (14).

With the solutions of the interface iteration, the boundary conditions on both sides of the liquid-gas interface, *i.e.*, on each cell face *lf* and *gf* along the interface, can be either directly specified or calculated, therefore coupling the two phases. The boundary conditions for each dependent variables are discussed below.

B.2.3.3 Boundary Conditions for Velocity

The normal derivative of the velocity at the liquid side is specified on the cell face *lf*

$$\begin{aligned} \mathbf{n}_{lf} \cdot \nabla \mathbf{u}_{lf} = &\mathbf{n}_{lf}(\mathbf{n}_{lf} \cdot \nabla \mathbf{u}_{lf}) \cdot \mathbf{n}_{lf} \\ &+ \mathbf{t}_{lf}(\mathbf{n}_{lf} \cdot \nabla \mathbf{u}_{lf}) \cdot \mathbf{t}_{lf}. \end{aligned}$$ (286)

The second term on the right hand side of (286) represents the tangential contribution,

which can be calculated based on the tangential stress balance (72)

$$
\begin{aligned}
\mathbf{t}_{lf}(\mathbf{n}_{lf} \cdot \nabla \mathbf{u}_{lf}) \cdot \mathbf{t}_{lf} &= \mathbf{n}_{lf} \cdot (\nabla \mathbf{u}_t)_{lf} \\
&= -\frac{\mu_g}{\mu_l} \left[\mathbf{n}_{gf} \cdot (\nabla \mathbf{u}_t)_{gf} \right] \\
&\quad + \frac{\mu_g - \mu_l}{\mu_l} \left(\nabla_s \mathbf{u}_{lf} \cdot \mathbf{n}_{lf} \right) \\
&\quad - \frac{\gamma}{\mu_l} \nabla_s T_l,
\end{aligned}
\tag{287}
$$

where the normal gradient of the tangential velocity on the gas side is evaluated using the one sided first order approximation (275).

The normal derivative of the velocity at the liquid side (286) is therefore updated with the help of (287) and (275)

$$
\begin{aligned}
\mathbf{n}_{lf} \cdot \nabla \mathbf{u}_{lf} &\approx \mathbf{n}_{lf}(\mathbf{n}_{lf} \cdot \nabla \mathbf{u}_{lf}) \cdot \mathbf{n}_{lf} \\
&\quad - \frac{\mu_g}{\mu_l} \frac{(\mathbf{u}_{gP})_t - (\mathbf{u}_{lf})_t}{\delta_{gf}} \\
&\quad + \frac{\mu_g - \mu_l}{\mu_l} \left(\nabla_s \mathbf{u}_{lf} \cdot \mathbf{n}_{lf} \right) \\
&\quad - \frac{\gamma}{\mu_l} \nabla_s T_l,
\end{aligned}
\tag{288}
$$

where $(\mathbf{u}_{lP})_t$ is the tangential velocity at the cell centroid, and $(\mathbf{u}_{lf})_t$ is the tangential velocity at the cell face center, which is updated using (291) and (292).

The first term on the right hand side of (288) represents the normal contribution, which can be estimated directly based on the one sided first order approximation

$$
\mathbf{n}_{lf}\mathbf{n}_{gf} \cdot \nabla(\mathbf{u}_{gf}) \cdot \mathbf{n}_{gf} \approx \mathbf{n}_{lf} \frac{(\mathbf{u}_{gP})_n - (\mathbf{u}_{lf})_n}{\delta_{gf}},
\tag{289}
$$

or through the surface divergence of the velocity at the interface using (66) since the flow is incompressible

$$
\mathbf{n}_{lf}(\mathbf{n}_{lf} \cdot \nabla \mathbf{u}_{lf}) \cdot \mathbf{n}_{lf} = -\mathbf{n}_{lf}(\nabla_s \cdot \mathbf{u}_{lf})
\tag{290}
$$

On the gas side, the velocity $\mathbf{u}_{lf}$ is specified on the cell face gf, which requires the calculation of both the tangential and the normal component. Along the tangential direction,

the velocity is assumed to be continuous (61)

$$(\mathbf{u}_{lf})_t = (\mathbf{u}_{gf})_t = (\mathbf{u}_i)_t, \tag{291}$$

with the help of the one sided first order approximation (275) and the tangential stress balance (287), the tangential component of the velocity at the interface

$$\begin{aligned}
(\mathbf{u}_i)_t = &\mathcal{M}\left[\frac{\mu_l}{\delta_{lf}}(\mathbf{u}_{lf})_t + \frac{\mu_g}{\delta_{gf}}(\mathbf{u}_{gf})_t\right] \\
&- \mathcal{M}\left(\frac{\gamma}{\mu_l}\nabla_s T_l\right) \\
&+ \mathcal{M}\left[(\mu_g - \mu_l)\left(\nabla_s \mathbf{u}_{lf} \cdot \mathbf{n}_{lf}\right)\right],
\end{aligned} \tag{292}$$

where

$$\mathcal{M} = \frac{\mu_l}{\delta_{lf}} + \frac{\mu_g}{\delta_{gf}} \tag{293}$$

In the normal direction, the velocity at the gas side is updated based on solution V_n from the interface iteration

$$(\mathbf{u}_{gf})_n = (\mathbf{u}_i)_n + \mathbf{n}_{gf} V_n, \tag{294}$$

where $(\mathbf{u}_i)_n$ is the normal velocity at the cell face center (at the interface), and is calculated from the volumetric flux $\dot{V}_{gf}$ through the cell face S_{gf}

$$(\mathbf{u}_i)_n = \frac{\dot{V}_{gf}}{S_{gf}}\mathbf{n}_{gf}. \tag{295}$$

The velocity at the gas side is therefore

$$(\mathbf{u}_{gf}) = (\mathbf{u}_{gf})_t + (\mathbf{u}_{gf})_n, \tag{296}$$

where the tangential component is updated using (292), and the normal component is updated using (294).

B.2.3.4   Boundary Conditions for Pressure

Dynamic pressure p_d is used when solving the velocity and pressure field, which is related with the total pressure

$$p = p_d + \rho\mathbf{g}\cdot\mathbf{r}, \tag{297}$$

where **r** is the distance vector of the cell centroid.

The dynamic pressure at the liquid side $(p_{lf})_d$ is updated on the cell face lf, which is calculated based on the normal stress balance (68) with the help of (297)

$$
\begin{aligned}
(p_{lf})_d =& (p_{gf})_d + (\rho_g - \rho_l)\mathbf{g} \cdot \mathbf{r}_i \\
& - (\sigma\kappa)_{lf} \\
& + 2(\mu_g - \mu_l)\nabla_s \cdot \mathbf{u}_{lf}
\end{aligned}
\tag{298}
$$

At the gas side, the normal gradient of the dynamic pressure $\mathbf{n}_{gf} \cdot \nabla(p_{gf})_d$ is specified on the cell face gf, using the normal component of the momentum equation

$$
\mathbf{n}_{gf} \cdot \nabla(p_{gf})_d = -\rho_B \mathbf{n}_{gf} \cdot (\partial_t \mathbf{u} + \mathbf{u} \cdot \nabla\mathbf{u})_{gf} + \rho_B(T)\,\mathbf{n}_{gf} \cdot \mathbf{g}
\tag{299}
$$

B.2.3.5 Boundary Conditions for Temperature

At the gas side, the temperature T_{gf} at the cell face gf is specified with the solution of T_g from the interface iteration. When the NET and SRT model are used, T_g is solved separately from T_l, and

$$
T_{gf} = T_g,
\tag{300}
$$

when the KTG model is used, the temperature is assumed to be continuous across the interface and

$$
T_{gf} = T_i.
\tag{301}
$$

At the liquid side, the normal temperature gradient $\mathbf{n}_{lf} \cdot \nabla T_{lf}$ is updated based on the heat flux balance (45) with the help of the one sided first order approximation for the gas side temperature gradient (275)

$$
\mathbf{n}_{lf} \cdot \nabla T_{lf} = \frac{k_g}{k_l}\left(\frac{T_{gP} - T_{gf}}{\delta_{gf}}\right) - \frac{1}{k_l}(\mathcal{L}J).
\tag{302}
$$

Since the boundary conditions for the density of the dilute component is only required for the gas phase, the normal gradient of the concentration of the dilute component n is specified on the cell face gf with the solution from the interface iteration

$$\mathbf{n}_{gf} \cdot \nabla \rho_{gf}^{n} = \mathbf{n}_{gf} \cdot \nabla \rho_{gi}^{n}. \tag{303}$$

B.3 Solution Procedure

For a transient problem for the two phase non-isothermal flow, with the moving mesh method with finite volume method, the velocity $\mathbf{u}$, the pressure p, the temperature T and the density ρ^{n} for the dilute component (in case of a binary mixture) are solved for at the centroids of the computational cells from the discretized governing equations, which are sets of algebraic equations, subject to the movement of the computational meshes and the boundary conditions at the solid walls as well as the interface. The movement of the mesh, the boundary conditions and the bulk field are coupled with each other, a segregated approach used in this study where the systems are solved iteratively.

B.3.1 Pressure-Velocity Coupling

The continuity equation and the Navier-Stokes equation are solved together for the velocity and the pressure. Using the segregated procedure, the pressure is decoupled from the Navier-Stokes equations, while the pressure equation is obtained from combing the continuity equation and the momentum equation.

As discussed in B.1, the discretized continuity equation is

$$\sum_{f} \left(\mathbf{S}_{f}^{n} \cdot \mathbf{u}_{f}^{n} \right) = 0, \tag{304}$$

and the algebraic equation after discretization of the Navier-Stokes equation is

$$\mathcal{A}_{\mathbf{u},P}^{n} \mathbf{u}_{P}^{n} + \sum_{N} \mathcal{A}_{\mathbf{u},N}^{n} \mathbf{u}_{P}^{n} = -\nabla p_{P}^{n} + \mathcal{B}_{\mathbf{u},P}^{n}, \tag{305}$$

where the pressure force is not discretized here in order to construct the pressure equation later.

PISO (Pressure Implicit with Splitting of Operators) algorithm [226] is used in this study, where the velocity field is predicted before the pressure equation is solved so that continuity is satisfied, and velocity is then corrected based on changes in pressure field. It is an iterative procedure which is discussed below until both the pressure and the velocity field converge.

1. **Predict the velocity**

   The prediction of the velocity is obtained from the discretized momentum equation (305) using the pressure field from the previous time step

   $$\mathbf{u}_P^n = \frac{1}{\mathcal{A}_{\mathbf{u},P}^n}\mathcal{H}_{\mathbf{u},P}^n - \frac{1}{\mathcal{A}_{\mathbf{u},P}^n}\nabla p_P^{n-1}, \tag{306}$$

   where the operator $\mathcal{H}_{\mathbf{u},P}^n$ combines the contribution from the neighboring cells (except the pressure force) and the source terms

   $$\mathcal{H}_{\mathbf{u},P}^n = -\sum_N \mathcal{A}_{\mathbf{u},N}^n \mathbf{u}_P^n + \mathcal{B}_{\mathbf{u},P}^n. \tag{307}$$

2. **Solve the pressure equation**

   The discretized pressure equation is obtained based on the continuity equation (304), therefore the velocity at the cell faces $\mathbf{u}_f^n$ are required, which can be written in a similar form as (306)

   $$\mathbf{u}_f^n = \left(\frac{\mathcal{H}_{\mathbf{u}}}{\mathcal{A}_{\mathbf{u}}}\right)_f^n - \left(\frac{1}{\mathcal{A}_{\mathbf{u}}}\nabla p\right)_f^n, \tag{308}$$

   where different interpolation schemes [227–230] can be used in order to estimate the operator $\left(\frac{\mathcal{H}_{\mathbf{u}}}{\mathcal{A}_{\mathbf{u}}}\right)_f^n$ and $\left(\frac{1}{\mathcal{A}_{\mathbf{u}}}\right)_f^n$ at the cell faces.

   Substituting the predicted velocity at the cell faces (308) into the discretized continuity equation (304), the discretized pressure equation is

   $$\sum_f \left[\mathbf{S}_f^n \cdot \left(\frac{1}{\mathcal{A}_{\mathbf{u}}}\right)_f^n (\nabla p)_f^n\right] = \sum_f \left[\mathbf{S}_f^n \cdot \left(\frac{\mathcal{H}_{\mathbf{u}}}{\mathcal{A}_{\mathbf{u}}}\right)_f^n\right], \tag{309}$$

which can be solved for the pressure field that satisfy the continuity equation.

3. **Correct the velocity and the flux**

   After solving the pressure field, the velocity field is hence corrected explicitly based on the fully discretized momentum equation of (306) with the solution of the pressure field

   $$\mathbf{u}_P^n = \frac{1}{\mathcal{A}_{\mathbf{u},P}^n} \mathcal{H}_{\mathbf{u},P}^n - \frac{1}{\mathcal{A}_{\mathbf{u},P}^n} \sum_f \mathbf{S}_f^n p_f^n. \tag{310}$$

   The face volume flux $\dot{V}_f^n = \mathbf{S}_f^n \cdot \mathbf{u}_f^n$ is then also updated based on the velocity at the cell faces,

   $$\mathbf{u}_f^n = \left(\frac{\mathcal{H}_{\mathbf{u}}}{\mathcal{A}_{\mathbf{u}}} \right)_f^n - \left(\frac{1}{\mathcal{A}_{\mathbf{u}}} \right)_f^n \sum_f \mathbf{S}_f^n p_f^n. \tag{311}$$

   which again satisfy the continuity equation.

With a segregated approach, iterations for steps 1 to 3 are required until the pressure and the velocity field converge.

B.3.2   Temperature and Density Field

The solution of the temperature and the density field are decoupled from the solution of the pressure and the velocity field and hence are only solved for after the PISO loop converge.

The transport equations are also discretized into sets of algebraic equations

$$\mathcal{A}_{T,P}^n T_P^n + \sum_N \mathcal{A}_{T,N}^n T_P^n = \mathcal{B}_{T,P}^n \tag{312}$$

for the temperature field, and

$$\mathcal{A}_{\rho,P}^n \rho_P^n + \sum_N \mathcal{A}_{\rho,N}^n \rho_P^n = \mathcal{B}_{\rho,P}^n \tag{313}$$

for the density field of the dilute component, when the gas phase is a binary mixture.

The velocity obtained from the previous PISO loop is used for calculating the operators $\mathcal{A}_P^n$, $\mathcal{A}_N^n$ as well as the source terms $\mathcal{B}_P^n$. After temperature and the density field are updated,

202

pressure field and the velocity field are updated again using the PISO loop, until all the fields converge.

Before updating the fields in the bulk, the computational mesh and the boundary conditions for all the fields need to be updated, which requires another level of iterations between them. The complete solution procedure is discussed in the following section.

B.3.3 Sequence of Solution

Each time step involves three major parts: updating the interface shape and the computational mesh; updating the boundary conditions on the velocity, pressure, temperature and density fields; and updating pressure, velocity, temperature, density and concentration fields in the bulk. Since the shape of the interface, the boundary conditions, and the bulk fields are coupled, these three parts are repeated iteratively, until convergence.

The solution procedure are as follows:

1. Initialize the velocity, pressure, temperature and density field with the corresponding values at the previous time step.

2. Initialize the face volume fluxes $\dot{V}_f$ using (246) and (311) with the velocity from the previous time step.

3. Update the pressure offset using (40) with the density from the previous time step.

4. Start the outer iteration, which updates the computational mesh

   (a) Update the position of the interface mesh as discussed in B.2.2.1.

   (b) Update the entire computational mesh on both sides of the interface as discussed in B.2.2.2, which accommodates the movement of the interface.

   (c) Update the face volume flux $\dot{V}_s$ using (264).

   (d) Start the inner iteration, which updates the velocity, pressure, temperature and density with the updated mesh

i. Update the boundary conditions for the velocity and the pressure at both sides of the interface, as discussed in B.2.3.3 and B.2.3.4, respectively, as well as on all the solid walls as discussed in 2.6.2.

ii. Start the PISO loop, which updates only the velocity and the pressure, as discussed in B.3.1:

    A. Update the discretized momentum equation (305), predict the velocity using (306).

    B. Construct and solve the pressure equation (309).

    C. Correct the velocity using (310).

    D. Correct the face volume flux $\dot{V}_f$ using (246) and (311) with the corrected velocity

    E. Check the convergence criteria for the velocity and the pressure, if they don not converge, go back to the beginning of the PISO loop, step (A).

iii. Update all the relevant boundary conditions at the interface using the interface iteration, as discussed in B.2.3.2.

iv. Update the boundary conditions for the temperature and the density at the interface, as discussed in B.2.3.5 and B.2.3.6, respectively, as well as at all the solid walls as discussed in 2.6.2.

v. Solve the discretized temperature equation (312) and update the temperature field.

vi. When the gas phase is a binary mixture, solve the discretized density equation (313) and update the density field, as well as the concentration field using (16).

vii. Check the convergence criteria for the temperature and the density, if they don't converge, go back to the beginning of the inner iteration, step (i).
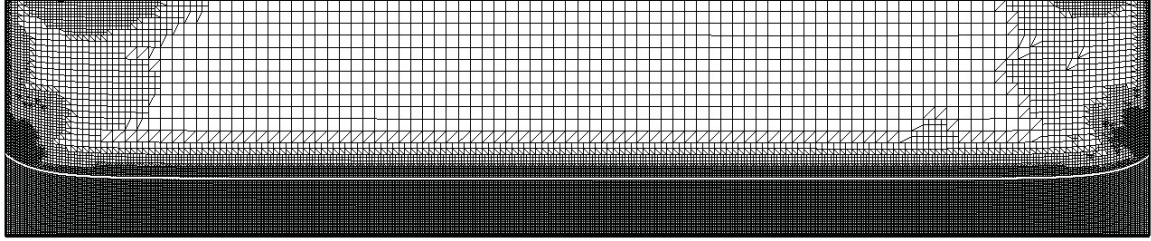
Figure 62: Typical 2D computational mesh showing multiple levels of refinement. All the computational mesh cells are hexahedrons (diagonal lines are rendering artifacts). The largest mesh cell size is 0.5 mm and the smallest mesh cell size is 1/16 mm (= 0.0625 mm). The white solid line indicates the position of the free surface.

(e) Update the face volume fluxes $\dot{V}_f$ at the interface and check the difference between net face fluxes and the mass flux due to phase change. If the residual does not satisfy the criteria, go back to the beginning of the outer iteration, steps (a).

5. If the specified final time is not reached, start a new time step and go back to (1).

B.3.4 Mesh Refinement

In this study, the rectangular domain is discretized into a set of three-dimensional hexahedral mesh cells. In order to perform two-dimensional numeric simulations in the 2D plane, the domain is not discretized into multiple mesh cells along the third dimension. (*i.e.*, the domain is discretized into one layer of mesh cells lying on the 2D plane), and the boundaries in the third dimension, which consist of the cell faces that lies on the 2D plane, are omitted.

As previous numerical studies [19] discovered, and the numerical simulations confirmed, the size of the mesh cells needs to be small enough to resolve the fine structure of the flow, especially in the liquid layer. For instance, it is found that, in order to properly resolve convection rolls in the liquid, the mesh resolution should be at least 1/8 mm (= 0.125 mm). Finer meshes have a greater number of cells and require smaller time steps and, hence, are more computationally expensive. Since the initial transient state is of secondary interest, the system is relaxed to the asymptotic state using a coarse hexahedral mesh (initially all cells are cubical with side 0.5 mm).

Once the transient dynamics have died down, the mesh is refined in several steps, until the results become mesh independent. At each level, the mesh is refined uniformly (by splitting each cell in all three directions) in the liquid phase and in the gas phase just above the free surface. Additionally the mesh in the gas phase is refined in the regions (typically near the contact lines) where the second derivatives of the physical fields (pressure, velocity, or temperature) exceed specified thresholds. A typical mesh applied at the final stage of a simulation is shown in Fig. 62.

APPENDIX C

PROCEDURE FOR NUMERICAL SIMULATIONS

C.1 Problem Specification

In this section, one case is chosen as an example to demonstrate the procedure of the setting up the case, run the numerical simulations, and the mesh refinement. A more detailed tutorial of OpenFOAM is provided in Ref. [212]

The sample case corresponds to a 2-D simulation discussed in Chapter 3. The rectangular test cell has the inner dimensions of the length L = 48.5 mm, the width W = 10 mm, and the height H = 10 mm. As shown in Fig. 4, a layer of liquid (0.65 cSt silicone oil, hexamethyldisloxane) is confined in the test cell below a layer of gas, which is a mixture of vapor and air, held at ambient pressure. The walls of the test cell are made of quartz (fused silica) with thermal conductivity k_w = 1.4 W/(m-K) and have a thickness h_w = 1.25 mm. The temperature difference applied between the outer surface of the walls ΔT = 10 K, and the contact angle θ = 50°.

In OpenFOAM, all the relevant information and results are stored in one directory, which is referred as case directory. The case directory in general has the structure shown as below:

```
                                        polyMesh ———— points
                        t₀,t₁...
                                        p,U,T,rho1...

                                        polyMesh ———— blockMeshDict

                                        faMesh ———— faMeshDefinition
                        constant
                                        dynamicMeshDict

                                        freeSurfaceProperties

                                        controlDict

                                        fvSchemes,fvSolution
        Case
                        system          faSchemes,faSolution

                                        decomposeParDict

                                        cellSetDict,faceSetDict

                        Allrun,Allclean,...
```
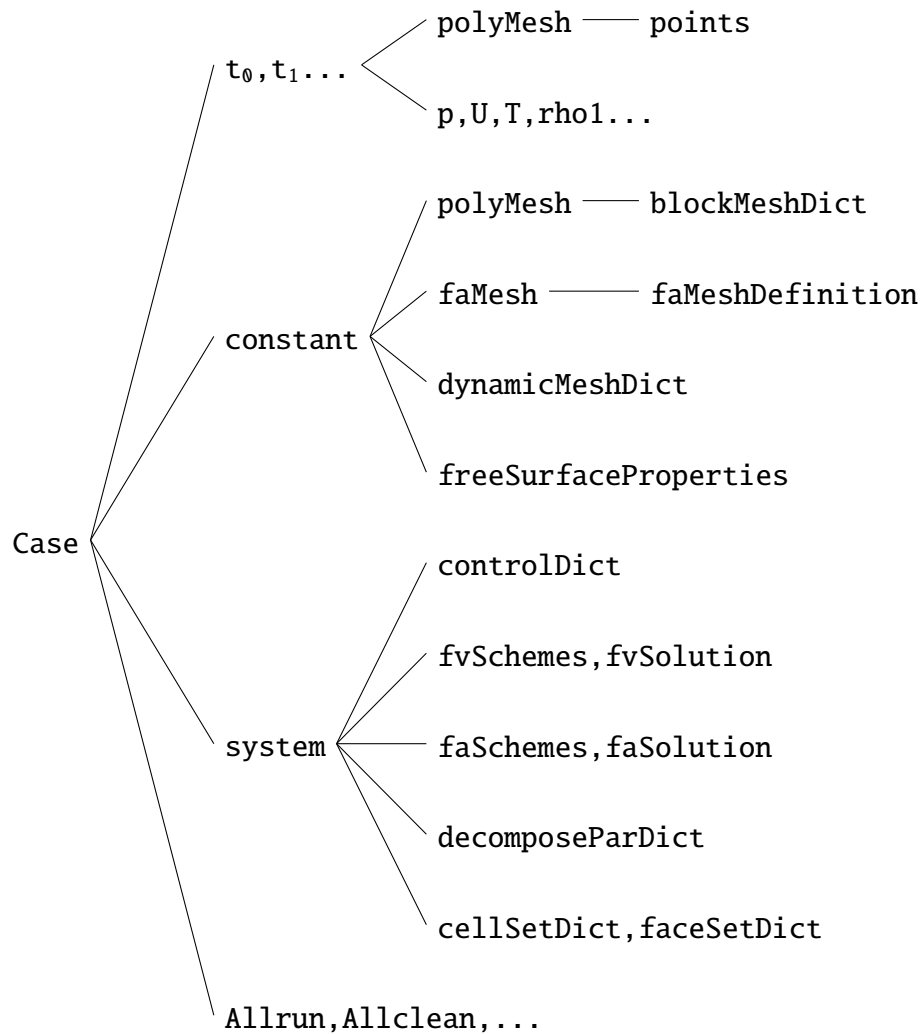
There are three major subdirectories in the case directory. The time directories (t_0, t_1 ...) store the initial values for various fields and their boundary conditions at t_0, as well as the results at specified time (*e.g.*, t_1). The subdirectory `constant` includes the files for generating the volume and surface mesh, for choosing the mesh motion solver, and that specify the relevant material properties. The subdirectory `system` includes files which specify the control parameters for the simulation, the numerical discretization schemes and the linear solver, etc. Finally, the case file also includes some script files (`Allrun,Allclean,...`) which simplify the execution of multiple commands. The details are discussed in the following sections.

C.2 Mesh Generation

In order to generate computational mesh for simulations of the two-phase flow, the space domain need to be discretized in each phase. In addition, the surfaces that represent the interface between the two phases need to be discretized.

C.2.1 Volume Mesh Generation

The computational mesh on both sides of the interface is generated using the mesh generator from OpenFOAM, `blockMesh`, on the input dictionary file, `blockMeshDict`, which is located in the `constant/polyMesh` directory of the case, as shown below:

```
1 /*--------------------------------*- C++ -*----------------------------------*\
2 | =========                 |                                                 |
3 | \\      /  F ield          | OpenFOAM: The Open Source CFD Toolbox          |
4 | \\    /   O peration       | Version:  1.5                                  |
5 |  \\  /    A nd             | Web:      http://www.OpenFOAM.org             |
6 |   \\/     M anipulation    |                                               |
7 \*---------------------------------------------------------------------------*/
8 FoamFile
9 {
10     version     2.0;
11     format      ascii;
12     class       dictionary;
13     object      blockMeshDict;
14 }
15 // * * * * * * * * * * * * * * * * * * * * * * * * * * * * * * * * * * * * * //
16
17 convertToMeters 0.01;
18
19 vertices
20 (
21     (0 0 0)
22     (4.85 0 0)
23     (4.85 0.25 0)
24     (4.85 1 0)
25     (0 1 0)
26     (0 0.25 0)
27     (0 0 0.1)
28     (4.85 0 0.1)
29     (4.85 0.25 0.1)
30     (4.85 1 0.1)
31     (0 1 0.1)
32     (0 0.25 0.1)
33     (4.85 0.25 0)
34     (0 0.25 0)
35     (4.85 0.25 0.1)
36     (0 0.25 0.1)
37 );
38
39 blocks
40 (
41     hex  (0 1 2 5 6 7 8 11) (96 5 1) simpleGrading (1 1 1)
42     hex  (13 12 3 4 15 14 9 10) (96 15 1) simpleGrading (1 1 1)
43 );
44
45 edges
46 (
47 );
```

```
48
49 patches
50 (
51     patch freeSurface
52     (
53         (11 8 2 5)
54     )
55     patch freeSurfaceShadow
56     (
57         (13 12 14 15)
58     )
59     wall leftWall
60     (
61         (0 6 11 5)
62         (13 15 10 4)
63     )
64     wall rightWall
65     (
66         (1 2 8 7)
67         (12 3 9 14)
68     )
69     wall bottomWall
70     (
71         (0 1 7 6)
72     )
73     wall topWall
74     (
75         (4 10 9 3)
76     )
77
78     empty frontAndBack
79     (
80         (6 7 8 11)
81         (15 14 9 10)
82         (0 5 2 1)
83         (13 4 3 12)
84     )
85 );
86
87 mergePatchPairs
88 (
89 );
90
91 // ************************************************************************* //
```

All the input dictionary files will in general include the header information (lines 1-7) and the file information (lines 8-14) at the beginning. In order to save space, the header information will not be included in the verbatim quoting of the case files.

The blockMesh file defines a conversion ratio to convert the input values to the actual dimensions with the unit of meters, for example, with the convertion ratio of 0.01, the coordinate (4.85, 0.25, 0) represents the location (4.85 cm, 0.25 cm, 0).

A 3-D Cartesian coordinate system is applied by OpenFOAM to generate the computational mesh. First, the coordinates of all the vertices of the blocks are specified (lines

19-37), then two blocks are defined (lines 39-43) based on the labels of the vertices, which represent the liquid and the gas phase. The blocks are discretized into a set of hexahedral mesh cells by specifying the number of the mesh cells and the size ratio between the two consecutive mesh cells along each direction. In this study, the computations start with a uniform mesh with cell size 0.5 mm $\times$ 0.5 mm $\times$ 0.5 mm.

The boundaries of the computational domain are defined afterwards (lines 49-85) based on the vertices labels, and the types of boundaries are also specified.

OpenFOAM operates in 3-D by default. For 2-D calculations, the number of the mesh cells along the third dimension is set to be unity, while the types for the boundaries that lie on the 2-D plane are specified as "empty".

The volume mesh is generated by typing:

`blockMesh`

in the terminal from within the case directory.

C.2.2 Surface Mesh Generation

The mesh at the interface is generated using the mesh generator `makeFaMesh` from Open-FOAM, on the input dictionary file, `faMeshDefinition`, which is located in the `constant/faMesh` directory of the case, as shown below:

```
8 FoamFile
9 {
10    version     2.0;
11    format      ascii;
12    class       dictionary;
13    location    "constant/faMesh";
14    object      faMeshDefinition;
15 }
16 // * * * * * * * * * * * * * * * * * * * * * * * * * * * * * * * * * * * * * * //
17
18 polyMeshPatches  1( freeSurface );
19
20 boundary
21 {
22    left
23    {
24        type                patch;
25        ownerPolyPatch      freeSurface;
26        neighbourPolyPatch  leftWall;
27    }
28
29    right
30    {
31        type                patch;
```

```
32          ownerPolyPatch      freeSurface;
33          neighbourPolyPatch  rightWall;
34      }
35
36      frontAndBack
37      {
38          type                empty;
39          ownerPolyPatch      freeSurface;
40          neighbourPolyPatch  frontAndBack;
41      }
42 }
```

The `faMeshDefinition` file specifies the surface mesh that represents the interface, and its boundaries, which are the contact lines of the interface on the walls.

The volume mesh is generated after the volume mesh is generated by typing:

`makeFaMesh`

in the terminal from within the case directory.

C.3   Boundary and Initial Conditions

Boundary conditions and the initial conditions need to be specified for all the variables that are solved for. These values are specified in separate files for different fields at the starting time $t = t_0$, which locate in the subdirectory t_0 of the case file directory. For example, when the case starts from $t = 0$ s, the boundary conditions and the initial values for the velocity field **u** is specified in the file 0/U of the case directory, as shown below:

```
8 FoamFile
9 {
10     version     2.0;
11     format      ascii;
12     class       volVectorField;
13     location    "0";
14     object      U;
15 }
16 // * * * * * * * * * * * * * * * * * * * * * * * * * * * * * * * * * * * * //
17
18 dimensions      [0 1 -1 0 0 0 0];
19
20 internalField   uniform (0 0 0);
21
22 boundaryField
23 {
24     freeSurface
25     {
26         type            fixedGradient;
27         gradient        uniform (0 0 0);
28     }
29     freeSurfaceShadow
30     {
```

```
31          type            fixedValue;
32          value           uniform (0 0 0);
33      }
34      leftWall
35      {
36          type            fixedValue;
37          value           uniform (0 0 0);
38      }
39      rightWall
40      {
41          type            fixedValue;
42          value           uniform (0 0 0);
43      }
44      bottomWall
45      {
46          type            fixedValue;
47          value           uniform (0 0 0);
48      }
49      topWall
50      {
51          type            fixedValue;
52          value           uniform (0 0 0);
53      }
54      frontAndBack
55      {
56          type            empty;
57      }
58 }
59
60
61 // ************************************************************************* //
```

There are three major sections in this file. `dimensions` specifies the dimensions of the variabl(line 18). `internalField` specifies the values for the variable at time t, which is usually set as a uniform value initially. `boundaryField` specifies the boundary conditions at each boundary patches at time t. For the velocity, the flow is at rest initially and is set with uniform value (`0 0 0`) for the `internalField`. In OpenFOAM, `fixedValue` represents Dirichlet boundary condition, while `fixedGradient` represents Neumann boundary condition. All the boundary conditions at the walls are of type `fixedValue` and the values (`0 0 0`), based on the no-slip boundary condition ($\mathbf{u_b} = 0$).

Similarly, the boundary conditions and the initial condition of the dynamic pressure field p is specified in the file `0/p` of the case directory, as shown below:

```
8 FoamFile
9 {
10     version     2.0;
11     format      ascii;
12     class       volScalarField;
13     location    "0";
14     object      p;
15 }
```

```
16 // * * * * * * * * * * * * * * * * * * * * * * * * * * * * * * * * * * * * * * * * //
17
18 dimensions      [1 -1 -2 0 0 0 0];
19
20 internalField   uniform 0;
21
22 boundaryField
23 {
24     freeSurface
25     {
26         type            fixedValue;
27         value           uniform 0;
28     }
29     freeSurfaceShadow
30     {
31         type            fixedGradient;
32         gradient        uniform 0;
33     }
34     leftWall
35     {
36         type            fixedGradient;
37         gradient        uniform 0;
38     }
39     rightWall
40     {
41         type            fixedGradient;
42         gradient        uniform 0;
43     }
44     bottomWall
45     {
46         type            fixedGradient;
47         gradient        uniform 0;
48     }
49     topWall
50     {
51         type            fixedGradient;
52         gradient        uniform 0;
53     }
54     frontAndBack
55     {
56         type            empty;
57     }
58 }
59
60 // ********************************************************************* //
```

The boundary conditions and the initial condition of the temperature field T is specified

in the file 0/T of the case directory, as shown below:

```
8 FoamFile
9 {
10     version     2.0;
11     format      ascii;
12     class       volScalarField;
13     location    "0";
14     object      T;
15 }
16 // * * * * * * * * * * * * * * * * * * * * * * * * * * * * * * * * * * * * * * * * //
17
18 dimensions      [0 0 0 1 0 0 0];
19
20 internalField   uniform 293;
21
```

```
22 boundaryField
23 {
24     freeSurface
25     {
26         type            fixedGradient;
27         gradient        uniform 0;
28     }
29     freeSurfaceShadow
30     {
31         type            fixedValue;
32         value           uniform 293;
33     }
34     leftWall
35     {
36         type            fixedValue;
37         value           uniform 288;
38     }
39     rightWall
40     {
41         type            fixedValue;
42         value           uniform 298;
43     }
44     bottomWall
45     {
46         type            zeroGradient;
47     }
48     topWall
49     {
50         type            zeroGradient;
51     }
52     frontAndBack
53     {
54         type            empty;
55     }
56 }
57
58
59 // ************************************************************************* //
```

The initial value for temperature is specified as $T = T_0$ uniformly. For temperature, the initially value is set with uniform value $T = T_0$ at the `internalField`. The top and bottom walls are assumed to be adiabatic and therefore the boundary conditions are specified as `zeroGradient`.

When the gas phase is a binary mixture, the boundary conditions and the initial condition of the density of the dilute component ρ_1 is specified in the file `0/rho1` of the case directory, as shown below:

```
8 FoamFile
9 {
10     version     2.0;
11     format      ascii;
12     class       volScalarField;
13     location    "0";
14     object      rho1;
15 }
16 // * * * * * * * * * * * * * * * * * * * * * * * * * * * * * * * * * * * * * //
```

```
17
18 dimensions      [1 -3 0 0 0 0 0];
19
20 internalField   uniform 0.17;
21
22 boundaryField
23 {
24     freeSurface
25     {
26         type            fixedValue;
27         value           uniform 0.17;
28     }
29     freeSurfaceShadow
30     {
31         type            fixedGradient;
32         gradient        uniform 0;
33     }
34     leftWall
35     {
36         type            zeroGradient;
37     }
38     rightWall
39     {
40         type            zeroGradient;
41     }
42     bottomWall
43     {
44         type            zeroGradient;
45     }
46     topWall
47     {
48         type            zeroGradient;
49     }
50     frontAndBack
51     {
52         type            empty;
53     }
54 }
55
56
57 // ********************************************************************* //
```

There is no mass flux through the solid walls, therefore all the boundary conditions on

the solid walls are specified as `zeroGradient`.

C.4 Physical Properties

All the relevant physical properties need to be specified in the case file, including the material properties of the liquid, the gas (both vapor and the air when the gas phase is a binary mixture), and also of the test cell. Both the values and the units of these properties are specified in the file `freeSurfaceProperties`, which is located at `constant` subdirectory of the case directory, as shown below:

```
8 FoamFile
9 {
10     version     2.0;
11     format      ascii;
12     class       dictionary;
13     location    "constant";
```

```
14    object       freeSurfaceProperties;
15 }
16 // * * * * * * * * * * * * * * * * * * * * * * * * * * * * * * * * * * * * * * //
17
18 twoFluids yes;
19
20 nFreeSurfaceCorrectors 1;
21
22 smoothing no;
23 correctPointNormals no;
24 correctDisplacement no;
25 correctCurvature no;
26 curvExtrapOrder 0;
27
28 cleanInterface yes;
29 normalMotionDir no;
30
31 muFluidA         muFluidA    [ 1 -1 -1 0 0 0 0 ]    5.272e-4;
32 muFluidB         muFluidB    [ 1 -1 -1 0 0 0 0 ]    1.81353e-5;
33 muFluidB1        muFluidB1   [ 1 -1 -1 0 0 0 0 ]    5.841e-6;
34
35 rhoFluidA        rhoFluidA   [ 1 -3  0 0 0 0 0 ]    765.5;
36 rhoFluidB        rhoFluidB   [ 1 -3  0 0 0 0 0 ]    1.427;
37 rhoFluidB1       rhoFluidB1  [ 1 -3  0 0 0 0 0 ]    0.270;
38
39
40 kFluidA          kFluidA     [ 1 1 -3 -1 0 0 0 ]    0.1098;
41 kFluidB          kFluidB     [ 1 1 -3 -1 0 0 0 ]    0.025695816;
42 kFluidB1         kFluidB1    [ 1 1 -3 -1 0 0 0 ]    0.0112;
43
44 CpFluidA         CpFluidA [ 0 2 -2 -1 0 0 0 ] 1914.09;
45 CpFluidB         CpFluidB [ 0 2 -2 -1 0 0 0 ] 1004.14;
46 CpFluidB1        CpFluidB1 [ 0 2 -2 -1 0 0 0 ] 1482.33;
47
48 betaFluidA         betaFluidA [ 0 0 0 -1 0 0 0 ] 1.319e-3;
49
50 DfFluidA         DfFluidA    [ 0 2 -1 0 0 0 0 ]    5.837e-6;
51 DfFluidB         DfFluidB    [ 0 2 -1 0 0 0 0 ]    5.837e-6;
52
53 latentHeat        latentHeat     [ 0 2 -2 0 0 0 0 ] 225.21e3;
54 gasConstant1       gasConstant1 [ 0 2 -2 -1 0 0 0 ] 51.2;
55 gasConstantD       gasConstantD [ 0 2 -2 -1 0 0 0 ] 287.00;
56
57 antoineA         antoineA  [ 0 0 0 0 0 0 0 ]  6.95255;
58 antoineB         antoineB  [ 0 0 0 0 0 0 0 ]  1285.12;
59 antoineC         antoineC  [ 0 0 0 0 0 0 0 ]  215.098;
60
61 kWall        kWall [ 1 1 -3 -1 0 0 0 ]     1.4;
62 thWall        thWall [ 1 0 0 0 0 0 0 ] 1.25e-3;
63
64 TLeft        TLeft [ 0 0 0 1 0 0 0 ] 288;
65 TRight        TRight [ 0 0 0 1 0 0 0 ] 298;
66
67 acmCoef        acmCoef [ 0 0 0 0 0 0 0 ] 1.0;
68
69 ctangle        ctangle [ 0 0 0 0 0 0 0 ] 50;
70 pTotal        pTotal [ 0 0 0 0 0 0 0 ] 101325;
71 c0        c0 [ 0 0 0 0 0 0 0 ] 0.04;
72
73 molarMass1        molarMass1 [1 0 0 0 0 0 0] 162.4e-3;
74 molarMassD        molarMassD [1 0 0 0 0 0 0] 28.97e-3;
75
76 Mair0        Mair0 [1 0 0 0 0 0 0] 4.208e-07;
77
78 referenceTemperature        referenceTemperature [ 0 0 0 1 0 0 0 ] 293.00;
79
80 g        g          [ 0 1 -2 0 0 0 0 ] (0 -9.81 0);
81
```

```
82 surfaceTension          surfaceTension [ 1 -2 0 0 0 0 0 ] 0.01584;
83
84 tempCoeffSurfTension            tempCoeffSurfTension [ 1 0 -2 -1 0 0 0 ]    -8.94144e-5;
85
86 tempCoefflatentHeat           tempCoefflatentHeat [ 0 0 0 -1 0 0 0 ]    -1.59687e-3;
87 tempCoeffmuFluidA         tempCoeffmuFluidA [ 0 0 0 -1 0 0 0 ]    -0.013743437;
88 tempCoeffkFluidA          tempCoeffkFluidA [ 0 0 0 -1 0 0 0 ]     -2.3159e-3;
89 tempCoeffCpFluidA          tempCoeffCpFluidA [ 0 0 0 -1 0 0 0 ]    1.25572e-3;
90 tempCoeffbetaFluidA          tempCoeffbetaFluidA [ 0 0 0 -1 0 0 0 ]    3.18423e-3;
91
92 tempCoeffmuFluidB          tempCoeffmuFluidB [ 0 0 0 -1 0 0 0 ]    2.644715e-3;
93 tempCoeffkFluidB         tempCoeffkFluidB [ 0 0 0 -1 0 0 0 ]    3.06632366e-3;
94 tempCoeffCpFluidB          tempCoeffCpFluidB [ 0 0 0 -1 0 0 0 ]     0;
95 tempCoeffDfFluidB          tempCoeffDfFluidB [ 0 0 0 -1 0 0 0 ]    7.48745e-3;
96
97 fixedFreeSurfacePatches         0();
98
99 pointNormalsCorrectionPatches   2( left right );
100
101 surfactantProperties
102 {
103 bulkConc              bulkConc           [ 0 -3  0 0  1 0 0 ] 1.0e-2;
104
105 saturatedConc         saturatedSurfConc   [ 0 -2  0 0  1 0 0 ] 5.0e-6;
106
107 adsorptionCoeff       adsorptionCoeff     [ 0  3 -1 0 -1 0 0 ] 40.0;
108
109 desorptionCoeff       desorptionCoeff     [ 0 -3  0 0  1 0 0 ] 8.93e-2;
110
111 bulkDiffusion         bulkDiffusion       [ 0  2 -1 0  0 0 0 ] 1.0e-9;
112
113 diffusion             diffusion           [ 0  2 -1 0  0 0 0 ] 1.0e-9;
114
115 }
116
117 // ************************************************************************* //
```

C.5   Control Parameters

The controlling parameters related with running the case are specified in the `controlDict`
file, which is located at `system` subdirectory of the case directory, as shown below:

```
8 FoamFile
9 {
10     version    2.0;
11     format     ascii;
12     class      dictionary;
13     location   "system";
14     object     controlDict;
15 }
16 // * * * * * * * * * * * * * * * * * * * * * * * * * * * * * * * * * * * * * //
17
18 applicationClass    icoFoam;
19
20 startFrom           startTime;
21
22 startTime           0;
23
24 stopAt              endTime;
25
26 endTime             500;
27
28 deltaT              1e-3;
29
```

```
30 writeControl        runTime;
31
32
33 writeInterval       1;
34
35 cycleWrite          0;
36
37 writeFormat         ascii;
38
39 writePrecision      12;
40 writeCompression    uncompressed;
41
42 timeFormat          general;
43
44 timePrecision       5;
45
46 runTimeModifiable   yes;
47
48 // functions
49 // (
50 //      history
51 //      {
52 //          type sloshingHistory;
53 //          functionObjectLibs
54 //          (
55 //              "libsloshingHistory.so"
56 //          );
57 //      }
58 // );
59
60 // ************************************************************************* //
```

The file specifies the time step Δt, as well as the start time t_0 and end time t_e. When the case is started, OpenFOAM will read the initial values from the subdirectory t_0, and continue with the specified time step, until it reaches the specified end time and stop.

While the program is running, OpenFOAM can also store the intermediate results at specified time, by creating the subdirectory named after the specified time, and writing various fields into separate files with specified format (`ascii` or `binary`) and precision. These results can be either viewed with the post-processing package or output directly.

C.6   Discretization Schemes and the Linear Solver

The numerical schemes can be specified either directly in the numerical code, or in the case file. The finite volume discretization schemes for different terms in the transport equations are specified in the file `fvSchemes`, while the linear solvers for the discretized equations and the tolerances are specified in the file `fvSolution`. Similarly, finite area discretization schemes and their linear solvers are specified in the file `faSchemes` and `faSolution`. All

these files are located in the `system` subdirectory of the case directory, as shown below[1]:

- `fvSchemes`

```
8 FoamFile
9 {
10     version     2.0;
11     format      ascii;
12     class       dictionary;
13     location    "system";
14     object      fvSchemes;
15 }
16 // * * * * * * * * * * * * * * * * * * * * * * * * * * * * * * * * * * * * //
17
18 ddtSchemes
19 {
20     ddt(rho,U) backward;
21     ddt(U) backward;
22     ddt(T) backward;
23     ddt(con1) backward;
24     ddt(con2) backward;
25     ddt(con) backward;
26     ddt(rho1) backward;
27     ddt(rho2) backward;
28 }
29
30 gradSchemes
31 {
32     default Gauss linear;
33 }
34
35 divSchemes
36 {
37     div(phi,T)       explicit upwind;
38     div(phi,U)    Gauss linear;
39     div(phi,con1)   explicit upwind;
40     div(phi,con2)   explicit upwind;
41     div(phi,con)    explicit upwind;
42     div(phi,rho1)   explicit upwind;
43     div(phi,rho2)   explicit upwind;
44 }
45
46 laplacianSchemes
47 {
48     default none;
49
50     laplacian(mu,U) Gauss linear corrected;
51     laplacian((1|A(U)),p) Gauss linear corrected;
52     laplacian((1|interpolate(A(U))),p) Gauss linear corrected;
53
54     laplacian(kappa,T) Gauss harmonic limited 0.5;
55
56     laplacian(Df1,con1) Gauss harmonic limited 0.5;
57     laplacian(Df2,con2) Gauss harmonic limited 0.5;
58     laplacian(Df,rho1)  Gauss harmonic limited 0.5;
59     laplacian(Df1,rho1) Gauss harmonic limited 0.5;
60     laplacian(Df2,rho2) Gauss harmonic limited 0.5;
61
62     laplacian(diffusivity,cellDisplacement) Gauss linear corrected;
63     laplacian(diffusivity,cellMotionU) Gauss linear corrected;
```

---

[1]The finite area discretization numerical schemes are specified in `faSchemes`, which will be used for calculating the surface gradient, *etc.* However, there are no transport equations need to be solved at the interface, therefore `faSolution` file is empty and not shown here.

```
64 }
65
66 interpolationSchemes
67 {
68     default          linear;
69 }
70
71 snGradSchemes
72 {
73     default          corrected;
74 }
75
76 fluxRequired
77 {
78     p;
79 }
80
81 // ************************************************************************* //
```

- fvSolution

```
8 FoamFile
9 {
10     version     2.0;
11     format      ascii;
12     class       dictionary;
13     location    "system";
14     object      fvSolution;
15 }
16 // * * * * * * * * * * * * * * * * * * * * * * * * * * * * * * * * * * * * * //
17
18 solvers
19 {
20
21     cellDisplacement
22     {
23         solver          ICCG;
24         preconditioner  DIC;
25         tolerance       1e-9;
26         relTol          0;
27     }
28
29     cellMotionU
30     {
31         solver          ICCG;
32         preconditioner  DIC;
33         tolerance       1e-9;
34         relTol          0;
35     }
36     p
37     {
38         solver          ICCG;
39         preconditioner  DIC;
40         tolerance       1e-9;
41         relTol          0;
42     }
43
44     U
45     {
46         solver          BICCG;
47         preconditioner  DILU;
48         tolerance       1e-8;
49         relTol          0;
50     }
51
```

```
52    T
53    {
54        solver          BICCG;
55        preconditioner  diagonal;
56        tolerance       1e-10;
57        relTol          1e-10;
58    }
59
60    rho1
61    {
62        solver          BICCG;
63        preconditioner  none;
64        tolerance       1e-10;
65        relTol          1e-10;
66    }
67
68    con2
69    {
70        solver          BICCG;
71        preconditioner  none;
72        tolerance       1e-10;
73        relTol          1e-10;
74    }
75 }
76
77 PISO
78 {
79     nOuterCorrectors          10;
80     nCorrectors               2;
81     nNonOrthogonalCorrectors  1;
82     ddtPhiCorr no;
83
84     pRefPoint (0 0.009 0);
85     pRefValue 0;
86 }
87
88 FreeSurface
89 {
90     nFreeSurfCorr 1;
91 }
92
93 relaxationFactors
94 {
95     p               1;
96     U               1;
97 }
98
99 // ************************************************************************* //
```

- faSchemes

```
8 FoamFile
9 {
10     version    2.0;
11     format     ascii;
12     class      dictionary;
13     location   "system";
14     object     faSchemes;
15 }
16 // * * * * * * * * * * * * * * * * * * * * * * * * * * * * * * * * * * * * * //
17
18
19 ddtSchemes
20 {
21     ddt(faPhi) backward;
```

```
22 }
23
24
25 gradSchemes
26 {
27     default           none;
28     grad(Us)          Gauss linear;
29     grad(Ti)          Gauss linear;
30     grad(con2i)       Gauss linear;
31 }
32
33 divSchemes
34 {
35     default           none;
36     div(Us)           Gauss linear;
37 }
38
39 laplacianSchemes
40 {
41     default           none;
42 }
43
44 interpolationSchemes
45 {
46     default none;
47 }
48
49 snGradSchemes
50 {
51     default none;
52 }
53
54 fluxRequired
55 {
56     p;
57 }
58
59 // ************************************************************************* //
```

C.7   Mesh Motion Solver

The moving mesh method is used for simulating the two phase flow. The mesh motion
solver and the relevant control parameters are specified in dynamicMeshDict file, which
is located in constant subdirectory of the case file, as shown below:

```
8 FoamFile
9 {
10     version    2.0;
11     format     ascii;
12     class      dictionary;
13     object     dynamicMeshDict;
14 }
15 // * * * * * * * * * * * * * * * * * * * * * * * * * * * * * * * * * * * * //
16
17 dynamicFvMesh dynamicMotionSolverFvMesh;
18
19 solver liquidFilm;
20
21
22 motionDirection (0 1 0);
23 diffusivity linear;
24
25 distancePatches 2 (freeSurface freeSurfaceShadow);
```

```
26
27 frozenDiffusion no;
28
29 // pseudoSolid
30 // {
31 //    poissonsRatio          0.3;
32 //    nCorrectors            3;
33 //    convergenceTolerance   1e-9;
34 // };
35
36 // ************************************************************************* //
```

C.8   Running the Case

To start the numerical simulation, simply type `./Allrun` in the terminal from within the case directory, where the file `Allrun` is located at the case directory, as shown below:

```
1 #!/bin/sh
2
3 . $WM_PROJECT_DIR/bin/tools/RunFunctions
4
5 application="newInterTrackFoam"
6
7 runApplication blockMesh
8 runApplication makeFaMesh
9 runApplication $application
```

The commands can also be executed by typing each command (`blockMesh`, `makeFaMesh`, `newInterTrackFoam`) one by one in the terminal from the case file directory.

C.9   Mesh Refinement

The mesh refinement procedure is used in this study where a new case is created based on the finished case on a coarser mesh. The new case file directory is created in the same directory where the finished case is located. Before the mesh refinement, the folders t_0, t_e, `constant`, `system` are copied from the finished case to the new case directory. The mesh of the new case can be refined before resuming the calculation from time t_e, which is the end time of the old case, by typing

`./Allmeshrefinement`

in the terminal within the new case directory. The `Allmeshrefinement` file is located in the new case directory, as shown below:

```
1 #!/bin/sh
2
```

```
 3 # Source tutorial run functions
 4 . $WM_PROJECT_DIR/bin/tools/RunFunctions
 5
 6 time="500"
 7 case1="uni-0.5mm"
 8
 9 application="fieldVari-sim-vac"
10
11 chooseFaceSet()
12 {
13     echo "creating face set for primary zone - $1"
14     cp system/faceSetDict.$1 system/faceSetDict
15     faceSet > log.faceSet.$1
16 }
17
18 chooseCellSet()
19 {
20     echo "creating cell set for primary zone - $1"
21     cp system/cellSetDict.$1 system/cellSetDict
22     cellSet > log.cellSet.$1
23 }
24
25 refineMeshByCellSet()
26 {
27     echo "refining primary zone - $1"
28     cp system/refineMeshDict.$1 system/refineMeshDict
29
30     refineMesh -dict -overwrite > log.refineMesh.$1
31 }
32
33 deleteFiles ()
34 {
35     echo "delete field files except polyMesh"
36     rm -rf $time/uniform
37     rm $time/*
38     rm log.*
39 }
40
41 mapResults()
42 {
43     echo "map the results from coarse mesh to refined mesh case"
44     mapFields ../$case1 -consistent
45
46     cp 0/motionU* $time/
47     cp 0/contactAngle $time/
48     cp 0/pointMotion* $time/
49
50     cp -r $time/polyMesh/* constant/polyMesh/
51 }
52
53 makefieldGradient()
54 {
55
56 cp 0/motionU* $time/
57 cp 0/contactAngle $time/
58 cp 0/pointMotion* $time/
59 echo "produce gradient fields"
60 $application
61 }
62
63 chooseFaceSet 1
64 chooseCellSet 1
65 refineMeshByCellSet 1
66 deleteFiles
67 mapResults
```

First the mesh cells that requires refinement are chosen (lines 11-23), which are all the mesh cells in the liquid phase, and in the gas phase where the second derivatives of the variable exceed the specified thresholds. Then the mesh is refined using the utility `refineMesh` on the dictionary file `refineMeshDict` (lines 25-30). The fields from the old case are therefore deleted (lines 33-39) since they are not compatible with the refined computational mesh, and new fields are generated by mapping the results from the coarser mesh of the old case to the refined mesh of the new case (lines 41-51).

The utility `refineMesh` of OpenFOAM will refine the mesh based on the dictionary file `refineMeshDict`, which is located in the `system` subdirectory of the case file, as shown below:

```
 8 FoamFile
 9 {
10     version     2.0;
11     format      ascii;
12     class       dictionary;
13     object      refineMeshDict;
14 }
15 // * * * * * * * * * * * * * * * * * * * * * * * * * * * * * * * * * //
16
17 set c1;
18
19 coordinateSystem global;
20
21 globalCoeffs
22 {
23     tan1 (1 0 0);
24     tan2 (0 1 0);
25     normal;
26 }
27
28 directions
29 (
30     tan1
31     tan2
32 //    normal
33 );
34
35 useHexTopology yes;
36
37 geometricCut no;
38
39 writeMesh no;
40
41 // ************************************************************************* //
```

A set of mesh cells (`c1`) is refined by splitting the original cell evenly along the specified directions (lines 28-33). For 2-D calculations, the third direction (`normal`) is omitted and

one mesh cell is split into four new mesh cells; for 3-D calculations, one mesh cell is split into eight new mesh cells.

The mesh cell set (c1) consists of all the mesh cells that require refinement, and is chosen based on the specifications in the file cellSetDict, which selects all the mesh cells in the liquid phase and that in the gas phase where the criteria is satisfied. Moreover, in order to make sure that the area meshes at the interface remain consistent between the two phases, all the cells that lie on both side of the interface need to be included in cell set (c1). In order to select these mesh cells, first the face set f1, which consists of all the mesh faces at the interface, is generated via the specifications in the file faceSetDict; then all the mesh cells that have cell face in f1 will be selected. Both cellSetDict and faceSetDict are located in the system subdirectory of the case file, as shown below:

- cellSetDict

```
 8 FoamFile
 9 {
10     version    2.0;
11     format     ascii;
12     class      dictionary;
13     object     cellSetDict;
14 }
15
16 // * * * * * * * * * * * * * * * * * * * * * * * * * * * * * * * * * * * * * * //
17
18 // Name of set to operate on
19 name c1;
20
21 // One of clear/new/invert/add/delete|subset/list
22 action new;
23
24 // Actions to apply to cellSet. These are all the topoSetSource's ending
25 // in ..ToCell (see the meshTools library).
26
27 topoSetSources
28 (
29
30     // Select based on faceSet
31     faceToCell
32     {
33         set f1;              // Name of faceSet
34         //option neighbour; // cell with neighbour in faceSet
35         //option owner;      //  ,,        owner
36         option any;          // cell with any face in faceSet
37         //option all;        // cell with all faces in faceSet
38     }
39
40     // Cells with cell centre within box
41
42
43     boxToCell
```

```
44      {
45          box   (0 0 0) (48.5e-3 3e-3 1e-3);
46      }
47
48      boxToCell
49      {
50          box   (0 0 0) (0.25e-3 10e-3 1e-3);
51      }
52
53      boxToCell
54      {
55          box   (48.25e-3 0 0) (48.5e-3 10e-3 1e-3);
56      }
57
58      // values of field within certain range
59      fieldToCell
60      {
61          fieldName   fieldVari2;
62          min         0.0005;
63          max         10;
64      }
65 );
66
67
68 // ************************************************************************* //
```

- faceSetDict

```
8 FoamFile
9 {
10      version    2.0;
11      format     ascii;
12      class      dictionary;
13      object     faceSetDict;
14 }
15
16 // * * * * * * * * * * * * * * * * * * * * * * * * * * * * * * * * * * * * * //
17
18 // Name of set to operate on
19 name f1;
20
21 // One of clear/new/invert/add/delete|subset/list
22 action new;
23
24 // Actions to apply to pointSet. These are all the topoSetSource's ending
25 // in ..ToFace (see the meshTools library).
26 topoSetSources
27 (
28
29      // All faces of patch
30      patchToFace
31      {
32          name "freeSurface";        // Name of patch, regular expressions allowed
33      }
34
35      patchToFace
36      {
37          name "freeSurfaceShadow";        // Name of patch, regular expressions allowed
38      }
39
40 );
41
42 // ************************************************************************* //
```

After the new case is set up, the simulation can be resumed from time t_e, using the same commands as discussed in C.8.

REFERENCES

[1] Y. Li, R. O. Grigoriev, and M. Yoda, "Experimental study of the effect of noncondensables on buoyancy-thermocapillary convection in a volatile low-viscosity silicone oil," *Phys. Fluids*, vol. 26, p. 122112, 2014.

[2] G. Peterson, *An Introduction to Heat Pipes: Modeling, Testing, and Applications*. New York: Wiley-Interscience, 1994.

[3] J. Collier and J. Thome, *Convective Boiling and Condensation*. Oxford: Clarendon Press, 1996.

[4] R. V. Birikh, "Thermocapillary convection in a horizontal layer of liquid," *J. Appl. Mech. Tech. Phys.*, vol. 7, pp. 43–44, 1966.

[5] A. G. Kirdyashkin, "Thermogravitational and thermocapillary flows in a horizontal liquid layer under the conditions of a horizontal temperature gradient," *Int. J. Heat Mass Transfer*, vol. 27, pp. 1205–1218, 1984.

[6] M. K. Smith and S. H. Davis, "Instabilities of dynamic thermocapillary liquid layers. part 1. convective instabilities," *J. Fluid Mech.*, vol. 132, pp. 119–144, 1983.

[7] M. K. Smith and S. H. Davis, "Instabilities of dynamic thermocapillary liquid layers. part 2. surface-wave instabilities," *J. Fluid Mech.*, vol. 132, pp. 145–162, 1983.

[8] M. F. Schatz and G. P. Neitzel, "Experiments on thermocapillary instabilities," *Annu. Rev. Fluid Mech.*, vol. 33, pp. 93–127, 2001.

[9] D. Villers and J. K. Platten, "Coupled buoyancy and marangoni convection in acetone: experiments and comparison with numerical simulations," *J. Fluid Mech.*, vol. 234, pp. 487–510, 1992.

[10] C. De Saedeleer, A. Garcimartín, G. Chavepeyer, J. K. Platten, and G. Lebon, "The instability of a liquid layer heated from the side when the upper surface is open to air," *Phys. Fluids*, vol. 8, no. 3, pp. 670–676, 1996.

[11] A. Garcimartín, N. Mukolobwiez, and F. Daviaud, "Origin of waves in surface-tension-driven convection," *Phys. Rev. E*, vol. 56, pp. 1699–1705, 1997.

[12] R. J. Riley and G. P. Neitzel, "Instability of thermocapillarybuoyancy convection in shallow layers. Part 1. Characterization of steady and oscillatory instabilities," *J. Fluid Mech.*, vol. 359, pp. 143–164, 1998.

[13] J. Burguete, N. Mukolobwiez, F. Daviaud, N. Garnier, and A. Chiffaudel, "Buoyant-thermocapillary instabilities in extended liquid layers subjected to a horizontal temperature gradient," *Phys. Fluids*, vol. 13, no. 10, pp. 2773–2787, 2001.

[14] P. M. Parmentier, V. C. Regnier, and G. Lebon, "Buoyant-thermocapillary instabilities in medium-prandtl-number fluid layers subject to a horizontal gradient," *Int. J. Heat Mass Transfer*, vol. 36, pp. 2417–2427, 1993.

[15] C. L. Chan and C. F. Chen, "Effect of gravity on the stability of thermocapillary convection in a horizontal fluid layer," *J. Fluid Mech.*, vol. 647, pp. 91–103, 2010.

[16] J. F. Mercier and C. Normand, "Buoyant-thermocapillary instabilities of differentially heated liquid layers," *Phys. Fluids*, vol. 8, pp. 1433–1445, 1996.

[17] J. Mercier and C. Normand, "Influence of the prandtl number on the location of recirculation eddies in thermocapillary flows," *Int. J. Heat Mass Transfer*, vol. 45, pp. 793–801, 2002.

[18] J. Priede and G. Gerbeth, "Convective, absolute, and global instabilities of thermocapillary-buoyancy convection in extended layers," *Phys. Rev. E*, vol. 56, no. 4, pp. 4187–4199, 1997.

[19] H. Ben Hadid and B. Roux, "Buoyancy- and thermocapillary-driven flows in differentially heated cavities for low-prandtl-number fluids," *J. Fluid Mech.*, vol. 235, pp. 1–36, 1992.

[20] M. Mundrane and A. Zebib, "Oscillatory buoyant thermocapillary flow," *Phys. Fluids*, vol. 6, no. 10, pp. 3294–3306, 1994.

[21] X. Lu and L. Zhuang, "Numerical study of buoyancy- and thermocapillary-driven flows in a cavity," *Acta Mech Sinica (English Series)*, vol. 14, no. 2, pp. 130–138, 1998.

[22] V. M. Shevtsova, A. A. Nepomnyashchy, and J. C. Legros, "Thermocapillary-buoyancy convection in a shallow cavity heated from the side," *Phys. Rev. E*, vol. 67, p. 066308, 2003.

[23] V. M. Shevtsova and J. C. Legros, "Instability in thin layer of liquid confined between rigid walls at different temperatures," *Acta Astronautica*, vol. 52, no. 7, pp. 541–549, 2003.

[24] Y.-R. Li, H.-R. Zhang, C.-M. Wu, and J.-L. Xu, "Numerical study of the turbulent flow past an airfoil with trailing edge separation," *Heat Mass Transfer*, vol. 48, pp. 241–251, 2012.

[25] Y. Ji, Q.-S. Liu, and R. Liu, "Coupling of evaporation and thermocapillary convection in a liquid layer with mass and heat exchanging interface," *Chin. Phys. Lett.*, vol. 25, pp. 608–611, 2008.

[26] W. Nusselt, "Die oberflachenkondensation des wasserdampfes," *Zeitschrift des Vereins Deutscher Ingenieure*, vol. 60, p. 569, 1916.

[27] L. A. Bromley, "Effect of heat capacity of condensate," *Industrial and Engineering Chemistry*, vol. 44, no. 12, pp. 2966–2969, 1952.

[28] W. M. Rohsenow, "A method of correlating heat transfer data for surface boiling liquids," *Trans. ASME*, vol. 74, no. 12, p. 969979, 1952.

[29] W. Rohsenow, J. Webber, and T. Ling, "Effect of vapor velocity on laminar and turbulent film condensation," *Trans. ASME*, vol. 78, p. 16371643, 1956.

[30] D. Butterworth, "Simplified methods for condensation on a vertical surface with vapor shear," *UKAEA Rept. AERE-R9683*, 1981.

[31] E. M. Sparrow and J. L. Gregg, "A boundary-layer treatment of laminar film condensation," *J.Heat Transfer*, vol. 81, pp. 13–18, 1959.

[32] E. M. Sparrow, R. Eichhorn, and J. L. Gregg, "Combined forced and free convection in a boundary layer flow," *Physics of Fluids*, vol. 2, no. 3, pp. 319–328, 1959.

[33] J. Koh, E. Sparrow, and J. Hartnett, "The two phase boundary layer in laminar film condensation," *International Journal of Heat and Mass Transfer*, vol. 2, no. 12, pp. 69 – 82, 1961.

[34] R. Ranjan, J. Y. Murthy, and S. V. Garimella, "A microscale model for thin-film evaporation in capillary wick structures," *International Journal of Heat and Mass Transfer*, vol. 54, no. 13, pp. 169 – 179, 2011.

[35] A. Faghri, "Heat pipes: Review, opportunities and challenges," *Frontiers in Heat Pipes*, vol. 5, no. 1, p. 013001, 2014.

[36] D. Bharathan and G. Wallis, "Air-water countercurrent annular flow," *International Journal of Multiphase Flow*, vol. 9, no. 4, pp. 349 – 366, 1983.

[37] M. A. Grolmes, G. A. Lambert, and H. K. Fauske, "Flooding in vertical tubes," in *AIChE Symposium Series No. 38, Multiphase Flow Systems*, pp. paper A–4, 1974.

[38] J. G. Reed and C. L. Tien, "Modeling of the two-phase closed thermosyphon," *Journal of Heat Transfer*, vol. 109, no. 3, pp. 722–730, 1987.

[39] S. Roesler and M. Groll, "Flow visualization and analytical modelling of interaction phenomena in closed two-phase flow systems," in *Proc. of the 8th International Heat Pipe Conference*, pp. 26–32, 1992.

[40] J. Linehan, *The interaction of two-dimensional stratified, turbulent air water and steam-water flows*. Ph.d. dissertation, University of Wisconsin, 1968.

[41] R. A. Seban and J. A. Hodgson, "Laminar-film condensation in a tube with upward vapor flow," *International Journal of Heat and Mass Transfer*, vol. 25, no. 9, pp. 1291–1300, 1982.

[42] M. S. ElGenk and H. H. Saber, "Flooding limit in closed, two-phase flow thermosyphons," *International Journal of Heat and Mass Transfer*, vol. 40, no. 9, pp. 2147–2164, 1997.

[43] M. S. El-Genk and H. H. Saber, "Determination of operation envelopes for closed, two-phase thermosyphons," *International Journal of Heat and Mass Transfer*, vol. 42, no. 5, pp. 889–903, 1999.

[44] F. Blangetti and M. Naushahi, "Influence of mass transfer on the momentum transfer in condensation and evaporation phenomena," *International Journal of Heat and Mass Transfer*, vol. 23, no. 12, pp. 1694 – 1695, 1980.

[45] S. J. Chen, J. G. Reed, and C. L. Tien, "Reflux condensation in a 2-phase closed thermosyphon," *International Journal of Heat and Mass Transfer*, vol. 27, no. 9, pp. 1587–1594, 1984.

[46] Y. Pan, "Condensation heat transfer characteristics and concept of sub-flooding limit in a two-phase closed thermosyphon," *International Communications in Heat and Mass Transfer*, vol. 28, no. 3, pp. 311 – 322, 2001.

[47] A. Oron, S. H. Davis, and S. G. Bankoff, "Long-scale evolution of thin liquid films," *Reviews of Modern Physics*, vol. 69, no. 3, pp. 931–980, 1997.

[48] G. P. Peterson and B. K. Bage, "Entrainment limitations in thermosyphons and heat pipes," *Journal of Energy Resources Technology*, vol. 113, no. 3, pp. 147–153, 1991.

[49] K. Kafeel and A. Turan, "Axi-symmetric simulation of a two phase vertical thermosyphon using eulerian two-fluid methodology," *Heat Mass Transfer*, vol. 49, pp. 1089–1099, 2013.

[50] B. Fadhl, L. C. Wrobel, and H. Jouhara, "Numerical modelling of the temperature distribution in a two-phase closed thermosyphon," *Applied Thermal Engineering*, vol. 60, pp. 122–131, 2013.

[51] F. L. Chang and Y. M. Hung, "The coupled effects of working fluid and solid wall on thermal performance of micro heat pipes," *International Journal of Heat and Mass Transfer*, vol. 73, no. 0, pp. 76 – 87, 2014.

[52] T. Cotter, "Principles and prospects for micro heat pipes," *NASA STI/Recon Technical Report N*, vol. 84, p. 29149, 1984.

[53] B. R. Babin and G. P. Peterson, "Experimental investigation of a flexible bellows heat pipe for cooling discrete heat-sources," *Journal of Heat Transfer-Transactions of the Asme*, vol. 112, no. 3, pp. 602–607, 1990.

[54] B. R. Babin, G. P. Peterson, and D. Wu, "Steady-state modeling and testing of a micro heat pipe," *Journal of Heat Transfer-Transactions of the Asme*, vol. 112, no. 3, pp. 595–601, 1990.

[55] S. Dasgupta, J. A. Schonberg, and P. C. Wayner, "Investigation of an evaporating extended meniscus based on the augmented young-laplace equation," *Journal of Heat Transfer-Transactions of the Asme*, vol. 115, no. 1, pp. 201–208, 1993.

[56] S. Dasgupta, J. A. Schonberg, I. Y. Kim, and P. C. Wayner, "Use of the augmented young-laplace equation to model equilibrium and evaporating extended menisci," *Journal of Colloid and Interface Science*, vol. 157, no. 2, pp. 332–342, 1993.

[57] J. A. Schonberg, S. Dasgupta, and P. C. Wayner, "An augmented young-laplace model of an evaporating meniscus in a microchannel with high heat-flux," *Aerospace Heat Exchanger Technology 1993*, pp. 239–254, 1993.

[58] D. M. Anderson and S. H. Davis, "The spreading of volatile liquid droplets on heated surfaces," *Physics of Fluids*, vol. 7, no. 2, pp. 248–265, 1995.

[59] L. Deng, J. L. Plawsky, P. C. Wayner, and S. DasGupta, "Stability and oscillations in an evaporating corner meniscus," *Journal of Heat Transfer-Transactions of the Asme*, vol. 126, no. 2, pp. 169–178, 2004.

[60] G. P. Peterson and H. B. Ma, "Theoretical analysis of the maximum heat transport in triangular grooves: A study of idealized micro heat pipes," *Journal of Heat Transfer-Transactions of the Asme*, vol. 118, no. 3, pp. 731–739, 1996.

[61] B. Suman and P. Kumar, "An analytical model for fluid flow and heat transfer in a micro-heat pipe of polygonal shape," *International Journal of Heat and Mass Transfer*, vol. 48, no. 21-22, pp. 4498–4509, 2005.

[62] B. Suman, S. De, and S. Dasgupta, "A model of the capillary limit of a micro heat pipe and prediction of the dry-out length," *International Journal of Heat and Fluid Flow*, vol. 26, no. 3, pp. 495–505, 2005.

[63] B. Suman, "Effects of a surface-tension gradient on the performance of a micro-grooved heat pipe: an analytical study," *Microfluidics and Nanofluidics*, vol. 5, no. 5, pp. 655–667, 2008.

[64] B. Suman and R. Savino, "Capillary flow-driven heat transfer enhancement," *Journal of Thermophysics and Heat Transfer*, vol. 25, no. 4, pp. 553–560, 2011.

[65] B. Suman and N. Hoda, "Effect of variations in thermophysical properties and design parameters on the performance of a v-shaped micro grooved heat pipe," *International Journal of Heat and Mass Transfer*, vol. 48, no. 10, pp. 2090–2101, 2005.

[66] H. Ma, G. Peterson, and X. Lu, "The influence of vapor-liquid interactions on the liquid pressure drop in triangular microgrooves," *International Journal of Heat and Mass Transfer*, vol. 37, no. 15, pp. 2211 – 2219, 1994.

[67] D. Khrustalev and A. Faghri, "Thermal-analysis of a micro-heat pipe," *Journal of Heat Transfer-Transactions of the Asme*, vol. 116, no. 1, pp. 189–198, 1994.

[68] J. P. Longtin, B. B. Badran, and F. M. Gerner, "A one-dimensional model of a micro heat pipe during steady-state operation," *ASME. J. Heat Transfer.*, vol. 116, no. 3, pp. 709–715, 1994.

[69] H. B. Ma and G. P. Peterson, "Experimental investigation of the maximum heat transport in triangular grooves," *J. Heat Transfer.*, vol. 118, pp. 740–746, 1996.

[70] Y. M. Hung and K. K. Tio, "Analysis of microheat pipes with axial conduction in the solid wall," *Journal of Heat Transfer-Transactions of the Asme*, vol. 132, no. 7, 2010.

[71] Y. M. Hung and Q. Seng, "Effects of geometric design on thermal performance of star-groove micro-heat pipes," *International Journal of Heat and Mass Transfer*, vol. 54, no. 5-6, pp. 1198–1209, 2011.

[72] Y. M. Hung and K. K. Tio, "Thermal analysis of a water-filled micro heat pipe with phase-change interfacial resistance," *Journal of Heat Transfer-Transactions of the Asme*, vol. 134, no. 11, 2012.

[73] Y. M. Hung and K. K. Tio, "Thermal analysis of optimally designed inclined micro heat pipes with axial solid wall conduction," *International Communications in Heat and Mass Transfer*, vol. 39, no. 8, pp. 1146–1153, 2012.

[74] H. X. C. B. Sobhan and L. C. Yu, "Investigations on transient and steady-state performance of a micro heat pipe," *Journal of Thermophysics and Heat Transfer*, vol. 14, no. 2, pp. 161–169, 2000.

[75] F. M. White, *Viscous fluid flow*. New York: McGraw-Hill, 2nd ed., 1991.

[76] C. A. Bankston and H. J. Smith, "Incompressible laminar vapor flow in cylindrical heat pipes," *Mechanical Engineering*, vol. 94, no. 2, p. 52, 1972.

[77] J. H. Jang, A. Faghri, and W. S. Chang, "Analysis of the one-dimensional transient compressible vapor flow in heat pipes," *International Journal of Heat and Mass Transfer*, vol. 34, no. 8, pp. 2029–2037, 1991.

[78] P. Ayyaswamy, I. Catton, and D. Edwards, "Capillary flow in triangular grooves.," *Journal of Applied Mechanics, Transactions ASME*, vol. 41, no. 2, pp. 332–336, 1974.

[79] D. Khrustalev and A. Faghri, "Coupled liquid and vapor flow in miniature passages with micro grooves," *Journal of Heat Transfer*, vol. 121, no. 3, pp. 729–733, 1999.

[80] S. Thomas, R. Lykins, and K. Yerkes, "Fully developed laminar flow in trapezoidal grooves with shear stress at the liquid-vapor interface," *International Journal of Heat and Mass Transfer*, vol. 44, no. 18, pp. 3397–3412, 2001.

[81] S. J. Kim, J. K. Seo, and K. H. Do, "Analytical and experimental investigation on the operational characteristics and the thermal optimization of a miniature heat pipe with a grooved wick structure," *International Journal of Heat and Mass Transfer*, vol. 46, no. 11, pp. 2051 – 2063, 2003.

[82] J. Zhang, S. J. Watson, and H. Wong, "Fluid flow and heat transfer in a dual-wet micro heat pipe," *J. Fluid Mech.*, vol. 589, pp. 1–31, 2007.

[83] A. Nouri-Borujerdi and M. Layeghi, "A review of concentric annular heat pipes," *Heat Transfer Engineering*, vol. 26, no. 6, pp. 45–58, 2005.

[84] A. Faghri, "Vapor flow-analysis in a double-walled concentric heat pipe," *Numerical Heat Transfer*, vol. 10, no. 6, pp. 583–595, 1986.

[85] A. Faghri and S. Parvani, "Numerical analysis of laminar flow in a double-walled annular heat pipe," *Journal of Thermophysics and Heat Transfer*, vol. 2, no. 2, pp. 165–171, 1988.

[86] A. Faghri, "Performance characteristics of a concentric annular heat pipe: Part ii-vapor flow analysis," *Journal of Heat Transfer-Transactions of the Asme*, vol. 111, no. 1-4, pp. 851–857, 1989.

[87] H. Wang, J. Y. Murthy, and S. V. Garimella, "Transport from a volatile meniscus inside an open microtube," *Int. J. Heat Mass Transfer*, vol. 51, pp. 3007–3017, 2008.

[88] H. Wang, Z. Pan, and S. V. Garimella, "Numerical investigation of heat and mass transfer from an evaporating meniscus in a heated open groove," *Int. J. Heat Mass Transfer*, vol. 54, p. 30153023, 2011.

[89] Z. Pan and H. Wang, "Symmetry-to-asymmetry transition of marangoni flow at a convex volatizing meniscus," *Microfluidics and Nanofluidics*, vol. 9, pp. 657–669, 2010.

[90] G. V. Kuznetzov and A. E. Sitnikov, "Numerical modeling of heat and mass transfer in a low-temperature heat pipe," *J. Eng. Phys. Thermophys.*, vol. 75, pp. 840–848, 2002.

[91] T. Kaya and J. Goldak, "Three-dimensional numerical analysis of heat and mass transfer in heat pipes," *Heat Mass Transfer*, vol. 43, pp. 775–785, 2007.

[92] D. F. Othmer, "The condensation of steam," *Ind. Eng. Chem.*, vol. 21, no. 6, p. 576583, 1929.

[93] S. J. Meisenburg, R. M. Boarts, and W. L. Badger, "The influence of small concentrations of air in steam on the steam film coefficient of heat transfer," *Transactions of the American Institute of Chemical Engineers*, vol. 31, pp. 622–638, 1935.

[94] H. K. Aldiwany and J. W. Rose, "Free convection film condensation of steam in presence of non-condensing gases," *International Journal of Heat and Mass Transfer*, vol. 16, no. 7, pp. 1359–1369, 1973.

[95] Henderso.Cl and Marchell.Jm, "Film condensation in presence of a noncondensable gas," *Journal of Heat Transfer*, vol. 91, no. 3, p. 447, 1969.

[96] D. Kroger and W. Rohsenow, "Condensation heat transfer in the presence of a non-condensable gas," *Int. J. Heat Mass Trans.*, vol. 11, p. 15, 1968.

[97] K. M. Vierow, *Behavior of steam-air systems condensing in cocurrent vertical down-flow*. University of California, Berkeley, 1990.

[98] S. Kuhn, V. Schrock, and P. Peterson, "An investigation of condensation from steam-gas mixtures flowing downward inside a vertical tube," *Nuclear Engineering and Design*, vol. 177, no. 13, pp. 53 – 69, 1997.

[99] K.-Y. Lee and M. H. Kim, "Experimental and empirical study of steam condensation heat transfer with a noncondensable gas in a small-diameter vertical tube," *Nuclear Engineering and Design*, vol. 238, no. 1, pp. 207 – 216, 2008.

[100] A. P. Colburn, "Calculation of condensation with a portion of condensate layer in turbulent motion," *Industrial and Engineering Chemistry*, vol. 26, pp. 432–434, 1934.

[101] A. P. Colburn and O. A. Hougen, "Design of cooler condensers for mixtures of vapors with noncondensing gases," *Industrial and Engineering Chemistry*, vol. 26, pp. 1178–1182, 1934.

[102] T. H. Chilton and A. P. Colburn, "Mass transfer (absorption) coefficients - prediction from data on great transfer and fluid friction," *Industrial and Engineering Chemistry*, vol. 26, pp. 1183–1187, 1934.

[103] M. L. Corradini, "Turbulent condensation on a cold wall in the presence of a non-condensable gas," *Nuclear Technology*, vol. 64, no. 2, pp. 186–195, 1984.

[104] M. H. Kim and M. L. Corradini, "Modeling of condensation heat-transfer in a reactor containment," *Nuclear Engineering and Design*, vol. 118, no. 2, pp. 193–212, 1990.

[105] P. F. Peterson, V. E. Schrock, and T. Kageyama, "Diffusion layer theory for turbulent vapor condensation with noncondensable gases," *Journal of Heat Transfer-Transactions of the Asme*, vol. 115, no. 4, pp. 998–1003, 1993.

[106] T. Kageyama, P. F. Peterson, and V. E. Schrock, "Diffusion layer modeling for condensation in vertical tubes with noncondensable gases," *Nuclear Engineering and Design*, vol. 141, no. 1-2, pp. 289–302, 1993.

[107] E. M. Sparrow and E. R. G. Eckert, "Effects of superheated vapor and noncondensable gases on laminar film condensation," *Aiche Journal*, vol. 7, no. 3, pp. 473–477, 1961.

[108] E. M. Sparrow and S. H. Lin, "Condensation heat transfer in the presence of a non-condensable gas," *Journal of Heat Transfer*, vol. 86, no. 3, pp. 430–436, 1964.

[109] W. Minkowycz and E. Sparrow, "Condensation heat transfer in the presence of noncondensables, interfacial resistance, superheating, variable properties, and diffusion," *Int. J. Heat Mass Trans.*, vol. 9, p. 1125, 1966.

[110] E. Sparrow, W. Minkowycz, and M. Saddy, "Forced convection condensation in the presence of noncondensables and interfacial resistance," *Int. J. Heat Mass Trans.*, vol. 10, p. 1829, 1967.

[111] Y. Mori and K. Hijikata, "Free convective condensation heat-transfer with noncondensable gas on a vertical surface," *International Journal of Heat and Mass Transfer*, vol. 16, no. 12, p. 2229, 1973.

[112] V. E. Denny, A. F. Mills, and V. J. Jusionis, "Laminar film condensation from a steam-air mixture undergoing forced flow down a vertical surface," *Journal of Heat Transfer*, vol. 93, no. 3, p. 297, 1971.

[113] V. E. Denny and V. J. Jusionis, "Effects of noncondensable gas and forced flow on laminar film condensation," *International Journal of Heat and Mass Transfer*, vol. 15, no. 2, p. 315, 1972.

[114] E. C. Siow, S. J. Ormiston, and H. M. Soliman, "Fully coupled solution of a two-phase model for laminar film condensation of vapor-gas mixtures in horizontal channels," *International Journal of Heat and Mass Transfer*, vol. 45, no. 18, pp. 3689–3702, 2002.

[115] E. C. Siow, S. J. Ormiston, and H. M. Soliman, "A two-phase model for laminar film condensation from steam-air mixtures in vertical parallel-plate channels," *Heat and Mass Transfer*, vol. 40, no. 5, pp. 365–375, 2004.

[116] E. C. Siow, S. J. Ormiston, and H. M. Soliman, "Two-phase modelling of laminar film condensation from vapour-gas mixtures in declining parallel-plate channels," *International Journal of Thermal Sciences*, vol. 46, no. 5, pp. 458–466, 2007.

[117] R. H. Pletcher, "Prediction of transpired turbulent boundary layers," *ASME. J. Heat Transfer.*, vol. 96, no. 1, pp. 89–94, 1974.

[118] B. L. W.P. Jones, "The predictions of laminarization with a two-equation model of turbulence," *Int. J. Heat Mass Transfer*, vol. 15, p. 301314, 1972.

[119] R. Yuann, *Condensation from vapor-gas mixtures for forced downflow inside a tube*. Ph.d. thesis, University of California, Berkeley, 1993.

[120] M. K. Groff, S. J. Ormiston, and H. M. Soliman, "Numerical solution of film condensation from turbulent flow of vapor-gas mixtures in vertical tubes," *International Journal of Heat and Mass Transfer*, vol. 50, no. 19-20, pp. 3899–3912, 2007.

[121] J. M. Martin-Valdepenas, M. A. Jimenez, F. Martin-Fuertes, and J. A. Fernandez, "Improvements in a cfd code for analysis of hydrogen behaviour within containments," *Nuclear Engineering and Design*, vol. 237, no. 6, pp. 627–647, 2007.

[122] K. Karkoszka and H. Anglart, "Multidimensional effects in laminar filmwise condensation of water vapour in binary and ternary mixtures with noncondensable gases," *Nuclear Engineering and Design*, vol. 238, no. 6, pp. 1373–1381, 2008.

[123] A. Dehbi, F. Janasz, and B. Bell, "Prediction of steam condensation in the presence of noncondensable gases using a cfd-based approach," *Nuclear Engineering and Design*, vol. 258, pp. 199–210, 2013.

[124] G. Zschaeck, T. Frank, and A. D. Burns, "Cfd modelling and validation of wall condensation in the presence of non-condensable gases," *Nuclear Engineering and Design*, vol. 279, pp. 137–146, 2014.

[125] R. Marek and J. Straub, "The origin of thermocapillary convection in subcooled nucleate pool boiling," *International Journal of Heat and Mass Transfer*, vol. 44, no. 3, pp. 619–632, 2001.

[126] M. Barthes, C. Reynard, R. Santini, and L. Tadrist, "Non-condensable gas influence on the marangoni convection during a single vapour bubble growth in a subcooled liquid," *Epl*, vol. 77, no. 1, 2007.

[127] C. Reynard, M. Barthes, R. Santini, and L. Tadrist, "Experimental study of the onset of the 3d oscillatory thermocapillary convection around a single air or vapor bubble. influence on heat transfer," *Experimental Thermal and Fluid Science*, vol. 29, no. 7, pp. 783–793, 2005.

[128] F. Chauvet, S. Dehaeck, and P. Colinet, "Threshold of benard-marangoni instability in drying liquid films," *Epl*, vol. 99, no. 3, 2012.

[129] C. W. Hirt and B. D. Nichols, "Volume of fluid (vof) method for the dynamics of free boundaries," *Journal of Computational Physics*, vol. 39, no. 1, pp. 201–225, 1981.

[130] R. Scardovelli and S. Zaleski, "Direct numerical simulation of free-surface and interfacial flow," *Annual Review of Fluid Mechanics*, vol. 31, pp. 567–603, 1999.

[131] D. Gueyffier, J. Li, A. Nadim, R. Scardovelli, and S. Zaleski, "Volume-of-fluid interface tracking with smoothed surface stress methods for three-dimensional flows," *Journal of Computational Physics*, vol. 152, no. 2, pp. 423–456, 1999.

[132] P. Queutey and M. Visonneau, "An interface capturing method for free-surface hydrodynamic flows," *Computers & Fluids*, vol. 36, no. 9, pp. 1481–1510, 2007.

[133] M. Sussman, P. Smereka, and S. Osher, "A level set approach for computing solutions to incompressible 2-phase flow," *Journal of Computational Physics*, vol. 114, no. 1, pp. 146–159, 1994.

[134] J. A. Sethian, "Evolution, implementation, and application of level set and fast marching methods for advancing fronts," *Journal of Computational Physics*, vol. 169, no. 2, pp. 503–555, 2001.

[135] S. Osher and R. P. Fedkiw, "Level set methods: An overview and some recent results," *Journal of Computational Physics*, vol. 169, no. 2, pp. 463–502, 2001.

[136] F., R. Fedkiw, and S. Osher, "Spatially adaptive techniques for level set methods and incompressible flow," *Computers & Fluids*, vol. 35, no. 10, pp. 995–1010, 2006.

[137] T. Nakamura, R. Tanaka, T. Yabe, and K. Takizawa, "Exactly conservative semi-lagrangian scheme for multi-dimensional hyperbolic equations with directional splitting technique (vol 174, pg 171, 2001)," *Journal of Computational Physics*, vol. 175, no. 2, pp. 792–792, 2002.

[138] D. Jacqmin, "Calculation of two-phase navier-stokes flows using phase-field modeling," *Journal of Computational Physics*, vol. 155, no. 1, pp. 96–127, 1999.

[139] B. Lafaurie, C. Nardone, R. Scardovelli, S. Zaleski, and G. Zanetti, "Modeling merging and fragmentation in multiphase flows with surfer," *Journal of Computational Physics*, vol. 113, no. 1, pp. 134–147, 1994.

[140] S. Popinet and S. Zaleski, "A front-tracking algorithm for accurate representation of surface tension," *International Journal for Numerical Methods in Fluids*, vol. 30, no. 6, pp. 775–793, 1999.

[141] M. M. Francois, S. J. Cummins, E. D. Dendy, D. B. Kothe, J. M. Sicilian, and M. W. Williams, "A balanced-force algorithm for continuous and sharp interfacial surface tension models within a volume tracking framework," *Journal of Computational Physics*, vol. 213, no. 1, pp. 141–173, 2006.

[142] J. Glimm, O. Mcbryan, R. Menikoff, and D. H. Sharp, "Front tracking applied to rayleigh-taylor instability," *Siam Journal on Scientific and Statistical Computing*, vol. 7, no. 1, pp. 230–251, 1986.

[143] J. Glimm, J. Grove, B. Lindquist, O. A. Mcbryan, and G. Tryggvason, "The bifurcation of tracked scalar waves," *Siam Journal on Scientific and Statistical Computing*, vol. 9, no. 1, pp. 61–79, 1988.

[144] S. O. Unverdi and G. Tryggvason, "A front-tracking method for viscous, incompressible, multi-fluid flows," *Journal of Computational Physics*, vol. 100, no. 1, pp. 25–37, 1992.

[145] D. Juric and G. Tryggvason, "A front-tracking method for dendritic solidification," *Journal of Computational Physics*, vol. 123, no. 1, pp. 127–148, 1996.

[146] G. Tryggvason, B. Bunner, A. Esmaeeli, D. Juric, N. Al-Rawahi, W. Tauber, J. Han, S. Nas, and Y. J. Jan, "A front-tracking method for the computations of multiphase flow," *Journal of Computational Physics*, vol. 169, no. 2, pp. 708–759, 2001.

[147] G. Ryskin and L. G. Leal, "Numerical-solution of free-boundary problems in fluid-mechanics .1. the finite-difference technique," *Journal of Fluid Mechanics*, vol. 148, no. Nov, pp. 1–17, 1984.

[148] G. Ryskin and L. G. Leal, "Numerical-solution of free-boundary problems in fluid-mechanics .2. buoyancy-driven motion of a gas bubble through a quiescent liquid," *Journal of Fluid Mechanics*, vol. 148, no. Nov, pp. 19–35, 1984.

[149] G. Ryskin and L. G. Leal, "Numerical-solution of free-boundary problems in fluid-mechanics .3. bubble deformation in an axisymmetric straining flow," *Journal of Fluid Mechanics*, vol. 148, no. Nov, pp. 37–43, 1984.

[150] S. Takagi and Y. Matsumoto, "3-dimensional deformation of a rising bubble," *Proceedings of the German-Japanese Symposium on Multi-Phase Flow*, pp. 499–511, 1994.

[151] B. Yang and A. Prosperetti, "A second-order boundary-fitted projection method for free-surface flow computations," *Journal of Computational Physics*, vol. 213, no. 2, pp. 574–590, 2006.

[152] M. Z. Dai and D. P. Schmidt, "Adaptive tetrahedral meshing in free-surface flow," *Journal of Computational Physics*, vol. 208, no. 1, pp. 228–252, 2005.

[153] S. P. Quan and D. P. Schmidt, "A moving mesh interface tracking method for 3d incompressible two-phase flows," *Journal of Computational Physics*, vol. 221, no. 2, pp. 761–780, 2007.

[154] S. P. Quan, J. Lou, and D. P. Schmidt, "Modeling merging and breakup in the moving mesh interface tracking method for multiphase flow simulations," *Journal of Computational Physics*, vol. 228, no. 7, pp. 2660–2675, 2009.

[155] Z. Tukovic and H. Jasak, "A moving mesh finite volume interface tracking method for surface tension dominated interfacial fluid flow," *Computers & Fluids*, vol. 55, pp. 70–84, 2012.

[156] S. Chapman and T. Cowling, *The mathematical theory of non-uniform gases: an account of the kinetic theory of viscosity, thermal conduction, and diffusion in gases*. Cambridge: Cambridge University Press, 1990.

[157] R. W. Schunk, "Mathematical structure of transport equations for multispecies flows," *Reviews of Geophysics*, vol. 15, no. 4, pp. 429–445, 1977.

[158] H. Grad, "On the kinetic theory of rarefied gases," *Communications on Pure and Applied Mathematics*, vol. 2, no. 4, pp. 331–407, 1949.

[159] B. B. Hamel, "Two-fluid hydrodynamic equations for a neutral, disparate-mass, binary mixture," *Phys. Fluids*, vol. 9, p. 12, 1966.

[160] M. J. Moran and H. N. Shapiro, *Fundamentals of engineering thermodynamics*. Wiley, 2004.

[161] C. L. Yaws, *Yaws' Handbook of Thermodynamic and Physical Properties of Chemical Compounds (Electronic Edition): physical, thermodynamic and transport properties for 5,000 organic chemical compounds*. Norwich: Knovel, 2003.

[162] C. L. Yaws, *Yaws' Thermophysical Properties of Chemicals and Hydrocarbons (Electronic Edition)*. Norwich: Knovel, 2009.

[163] R. Reid, J. Prausnitz, and B. Poling, *The Properties of Gases and Liquids*. Chemical engineering series, McGraw-Hill, 1987.

[164] K. E. Grew and T. L. Ibbs, *Thermal diffusion in gases*. Cambridge monographs on physics, Cambridge [Eng.] University Press, 1952., 1952.

[165] L. Landau and E. Lifshitz, *Fluid Mechanics*. Elsevier Science, 2013.

[166] R. B. Bird, *Dynamics of polymeric liquids*. New York : Wiley, c1977., 1977.

[167] J. Hirschfelder, C. Curtiss, and R. Bird, *Molecular theory of gases and liquids*. Structure of matter series, Wiley, 1954.

[168] O. L. Flaningam, "Vapor pressures of poly(dimethylsiloxane) oligomers," *J. Chem. Eng. Data*, vol. 31, pp. 266–272, 1986.

[169] C. R. Wilke, "Viscosity equation for gas mixtures," *Journal of Chemical Physics*, vol. 18, pp. 517 – 519, 1950.

[170] W. Sutherland, "Lii. the viscosity of gases and molecular force," *Philosophical Magazine Series 5*, vol. 36, no. 223, pp. 507–531, 1893.

[171] F. White, *Heat and Mass Transfer*. Addison-Wesley series in mechanical engineering, Addison-Wesley, 1988.

[172] R. W. Schrage, *A Theoretical Study of Interface Mass Transfer*. New York: Columbia University Press, 1953.

[173] G. Wyllie, "Evaporation and surface structure of liquids," *Proc. Royal Soc. London*, vol. 197, pp. 383–395, 1949.

[174] R. Rudolf, M. Itoh, Y. Viisanen, and P. Wagner, "Sticking probabilities for condensation of polar and nonpolar vapor molecules," in *Nucleation and Atmospheric Aerosols* (N. Fukuta and P. E. Wagner, eds.), pp. 165–168, Hampton: A. Deepak Publishing, 1992.

[175] G. Balekjian and D. L. Katz, "Heat transfer from superheated vapors to a horizontal tube," *AIChE Journal*, vol. 4, no. 1, pp. 43–48, 1958.

[176] J. Klentzman and V. S. Ajaev, "The effect of evaporation on fingering instabilities," *Phys. Fluids*, vol. 21, p. 122101, 2009.

[177] S. Kjelstrup and D. Bedeaux, *Non-Equilibrium Thermodynamics of Heterogeneous Systems*. Singapore: World Scientific, 2008.

[178] H. Struchtrup, S. Kjelstrup, and D. Bedeaux, "Temperature-difference-driven mass transfer through the vapor from a cold to a warm liquid," *Phys. Rev. E*, vol. 85, p. 061201, 2012.

[179] C. A. Ward, R. D. Findlay, and M. Rizk, "Statistical rate theory of interfacial transport. i. theoretical development," *J. Chem. Phys.*, vol. 76, p. 5599, 1982.

[180] C. A. Ward and G. Fang, "Expression for predicting liquid evaporation flux: Statistical rate theory approach," *Phys. Rev. E*, vol. 59, pp. 429–440, Jan 1999.

[181] G. Fang and C. A. Ward, "Temperature measured close to the interface of an evaporating liquid," *Phys. Rev. E*, vol. 59, pp. 417–428, 1999.

[182] V. K. Badam, V. Kumar, F. Durst, and K. Danov, "Experimental and theoretical investigations on interfacial temperature jumps during evaporation," *Exp. Therm. and Fluid Sci.*, vol. 32, pp. 276–292, 2007.

[183] M. Bond and H. Struchtrup, "Mean evaporation and condensation coefficients based on energy dependent condensation probability," *Phys. Rev. E*, vol. 70, p. 061605, Dec 2004.

[184] D. Villers and J. K. Platten, "Separation of marangoni convection from gravitational convection in earth experiments," *Phys. Chem. Hydrodyn.*, vol. 8, pp. 173–183, 1987.

[185] T. Qin, Ž. Tuković, and R. O. Grigoriev, "Buoyancy-thermocapillary convection of volatile fluids under atmospheric conditions," *Int. J Heat Mass Transf.*, vol. 75, pp. 284–301, 2014.

[186] G. K. Batchelor, *An Introduction to Fluid Dynamics*. Cambridge: Cambridge University Press, 1967.

[187] P. Hintz, D. Schwabe, and H. Wilke, "Convection in a czochralski crucible - part 1 : non-rotating crystal," *Journal of Crystal Growth*, vol. 222, pp. 343–355, 2001.

[188] P. Gillon and G. M. Homsy, "Combined thermocapillary-buoyancy convection in a cavity: An experimental study," *Phys. Fluids*, vol. 8, pp. 2953–2963, 1996.

[189] J. M. Ha and G. P. Peterson, "Analytical prediction of the axial dryout point for evaporating liquids in triangular microgrooves," *ASME J. Heat Transfer*, vol. 116, pp. 498–503, 1994.

[190] M. Markos, V. S. Ajaev, and G. M. Homsy, "Steady flow and evaporation of a volatile liquid in a wedge," *Phys. Fluids*, vol. 18, p. 092102, 2006.

[191] A. Faghri, *Heat Pipe Science And Technology*. Boca Raton: Taylor & Francis Group, 1995.

[192] T. Qin, Ž. Tuković, and R. O. Grigoriev, "Buoyancy-thermocapillary convection of volatile fluids under their vapors," *Int. J Heat Mass Transf.*, vol. 80, pp. 38–49, 2015.

[193] T. Qin and R. O. Grigoriev, "Convection, evaporation, and condensation of simple and binary fluids in confined geometries," in *Proc. of the 3rd Micro/Nanoscale Heat & Mass Transfer International Conference*, pp. paper MNHMT2012–75266, 2012.

[194] J. P. Burelbach, S. G. Bankoff, and S. H. Davis, "Nonlinear stability of evaporating/condensing liquid films," *J. Fluid Mech.*, vol. 195, pp. 463–494, 1988.

[195] C. Normand, Y. Pomeau, and M. Velarde, "Convective instability: A physicist's approach," *Rev. Modern Phys.*, vol. 49, p. 581, 1977.

[196] C. A. Ward and D. Stanga, "Interfacial conditions during evaporation or condensation of water," *Phys. Rev. E*, vol. 64, p. 051509, 2001.

[197] F. Duan, C. A. Ward, V. K. Badam, and F. Durst, "Role of molecular phonons and interfacial-temperature discontinuities in water evaporation," *Phys. Rev. E*, vol. 78, p. 041130, 2008.

[198] B. Paul, "Complication of evaporation coefficients," *ARS J*, vol. 32, pp. 1321–1328, 1962.

[199] R. Marek and J. Straub, "Analysis of the evaporation coefficient and the condensation coefficient of water," *Int. J Heat Mass. Transf.*, vol. 44, p. 3953, 2001.

[200] T. Qin and R. O. Grigoriev, "The effect of noncondensables on buoyancy-thermocapillary convection of volatile fluids in confined geometries," *Int. J Heat Mass Transf.*, vol. 90, pp. 678–688, 2015.

[201] A. Mozumder, A. Akon, M. Chowdhury, and S. Banik, "Performance of heat pipe for different working fluids and fill ratios," *Journal of Mechanical Engineering*, vol. 41, no. 2, pp. 96–102, 2010.

[202] M. C. Cross and H. Greenside, *Pattern Formation and Dynamics in Nonequilibrium Systems*. Cambridge: Cambridge University Press, 2009.

[203] P. Kavehpour, B. Ovryn, and G. H. McKinley, "Evaporatively-driven marangoni instabilities of volatile liquid films spreading on thermally conductive substrates," *Colloids and Surfaces A: Physicochemical and Engineering Aspects*, vol. 206, no. 13, pp. 409 – 423, 2002.

[204] Y. Li and M. Yoda, "The wave length of the pattern for buoyancy-thermocapillary convection in 0.65 cSt silicone oil." private communication, 2015.

[205] P. G. Daniels, "High rayleigh number thermal convection in a shallow laterally heated cavity," *Proceedings of the Royal Society of London. Series A: Mathematical and Physical Sciences*, vol. 440, pp. 273–289, 1993.

[206] P. Wang and P. G. Daniels, "Numerical solutions for the flow near the end of a shallow laterally heated cavity," *J. Eng. Math.*, vol. 28, pp. 211–226, 1994.

[207] N. Riley, "Heat transfer in Jeffery-Hamel flow," *Q. J. Mech. Appl. Math.*, vol. 42, pp. 203–211, 1989.

[208] D. M. Anderson and S. H. Davis, "Local fluid and heat flow near contact lines," *J. Fluid Mech.*, vol. 268, pp. 231–265, 1994.

[209] S. J. S. Morris, "A phenomenological model for the contact region of an evaporating meniscus on a superheated slab," *J. Fluid Mech.*, vol. 411, pp. 59–89, 2000.

[210] S. J. S. Morris, "Heat flow near the triple junction of an evaporating meniscus and a substrate," *Proc. R. Soc. Lond. A*, vol. 460, pp. 2487–2503, 2004.

[211] V. S. Ajaev and G. M. Homsy, "Steady vapor bubbles in rectangular microchannels," *Journal of Colloid and Interface Science*, vol. 240, pp. 259–271, 2001.

[212] http://www.openfoam.com.

[213] J. C. Tannehill, D. A. Anderson, and R. H. Pletcher, *Computational fluid mechanics and heat transfer*. Washington, DC: Taylor & Francis, 2nd ed., 1997.

[214] J. H. Ferziger and M. Peric, *Computational methods for fluid dynamics*. Berlin: Springer, 1997.

[215] I. DemirdÅi and S. Muzaferija, "Numerical method for coupled fluid flow, heat transfer and stress analysis using unstructured moving meshes with cells of arbitrary topology," *Computer Methods in Applied Mechanics and Engineering*, vol. 125, no. 14, pp. 235 – 255, 1995.

[216] H. Jasak, *Error analysis and estimation for the finite volume method with applications to fluid flows*. PhD thesis, 1996.

[217] C. M. Rhie and W. L. Chow, "Numerical study of the turbulent flow past an airfoil with trailing edge separation," *AIAA Journal*, vol. 21, pp. 1525–1532, Nov. 1983.

[218] T. Theodoropoulos, *Prediction of three-dimensional engine ow on unstructured meshes*. PhD thesis, 1990.

[219] G. Golub and C. Van Loan, *Matrix Computations*. Johns Hopkins University Press, 2012.

[220] H. Rusche, *Computational fluid dynamics of dispersed two-phase flows at high phase fractions*. PhD thesis, 2002.

[221] I. Demirdzic and M. Peric, "Space conservation law in finite volume calculations of fluid-flow," *International Journal for Numerical Methods in Fluids*, vol. 8, no. 9, pp. 1037–1050, 1988.

[222] P. Geuzaine, C. Grandmont, and C. Farhat, "Design and analysis of ale schemes with provable second-order time-accuracy for inviscid and viscous flow simulations," *Journal of Computational Physics*, vol. 191, no. 1, pp. 206–227, 2003.

[223] C. Farhat and P. Geuzaine, "Design and analysis of robust ale time-integrators for the solution of unsteady flow problems on moving grids," *Computer Methods in Applied Mechanics and Engineering*, vol. 193, no. 39-41, pp. 4073–4095, 2004.

[224] H. Jasak and Z. Tukovic, "Dynamic mesh handling in openfoam applied to fluid-structure interaction simulations," in *Proceedings of the V European Conference on Computational Fluid Dynamics (ECCOMAS CFD)*, 2010.

[225] S. Muzaferija and M. Peric, "Computation of free-surface flows using the finite-volume method and moving grids," *Numerical Heat Transfer Part B-Fundamentals*, vol. 32, no. 4, pp. 369–384, 1997.

[226] R. I. Issa, "Solution of the implicitly discretized fluid flow equations by operator-splitting," *J. Comp. Phys.*, vol. 62, pp. 40–65, 1986.

[227] C. M. Rhie and W. L. Chow, "Numerical study of the turbulent-flow past an airfoil with trailing edge separation," *Aiaa Journal*, vol. 21, no. 11, pp. 1525–1532, 1983.

[228] B. Yu, Y. Kawaguchi, W. Q. Tao, and H. Ozoe, "Checkerboard pressure predictions due to the underrelaxation factor and time step size for a nonstaggered grid with momentum interpolation method," *Numerical Heat Transfer Part B-Fundamentals*, vol. 41, no. 1, pp. 85–94, 2002.

[229] B. Yu, W. Q. Tao, J. J. Wei, Y. Kawaguchi, T. Tagawa, and H. Ozoe, "Discussion on momentum interpolation method for collocated grids of incompressible flow," *Numerical Heat Transfer Part B-Fundamentals*, vol. 42, no. 2, pp. 141–166, 2002.

[230] W. Z. Shen, J. A. Michelsen, and J. N. Sorensen, "Improved rhie-chow interpolation for unsteady flow computations," *Aiaa Journal*, vol. 39, no. 12, pp. 2406–2409, 2001.